Volume 98, Number 3, May–June 1993
Journal of Research of the National Institute of Standards and Technology

Contents

Articles

Conference Reports

News Briefs

Volume 98, Number 3, May–June 1993
Journal of Research of the National Institute of Standards and Technology

Volume 98, Number 3, May–June 1993
Journal of Research of the National Institute of Standards and Technology

Volume 98, Number 3, May-June 1993
Journal of Research of the National Institute of Standards and Technology

[J. Res. Natl. Inst. Stand. Technol. 98, 287 (1993)]

Coil Probe Dimension and Uncertainties During Measurements of Nonuniform ELF Magnetic Fields

Volume 98 Number 3 May-June 1993

Martin Misakian

National Institute of Standards and Technology,
Gaithersburg, MD 20899-0001

Comparisons are made between the calculated average magnetic flux density for single-axis and three-axis circular coil probes and the calculated magnetic flux density at the center of the probes. The results, which are determined assuming a dipole magnetic field, provide information on the uncertainty associated with measurements of nonuniform extremely low frequency (ELF) magnetic fields produced by some electrical appliances and other electrical equipment.

Key words: appliance; coil probe; dipole field; magnetic field; measurement; measurement uncertainty; power frequency; residential; transportation systems; work place.

Accepted: January 28, 1993

1. Introduction

The concern in the mid 1970s regarding health effects from exposure to electric and magnetic fields in the vicinity of power lines has shifted in recent years to health effect concerns from exposure to power frequency magnetic fields in residences, the work place, and in transportation systems [1–3]. The magnetic fields in these environments can be highly nonuniform, particularly near electrical equipment such as motors, transformers and heating elements. This paper considers the difference between the calculated average magnetic flux density, B_{av}, as determined using magnetic field meters with single-axis and three-axis circular coil probes, and the calculated magnetic flux density at the center of the probes, B_0 assuming the field is produced by a small loop of alternating current, i.e., a magnetic dipole. The magnetic dipole field is chosen as the relevant field because to a good approximation its geometry simulates the field geometry of many electrical appliances and equipment [4]. The difference between B_{av} and B_0 can be regarded as a source of measurement uncertainty because the center of the probe is normally considered the measurement location. While differences between B_{av} and B_0 will be small in many situations, e.g., near ground level in the vicinity of power lines where the field changes slowly, the difference can become significant in the highly nonuniform magnetic fields close to electrical equipment.

In this paper, two comparisons are made: (1) the maximum average magnetic field determined using a single-axis probe, B_{av1}, with B_0 as a function of r/a where r is the distance between the magnetic dipole and the center of the probe, and a is the radius of the probe, and (2) the resultant magnetic field determined using a three-axis probe with B_0 as a function of r/a. The resultant magnetic field, B_{av3}, is defined as [5]

$$B_{av3} = \sqrt{B_1^2 + B_2^2 + B_3^2}, \quad (1)$$

where B_1, B_2, and B_3 are average magnetic field components as measured by three orthogonally oriented coil probes.

Comparison (1) is made because maximum magnetic field values are sometimes measured, using single-axis field meters, to characterize the magnetic field [5,6]. However, for a given value of r/a, it will be seen that the difference between B_{av1} and B_0 will be a function of the orientation of the magnetic dipole relative to the probe. Because the relative orientation is not known during most measurements, what is of interest is the largest difference between B_{av1} and B_0 for a given value of r/a. This largest difference will be designated ΔB_{max1}.

The quantity ΔB_{max1} is determined in the following way. The single-axis probe is rotated for fixed values of r/a and the spherical coordinate, θ, [Fig. 1(a)] until the largest average magnetic field, B_{av1}, is found. This value of B_{av1} is compared with the magnetic field at the center of the probe, B_0 and the difference is recorded. The orientation of the magnetic dipole with respect to the probe is then varied by moving the probe to another location while keeping r/a fixed, i.e., by changing θ in Fig. 1(a). The probe is rotated again until the largest average magnetic field, B_{av1}, is found. B_{av1} is again compared with the magnetic field at the center of the probe, B_0, and the difference is recorded. This process is repeated for other dipole orientations (i.e., angle θ) until the largest difference, ΔB_{max1}, is found. An example of this process is shown in Sec. 3.1.

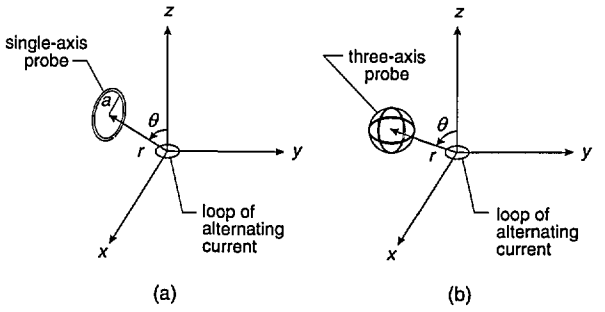

Fig. 1. (a) Single-axis and (b) three-axis circular coil probes in dipole magnetic field produced by small loop of current.

Comparison (2) is made as a three-axis probe is rotated about three axes parallel to the three Cartesian coordinates x, y, and z. The difference between B_{av3} and B_0 will vary as a function of rotation angle, but what will be of interest again is the largest difference, ΔB_{max3}, for a given r/a. Also as for comparison (1), because the relative orientations of the magnetic dipole and the three-axis probe will be unknown in most measurement situations, B_{av3} will be examined as a function of r/a and the spherical coordinate, θ, in order to determine the largest difference, ΔB_{max3}.

2. Expressions for Average Magnetic Flux Density

In the derivations given below, it is assumed that the cross sectional area of the wire in the coil probes and the opposing magnetic field produced by current induced in the probes are negligible. In addition, we assume for the three-axis probe that the three orthogonally oriented coils have circular cross sections of equal area. These assumptions either can be met in practice or can be taken into account via a calibration process.

2.1 Single-Axis Probe

The average magnetic flux density, B_{av}, for a single coil probe with cross sectional area A is given by

$$B_{av}=\frac{1}{A}\int\int_A \boldsymbol{B}\cdot\hat{n}\,dA, \tag{2}$$

where dA is an element of probe area, $\hat{n}$ is a unit vector perpendicular to A, and $\boldsymbol{B}$ is the magnetic flux density. In spherical coordinates, the magnetic flux density for a small current loop of radius b is [7]

$$\boldsymbol{B}=\frac{\mu_0 I b^2}{2r^3}\cos\theta\,\hat{u}_r+\frac{\mu_0 I b^2}{4r^3}\sin\theta\,\hat{u}_\theta, \tag{3}$$

where μ_0 is the permeability of vacuum, I is the alternating current, and $\hat{u}_r$ and $\hat{u}_\theta$ are unit vectors in the directions of increasing r and θ, respectively. The assumption is made that $b << r$ and the sinusoidal time dependence has been suppressed. The magnitude of the vector $\boldsymbol{B}$ given by Eq. (3) is B_0.

For our purposes, it is convenient to express $\boldsymbol{B}$ in terms of Cartesian coordinates. This is accomplished by using the following relations between spherical and Cartesian unit vectors and coordinates [8] in Eq. (3):

$$\begin{aligned}
\hat{u}_r &= \hat{\imath}\sin\theta\cos\phi+\hat{\jmath}\sin\theta\sin\phi+\hat{k}\cos\theta\\
\hat{u}_B &= \hat{\imath}\cos\theta\cos\phi+\hat{\jmath}\cos\theta\sin\phi-\hat{k}\sin\theta\\
x &= r\sin\theta\cos\phi\\
y &= r\sin\theta\sin\phi\\
z &= r\cos\theta.
\end{aligned} \tag{4}$$

After some algebra, $\boldsymbol{B}$ can be expressed as

$$\boldsymbol{B}=\hat{\imath}\frac{3Cxz}{2r^5}+\hat{\jmath}\frac{3Cyz}{2r^5}+\hat{k}\frac{C}{2r^3}\left(\frac{3z^2}{r^2}-1\right), \tag{5}$$

where $r=\sqrt{x^2+y^2+z^2}$ and C is the constant $\mu_0 Ib^2/2$.

To obtain an expression for B_{av}, we consider without loss of generality a probe with its center at $x=x_0, y=0$, and $z=z_0$ as shown in Fig. 2. We restrict the orientation of the probe so that its area is bisected by the x-z plane and first consider rotations of the probe about an axis parallel to the y-axis, i.e., the y'-axis shown in Fig. 2. For these conditions, the area of the coil probe, A, will be part of the surface given by the equation

$$z=m_\alpha(x-x_0)+z_0, \tag{6}$$

where α is the angle of rotation, $m_\alpha=\tan\alpha$, $x_0=r\sin\theta$, and $z_0=r\cos\theta$. The rotation of the probe corresponds to the rotation of this surface about the y'-axis, i.e., changing the slope of the surface (m_α) described by Eq. (6). It should be noted that the angle of rotation, α, shown in Fig. 2 is in the negative direction.

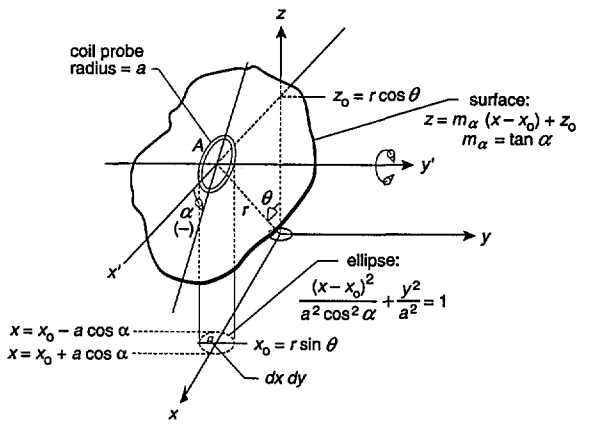

Fig. 2. Circular coil probe shown as part of a surface described by the equation $z=m_\alpha(x-x_0)+z_0$. The rotation of the probe corresponds to changing the slope of the surface, m_α. The projection of the probe cross sectional area onto the x-y plane will be an ellipse for $\alpha\neq 0$. The range of α is $-90°<\alpha<90°$.

The unit vector perpendicular to the probe surface, $\hat{n}$, is found by first taking the gradient [9] of the surface given by Eq. (6), $\nabla F(x,z)$, where $F(x,z)=z-m_\alpha(x-x_0)-z_0$ and normalizing it to unit value. This leads to

$$\hat{n}=(-m_\alpha\hat{\imath}+\hat{k})/\sqrt{m_\alpha^2+1}. \tag{7}$$

The element of area, dA, is [10]

$$dA=\sqrt{\left(\frac{\delta z}{\delta x}\right)^2+\left(\frac{\delta z}{\delta y}\right)^2+1}\,dx\,dy=\sqrt{m_\alpha^2+1}\,dx\,dy. \tag{8}$$

where $dx\,dy$ is an element of area in the x-y plane bounded by the projection of the probe cross section onto the x-y plane (Fig.2).

Combining Eqs. (2), (5), (7), and (8), the expression for B_{av} becomes

$$B_{av}=\frac{C}{2\pi a^2}\int_x\int_y\left\{\frac{-3xzm_\alpha}{r^5}+\frac{1}{r^3}\left(\frac{3z^2}{r^2}-1\right)\right\}dx\,dy. \tag{9}$$

By substituting for z in Eq. (9) using Eq. (6), the integrand becomes a function of x and y. The integration is first carried out analytically [11] over the variable y with (from Fig.2)

$$-\sqrt{a^2-((x-x_0)/\cos\alpha)^2}\le y\le$$

$$\sqrt{a^2-((x-x_0)/\cos\alpha)^2}.$$

The resulting expression for B_{av} is

$$B_{av}=-\frac{C}{\pi a^2}\int dx(m_\alpha xP+P^2)$$

$$\left\{\frac{\sqrt{a^2-\left(\frac{x-x_0}{\cos\alpha}\right)^2}}{(x^2+Q^2)\left(x^2+Q^2+a^2-\left(\frac{x-x_0}{\cos\alpha}\right)^2\right)^{3/2}}+\right.$$

$$\left.\frac{2\sqrt{a^2-\left(\frac{x-x_0}{\cos\alpha}\right)^2}}{(x^2+Q^2)^2\left(x^2+Q^2+a^2-\left(\frac{x-x_0}{\cos\alpha}\right)^2\right)^{1/2}}\right\}-$$

$$\frac{C}{\pi a^2}\int dx\frac{\sqrt{a^2-\left(\frac{x-x_0}{\cos\alpha}\right)^2}}{(x^2+Q^2)\left(x^2+Q^2+a^2-\left(\frac{x-x_0}{\cos\alpha}\right)^2\right)^{1/2}}, \tag{10}$$

where $P=(z_0-m_\alpha x_0)$ and $Q^2=(m_\alpha x+P)^2$.

The integration over x is then performed numerically using Simpson's Rule with the limits of integration given by (Fig. 2)

$$x_0-a\cos\alpha\le x\le x_0+a\cos\alpha,$$

where α is restricted to $-90°<\alpha<90°$.

B_{av} is evaluated for fixed values of θ and r/a as α is varied until a maximum average flux density, B_{av1}, is found. B_{av1} is then compared with B_0. As noted earlier, the process is repeated for the same r/a but different values of θ until the largest difference, ΔB_{max1}, is determined. Because we are seeking the maximum value of B_{av}, we do not consider further rotations of the probe because once B_{av1} is found, additional rotations are expected to lead to smaller values of B_{av}. This is most readily seen at θ equal to 0° and 90° for all values of r/a. B_{av1} occurs at $\alpha=0°$ and rotating the probe further results in smaller values of B_{av}.

2.2 Three-Axis Probe

In this section, expressions are developed for the average magnetic flux density for each coil of a three-axis probe as the probe is rotated about axes which are parallel to the x-, y-, and z-axes. Afterwards, for fixed values of θ and r/a, the average magnetic field values from the three orthogonally oriented probes are combined according to Eq. (1) to obtain B_{av3} which is then compared with B_0. As before, the process is repeated for different values of θ until the maximum difference between B_{av3} and B_0, ΔB_{max3}, is found.

It is noted that combinations of rotations about the different axes will not be possible using the expressions that are developed. That is, it will not be possible to calculate B_{av3} following rotations about two or three axes. This represents a limitation on the results and prevents us from learning whether there are significant effects on the value of ΔB_{max3} due to multiple rotations. Nevertheless, the departures from B_0 that are determined from rotations about each of the three axes will let us know what differences are possible as a function of r/a.

Figure 3 shows the orientation of the probe with respect to the magnetic dipole before rotations about each axis are considered. As in the previous section, the center of the probe is located at $x=x_0$, $y=0$, and $z=z_0$. The individual probes are labelled P1, P2, and P3, and initially P1 lies in the x'-y' plane, P2 is in the y'-z' plane, and P3 is in the x'-z' plane. When rotations are performed about the x'-axis (rotation angle β), the angle that P2 makes with the magnetic field remains unchanged. Similarly, rotations about the y'-axis (rotation angle α) and z'-axis (rotation angle γ) leave P3 and P1, respectively, "unchanged." This means that for constant values of r/a and θ, the average flux density values for these "fixed" probes remain constant as rotations of the probe occur.

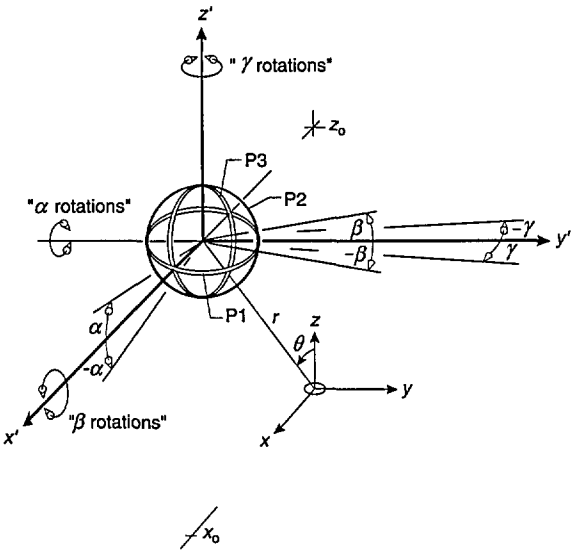

Fig. 3. Geometry for three-axis probe with center of probe in x-z plane. Varying the angle α result in rotations of probes P1 and P2 about the y'-axis ("α rotations") while orientation of probe P3 with respect to the dipole remains unchanged. Varying the angle β results in rotations of probes P1 and P3 about the x'-axis ("β rotations") while orientation of probe P2 remains unchanged. Varying the angle γ results in rotations of probes P2 and P3 about the z'-axis ("γ rotations") while orientation of probe P1 remains unchanged.

We begin the derivation for the three-axis probe by noting that part of the problem has already been solved in the previous section. That is, the expression for B_{av} following rotations about the y'-axis (α rotations) is given by Eq. (10). This expression is used to calculate the average flux density for probes P1 and P2 by considering pairs of the angle α which differ by 90°. The average flux density for the third probe, P3, is zero for this case because no component of the magnetic field is perpendicular to the area of the probe for any value of α or θ.

The derivations for B_{av} following β or γ rotations parallel the derivation for the α rotations. Examining the case of β rotations first, and referring to Fig. 4, it can be seen that the probe area, A, is part of the surface given by the equation

$$z=m_\beta y,+z_0, \qquad (11)$$

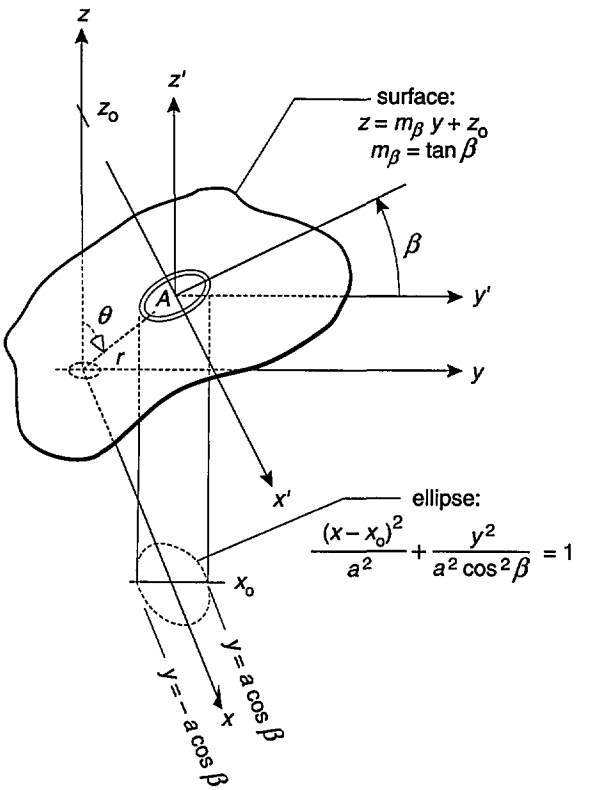

Fig. 4. Circular coil probe shown as part of a surface described by the equation $z = m_\beta y + z_0$. The rotation of the probe corresponds to changing the slope of the surface, m_β. The projection of the probe cross sectional area onto the x-y plane will be an ellipse for $\beta \neq 0$. The range of β is $-90° < \beta < 90°$.

where $m_\beta = \tan\beta$ and $z_0 = r\cos\theta$. The rotation of the probe corresponds to rotation of this surface about the x'-axis or alternatively, changing its slope, m_β. The unit vector normal to this surface is

$$\hat{n} = (-m_\beta \hat{j} + \hat{k})/\sqrt{m_\beta^2 + 1}, \tag{12}$$

and the element of area, dA, is

$$dA = \sqrt{\left(\frac{\delta z}{\delta x}\right)^2 + \left(\frac{\delta z}{\delta y}\right)^2 + 1}\, dx\, dy = \sqrt{m_\beta^2 + 1}\, dx\, dy. \tag{13}$$

Combining Eqs. (2), (5), (12), and (13), the expression for the average flux density following β rotations is

$$B_{av\beta} = \frac{1}{\pi a^2}\int_y\int_x \boldsymbol{B}\cdot\hat{n}\, dA =$$

$$-\frac{3Cm_\beta}{2\pi a^2}\int_y\int_x \frac{yz}{r^5}\, dx\, dy +$$

$$\frac{C}{2\pi a^2}\int_y\int_x \left(\frac{3z^2}{r^5} - \frac{1}{r^3}\right) dx\, dy. \tag{14}$$

Substituting for z in Eq. (14) using Eq. (11), the integrands become, recalling that $r = \sqrt{x^2+y^2+z^2}$, a function of x and y. The integration is first carried out analytically over the variable x with (Fig. 4)

$$x_0 - \sqrt{a^2 - (y/\cos\beta)^2} \le x \le x_0 + \sqrt{a^2 - (y/\cos\beta)^2}.$$

The y-integration is performed numerically with the limits of integration given by (Fig. 4)

$$-a\cos\beta \le y \le a\cos\beta,$$

where β is restricted to $-90° < \beta < 90°$.

Equation (14) is used to calculate the average flux density for probes P1 and P3 by considering pairs of the angle β which differ by 90°. The average flux density from the remaining probe, P2, remains constant during the β rotations and is determined from the expression for average flux density following γ rotation ($\gamma = 0$)—which is developed below. The reader is cautioned that during the numerical integration over the variable y, the denominator in the integrand vanishes for $y = 0$ when $\theta = 90°$.

In deriving the expression for average flux density following γ rotations, we note as shown in Fig. 5 that the probe area, A, is part of the surface given by the equation

$$x = m_\gamma y + x_0, \tag{15}$$

where $m_\gamma = \tan\gamma$ and $x_0 = r\sin\theta$. The rotation of the probe corresponds to rotation of this surface about the z'-axis, i.e., changing the slope of the surface, m_γ. The unit vector normal to this surface is

$$\hat{n} = (\hat{i} - m_\gamma \hat{j})/\sqrt{m_\gamma^2 + 1}, \tag{16}$$

and the element of area, dA, is

$$dA = \sqrt{\left(\frac{\delta x}{\delta y}\right)^2 + \left(\frac{\delta x}{\delta z}\right)^2 + 1}\, dy\, dz = \sqrt{m_\gamma^2 + 1}\, dy\, dz. \tag{17}$$

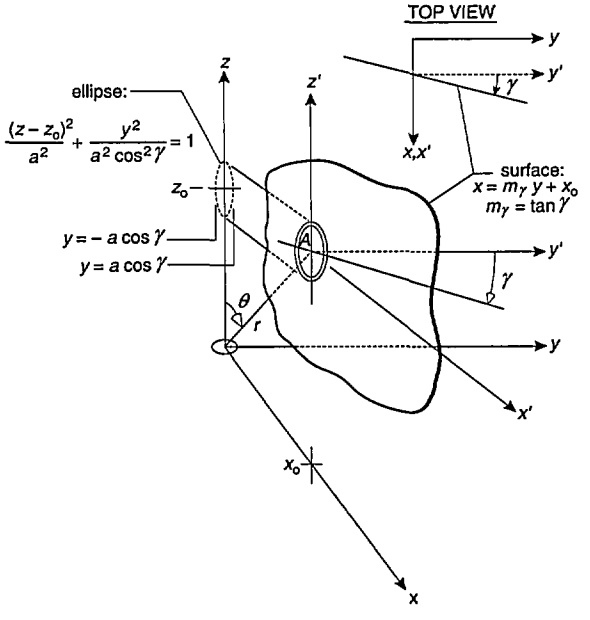

Fig. 5. Circular coil probe shown as part of a surface described by the equation $x = m_\gamma y + x_0$. The rotation of the probe corresponds to changing the slope of the surface, m_γ. The projection of the probe cross sectional area onto the y-z plane will be an ellipse for $\gamma \neq 0$. The range of γ is $-90° < \gamma < 90°$.

It should be noted that the projection of the probe's cross sectional area, unlike the previous two cases, is onto the y-z plane for γ rotations (the projections for α and β rotations were onto the x-y plane) and this fact affects the partial derivatives in the expression for dA, Eq. (17).

From Eqs. (2), (5), (16), and (17), the expression for average flux density following γ rotations is

$$B_{av\gamma} = \frac{1}{\pi a^2} \int_y \int_z \boldsymbol{B} \cdot \hat{n}\, dA =$$

$$\frac{3C}{2\pi a^2} \int_y \int_z \left(\frac{xz}{r^5} - \frac{m_\gamma yz}{r^5}\right) dz\, dy\,. \tag{18}$$

By substituting for x in Eq. (18) using Eq. (15), the integrand becomes a function of y and z. The integration is first carried out analytically over the variable z with (Fig. 5)

$$z_0 - \sqrt{a^2 - (y/\cos\gamma)^2} \leq z \leq z_0 + \sqrt{a^2 - (y/\cos\gamma)^2}.$$

The y-integration is performed numerically with the limits of integration given by

$$-a\cos\gamma \leq y \leq a\cos\gamma,$$

where γ is restricted to $-90° < \gamma < 90°$.

Equation (18) is used to calculate the average flux density for probes P2 and P3 by considering pairs of the angle, γ, which differ by 90°. The average flux density from the remaining probe, P1, remains constant during the γ rotations and is calculated from the expression for average flux density for α rotations [Eq. (10)] with α set equal to zero.

3. Results of Calculations

3.1 ΔB_{max1} for Single-Axis Probe

Using Eq. (10) and following the procedure described after Eq. (1), values of the maximum average magnetic field, B_{av1} for fixed values of r/a and θ were calculated and compared with the corresponding value of B_0. Figure 6 shows the differences in percent between B_{av1} and B_0 for $r/a = 3$ and for representative values of θ between 0° and 90° (because of symmetry arguments, one can infer the corresponding percentages for θ between 90° and 180°). The largest difference, ΔB_{max1}, is -14.6% and occurs when the single-axis probe is located along the axis of the magnetic dipole, i.e., the z-axis. The negative difference between B_{av1} and B_0 decreases as θ increases and turns positive near $\theta = 90°$. This pattern also occurs for other values of r/a greater than 3. Figure 6 also shows the largest negative and positive differences in percent for r/a equal to 5, 8, 10, and 12. The largest negative differences must be considered part of the measurement uncertainty when the probe-dipole geometry is unknown, which will be the case for example when magnetic field measurements are performed near many appliances. A tabulation of ΔB_{max1}, as a function of r/a is given in Table 1.

The calculations are not carried out for large values of r/a because the accuracy requirements for magnetic field measurements near appliances and other electrical equipment either have not been set or are not great. For example, the uncertainty tentatively allowed during calibration of magnetic field meters used for measuring magnetic fields near visual display terminals is ±5% [12].

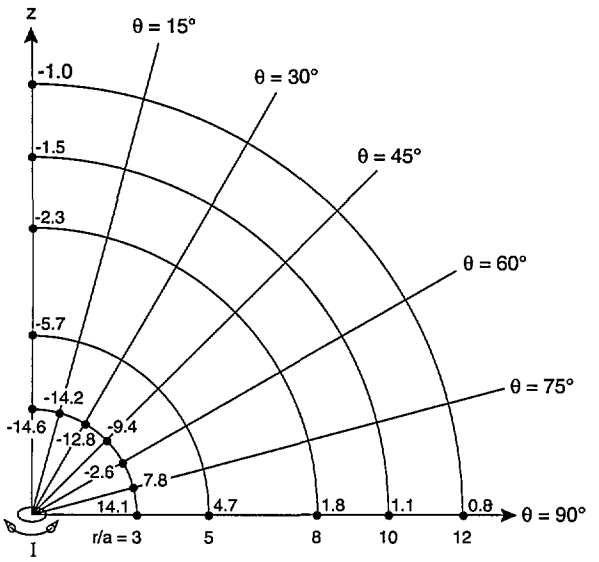

Fig. 6. Differences between values of B_{av1} and B_0, in percent, for different locations of single-axis probe relative to magnetic dipole which is aligned along the z-axis. For a given value of r/a, where r/a is ≥ 3, the largest difference, ΔB_{max1}, is negative and occurs when the probe is located along the z-axis.

Table 1. Values of ΔB_{max1} (single-axis probe) and ΔB_{max3} (three-axis probe) as a function of normalized distance (r/a) from magnetic dipole

r/a	ΔB_{max1} (%)	ΔB_{max3} (%)
3	−14.6	−19.6
4	−8.7	−10.8
5	−5.7	−6.9
6	−4.0	−4.8
7	−3.0	−3.5
8	−2.3	−2.7
9	−1.8	−2.1
10	−1.5	−1.7
11	−1.2	−1.4
12	−1.0	−1.2
13	−0.9	−1.0
14	−0.8	−0.9
15	−0.7	−0.8

3.2 ΔB_{max3} for Three-Axis Probe

The differences between B_{av3} and B_0 are considered in three steps. First, values of B_{av3} are calculated following α rotations using Eq. (10) and compared with B_0 for fixed values of r/a and representative values of θ between 0° and 90°. As noted earlier, the largest difference between B_{av3} and B_0 at each point, a "local maximum difference," is recorded. In the discussion that follows, the "local maximum difference," will be referred to simply as the "difference." The above procedure is repeated for β and γ rotations.

The differences between β_{av3} and β_0 following α rotations are plotted in Fig. 7 for r/a equal to 3, 5, 8, 10, and 12. The numbers in Fig. 7 represent differences in percent. The pattern observed for all values of r/a is that the difference at a point following α rotation is always negative and becomes more negative as θ increases to 90°.

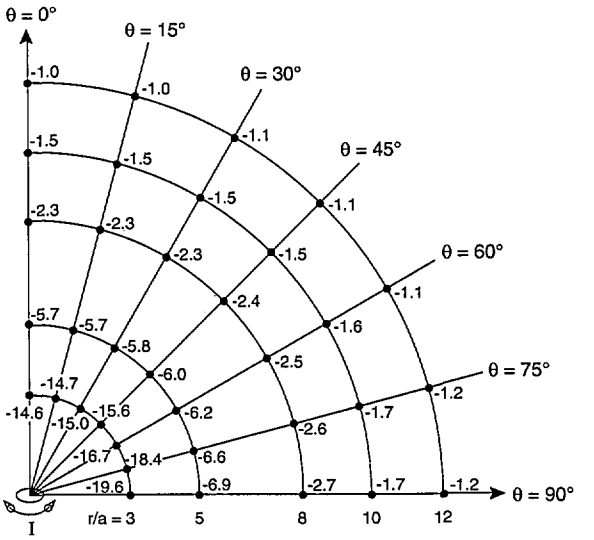

Fig. 7. Differences between values of B_{av3} and B_0 in percent, for different locations of three-axis probe relative to magnetic dipole, following α rotations. The differences are always negative and the greatest difference following α rotations occurs for $\theta = 90°$.

When the difference calculations are performed for β rotations using Eq. (14) and Eq. (18) (γ set equal to zero), a different pattern emerges. The differences between B_{av3} and B_0 are observed to change in sign at different points as shown in Fig. 8. By comparing the results in Figs. 7 and 8, it can be seen that, except for $\theta = 0$, the differences following β rotations are all less than the corresponding (i.e., same r/a and θ values) differences following α rotations. Although not indicated in Fig. 8 calculations show that for a given value of $r/a \geq 3$, the differences between B_{av3} and B_0 following β rotations for all values of θ are less than the difference following α rotations when $\theta = 90°$.

Similar results occur following γ rotations when B_{av3} is calculated using Eq. (18) and Eq. (10) (α set equal to zero) and is compared with B_0. Once again the differences between B_{av3} and B_0 change in sign as shown in Fig. 9. Also, by comparing results in Figs. 7 and 9, it is seen that, except for $\theta = 0°$, the

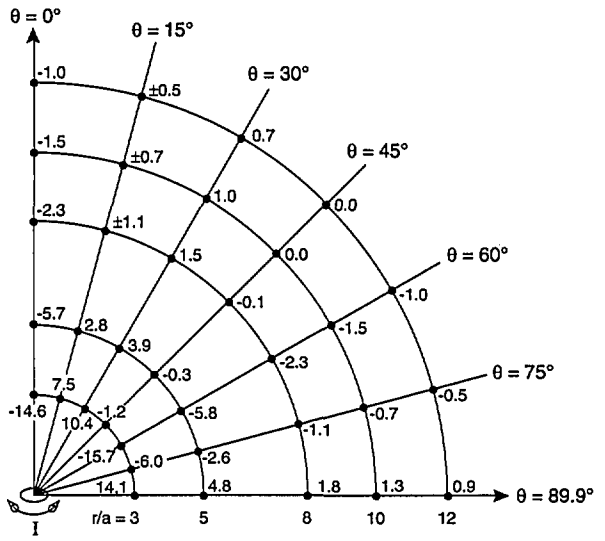

Fig. 8. Differences between values of B_{av3} and B_0 in percent, for different locations of three-axis probe relative to magnetic dipole, following β rotations. The differences vary in sign depending on angle θ. For $\theta = 15°$, there are several cases (indicated with the ± sign) for which the largest negative and positive differences are equal in magnitude.

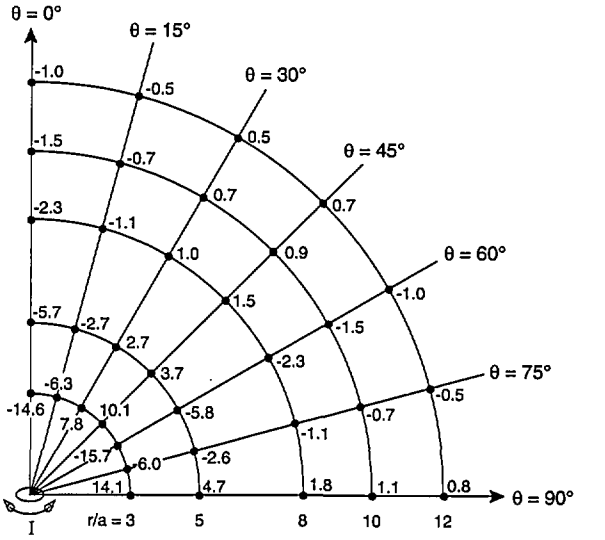

Fig. 9. Differences between values of B_{av3} and B_0 in percent, for different locations of three-axis probe relative to magnetic dipole, following γ rotations. The differences vary in sign depending on angle θ.

differences following γ rotations are all less than the corresponding differences following α rotations. As for the case of β rotations, calculations show that for a given value of $r/a \geq 3$, the largest difference following γ rotations will always be less than the difference following α rotations when $\theta = 90°$. Therefore, of the three types of three-axis probe rotations considered, the greatest difference between B_{av3} and B_0 can be found following α rotations and ΔB_{max3} occurs when $\theta = 90°$ for a given value of r/a. Table 1 provides a listing of ΔB_{max3} values as a function of r/a.

4. Discussion of Results

Once it has been decided what constitutes an acceptable level of uncertainty during magnetic field measurements near electrical equipment, the information in Table 1 should be considered when taking into account the various sources of measurement uncertainty. For example, if maximum magnetic fields at a distance r from appliances are to be measured with a total uncertainty of less than ±10%, magnetic field meters with probes having radii a such that $r/a \approx 3$ would immediately be considered unsuitable. Field meters with single-axis probes having radii such that $r/a = 5$ would be suitable if all other sources of uncertainty (e.g., calibration process, frequency response) amounted to about 8% or less, i.e., $\sqrt{5.7^2 + 8^2} = 9.8$, where 5.7 is taken from Table 1 for $r/a = 5$.

The measurement uncertainties associated with using three-axis probes are less clear because we have considered only separate rotations about three axes to obtain the values of ΔB_{max3}. The percentage differences in Table 1 indicate what uncertainties can occur but they may not be the largest uncertainties due to the averaging effects of the probe. However, until calculations can be devised which consider more complex rotations of three-axis probes, the ΔB_{max3} values in Table 1 can serve as a rough guide when deciding what are acceptable probe dimensions.

5. Acknowledgments

This work was performed in the Electricity Division, Electronics and Electrical Engineering Laboratory, National Institute of Standards and Technology, Technology Administration of the U.S. Department of Commerce. Support was received from the Office of Energy Management of the U.S. Department of Energy.

6. References

[1] N. Wertheimer and E. Leeper, Am. J. Epidemiol. **109**, 273 (1979).

[2] D. A. Savitz and E. E. Calle, J. Occup. Med. **29**, 47 (1987).
[3] Abstracts W1-W7, First World Congress for Electricity and Magnetism in Biology and Medicine, Lake Buena Vista, FL (1992), pp. 65–67.
[4] D. L. Mader and S. B. Peralta, Bioelectromagnetics **13**, 287 (1992).
[5] IEEE Magnetic Fields Task Force, A Protocol for Spot Measurements of Residential Power Frequency Magnetic Fields, IEEE Trans. Power Delivery, in press.
[6] J. R. Gauger, IEEE Trans. Power Appar. Syst. **PAS-104**, 2436 (1985).
[7] D. Corson and P. Lorrain, Introduction to Electromagnetic Fields and Waves, W. H. Freeman, San Francisco, CA (1962), p. 210.
[8] K. R. Symon, Mechanics, Addison-Wesley, Reading, MA (1953), p. 83.
[9] G. B. Thomas, Calculus and Analytic Geometry, Addison-Wesley, Reading, MA (1953), pp. 497–500.
[10] Ref. [9], pp. 550–553.
[11] C.R.C. Standard Mathematical Tables, Eleventh Edition, C. D. Hodgman, (ed.), Chemical Rubber Publ. Co., Cleveland, OH.
[12] IEEE Electromagnetic Compatibility Society, draft 9, Standard Procedures for the Measurement of Electric and Magnetic Fields from Video Display Terminals (VDTs) from 5 Hz to 400 kHz, July, 1992.

About the author: *M. Misakian is a physicist in the Electricity Division of NIST. The National Institute of Standards and Technology is an agency of the Technology Administration, U.S. Department of Commerce.*

Volume 98, Number 3, May–June 1993
Journal of Research of the National Institute of Standards and Technology

[J. Res. Natl. Inst. Stand. Technol. 98, 297 (1993)]

Characteristics of Unknown Linear Systems Deduced from Measured CW Magnitude

Volume 98 | Number 3 | May–June 1993

M. T. Ma and J. W. Adams

National Institute of Standards and Technology,
Boulder, CO 80303-3328

A method is presented for predicting the total response, in both frequency and time, of an unknown linear system when only the measured continuous wave (cw) magnitude is available. The approach is based on approximating the square of the measured magnitude by a rational function, from which various system transfer functions in terms of complex frequency are deduced. These transfer functions may or may not be at minimum phase. The corresponding impulse response is then obtained by taking the inverse Laplace transform of the transfer function. The impulse response of the minimum-phase case rises faster initially to its first maximum than the nonminimum-phase counterparts. This result confirms that, for the same cw magnitude response, the accumulative energy contained in the impulse response is the greatest when the transfer function is at minimum phase. Physical meaning of the energy content is also discussed.

Key words: Hilbert transform; impulse response; Laplace transform; linear system; minimum phase; system transfer function.

Accepted: December 17, 1992

1. Introduction

The total response in frequency and time of a system to an assumed excitation, whether it is continuous wave (cw) or pulsed, is usually unpredictable if the system involves nonlinear elements. Even for linear but complex systems, the task of obtaining the total response when the system is excited by a source is still formidable because the complete system transfer function (amplitude and phase) may be unknown. The transfer function is defined as the ratio of system output to input in the frequency domain. The output and input can be voltage, current, electric field, magnetic field, or combinations of them. The time response of such a system required for assessing its vulnerability to an unfriendly electromagnetic environment can be determined only by sophisticated time-domain measurements or by derivations from the frequency-domain amplitude and phase measurements. Unfortunately, such time-domain measurements or frequency-domain phase measurements require expensive equipment and special considerations on radiation hazards, regulatory compliance, and environmental pollution (if performed outdoors). On the other hand, measuring magnitude response data of an unknown, complex, linear system to cw excitations at low levels, indoors or outdoors, is relatively straightforward, less costly, and free from compliance and pollution problems. Further, if such measured cw magnitude data can be processed to deduce a system transfer function,

the phase characteristics and time response of such a system to a general excitation are then derivable.

In this paper, we present a method to deduce the total response of an unknown, complex, linear system from a given set of cw magnitude responses only. This is accomplished by approximating the square of the measured magnitude curve by a sum of ratios of two polynomials with real coefficients. Each of these ratios represents a second-order rational transfer function for a system with time-invariant lumped-constant elements. The exact number in the sum is determined by the number of resonant frequencies displayed in the measured magnitude data. Once the approximation work is done, the associated system transfer functions can then be obtained by using knowledge available from classical network theory. The transfer functions so obtained may or may not be at minimum phase. The corresponding phase characteristics and impulse responses are determined in a straightforward manner. For the same cw magnitude response, the accumulative energy associated with the impulse response corresponding to a minimum-phase transfer function is always greater than that corresponding to nonminimum-phase transfer functions. The derivations and detailed analysis are presented in Sec. 4.

The theoretical relationship between amplitude and phase of a system with a minimum-phase transfer function is outlined in Sec. 2. The conventional numerical approach for determining the phase characteristics and the corresponding time response of the linear minimum-phase system from the measured cw magnitude data, and the accuracy involved in this process are reviewed in Sec. 3. Examples are given in Secs. 4 and 5 to demonstrate the usefulness of the proposed method developed in Sec. 4. Energy contents associated with the given system are discussed in Sec. 6.

2. Theoretical Background

A stable linear system, however simple or complex, can be characterized by its transfer function $H(s)$, which has no poles in the right half of the complex frequency s-plane. That is, $H(s)$ is analytic in $Re(s) \geq 0$, where Re stands for the "real part of" [1]. We address only stable systems in this paper, because otherwise the system is not well designed, and therefore is not useful in application. In addition, when the system is made of only time-invariant and lumped-constant elements, its transfer function is then a rational function of s (a ratio of two polynomials with real coefficients) with the degree of the numerator polynomial lower than the degree of the denominator polynomial. When this transfer function is evaluated at $s = j\omega$, $H(j\omega)$ is then a complex function of ω, consisting of a real part $R(\omega)$ and an imaginary part $X(\omega)$, or a magnitude $|H(j\omega)|$ and a phase $\theta(\omega)$. That is,

$$H(j\omega) = R(\omega) + j\, X(\omega) = |H(j\omega)|\, e^{-j\theta(\omega)}, \quad (1)$$

where the convention of assigning a minus sign to the phase function is used. The magnitude function $|H(j\omega)|$ may also be expressed in terms of the attenuation function $\alpha(\omega)$:

$$|H(j\omega)| = e^{-\alpha(\omega)}, \qquad \ln|H(j\omega)| = -\alpha(\omega). \quad (2)$$

When $H(s)$ is analytic as defined above and the system under study is causal [$h(t) = 0$ when $t \leq 0$], as is usually the case in practice, the real and imaginary parts of $H(j\omega)$ are related by the Hilbert transform pair [2],

$$R(\omega) = \frac{2}{\pi} \int_0^\infty [yX(y)/(\omega^2 - y^2)]\, dy, \quad (3a)$$

and

$$X(\omega) = -\frac{2\omega}{\pi} \int_0^\infty [R(y)/(\omega^2 - y^2)]\, dy. \quad (3b)$$

In other words, the real and imaginary parts of this system are not independent. When one part is given either analytically or through measurement, the other part can be uniquely determined by performing one of integrals shown in Eq. (3). The complex transfer function $H(j\omega)$ is then completely obtained, from which the impulse response may be derived. In reality, however, Eq. (3) is not useful because we cannot just measure the real or imaginary part of the system response to a given excitation.

If $H(s)$, in addition to being analytic and causal, also has no zeros in the right half of the s-plane, the transfer function is said to be at minimum phase, herein denoted by $H_m(s)$. Under this condition, the attenuation function $\alpha(\omega)$ and phase function $\theta(\omega)$ are related by another Hilbert transform pair [2, 3, 4],

$$\theta(\omega) = \frac{\omega}{\pi} \int_{-\infty}^\infty [\alpha(y)/(y^2 - \omega^2)]\, dy$$

$$= -\frac{\omega}{\pi} \int_{-\infty}^\infty [\ln|H_m(jy)|/(y^2 - \omega^2)]\, dy, \quad (4a)$$

and

$$\alpha(\omega)=\alpha(0)-\frac{\omega^2}{\pi}\int_{-\infty}^{\infty}[\theta(y)/y(y^2-\omega^2)]\,dy. \quad (4b)$$

From Eq. (4b), we see that the attenuation function can be determined completely from a given phase function only when $\alpha(0)$ is also known. But, for our application, only Eq. (4a) is required because we assume that the magnitude (or attenuation) function is given by measurement. Once $\theta(\omega)$ is determined from Eq. (4a), the entire complex $H_m(j\omega)$ can be obtained from Eq. (1) because $|H_m(j\omega)|$ or $\alpha(\omega)$ is already given. The impulse response of this minimum-phase system for $t \geq 0$ is then calculated by the inverse Fourier transform,

$$h_m(t)=\frac{1}{2\pi}\int_{-\infty}^{\infty}H_m(j\omega)\,e^{j\omega t}\,dt. \quad (5)$$

The system's time response to a general excitation can be computed by the convolution integral $h_m(t)*e(t)$, where $e(t)$ represents an excitation, cw or pulse, applied to the system input. The success of determining the time response from magnitude data is based on the assumption that the system's transfer function is at minimum phase. The solution of impulse response so obtained constitutes the only solution.

In general, however, there may be multiple solutions, because other possible transfer functions with nonminimum phases giving the same magnitude response may exist. One way of obtaining them with our proposed method is to be shown in Sec. 4.

3. Conventional Approach

Since the improper integral in Eq. (4a) is not easy to compute, the conventional approach has been to apply a transformation of variables known as the Wiener-Lee transform to $\alpha(\omega)$ or $|H(j\omega)|$ to obtain the necessary $\theta(\omega)$. When the Wiener-Lee transform [2]

$$\omega = -\tan(\delta/2) \quad (6)$$

is applied, the integration interval $(-\infty, \infty)$ for ω in Eq. (4a) is transformed into $(-\pi, \pi)$ for δ. The original attenuation function $\alpha(\omega)$ and phase function $\theta(\omega)$ will be denoted, after transformation, respectively as $A(\delta)$ and $T(\delta)$. Since $\alpha(\omega)=-\ln|H(j\omega)|=-\frac{1}{2}\ln[R^2(\omega)+X^2(\omega)]$ is an even function of ω and $\theta(\omega)=-\tan^{-1}[X(\omega)/R(\omega)]$ is an odd function of ω, their respective transforms $A(\delta)$ and $T(\delta)$ will be even and odd functions of δ. As such, they may be expanded into Fourier cosine and sine series,

$$A(\delta)=a_0+a_1\cos\delta+a_2\cos 2\delta+\ldots+a_n\cos n\delta+\ldots,$$

and (7)

$$T(\delta)=b_1\sin\delta+b_2\sin 2\delta+\ldots+b_n\sin n\delta+\ldots,$$

where the expansion coefficients are determined by

$$a_0=\frac{1}{2\pi}\int_{-\pi}^{\pi}A(\delta)\,d\delta=\frac{1}{\pi}\int_{0}^{\pi}A(\delta)\,d\delta,$$

(8a)

$$a_n=\frac{1}{\pi}\int_{-\pi}^{\pi}A(\delta)\cos n\delta\,d\delta=\frac{2}{\pi}\int_{0}^{\pi}A(\delta)\cos n\delta\,d\delta,$$

and

$$b_n=\frac{1}{\pi}\int_{-\pi}^{\pi}T(\delta)\sin n\delta\,d\delta=\frac{2}{\pi}\int_{0}^{\pi}T(\delta)\sin n\delta\,d\delta.$$

(8b)

When the system under consideration is causal, the expansion coefficients in Eq. (8) are simply related by [2]

$$b_n=-a_n. \quad (9)$$

Thus, when $\alpha(\omega)$ or $|H(j\omega)|$ is given, $A(\delta)$ is known. Determination of a_n from Eq. (8a) automatically yields b_n from Eq. (9), which in turn gives $T(\delta)$ and $\theta(\omega)$ by means of Eq. (6), and hence the complex transfer function $H(j\omega)$. The impulse response is then obtained from Eq. (5).

The justification for using the Wiener-Lee transform and the procedures as outlined above seem straightforward. The transform succeeds in converting the original improper integral in Eq. (4a) to a proper integral in Eq. (8a). From the application point of view, the important question is then: if the integral in Eq. (4a) is difficult to compute before the Wiener-Lee transform is applied, is it easier to compute a_n in Eq. (8a) after the Wiener-Lee transform is used? The answer is most likely negative, because the integrand in Eq. (8a) involves complicated transcendental functions. This explains why, in practice, numerical computations are required. The entire procedure will then involve: (i) conversion of the measured data of $\alpha(\omega)$ or $|H(j\omega)|$ into

$A(\delta)$ by Eq. (6), (ii) numerical calculation of a_n from $A(\delta)$ by Eq. (8a), (iii) construction of a transformed phase function $T(\delta)$ by including only a finite number of terms in the Fourier sine series with $b_n = -a_n$, (iv) conversion of $T(\delta)$ back to $\theta(\omega)$, (v) determination of the complex transfer function $H(j\omega)$ based on the given $\alpha(\omega)$ and the newly constructed $\theta(\omega)$, and (vi) numerical computation of $h(t)$ by Eq. (5). The numerical solution so obtained constitutes the only answer. Other possible solutions with nonminimum phases can never be found. In addition, each of the above six steps is an approximation, thus exerting doubt about the accuracy in the final solution [5, 6].

Thus, while the Hilbert transform is useful for processing measured cw data directly [7], it may not always offer advantage, together with the Wiener-Lee transform, for deriving the minimum phase.

4. Alternative but Simpler Approach

Using passive network theory [8, 9], we can deduce a rational transfer function $H(s)$ directly and exactly from a squared magnitude function $|H(j\omega)|^2$ expressed as a ratio of two polynomials of even order in ω, where the order of the numerator polynomial is at least two degrees lower than that of the denominator polynomial. Thus, if an approximate squared magnitude function $|H(j\omega)|^2$ in such a form can be obtained from the measured cw magnitude data of an unknown, complex, linear system to some excitation, the task of deducing a rational transfer function, and subsequently, the associated phase function and impulse response (in time) is then straightforward. We will show later that multiple solutions for systems with the same $|H(j\omega)|$ are possible. The transfer functions so deduced may or may not be at minimum phase. In this process, we essentially have assumed that the original unknown linear system, which may consist of distributed elements and other complexities, can be approximated by an equivalent passive network system with only time-invariant and lumped-constant elements. The approximation is the only one involved in the process. The exact order in the final approximate $|H(j\omega)|^2$ depends on outstanding features in the given cw magnitude data. The most important feature displaying a strong resonance at a particular frequency can be approximated by a simple second-order transfer function.

4.1 Second-Order Transfer Function

The second-order transfer function may take either of the following two forms:

$$H_{2a} = A/(s^2 + as + b), \tag{10a}$$

or

$$H_{2b}(s) = A(s + c)/(s^2 + as + b), \tag{10b}$$

where the parameters A, a, b, and c are all real. In addition, we require

$$0 < a < 2\sqrt{b}, \tag{11}$$

so that the complex poles are in the left half of the s-plane. On the other hand, the parameter c in Eq. (10b) may be positive, negative, or 0. When c is positive, the zero of the transfer function is also in the left half-plane (in fact, on the negative real axis). In this case, the transfer function is at minimum phase. When c is negative, the zero is in the right half-plane, and the transfer function is at nonminimum phase. When $c = 0$, the zero is at the origin, also constituting a nonminimum-phase case, and the dc magnitude response at $\omega = 0$ is 0. The parameter A is used to match the given maximum magnitude response at the resonant frequency.

The outstanding features associated with the second-order transfer functions in Eq. (10) are examined in the following analysis.

4.1.1 Second-Order Transfer Function in the Form of Eq. (10a) In this case, we have

$$H_{2a}(j\omega) = A/(b - \omega^2 + j\omega a). \tag{12a}$$

The squared magnitude is given by

$$|H_{2a}(j\omega)|^2 = H_{2a}(j\omega)H_{2a}(-j\omega) = H_{2a}(s)H_{2a}(-s)|_{s=j\omega}$$

$$= \frac{A^2}{(b-\omega^2)^2 + a^2\omega^2} = \frac{A^2}{\omega^4 - (2b - a^2)\omega^2 + b^2}, \tag{12b}$$

where ω is the only variable.

Setting the derivative of this squared magnitude to 0 yields $\omega = 0$ and $\omega^2 = (2b - a^2)/2$. If $b > a^2/2$, $\omega = 0$ gives the location of the minimum, while $\omega^2 = (2b - a^2)/2$ gives the location of the maximum representing the location of the resonant frequency, herein designated as

$$\omega_0^2 = (2b - a^2)/2 > 0. \tag{13}$$

On the other hand, if $a^2/4 < b < a^2/2$, $|H(0)|^2$ will be the maximum. In this case, there is no resonant frequency. Thus, if a given magnitude curve has a resonant frequency at ω_0 (other than 0), we require

$$b > a^2/2 , \tag{14}$$

which is a stronger condition than that in Eq. (11).

In terms of ω_0, the squared magnitude can be written as

$$|H_{2a}(j\omega)|^2 = \frac{A^2}{\omega^4 - 2\omega_0^2\,\omega^2 + b^2} . \tag{15}$$

We then obtain the maximum

$$|H_{2a}(j\omega_0)|^2 = \frac{A^2}{b^2 - \omega_0^4} , \tag{16}$$

which is also nonnegative because of Eq. (13), where $b = \omega_0^2 + \frac{1}{2}a^2 > \omega_0^2$.

The relative minimum at $\omega = 0$ is given by

$$|H_{2a}(0)| = A/b . \tag{17}$$

When $\omega \to \infty$, $|H_{2a}(j\omega)| \to 0$.

The half-power points may be defined as the frequencies at which the magnitude response of a linear system decreases to $(1/\sqrt{2})$ of the peak response. The width between these frequencies represents a measure of sharpness of the magnitude response near the resonance. These frequencies are determined by

$$|H_{2a}(j\omega)|^2 = \frac{1}{2}|H_{2a}(j\omega_0)|^2 \tag{18}$$

or

$$\omega^4 - 2\omega_0^2\,\omega^2 + b^2 = 2(b^2 - \omega_0^4) , \tag{19}$$

which yields

$$\omega^2 = \omega_0^2 \pm \sqrt{b^2 - \omega_0^4} . \tag{20}$$

If we denote the half-power frequency on the left side of the resonant frequency by ω_1 and that on the right side by ω_2, we have

$$\omega_2^2 = \omega_0^2 + \sqrt{b^2 - \omega_0^4} , \quad \omega_1^2 = \omega_0^2 - \sqrt{b^2 - \omega_0^4} , \tag{21}$$

$$\omega_2^2 - \omega_1^2 = 2\sqrt{b^2 - \omega_0^4} , \ \omega_2^2 + \omega_1^2 = 2\omega_0^2 , \text{ and}$$

$$\omega_1^2\omega_2^2 = 2\omega_0^4 - b^2 .$$

Clearly, ω_1^2 and ω_2^2 are symmetric with respect to ω_0^2.

The quality factor of the system may be defined as

$$Q = \omega_0/(\omega_2 - \omega_1) , \tag{22}$$

where $\omega_2 - \omega_1$ may be called bandwidth of the system.

Mathematically, we need three conditions to determine the three parameters A, a, and b. From the application point of view, we can express A, a, and b in terms of ω_0, ω_1, ω_2, and $|H(j\omega_0)|$ from Eqs. (13), (16), and (21):

$$A = (\omega_2^2 - \omega_1^2)\,|H_{2a}(j\omega_0)|/2 ,$$

$$b^2 = \omega_0^4 + \frac{1}{4}(\omega_2^2 - \omega_1^2)^2 , \tag{23}$$

and

$$a^2 = 2[\sqrt{\omega_0^4 + (\omega_2 - \omega_1)^2\,(\omega_2 + \omega_1)^2/4} - \omega_0^2] .$$

Thus, when there is only one resonant frequency in the measured cw magnitude curve for an unknown linear system, such as that shown in Fig. 1, the special features such as ω_0, ω_1, ω_2, and $|H(j\omega_0)|$ can be read from it. The required parameters A, a, and b can then be determined from Eq. (23), regardless of whether the relation $\omega_1^2 + \omega_2^2 = 2\omega_0^2$ is satisfied. The square of the given magnitude may be approximately represented by Eq. (12b), and the unknown linear system may be represented by the second-order transfer function Eq. (10a),

$$H_{2a}(s) = A/(s^2 + as + b) = \frac{A}{(s + a/2)^2 + \beta^2} , \tag{24}$$

where

$$\beta^2 = b - a^2/4 . \tag{25}$$

Once this is done, we then obtain the associated phase function in accordance with the convention used in (1):

$$\theta_{2a}(\omega) = \frac{1}{2j}\arg[H_{2a}(-j\omega)/H_{2a}(j\omega)] = \tan^{-1}[a\omega/(b - \omega^2)] . \tag{26}$$

Since a and b are positive, $\theta_{2a}(\omega)$ varies from 0 to π when ω varies from 0 to ∞.

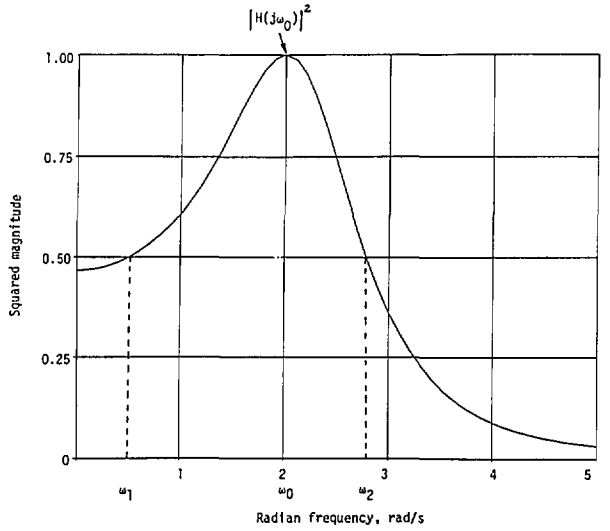

Fig. 1. A squared-magnitude response with only one resonant frequency.

The corresponding impulse response can be determined by taking the inverse Laplace transform [10] of $H_{2a}(s)$ in Eq. (24),

$$h_{2a}(t) = \frac{A}{\beta} e^{-at/2} \sin \beta t, \quad t \geq 0. \tag{27}$$

The time response $R(t)$ of this unknown linear system to a general excitation $e(t)$, cw or pulse, is then given by the convolution integral [10],

$$R(t) = e(t) * h_{2a}(t). \tag{28}$$

If indeed the given squared magnitude curve with only one resonant frequency shown in Fig. 1 is represented by Eq. (12b) and the transfer function is represented by Eq. (24), the system under consideration will be at minimum phase, because this transfer function has no zero in the right half of the s-plane. In general, however, the system may also be at nonminimum phase because the actual transfer function could be represented by a product of $H_{2a}(s)$ and an all-pass function. In this case, the system transfer function with a nonminimum phase is given by

$$H_n(s) = H_{2a}(s) H_{all}(s), \tag{29}$$

with the simplest (first order) all-pass function defined as

$$H_{all}(s) = (s-\alpha)/(s+\alpha), \tag{30}$$

where α is a real and positive number.

Since $|H_{all}(j\omega)|^2 = 1$, we have

$$|H_n(j\omega)|^2 = |H_{2a}(j\omega)|^2 \; |H_{all}(j\omega)|^2 = |H_{2a}(j\omega)|^2. \tag{31}$$

This implies that the same squared magnitude curve as that shown in Fig. 1 can be represented by either $H_{2a}(s)$ or $H_n(s)$.

In Eq. (30), the zero of $H_{all}(s)$ in the right half of the s-plane is the mirror image of the pole in the left half of the s-plane [8]. In general, the all-pass function may be of higher order with more zeros in the right half of the s-plane and the same number of mirror-image poles in the left half of the s-plane. These zeros are not necessarily limited to the real axis. They can take complex-conjugate pairs. If we restrict ourself, for the time being, to the first-order all-pass function given in Eq. (30), we can make further analysis. The impulse response for this nonminimum-phase transfer function may be determined from Eq. (29) by convolution integral [11],

$$h_n(t) = h_{2a}(t) * \mathcal{L}^{-1}\left[1 - \frac{2\alpha}{s+\alpha}\right]$$

$$= h_{2a}(t) - 2\alpha h_{2a}(t) * e^{-\alpha t}, \tag{32}$$

where $\mathcal{L}^{-1}$ is the inverse Laplace transform.

The impulse response can also be obtained by taking partial fractions of Eq. (29). That is,

$$H_n(s) = \frac{A(s-\alpha)}{(s^2+as+b)(s+\alpha)}$$

$$= A\left\{\frac{ps+q}{s^2+as+b} - \frac{p}{s+\alpha}\right\}$$

$$= A\left\{\frac{p(s+a/2)+q-ap/2}{(s+a/2)^2+\beta^2} - \frac{p}{s+\alpha}\right\}, \tag{33}$$

where

$$p = 2\alpha/(b+\alpha^2-a\alpha), \text{ and}$$

$$q = (b-\alpha^2+a\alpha)/(b+\alpha^2-a\alpha). \tag{34}$$

The impulse response is then

$$h_n(t) = A\left\{e^{-at/2}\left[p\cos\beta t + \frac{q-ap/2}{\beta}\sin\beta t\right] - p\,e^{-\alpha t}\right\}, \tag{35}$$

which is the same as Eq. (32) after the convolution is performed.

Both the minimum-phase impulse response $h_{2a}(t)$ in Eq. (27) and nonminimum-phase impulse response $h_n(t)$ in Eq. (35) vanish at $t=0$. This can be confirmed by the initial-value theorem [10]. More detailed behaviors of Eqs. (27) and (35) can be learned by examining their first time derivatives,

$$h'_{2a}(t)=\frac{A}{\beta}\,e^{-at/2}\left[\beta\cos\beta t-\frac{a}{2}\sin\beta t\right], \qquad (36a)$$

and

$$h'_n(t)=A\left\{(q-ap)\cos\beta t - \left[\frac{a(2q-ap)}{4\beta}+p\beta\right]\sin\beta t\right\}e^{-at/2} + Ap\alpha\, e^{-\alpha t} \qquad (36b)$$

Clearly, at $t=0$, $h'_{2a}(0)=h'_n(0)=A$. This means that both $h_{2a}(t)$ and $h_n(t)$ arise from 0 with the same starting rate. However, shortly afterward, they increase with different rates. At $t=\epsilon(1\gg\epsilon>0)$, we may expand those functions involved and keep the first-order term to obtain

$$h'_{2a}(\epsilon)\approx A(1-a\epsilon/2)^2\approx A(1-a\epsilon) \qquad (37a)$$

and

$$h'_n(\epsilon)\approx A[1-(a+\alpha)\epsilon]. \qquad (37b)$$

Since both a and α are real and positive, we conclude that

$$h'_n(\epsilon)<h'_{2a}(\epsilon). \qquad (38a)$$

By similar steps we can also show that

$$h_n(\epsilon)<h_{2a}(\epsilon). \qquad (38b)$$

The relations in Eqs. (38a) and (38b) imply that shortly after the system is excited by a source, $h_{2a}(t)$ associated with the minimum-phase system increases with a greater rate than the nonminimum-phase counterpart $h_n(t)$. Although this point is drawn from a special case (first-order all-pass function), it can be generalized to higher orders even though the algebraic derivations are much more involved. Equations (38a) and (38b) also mean that more energy accepted by the minimum-phase system is concentrated at the beginning ($t=0+$) of the excitation than the nonminimum-phase system [7, 12]. Details on energy consideration are found in Sec. 6. This observation is very important from the standpoint of electromagnetic interferences (EMI). If the minimum-phase system can survive the initial impact due to an unwanted external source, a nonminimum-phase system can also survive it. The minimum-phase system may be considered the worst case as far as the initial impact due to an unwanted signal is concerned. From the design point of view, if a system is minimum phase, the designer may wish to convert it to nonminimum phase by adding an all-pass network to reduce initial EMI impact.

From Eq. (36a) we know that the first maximum of $h_{2a}(t)$ occurs at t_{m0}, which is the smallest root of

$$\tan\beta t=2\beta/a. \qquad (39)$$

After reaching its first peak at t_{m0}, the impulse response $h_{2a}(t)$ varies sinusoidally with a decay rate of $a/2$ and with a period of β. Although it is not as straightforward to determine the exact location of the first maximum for $h_n(t)$ by setting Eq. (36b) to 0, we know that it also varies sinusoidally with the same period β but decays with a different rate because of the extra term $\exp(-\alpha t)$. A numerical example is here presented to illustrate this point.

Example 1. Suppose that the square of a "measured" cw magnitude curve can be represented by

$$f^2(\omega)=e^{-(\omega^2-4)^2} \qquad (40)$$

For this example, the resonant frequency occurs at $\omega_0=2$. The half-power frequencies are $\omega_1^2=3.1674$, and $\omega_2^2=4.8326$. The bandwidth is given by $\omega_2-\omega_1=0.4185$, and $Q=4.7780$. Since $\omega_1^2+\omega_2^2=2\omega_0^2$, we can use $H_{2a}(s)$. The required parameters can be obtained from Eq. (23) as: $a=0.4141$, $b=4.0857$, and $A=0.8326$ (carried to 4 digits). The approximate squared magnitude is then

$$|H_{2a}(j\omega)|^2=\frac{0.6931}{\omega^4-8\omega^2+16.6931}. \qquad (41)$$

By presenting the numerical results in Table 1, we see that the given curve in Eq. (40) and its approximation in Eq. (41) indeed match at ω_1, ω_2, and ω_0.

Table 1. Approximation of the given function in Eq. (40) by the squared-magnitude function in Eq. (41)

ω	$f^2(\omega)$	$\lvert H_{2a}(j\omega)\rvert^2$	Error
0.00	0.0000	0.0415	0.0415
0.50	0.0000	0.0470	0.0470
1.00	0.0001	0.0715	0.0714
1.50	0.0468	0.1846	0.1378
1.75	0.4152	0.4409	0.0257
1.80	0.5612	0.5454	−0.0158
1.85	0.7164	0.6752	−0.0413
1.90	0.8589	0.8200	−0.0389
1.95	0.9617	0.9467	−0.0150
2.00	1.0000	1.0000	0.0000
2.05	0.9598	0.9441	−0.0157
2.10	0.8453	0.8048	−0.0405
2.15	0.6787	0.6414	−0.0373
2.20	0.4938	0.4955	0.0017
2.25	0.3234	0.3804	0.0570
2.50	0.0063	0.1204	0.1141
3.00	0.0000	0.0270	0.0270

After obtaining Eq. (41), we have the following simplest solution to represent the transfer function with a minimum phase:

$$H_{2a}(s)=0.8326/(s^2+0.4141s+4.0857). \quad (42)$$

The associated phase function and impulse response are then respectively

$$\theta_m(\omega)=\tan^{-1}[a\omega/(b-\omega^2)]$$
$$=\tan^{-1}[0.4141\omega/(4.0857-\omega^2)] \quad (43)$$

and

$$h_{2a}(t)=0.4141\,e^{-0.2070t}\sin(2.0107t),\quad t\geq 0. \quad (44)$$

For the same $|H_{2a}(j\omega)|^2$ obtained in Eq. (41), we could also have a transfer function with a nonminimum phase by including an all-pass function, say, the first order with $\alpha=1$. We then have

$$H_n(s)=\frac{0.8326(s-1)}{(s^2+0.4141s+4.0857)(s+1)}. \quad (45)$$

The corresponding phase function and impulse function (after taking partial fractions) are

$$\theta_n(\omega)=\theta_m(\omega)+\tan^{-1}(\omega)+\pi, \quad (46)$$

with $\theta_m(\omega)$ given in Eq. (43) and

$$h_n(t)=[0.3564\cos(2.0107t)+0.2735\sin(2.0107t)]\,e^{-0.2070t}-0.3564\,e^{-t},\quad t\geq 0. \quad (47)$$

The impulse responses obtained in Eq. (44) and Eq. (47) are plotted in Fig. 2 to confirm the conclusions in Eqs. (38a) and (38b). Thus, more energy is concentrated in $h_{2a}(t)$ than in $h_n(t)$ at the beginning of excitation.

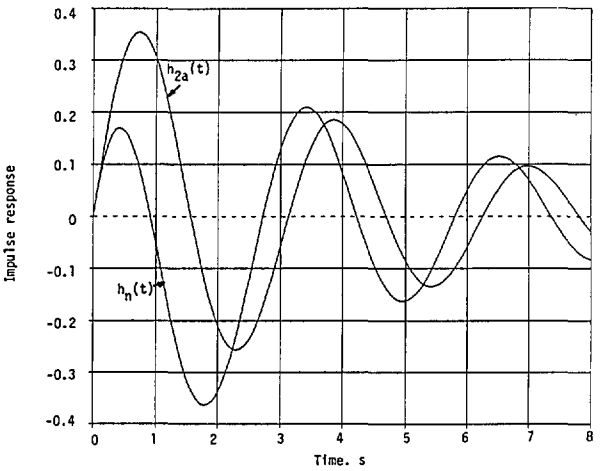

Fig. 2. Impulse responses of the minimum-phase and nonminimum-phase systems with their given squared-magnitude cw response in Eq. (40) and the approximate squared magnitude in Eq. (41).

The solutions for $\theta_n(\omega)$ and $h_n(t)$ are not unique because they depend on the choice of specific all-pass functions.

We note from Eq. (23) that the parameter a decreases with the bandwidth $(\omega_2-\omega_1)$ or is inversely proportional to Q, and that the parameter b is primarily determined by ω_0^2. These parameters decide respectively, in turn, the decay rate and period of variations of the impulse response.

4.1.2 Second-Order Transfer Function Taking the Form of Eq. (10b) For this case, we have

$$H_{2b}(j\omega)=\frac{A(c+j\omega)}{b-\omega^2+j\omega a} \quad (48)$$

and

$$|H_{2b}(j\omega)|^2=\frac{A^2(c^2+\omega^2)}{\omega^4-(2b-a^2)\omega^2+b^2}. \quad (49)$$

Now there are three solutions for $d|H_{2b}(j\omega)|^2/d\omega=0$. One of these, $\omega=0$, is the minimum with $|H(0)|^2=A^2c^2/b^2$. The other solution gives the resonant frequency,

$$\omega_0^2=-c^2+\sqrt{c^4+b^2+2bc^2-a^2c^2}\,, \tag{50}$$

which is always greater than 0 (as it should be) in view of Eq. (14). A third solution takes the same form as Eq. (50) except with a negative sign in front of the square-root sign. This third solution is obviously nonphysical.

The maximum value of the squared magnitude at ω_0 is, after substitution of Eq. (50) into Eq. (49) and some algebraic simplification, given by

$$|H_{2b}(j\omega_0)|^2=A^2/(2\omega_0^2-2b+a^2)\,. \tag{51}$$

Again, this is the only maximum. The general variation of $|H_{2b}(j\omega)|^2$ is similar to that in Fig. 1.

The half-power frequencies ω_1 and ω_2 are determined by

$$\frac{\omega^2+c^2}{\omega^4-(2b-a^2)\omega^2+b^2}=\frac{1}{4(\omega_0^2-b)+2a^2}$$

or

$$\omega^4+(2b-a^2-4\omega_0^2)\omega^2+b^2-c^2(4\omega_0^2+2a^2-4b)=0. \tag{52}$$

Instead of solving for ω_1 and ω_2, we note that

$$\omega_1^2+\omega_2^2=4\omega_0^2+a^2-2b\,, \tag{53}$$

and

$$\omega_1^2\omega_2^2=b^2-c^2(4\omega_0^2+2a^2-4b)\,. \tag{54}$$

The above derivations represent analysis for the particular transfer function $H_{2b}(s)$. From the application viewpoint, we can express a, b, and c in terms of ω_0, ω_1, and ω_2 by using Eqs. (50), (53), and (54),

$$\begin{aligned} b^2&=2\omega_0^4-\omega_1^2\omega_2^2\,,\\ c^2&=(\omega_0^4-\omega_1^2\omega_2^2)/(\omega_1^2+\omega_2^2-2\omega_0^2)\,,\\ a^2&=\omega_1^2+\omega_2^2-4\omega_0^2+2b\,. \end{aligned} \tag{55}$$

Thus, when ω_0, ω_1, and ω_2 are read from a measured magnitude curve, we can easily determine the required parameters b, c, and a from Eq. (55). Since a^2, b^2, and the denominator of c^2 [which is equal to the denominator of Eq. (51)] are all positive, and c^2 itself is nonnegative, we require

$$\omega_1^2+\omega_2^2>2\omega_0^2 \quad \text{and} \quad \omega_0^2\geq\omega_1\omega_2\,. \tag{56}$$

In addition, the constant factor A can be determined from Eq. (51),

$$A^2=(2\omega_0^2-2b+a^2)\,|H(j\omega_0)|^2\,, \tag{57}$$

where $|H(j\omega_0)|^2$ can also be obtained from the given magnitude curve.

For the special case $c=0$ when $\omega_0^2=\omega_1\omega_2$, we have

$$\begin{aligned} &b=\omega_0^2=\omega_1\omega_2\,,\\ &a^2=\omega_1^2+\omega_2^2-2\omega_0^2=\omega_1^2+\omega_2^2-2\omega_1\omega_2=(\omega_2-\omega_1)^2\,,\\ &[\text{or } a=\omega_2-\omega_1]\,, \end{aligned} \tag{58}$$

and

$$A^2=a^2\,|H(j\omega_0)|^2\,, \quad \text{or} \quad A=a\,|H(j\omega_0)|\,.$$

Here, the parameter a is controlled solely by the system's bandwidth, and b depends only on the resonant frequency. Also, for this special case, ω_0 is the geometrical mean of ω_1 and ω_2.

One unique feature associated with this case [Eq. (10b)] is that once an approximate squared magnitude in the form of Eq. (49) is obtained from the given magnitude curve by the procedures thus outlined, the solutions for the transfer function are not unique. One of the obvious solutions, herein designated as $H_m(s)$ takes the same expression given in Eq. (10b),

$$H_m(s)=\frac{A(s+c)}{s^2+as+b}\,, \tag{59}$$

where c is taken as a positive number from Eq. (55). In this case, the transfer function is in minimum phase.

The other solution is

$$H_n(s)=\frac{A(c-s)}{s^2+as+b}\,, \tag{60}$$

which represents a nonminimum-phase transfer function.

Clearly, we have $|H_m(j\omega)|^2=|H_n(j\omega)|^2$.

The associated phase function for $H_m(s)$ can be obtained directly from $H_m(j\omega)$ as

$$\theta_m(\omega)=\tan^{-1}[a\omega/(b-\omega^2)]-\tan^{-1}(\omega/c). \tag{61}$$

The second term becomes $\pi/2$ when $c=0$. Since the first term varies from 0 to π and the second term varies from 0 to $\pi/2$ as ω changes from 0 to ∞, the range of variation for $\theta_m(\omega)$ is hence from 0 to $\pi/2$.

The phase function for $H_n(s)$ is

$$\theta_n(\omega)=\tan^{-1}[a\omega/(b-\omega^2)]+\tan^{-1}(\omega/c), \quad (62)$$

whose range of variation is from 0 to $3\pi/2$.

According to the Hilbert transform given in Eq. (4a), the phase function $\theta_m(\omega)$ may also be obtained from the deduced squared magnitude,

$$\begin{aligned}\theta_m(\omega) &= -\frac{\omega}{\pi}\int_{-\infty}^{\infty}[\ln|H_m(jy)|/(y^2-\omega^2)]dy \\ &= -\frac{\omega}{\pi}\int_{-\infty}^{\infty}\frac{\ln(y^2+c^2)\,dy}{2(y^2-\omega^2)} \\ &\quad +\frac{\omega}{\pi}\int_{-\infty}^{\infty}\frac{\ln[y^4-(2b-a^2)y^2+b^2]dy}{2(y^2-\omega^2)}\end{aligned} \quad (63)$$

Because the integrands are even functions of y, we have

$$\begin{aligned}\theta_m(\omega) &= -\frac{\omega}{\pi}\int_0^{\infty}\frac{\ln(y^2+c^2)\,dy}{y^2-\omega^2} \\ &\quad +\frac{\omega}{\pi}\int_0^{\infty}\frac{\ln(y^2+m^2)\,dy}{y^2-\omega^2} \\ &\quad +\frac{\omega}{\pi}\int_0^{\infty}\frac{\ln(y^2+n^2)\,dy}{y^2-\omega^2},\end{aligned} \quad (64)$$

where we have broken the last integral in Eq. (63) into two parts with

$$m^2+n^2=-2b+a^2, \quad \text{and} \quad m^2n^2=b^2. \quad (65)$$

Since a known definite integral in the form of Eq. (64) is available [13],

$$\int_0^{\infty}\frac{\ln(f^2+g^2x^2)\,dx}{h^2x^2-k^2} = \frac{\pi}{hk}\tan^{-1}(gk/fh), \quad f,g,h,k>0, \quad (66)$$

we easily, after comparing Eqs. (64) and (66), identify $g=h=1$, $k=\omega$, $f=c, m$, and n respectively for the first, second, and third integrals in Eq. (64), and thus obtain

$$\begin{aligned}\theta_m(\omega) &= -\tan^{-1}(\omega/c)+\tan^{-1}(\omega/m)+\tan^{-1}(\omega/n), \\ &= -\tan^{-1}(\omega/c)+\tan^{-1}[a\omega/(b-\omega^2)]\end{aligned} \quad (67)$$

which is identical to Eq. (61). The last step in Eq. (67) is accomplished by combining $\tan^{-1}(\omega/m)$ and $\tan^{-1}(\omega/n)$ after using the relations in Eq. (65) and noting the requirements in Eq. (66). The phase function for $H_n(j\omega)$, however, cannot be obtained from the Hilbert transform.

The derivation of Eq. (67) from $|H_m(j\omega)|^2$ is exact. In general, there is no further approximation involved once an approximate squared magnitude in the form of a ratio of two polynomials in even orders of ω is deduced from a measured cw magnitude curve. In fact, the phase of the minimum-phase transfer function can be obtained directly from this deduced squared magnitude with the help of Eq. (4a) by the method proposed here. The type of integral formula given in Eq. (66) together with the Hilbert transform Eq. (4a) can also be applied to $H_{2a}(s)$ in Eq. (24) to obtain the same phase function $\theta_{2a}(\omega)$ in Eq. (26).

The corresponding impulse responses are determined from

$$H_m(s)=A\frac{(s+c)}{s^2+as+b}=A\frac{s+a/2+c-a/2}{(s+a/2)^2+\beta^2} \quad (68)$$

and

$$H_n(s)=A\frac{c+a/2-(s+a/2)}{(s+a/2)^2+\beta^2} \quad (69)$$

yielding respectively

$$h_m(t)=A\,e^{-at/2}[\cos\beta t+\frac{c-a/2}{\beta}\sin\beta t], \quad t\geq 0, \quad (70)$$

and

$$h_n(t)=-A\,e^{-at/2}[\cos\beta t-\frac{c+a/2}{\beta}\sin\beta t], \quad t\geq 0, \quad (71)$$

where β is given in Eq. (25).

These impulse functions are still, basically, a sinusoidal function with a decay rate of $a/2$, even though the form is little more complicated than that of $h_{2a}(t)$ given in Eq. (27). Again, the decay rate is related primarily to the bandwidth, and the period of variations to the resonant frequency.

From Eqs. (70) and (71), we see that $h_m(0+) = A\,[= -h_n(0+)]$, which is different from the previous case where $h_{2a}(0+)=0$. Both impulse responses start ($t=0$) at the same magnitude A. Since the parameter c can be greater than $a/2$, at $t=0+$, $h_m(t)$ may increase and reach the maximum before falling to its first zero. On the other hand, $|h_n(t)|$ always decreases beginning at $t=0+$. The first zero of $h_m(t)$ is determined by the smallest root of

$$\tan \beta t_m = -\beta/(c-a/2)\,, \tag{72}$$

while that of $h_n(t)$ is by the smallest root of

$$\tan \beta t_n = \beta/(c+a/2)\,. \tag{73}$$

A comparison of Eqs. (72) with (73) indicates, regardless of the relative values of c and $a/2$, that the first zero of $h_n(t)$, called t_{n0}, is no greater than that of $h_m(t)$, called t_{m0}. That is,

$$t_{n0} \leq t_m 0\,. \tag{74}$$

The equality sign holds when $c=0$.

Equation (74) implies that t_{n0} is closer to $t=0$ than is t_{m0}. Thus, the beamwidth of the impulse response $h_m(t)$ associated with the minimum-phase transfer function is wider than the beamwidth of $|h_n(t)|$ associated with the nonminimum-phase transfer function with the same squared-magnitude function. This, in turn, means that more energy is concentrated, at the beginning of excitation, in the minimum-phase system than in the nonminimum-phase system. Once again, the minimum-phase system may be considered as the worst case as far as the initial impact of the system by the interference source is concerned. Another example is presented for illustration.

Example 2. Suppose that the square of a given "measured" magnitude can be represented by a shifted Gaussian function,

$$f^2(\omega) = 4\,e^{-2(\omega-3)^2} \tag{75}$$

The resonant and two half-power frequencies are: $\omega_0=3$, $\omega_1=2.4113$, and $\omega_2=3.5887$, the system bandwidth is 1.1774, and $Q=2.5480$. The maximum at ω_0 is 4. Since $\omega_1^2+\omega_2^2$ is not equal to $2\omega_0^2$ in this case, we wish to approximate Eq. (75) by $|H_{2b}(j\omega)|^2$ given in Eq. (49). Using Eq. (55) we obtain the required parameters: $a^2=1.3606$, $b^2=87.1181$, $c^2=8.8267$, and $A^2=2.7725$. Then

$$|H_{2b}(j\omega)|^2 = \frac{2.7725(\omega^2+8.8267)}{\omega^4-17.3069\omega^2+87.1181}, \tag{76}$$

which is computed together with $f^2(\omega)$ in Table 2 to show the quality of approximation.

Table 2. Approximation of the given function in Eq. (75) by the squared-magnitude function in Eq. (76)

ω	$f^2(\omega)$	$\lvert H_{2b}(j\omega)\rvert^2$	Error
0.00	0.0000	0.2809	0.2809
0.25	0.0000	0.2864	0.2864
0.50	0.0000	0.3037	0.3037
0.75	0.0002	0.3350	0.3348
1.00	0.0013	0.3848	0.3835
1.25	0.0087	0.4607	0.4520
1.50	0.0444	0.5768	0.5324
1.75	0.1757	0.7579	0.5822
2.00	0.5413	1.0493	0.5080
2.25	1.2986	1.5323	0.2337
2.50	2.4261	2.3206	−0.1055
2.75	3.5300	3.3844	−0.1456
3.00	4.0000	4.0000	0.0000
3.25	3.5300	3.3851	−0.1449
3.50	2.4261	2.3215	−0.1046
3.75	1.2986	1.5294	0.2308
4.00	0.5413	1.0396	0.4983
4.25	0.1757	0.7398	0.5641
4.50	0.0444	0.5495	0.5051
4.75	0.0087	0.4231	0.4144
5.00	0.0013	0.3356	0.3343
5.25	0.0002	0.2728	0.2726
5.50	0.0000	0.2264	0.2264

The computation is carried out only from $\omega=0$ to $\omega=5.50$. The approximation around the important region near $\omega=\omega_0=3$ is very good, while that near the two ends ($\omega=0$ and $\omega=5.50$) is marginal. Physically, however, the less accurate results near the two frequency ends are of secondary importance.

If we deal with $|H_{2b}(j\omega)|^2$ alone without including extra all-pass functions, we have two possible solutions for the transfer function, one with a minimum phase and the other with a nonminimum phase,

$$H_m(s) = \frac{1.6651(s+2.9710)}{s^2+1.1664s+9.3337} = \frac{1.6651(s+0.5832+2.3878)}{(s+0.5832)^2+2.9989^2} \tag{77}$$

and

$$H_n(s) = \frac{1.6651(2.9710-s)}{s^2+1.1664s+9.3337} = \frac{1.6651[3.5542-(s+0.5832)]}{(s+0.5832)^2+2.9989^2}\,. \tag{78}$$

The corresponding phases are

$$\theta_m(\omega) = \tan^{-1}[1.1664\omega/(9.3337-\omega^2)] - \tan^{-1}(\omega/2.9710) \quad (79)$$

and

$$\theta_n(\omega) = \tan^{-1}[1.1664\omega/(9.3337-\omega^2)] + \tan^{-1}(\omega/2.9710) \quad (80)$$

The impulse responses are

$$h_m(t) = 1.6651[\cos(2.9989t) + 0.7962\sin(2.9989t)]\, e^{-0.5832t} \quad (81)$$

and

$$h_n(t) = -1.6651[\cos(2.9989t) - 1.1852\sin(2.9989t)]\, e^{-0.5832t} \quad (82)$$

Thus, this method not only yields a solution with a minimum-phase transfer function such as by the conventional numerical method described in Sec. 3, but also gives other possible solutions with non-minimum-phase transfer functions.

Figure 3 shows $h_m(t)$ and $|h_n(t)|$ for comparison purpose. Evidently, both $h_m(t)$ and $|h_n(t)|$ begin at $t=0$ with a magnitude of 1.6651. Then $h_m(t)$ increases to its maximum of 1.9030 at $t=0.1602$, and $-h_n(t)$ starts to decrease. The first zero of $h_n(t)$ is at $t=0.2337$, while that of $h_m(t)$ is at $t=0.7480$. Also, $|h_n(t)|_{max} < |h_m(t)|_{max}$ in this case. More energy is concentrated in $h_m(t)$ than in $h_n(t)$ near $t=0$.

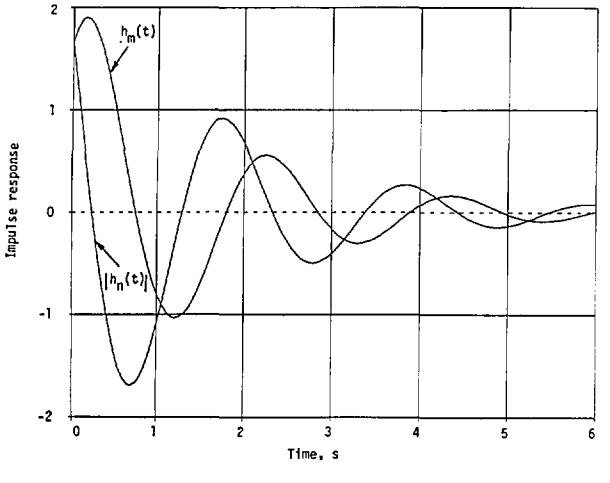

Fig. 3. Impulse responses with the given cw squared-magnitude response in Eq. (75) and the approximate squared magnitude in Eq. (76).

Comparing Eqs. (77) and (78), we may also express $H_n(s)$ in terms of $H_m(s)$ and a first-order all-pass function:

$$H_n(s) = H_m(s)\,\frac{2.9710-s}{2.9710+s}. \quad (83)$$

In general, the solution obtained in Eqs. (69) and (71) is not the only one with a nonminimum phase. In fact, the same given magnitude curve can also be represented by the product of $H_m(s)$ [or $H_n(s)$] and additional all-pass functions. The solutions depend on the choice of these extra all-pass functions.

4.2 First-Order Transfer Function

The two types of the second-order transfer function analyzed in Sec. 4.1 are the most important ones which can be used to approximate a measured magnitude curve with only one resonant frequency not at $\omega=0$. For studies of radiated susceptibility, these may be sufficient because it is difficult or meaningless for an antenna to measure the interference response of linear systems at $\omega=0$. However, when the dc interference is also possible, in addition to the cw interferences, for some practical systems, the response at $\omega=0$ may constitute a relative maximum. To cover this case, we can approximate this part of the given measured magnitude curve by a squared magnitude corresponding to the first-order stable transfer function

$$H_1(s) = A/(s+a), \quad (84)$$

where A and a are real and positive. Its squared magnitude is

$$|H_1(j\omega)|^2 = A^2/(\omega^2+a^2). \quad (85)$$

Obviously, its only maximum occurs at $\omega=0$, with $|H_1(0)|^2=(A/a)^2$. A representative curve for $|H_1(j\omega)|^2$ is shown in Fig. 4.

The half-power frequency may be determined by

$$1/(\omega^2+a^2) = 1/(2a^2), \quad (86)$$

which yields only one solution $\omega_2=a$ (the other half-power frequency $\omega_1=-a$ has no physical meaning). The bandwidth in this case is just $2\omega_2$.

The associated phase function can be obtained either from $H_1(j\omega)$ or from the Hilbert transform,

$$\theta_1(\omega) = \tan^{-1}(\omega/a), \quad (87)$$

which varies from 0 to $\pi/2$ as ω varies from 0 to ∞.

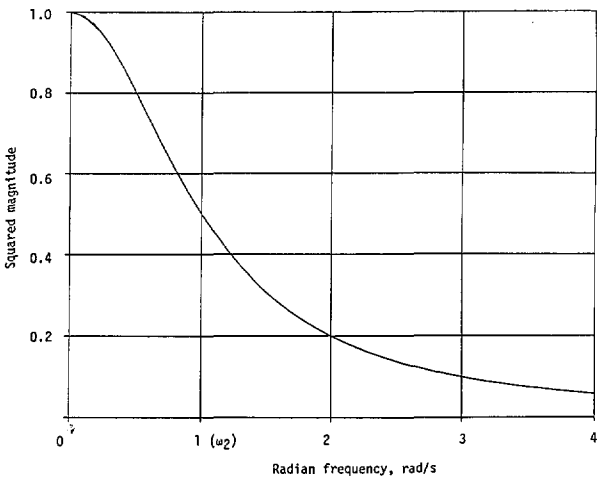

Fig. 4. A squared-magnitude response corresponding to the first-order transfer function, normalized Eq. (85).

The corresponding impulse response is

$$h_1(t)=A\,e^{-at},\quad t\geq 0\,. \tag{88}$$

The decay rate in this case equals numerically the half-power frequency.

4.3 More General Case

For a more general case where the measured magnitude curve has $N>1$ distinct resonant frequencies, it may be approximated with our proposed method by a sum of terms of the type $|H_{2a}(j\omega)|^2$ or $|H_{2b}(j\omega)|^2$ discussed in Sec. 4.1. To simplify the notation, let us temporarily drop the subscript a and b while maintaining the subscript 2 to indicate the order of the transfer function being considered. The approximated squared magnitude will then take the form:

$$|H(j\omega)|^2=\sum_{i=1}^{N}|H_{2i}(j\omega)|^2\,, \tag{89}$$

with the required parameters a, b, A, and possibly c in each $|H_2(j\omega)|^2$ to be determined by the outstanding features associated with each resonant frequency. Should there also be a relative maximum at $\omega=0$, another term in the form of Eq. (85) for a first-order transfer function may be added to Eq. (89). Once this approximation is accomplished, the system transfer functions can then be deduced by the classical method [8]. We can then determine from these transfer functions the corresponding phase functions and impulse responses to give the complete characteristics of the unknown linear system. Another example is given below to illustrate this point.

Example 3. Suppose that the square of a measured cw magnitude curve can be represented by a sum of two mathematical expressions

$$f^2(\omega)=f_1^2(\omega)+f_2^2(\omega)\,, \tag{90}$$

where

$$f_1^2(\omega)=e^{-2\omega} \tag{91}$$

is used to simulate a possible maximum at $\omega=0$, and

$$f_2^2(\omega)=4\,e^{-2(\omega-3)^2} \tag{92}$$

is simulated for a possible resonant frequency at $\omega_0=3$. The expression in Eq. (92) is the same as that presented in example 2.

Since the maximum of $f_1^2(\omega)$ occurs at $\omega=0$ with $f_1^2(0)=1$, and the half-power frequency is $\omega_2=0.3466$, we approximate $f_1^2(\omega)$ by a linear system with lumped-constant elements represented by a squared-magnitude function in the form of Eq. (85),

$$|H_1(j\omega)|^2=\frac{0.3466^2}{\omega^2+0.3466^2}\,, \tag{93}$$

which is plotted in Fig. 5 together with $f_1^2(\omega)$ to show the approximation involved.

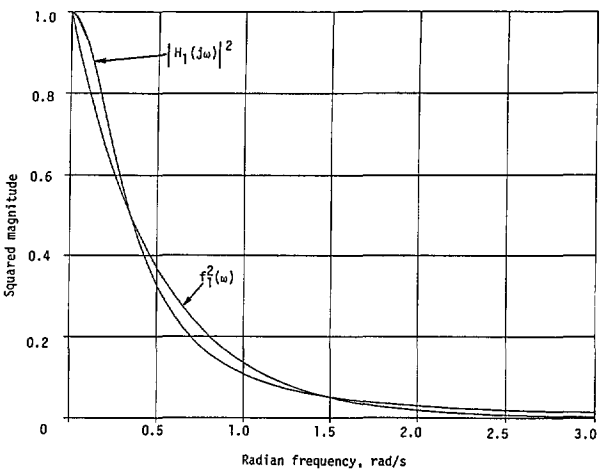

Fig. 5. Comparison of functions given in Eqs. (91) and (93).

For $f_2^2(\omega)$, we have $\omega_0=3$ with $f_2^2(3)=4$. The half-power frequencies ($\omega_1=2.4113$ and $\omega_2=3.5887$) have been obtained in example 2. Even though the relation $\omega_0^2=\omega_1\omega_2$ is not satisfied, this time we choose $c=0$ in $H_{2b}(s)$ to make a better approximation at $\omega=0$. The other required parameters are determined from Eqs. (55) and (57): $b=\omega_0^2=9$, $a^2=\omega_1^2+\omega_2^2-2\omega_0^2=0.6931$, $a=0.8325$, and $A^2=a^2f_2^2(3)=2.7725$. We then have the following to approximate the given $f_2^2(\omega)$:

$$|H_{2b}(j\omega)|^2=\frac{2.7725\omega^2}{\omega^4-17.3069\omega^2+81}, \qquad (94)$$

which is plotted in Fig. 6 together with the given $f_2^2(\omega)$ for comparison purpose. The approximation shown here may be compared with that shown in Table 2, where c is chosen not equal to 0.

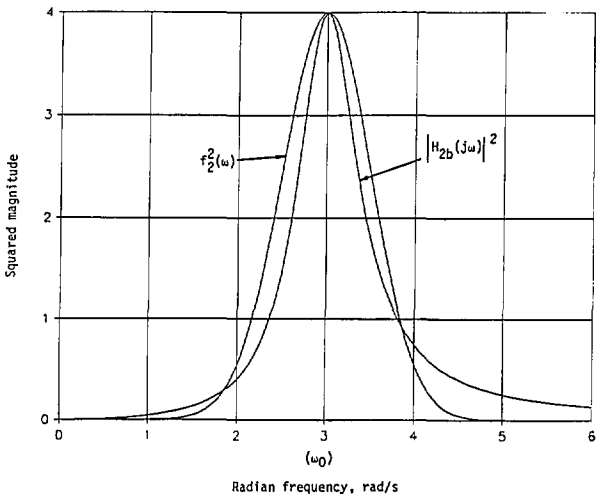

Fig. 6. Comparison of functions given in Eqs. (92) and (94).

The total squared magnitude to approximate $f^2(\omega)$ in Eq. (90) is then given by the sum of expressions in Eqs. (93) and (94):

$$|H(j\omega)|^2=\frac{0.1201}{\omega^2+0.1201}+\frac{2.7725\omega^2}{\omega^4-17.3069\omega^2+81}$$

$$=\frac{2.8926(\omega^4-0.6036\omega^2+3.3639)}{(\omega^2+0.1201)(\omega^4-17.3069\omega^2+81)}$$

$$=H(s)H(-s)|_{s=j\omega}, \qquad (95)$$

which is plotted in Fig. 7 together with $f^2(\omega)$.

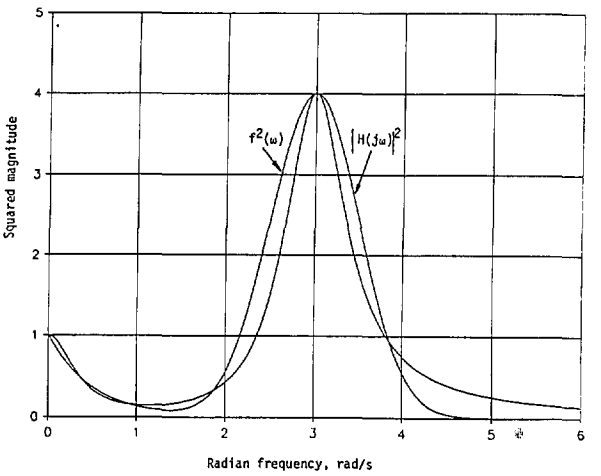

Fig. 7. Comparison of the functions given in Eqs. (90) and (95).

From Eq. (95) we can apply the classical method in network theory [8] to extract the transfer functions as follows:

$$H(s)H(-s)=\frac{2.8926(s^4+0.6036s^2+3.3639)}{(0.1201-s^2)(s^4+17.3069s^2+81)}$$

$$=\frac{2.8926N(s)}{D(s)}, \qquad (96)$$

where

$$N(s)=(s^2+1.7506s+1.8341)(s^2-1.7506s+1.8341), \qquad (97)$$

and

$$D(s)=(0.3466+s)(0.3466-s)\times(s^2+0.8325s+9)(s^2-0.8325s+9). \qquad (98)$$

From the formats specifically expressed in Eqs. (97) and (98), we can assign appropriate factors to $H(s)$ and $H(-s)$. Obviously, the factors with positive signs in Eq. (98) have to be assigned to the denominator of $H(s)$ because the poles are required to be in the left half of the s-plane for the linear system to be stable. The remaining factors in Eq. (98) with negative signs belong to the denominator of $H(-s)$. However, either factor in Eq. (97) can be assigned to the numerator of $H(s)$ because the zeros can be in the left-half or right-half plane. If the zeros are in the left half-plane, the system is at minimum phase. If they are in the right half-plane, the system is at nonminimum phase. Thus, we obtain the minimum-phase system,

$$H_m(s) = \frac{1.7008(s^2+1.7506s+1.8341)}{(s^2+0.3466)(s^2+0.8325s+9)}$$
$$= 1.7008[0.1526/(s+0.3466) + (0.8474s+1.3299)/(s^2+0.8325s+9)], \quad (99)$$

and the nonminimum-phase system,

$$H_n(s) = \frac{1.7008(s^2-1.7506s+1.8341)}{(s+0.3466)(s^2+0.8325s+9)}$$
$$= 1.7008[0.2900/(s+0.3466) + (0.7100s-2.2381)/(s^2+0.8325s+9)]. \quad (100)$$

We can verify that $|H_m(j\omega)|^2=|H_n(j\omega)|^2$ and that they both equal the squared magnitude in Eq. (95). Now, the nonminimum-phase transfer function in Eq. (100) can also be expressed in terms of the minimum-phase transfer function in Eq. (99) and an all-pass function

$$H_n(s)=H_m(s)H_{all}(s), \quad (101)$$

where

$$H_{all}(s) = (s^2-1.7506s+1.8341)/(s^2+1.7506s+1.8341), \quad (102)$$

is a second-order all-pass function with the complex-pair zeros in the right half-plane as mirror images of the poles in the left half-plane.

The associated phase functions are respectively

$$\theta_m(\omega)=\theta_1(\omega)+\theta_2(\omega)-\theta_3(\omega) \quad (103)$$

and

$$\theta_n(\omega)=\theta_1(\omega)+\theta_2(\omega)+\theta_3(\omega), \quad (104)$$

where θ_1 and θ_2 are due to the denominator factors in Eq. (99) and θ_3 is due to the numerator in Eq. (99). They are:

$$\theta_1(\omega) = \tan^{-1}(\omega/0.3466),$$
$$\theta_2(\omega) = \tan^{-1}[0.8325\omega/(9-\omega^2)],$$

and

$$\theta_3(\omega) = \tan^{-1}[1.7506\omega/(1.8341-\omega^2)]. \quad (105)$$

The minimum phase $\theta_m(\omega)$ in Eq. (103) can also be obtained from Eq. (95) with the Hilbert transform, as demonstrated before.

The impulse responses are:

$$h_m(t)/1.7008 = 0.1526\,e^{-0.3466t} + [0.8474\cos(2.9710t) + 0.3289\sin(2.9710t)]\,e^{-0.4163t} \quad (106)$$

and

$$h_n(t)/1.7008 = 0.2900\,e^{-0.3466t} + [0.7100\cos(2.9710t) - 0.8528\sin(2.9710t)]\,e^{-0.4163t} \quad (107)$$

where both $h_m(t)$ and $h_n(t)$ are normalized with respect to the common constant factor 1.7008.

The normalized impulse responses in Eqs. (106) and (107) are plotted in Fig. 8. Here, they both start with 1 at $t=0$. The normalized $h_n(t)$ decreases much faster than the normalized $h_m(t)$. Thus, $h_n(t)$ has a narrower beamwidth than $h_m(t)$, or less energy is concentrated initially with $h_n(t)$ than with $h_m(t)$.

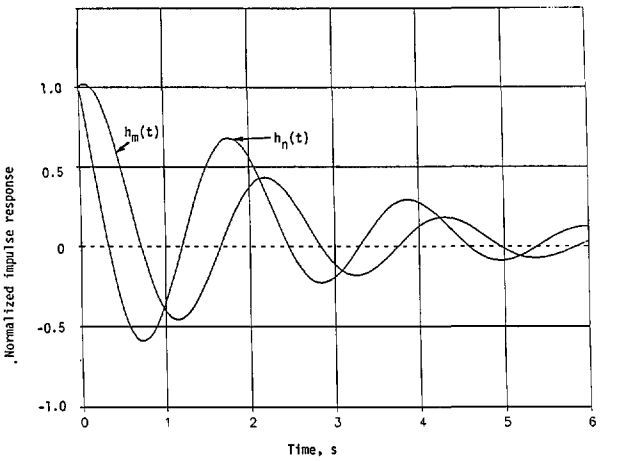

Fig. 8. Normalized impulse responses of the linear system with its given cw squared-magnitude response in Eq. (90) and the approximate squared magnitude in Eq. (95).

The procedures demonstrated in example 3 can be easily extended to cases with more resonant frequencies, where there will be more terms in Eq. (89). More algebraic processes will be involved. When extracting transfer functions from the

approximate squared magnitude, we will find more combinations for those with nonminimum phases while there is still only one solution for the transfer function with a minimum phase. Once the transfer functions are obtained, the remaining task for determining the corresponding phases and impulse responses is relatively straightforward. Determination of passive elements and a specific circuit structure to represent the extracted transfer function is a typical network synthesis problem [4, 8, 9], which is not within our scope of analysis. Once a network is synthesized, we can then use this model to make further analysis and even measurement of the network response due to any excitation, cw or pulse, with little effort and cost.

One caution, however, must be exercised for dealing with the cases where two resonant frequencies happen to be very close together. In these cases, the half-power frequencies associated with each resonant frequency must be entered into the computing process with smaller values than the actual values such that the final approximate squared magnitude still exhibits two distinct maxima at those resonant frequencies (rather than smeared together to have only one maximum).

The three examples presented so far are simulations where the given magnitudes are expressed in terms of neat mathematical functions and the resonant frequencies are small and easily manipulable numbers. In the real world, this is definitely not the case. Our goal is still to deduce an approximate squared magnitude from the given measured cw magnitude data so that a set of transfer functions and related characteristics can be determined and analyzed. Another example under this situation will be presented later in Sec. 5.

5. Frequency Transformation

In Sec. 4 the variable ω was loosely called frequency. Strictly speaking, ω is the normalized radian frequency. It can be translated into any frequency of interest by a simple frequency transformation [8],

$$\omega' = B\omega\,, \tag{108}$$

where B is a normalization constant, ω is the normalized radian frequency, and ω' is the actual radian frequency.

In presenting example 1 in Sec. 4.1, we cited $\omega_0 = 2$ as the resonant frequency. If the actual resonant frequency occurs at 20 MHz, we should have used $\omega_0 = 4\pi(10)^7$ rad. Instead, we chose then to use $\omega_0 = 2$ to avoid manipulations with large numbers. After obtaining $|H_{2a}(j\omega)|^2$, $H_{2a}(s)$, $\theta_m(\omega)$, and $h_{2a}(t)$ in Eqs. (41) through (44), we can apply Eq. (108) with $B = 2\pi(10)^7$ to transform the results from ω to ω' with $\omega = \omega'/B$. Thus, the solutions in Eqs. (41-44) become respectively

$$|G_{2a}(j\omega')|^2 = \frac{0.6931B^4}{\omega'^4 - 8B^2\omega'^2 + 16.6931B^4}$$

$$= G_{2a}(s')G_{2a}(-s')|_{s'=j\omega'},$$

$$G_{2a}(s') = \frac{0.8326B^2}{s'^2 + 0.4141Bs' + 4.0857B^2},$$

$$\theta_m(\omega') = \tan^{-1}[0.4141B\omega'/(4.0857B^2 - \omega'^2)], \tag{109}$$

and

$$h_{2a}(t) = 0.4141B\, e^{-0.2070Bt} \sin(1.0107Bt).$$

These procedures apply also to the other type of second-order and higher-order transfer functions. With this explained, we now are ready to give another example based on the real-world data shown in Fig. 9. The data represent the measured but normalized electric fields (magnitude) of vertical polarization, reflected from a helicopter when it is irradiated by an impulse signal. By examining the curve in Fig. 9, we notice four significant resonant frequencies at 16.50, 26.25, 41.00, and 53.375 MHz. The frequency near 3 MHz is ignored because its magnitude response is rather small (close to background noise). It can, however, be added if necessary.

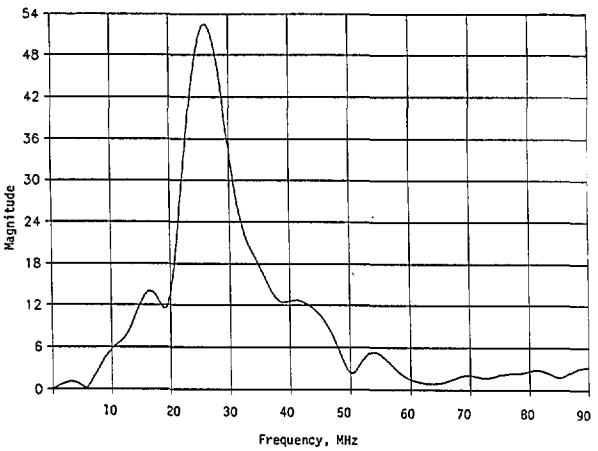

Fig. 9. Measured electric-field magnitude (vertical polarization) reflected from a helicopter when radiated by an external impulse signal.

To simplify the analysis, we temporarily designate $\omega_{01}=2\pi\times16.50=103.6726$, $\omega_{02}=52.5\pi=164.9336$, $\omega_{03}=82\pi=257.6106$, and $\omega_{04}=106.75\pi=335.3650$. From Fig. 9, we also see that the respective maximum responses at these resonant frequencies are 14.00 (22.92 dB), 52.52 (34.41 dB), 13.00 (22.28 dB), and 5.33 (14.53 dB). Their half-power frequencies are approximately $\omega_{11}=29\pi=91.1062$, $\omega_{12}=36\pi=113.0973$; $\omega_{21}=46\pi=144.5132$, $\omega_{22}=59\pi=185.3540$; $\omega_{31}=76\pi=238.7610$, $\omega_{32}=90\pi=282.7433$; and $\omega_{41}=104\pi=326.7256$, $\omega_{42}=108.6\pi=341.1770$. Here the first subscript refers to the resonant frequency, the second subscript 1 refers to the half-power frequency on the left side of the respective resonant frequency, and the second subscript 2 refers to the half-power frequency on the right side of the respective resonant frequency. The two half-power frequencies, $\omega_{12}=36\pi$ and $\omega_{31}=76\pi$, are not real, but extrapolated for the analysis. Also, we later use $B=10^6$, in accordance with Eq. (108), as the transformation constant.

Even though the condition $\omega_1^2+\omega_2^2=2\omega_0^2$ is not exactly satisfied at either of the four resonant frequencies, we choose to use the type of second-order transfer function in Eq. (10a) for obtaining the approximate squared magnitudes. Using Eq. (23), we have for the first resonant frequency at ω_{01},

$$A_1=3.1435(10^4),\ b_1=1.0980(10^4),\ a_1=21.5420,$$

and

$$|H_1(j\omega)|^2=9.8816(10^8)/[\omega^4-2.1496(10^4)\omega^2+1.2056(10^8)]; \quad (110)$$

for the second resonant frequency at ω_{02},

$$A_2=3.5377(10^5),\ b_2=2.8025(10^4),\ a_2=40.5358,$$

and

$$|H_2(j\omega)|^2=12.5153(10^{10})/[\omega^4-5.4406(10^4)\omega^2+7.8538(10^8)]; \quad (111)$$

for the third resonant frequency at ω_{03},

$$A_3=1.4909(10^5),\ b_3=6.7347(10^4),\ a_3=44.3546,$$

and

$$|H_3(j\omega)|^2=2.2228(10^{10})/[\omega^4-1.3273(10^5)\omega^2+4.5356(10^9)]; \quad (112)$$

and for the last resonant frequency at ω_{04},

$$A_4=2.5723(10^4),\ b_4=1.1257(10^5),\ a_4=14.3871,$$

and

$$|H_4(j\omega)|^2=6.6166(10^8)/[\omega^4-2.2494(10^5)\omega^2+1.2673(10^{10})]; \quad (113)$$

The final approximate squared magnitude is then

$$\begin{aligned}|H(j\omega)|^2&=|H_1(j\omega)|^2+|H_2(j\omega)|^2+|H_3(j\omega)|^2+|H_4(j\omega)|^2\\&=1.4903(10^{11})N(\omega^2)/D(\omega^2),\end{aligned} \quad (114)$$

where

$$\begin{aligned}N(\omega^2)&=\omega^{12}-3.6694(10^5)\omega^{10}+5.1348(10^{10})\omega^8-3.4113(10^{15})\omega^6+1.0820(10^{20})\omega^4\\&\quad-1.3940(10^{24})\omega^2+6.2996(10^{27})\\&=[\omega^4-2.1747(10^4)\omega^2+1.2577(10^8)]\\&\quad\times[\omega^4-1.2098(10^5)\omega^2+3.9741(10^9)]\\&\quad\times[\omega^4-2.2422(10^5)\omega^2+1.2615(10^{10})],\end{aligned} \quad (115)$$

and $D(\omega^2)$ is the product of the four denominators in Eqs. (110) through (113). The magnitude in Eq. (114) is shown in Fig. 10 together with the component magnitude functions obtained in Eqs. (110) through (113). Comparing Figs. 9 and 10, we see, except the frequency scale, the approximation in Eq. (114) is generally very good. The dominant features at ω_{02} and its half-power frequencies are indeed excellent. The shifts in ω_{01}, and ω_{03}, are minor. The position of ω_{04} remains practically the same. The only major changes are the magnitudes at $\omega=0$ and ω_{01}. This deficiency can be improved if we choose the second-order transfer function of Eq. (10b) or the approximate squared-magnitude function in Eq. (49) with $c=0$ at the beginning for $|H_2(j\omega)|^2$. From Eq. (115) we already see the large coefficients even when we used the normalized frequency to begin with. If we wish to convert the frequency into megahertz, the numerator in Eq. (114) will become

$$\begin{aligned}&(1/B^{12})[\omega^4-2.1747(10^4)B^2\omega^2+1.2577(10^8)B^4]\\&\quad\times[\omega^4-1.2098(10^5)B^2\omega^2+3.9741(10^9)B^4]\\&\quad\times[\omega^4-2.2422(10^5)B^2\omega^2+1.2615(10^{10})B^4],\end{aligned} \quad (116)$$

and the denominator of Eq. (114) will become

$$(1/B^{16})\,[\omega^4-2.1496(10^4)B^2\omega^2+1.2056(10^8)B^4] \times[\omega^4-5.4406(10^4)B^2\omega^2+7.8538(10^8)B^4] \times[\omega^4-1.3272(10^5)B^2\omega^2+4.5356(10^9)B^4] \times[\omega^4-2.2494(10^5)B^2\omega^2+1.2673(10^{10})B^4], \quad (117)$$

where $B=10^6$.

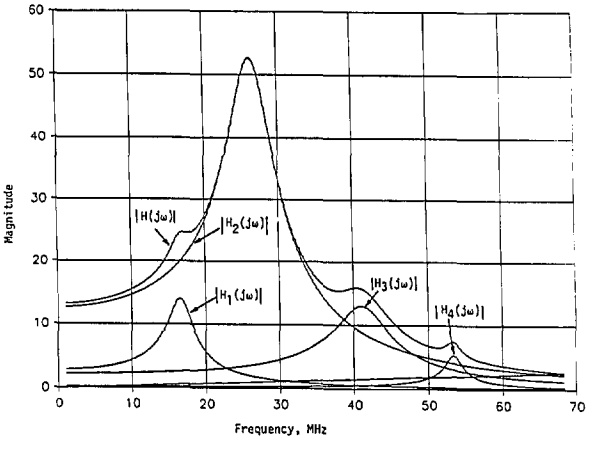

Fig. 10. The approximate magnitude to that in Fig. 9, together with component magnitude functions identified for each resonant frequency, where $|H(j\omega)|=[|H_1(j\omega)|^2+|H_2(j\omega)|^2+|H_3(j\omega)|^2+|H_4(j\omega)|^2]^{1/2}$, Eq. (114).

Referring to Eq. (114) and setting $|H(j\omega)|^2=H(s)H(-s)|_{s=j\omega}$, we obtain

$$H(s)H(-s) = 1.4903(10^{11})N(-s^2)/D(-s^2), \quad (118)$$

where

$$N(-s^2)=N_1(+)N_2(+)N_3(+)N_1(-)N_2(-)N_3(-), \quad (119)$$

and

$$D(-s^2)=D_1(+)D_2(+)D_3(+)D_4(+)D_1(-) \times D_2(-)D_3(-)D_4(-), \quad (120)$$

with

$$N_1(+)=s^2+26.1252s+1.1215(10^4),$$
$$N_1(-)=s^2-26.1252s+1.1215(10^4),$$
$$N_2(+)=s^2+71.4229s+6.3040(10^4),$$
$$N_2(-)=s^2-71.4229s+6.3040(10^4),$$
$$N_3(+)=s^2+20.5139s+1.1232(10^5),$$
$$N_3(-)=s^2-20.5139s+1.1232(10^5);$$
$$D_1(+)=s^2+21.5420s+1.0980(10^4),$$
$$D_1(-)=s^2-21.5420s+1.0980(10^4),$$
$$D_2(+)=s^2+40.5358s+2.8025(10^4),$$
$$D_2(-)=s^2-40.5358s+2.8025(10^4),$$
$$D_3(+)=s^2+44.3546s+6.7347(10^4),$$
$$D_3(-)=s^2-44.3546s+6.7347(10^4),$$
$$D_4(+)=s^2+14.3871s+1.1257(10^5),$$
$$D_4(-)=s^2-14.3871s+1.1257(10^5).$$

Since we require the system to be stable (no poles in the right half of the s-plane), we have to assign $D_1(+)D_2(+)D_3(+)D_4(+)$ as the denominator for $H(s)$. Thus, $D_1(-)D_2(-)D_3(-)D_4(-)$ belongs to $H(-s)$. As far as the numerator for $H(s)$ is concerned, we have many choices from Eq. (119). When $N_1(+)N_2(+)N_3(+)$ is assigned as the numerator of $H(s)$, $N_1(-)N_2(-)N_3(-)$ then belongs to $H(-s)$. In this case, there are no zeros in the right half of the s-plane. The result is a minimum-phase transfer function. We then have

$$H_m(s) = 3.8604(10^5)N_1(+)N_2(+)N_3(+)/[D_1(+)D_2(+)D_3(+)D_4(+)]$$
$$= 3.8604(10^5)\left\{\frac{F_1s+G_1}{D_1(+)}+\frac{F_2s+G_2}{D_2(+)}+\frac{F_3s+G_3}{D_3(+)}+\frac{F_4s+G_4}{D_4(+)}\right\}, \quad (121)$$

where

$$F_1=2.3245/10^4, \quad G_1=1.3664/10^2,$$
$$F_2=5.3398/10^4, \quad G_2=0.8742,$$
$$F_3=-6.8335/10^4, \quad G_3=0.1055,$$
$$F_4=-8.3091/10^5, \quad G_4=1.7752/10^3.$$

Applying the following two Laplace transform pairs [9] to Eq. (121):

$$(s+\alpha)/[(s+\alpha)^2+\beta^2] \leftrightarrow e^{-\alpha t}\cos\beta t, \quad (122a)$$

and

$$1/[(s+\alpha)^2+\beta^2] \leftrightarrow (1/\beta)\,e^{-\alpha t}\sin\beta t, \quad (122b)$$

we obtain the impulse response of this system,

$$h_m(t)=3.8604(10^2)\left\{(0.2325\cos\beta_1 t+0.1071\sin\beta_1 t)\times e^{-\alpha_1 t}+(0.5340\cos\beta_2 t+5.1959\sin\beta_2 t)\,e^{-\alpha_2 t}+(-0.6833\cos\beta_3 t+0.4665\sin\beta_3 t)\,e^{-\alpha_3 t}+(-0.0831\cos\beta_4 t+0.0071\sin\beta_4 t)\,e^{-\alpha_4 t}\right\}, \quad (123)$$

where

$\alpha_i = a_i/2$, and $\beta_i = \sqrt{b_i - (a_i/2)^2}$, $i = 1,2,3,$ and 4.

More specifically, we have

$\alpha_1 = 10.7710$, $\alpha_2 = 20.2679$, $\alpha_3 = 22.1773$,
$\alpha_4 = 7.1936$, $\beta_1 = 104.2305$, $\beta_2 = 166.1740$,
$\beta_3 = 258.5634$, $\beta_4 = 335.4422$.

Equation (123) shows that at $t = 0$, $h_m(t) = 0$. This agrees with the result predicted by the initial-value theorem [10, 12]. The largest coefficient is with $\sin \beta_2 t$ associated with the second resonant frequency. This is obvious when we refer to Fig. 10 where ω_{02} is dominant.

With the impulse response so determined, the system's response to a general excitation can then be computed by convolution integral [12]. When referring to frequencies in megahertz, we simply modify the impulse response in Eq. (123) by multiplying the coefficient $3.8604(10^2)$, α_i, and $\beta_i (i = 1, 2, 3, 4)$ by the transformation constant $B = 10^6$. The impulse response $h_m(t)$ before applying the frequency transformation is presented in Fig. 11, where the coefficient of $3.8604(10^2)$ in Eq. (123) has been dropped. We see, from Fig. 11, that the period is about 0.019 s, giving $0.019\,\beta_2 \approx \pi$. The major maximum occurs approximately at $t_1 = 0.008\,s$ with $h_m(t_1)/3.8604(10^2) = 5.3094$, and the second maximum occurs approximately at $t_2 = 0.026\,s$ with $h_m(t_2)/3.8604(10^2) = -3.2652$. The ratio of $h_m(t_1)/|h_m(t_2)| = 1.6261$, which is close to $e^{\alpha_2(t_2 - t_1)}$. Thus, the second resonant frequency is, indeed, the dominant one [14].

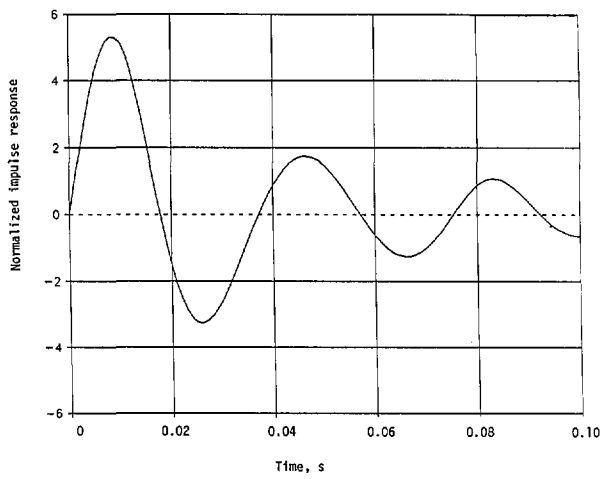

Fig. 11. Normalized impulse response of the linear system whose approximate magnitude of the transfer function is shown in Fig. 10. This is for the minimum-phase case with its transfer function given in Eq. (121).

The associated phase is given by

$$\theta_m(\omega) = \theta_1(\omega) + \theta_2(\omega) + \theta_3(\omega) + \theta_4(\omega) - \theta_5(\omega) - \theta_6(\omega) - \theta_7(\omega), \quad (124)$$

where the first four component phases are due to $D_1(+)D_2(+)D_3(+)D_4(+)$, and the last three are due to $N_1(+)N_2(+)N_3(+)$. That is,

$$\theta_1(\omega) = \tan^{-1}\left[\frac{21.5420\omega}{1.0980(10^4) - \omega^2}\right],$$

$$\theta_2(\omega) = \tan^{-1}\left[\frac{40.5358\omega}{2.8025(10^4) - \omega^2}\right],$$

$$\theta_3(\omega) = \tan^{-1}\left[\frac{44.3546\omega}{6.7347(10^4) - \omega^2}\right],$$

$$\theta_4(\omega) = \tan^{-1}\left[\frac{14.3871\omega}{1.1257(10^5) - \omega^2}\right],$$

$$\theta_5(\omega) = \tan^{-1}\left[\frac{26.1252\omega}{1.1215(10^4) - \omega^2}\right],$$

$$\theta_6(\omega) = \tan^{-1}\left[\frac{71.4229\omega}{6.3040(10^4) - \omega^2}\right],$$

and

$$\theta_7(\omega) = \tan^{-1}\left[\frac{20.5139\omega}{1.1232(10^5) - \omega^2}\right]. \quad (125)$$

Expressing the phase in terms of megahertz, we multiply the numerator inside the arctangents by the normalization constant B and the constant term in the denominator by B^2. The minimum phase θ_m in Eq. (124) before frequency transformation is presented in Fig. 12.

Seven other possible solutions for the transfer function with nonminimum phases can be obtained from Eqs. (118) and (119) as

$$H_{n1}(s) = CN_1(+)N_2(+)N_3(-),$$
$$H_{n2}(s) = CN_1(+)N_2(-)N_3(+),$$
$$H_{n3}(s) = CN_1(-)N_2(+)N_3(+),$$
$$H_{n4}(s) = CN_1(+)N_2(-)N_3(-),$$
$$H_{n5}(s) = CN_1(-)N_2(+)N_3(-),$$
$$H_{n6}(s) = CN_1(-)N_2(-)N_3(+),$$

and

$$H_{n7}(s) = CN_1(-)N_2(-)N_3(-), \quad (126)$$

where

$$C = 3.8604(10^5)/[D_1(+)D_2(+)D_3(+)D_4(+)].$$

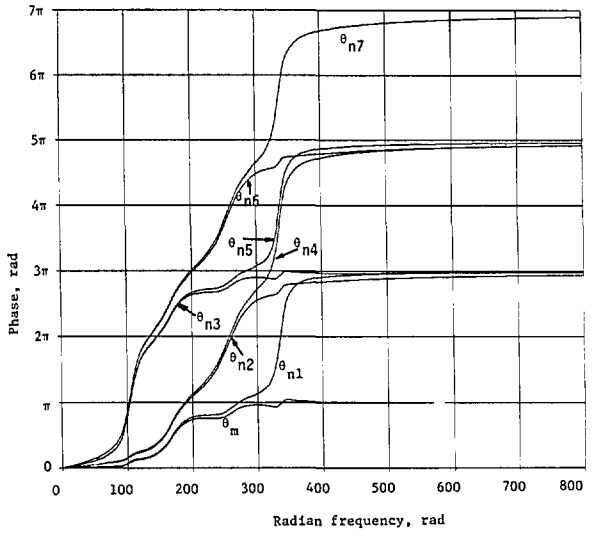

Fig. 12. Phases of the sample linear system whose approximate cw magnitude response is shown in Fig. 10.

Following the same procedures of partial fractions as in Eq. (121), we list the expansion coefficients for the 7 nonminimum-phase cases in Table 3.

The corresponding impulse responses also take the same form as in Eq. (123) with the same α_i and β_i but with different coefficients associated with the cosine and sine terms. These coefficients are listed in Table 4.

These impulse responses with nonminimum phases, without including the frequency transformation, are shown in Figs. 13 (a) and (b) to compare with that in Fig. 11 for the minimum-phase case. It happens that the first maxima of $h_{ni}(t)$ are all below the first maximum of $h_m(t)$, and that the first nulls of $h_{ni}(t)$ are also closer to the origin than the first null of $h_m(t)$. More energy is concentrated near $t=0$ in $h_m(t)$ than any of the $h_{ni}(t)$, $i=1, 2, \ldots, 7$.

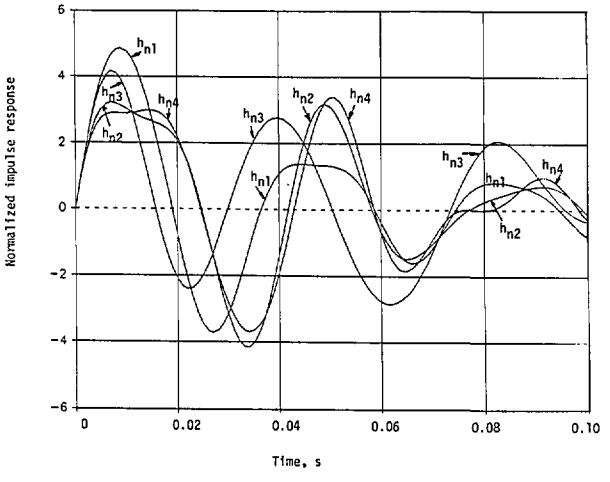

Fig. 13 (a). Normalized impulse response of the helicopter with the approximate magnitude response given in Fig. 10, but with the nonminimum-phase transfer functions given in Eq. (126).

Table 3. Partial fraction expansion coefficients for nonminimum-phase transfer functions

Non-Min.	$F_1\times10^3$	$G_1\times10$	$F_2\times10^3$	G_2	$F_3\times10^3$	$G_3\times10$	$F_4\times10^4$	$G_4\times10$
n1	0.2290	0.1470	0.1253	0.8842	−0.8235	0.6849	4.6925	0.1281
n2	0.2017	0.2034	−3.0480	0.8467	2.8954	1.1708	−0.4910	0.2434
n3	−2.5895	−0.0188	3.2415	0.8940	−0.5711	1.5046	−0.8103	0.0653
n4	0.1952	0.2124	−3.5248	0.8083	2.9958	2.9139	3.3377	−1.2197
n5	−2.6114	−0.1339	2.8849	0.9406	−0.7427	1.2150	4.6927	−0.1422
n6	−2.6634	−0.8067	−0.2450	1.1784	2.9444	−0.6197	−0.3600	0.2700
n7	−2.6541	−0.9251	−0.8178	1.1789	3.2050	1.0964	2.6693	−1.4034

Table 4. Coefficients associated with cosine and sine terms in impulse responses for nonminimum-phase cases

Non-Min.	$\cos\beta_1 t$	$\sin\beta_1 t$	$\cos\beta_2 t$	$\sin\beta_2 t$	$\cos\beta_3 t$	$\sin\beta_3 t$	$\cos\beta_4 t$	$\sin\beta_4 t$
n1	0.2290	0.1174	0.1253	5.3059	−0.8235	0.3355	0.4692	0.0281
n2	0.2017	0.1743	−3.0486	5.4673	2.8954	0.2045	−0.0491	0.0736
n3	−2.5894	0.2496	3.2415	4.9846	−0.5711	0.6309	−0.0810	0.0212
n4	0.1952	0.1836	−3.5248	5.2943	2.9958	0.8700	0.3338	−0.3708
n5	−2.6114	0.1414	2.8849	5.3084	−0.7427	0.5336	0.4693	−0.0525
n6	−2.6634	−0.4987	−0.2450	7.1213	2.9444	−0.4922	−0.0360	0.0813
n7	−2.6541	−0.6133	−0.8178	7.1940	3.2050	0.1491	0.2669	−0.4241

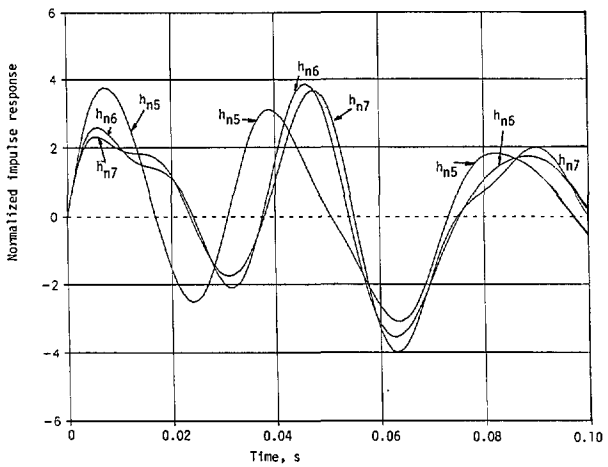

Fig. 13 (b). Normalized impulse response of the helicopter with the approximate magnitude response given in Fig. 10, but with the nonminimum-phase transfer functions given in Eq. (126). Continuation of Fig. 13 (a).

The phases associated with the transfer function in Eq. (126) are respectively:

$$\begin{aligned}
\theta_{n1} &= \theta_1+\theta_2+\theta_3+\theta_4-\theta_5-\theta_6+\theta_7,\\
\theta_{n2} &= \theta_1+\theta_2+\theta_3+\theta_4-\theta_5+\theta_6-\theta_7,\\
\theta_{n3} &= \theta_1+\theta_2+\theta_3+\theta_4+\theta_5-\theta_6-\theta_7,\\
\theta_{n4} &= \theta_1+\theta_2+\theta_3+\theta_4-\theta_5+\theta_6+\theta_7,\\
\theta_{n5} &= \theta_1+\theta_2+\theta_3+\theta_4+\theta_5-\theta_6+\theta_7,\\
\theta_{n6} &= \theta_1+\theta_2+\theta_3+\theta_4+\theta_5+\theta_6-\theta_7,
\end{aligned}$$

and

$$\theta_{n7} = \theta_1+\theta_2+\theta_3+\theta_4+\theta_5+\theta_6+\theta_7, \qquad (127)$$

where

θ_i, $i=1,2,\ldots,7$, are given in Eq. (125) before normalization.

Graphs for θ_{ni} are also plotted in Fig. 12 for comparison purpose. Clearly we see that $\theta_{ni} > \theta_m$, because each component phase given in Eq. (125) is nonnegative, varying from 0 to π as ω varies from 0 to ∞.

6. Consideration of Energy Contents

To assess the ability of a system to withstand damage from an external unwanted excitation, it is often useful to compute the energy content associated with an impulse response [15]. Indeed, if $h(t)$ represents a voltage waveform across a 1 Ω resistor, the quantity

$$E = \int_0^\infty h^2(t)\,dt, \qquad (128)$$

equals the total energy delivered to the resistor by the impulsive excitation [2]. Equation (128) also represents the area under the curve $h^2(t)$.

The energy E may also be computed, in view of Parseval's theorem [2], by

$$E = \frac{1}{2\pi}\int_{-\infty}^{\infty} |H(j\omega)|^2\,d\omega. \qquad (129)$$

Thus, when the minimum-phase impulse response $h_m(t)$ and the associated nonminimum-phase impulse response $h_n(t)$ have an identical $|H(j\omega)|^2$, their respective total energies [in $0 \leq t \leq \infty$] are equal even though $h_n(t) < h_m(t)$ during the initial period near $t = 0+$, as discussed in Sec. 4. These facts can also be demonstrated by referring to the examples given earlier.

For example 1 in Eq. (40), $|H_{2a}(j\omega)|^2$ is given in Eq. (41). Its energy content, according to Eq. (129), is

$$\begin{aligned}
E &= \frac{0.6931}{2\pi}\int_{-\infty}^{\infty}\frac{d\omega}{\omega^4-8\omega^2+16.6931}\\
&= \frac{0.6931}{\pi}\int_0^{\infty}\frac{d\omega}{(\omega^2+p^2)(\omega^2+p^{*2})}\\
&= \frac{0.6931}{j1.6650\pi}\int_0^{\infty}\left[\frac{1}{\omega^2+p^2}-\frac{1}{\omega^2+p^{*2}}\right]d\omega\\
&= 0.2049, \qquad (130)
\end{aligned}$$

where

$p^2 = -4-j0.8325$, and
p^* = complex conjugate of p.

The last step in Eq. (130) is obtained by using

$$\int_0^{\infty}\frac{\cos(qx)\,dx}{x^2+p^2} = \frac{\pi}{2p}e^{-qp},$$

with $q \geq 0$

and $Re(p) > 0$. (131)

We can also obtain the energy by referring to the impulse response given in Eq. (44) for the minimum-phase case,

$$E_m = \int_0^\infty h_{2a}^2(t)\,dt$$

$$= 0.1715 \int_0^\infty e^{-0.4140t}\sin^2(2.0107t)\,dt$$

$$= 0.2049, \qquad (132)$$

which is indeed the same as in Eq. (130).

Using the corresponding impulse response given in Eq. (47) for the nonminimum-phase case yields the same result. That is,

$$E_n = \int_0^\infty h_n^2(t)\,dt = 0.2049. \qquad (133)$$

For example 2 presented in Eq. (75), the corresponding $|H_{2b}(j\omega)|^2$, $h_m(t)$, and $h_n(t)$ can be found respectively in Eqs. (76), (81), and (82). The total energy for this system is

$$E = \frac{1}{2\pi}\int_{-\infty}^\infty |H_{2b}(j\omega)|^2\,d\omega$$

$$= \int_0^\infty h_m^2(t)\,dt$$

$$= \int_0^\infty h_n^2(t)\,dt$$

$$= 2.3124. \qquad (134)$$

If we replace the upper integration limit ∞ in Eq. (128) by a finite T, we can analyze the energy content absorbed by the system during the initial period after an external excitation is applied. Referring again to example 1 with $h_{2a}(t)$ given in Eq. (44) and $h_n(t)$ in Eq. (47), and carrying out the details, we have

$$h_{2a}^2(t) = 0.1714\,e^{-\alpha_1 t}\sin^2\beta t$$

$$= 0.0857\,e^{-\alpha_1 t}(1-\cos 2\beta t),$$

$$h_n^2(t) = 0.1270\,e^{-2t} - (0.2540\cos\beta t + 0.1950\sin\beta t)\,e^{-1.2070t} + (0.1009 + 0.0261\cos 2\beta t + 0.0975\sin 2\beta t)\,e^{-\alpha_1 t},$$

$$E_m = \int_0^T h_{2a}^2(t)\,dt = 0.2048 - 0.2070\,e^{-\alpha_1 T} - 0.0052\,e^{-\alpha_1 T}(-\alpha_1\cos 2\beta T + 2\beta\sin 2\beta T),$$

and

$$E_n = \int_0^T h_n^2(t)\,dt = 0.1413 + 0.0635(1-e^{-2T}) + (-0.2437 - 0.0246\cos 2\beta T + 0.0039\sin 2\beta T)\,e^{-\alpha_1 T} + (0.1270\cos\beta T - 0.0501\sin\beta T)\,e^{-1.2070T}, \qquad (135)$$

where

$$\alpha_1 = 0.4141, \quad \text{and} \quad \beta = 2.0107.$$

Numerical results for both E_m and E_n are shown in Fig. 14 and indicate clearly that $E_n < E_m$ [12]. They are equal only when $T \to \infty$. This reconfirms that the impulse response and transfer function with a minimum phase deduced from a given magnitude can be used as the worst case for analysis purpose, as far as the initial impact to the system under study by an external unwanted source is concerned.

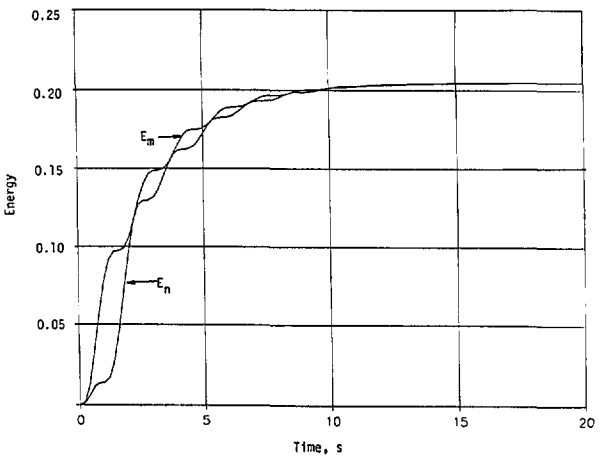

Fig. 14. Energy contents of the sample system whose transfer functions are given in Eqs. (42) and (45).

For the practical example shown in Figs. 9 and 10, we present the results on energy content in Fig. 15. Again, we have $E_{ni} < E_m$, $i = 1, 2, \ldots, 7$.

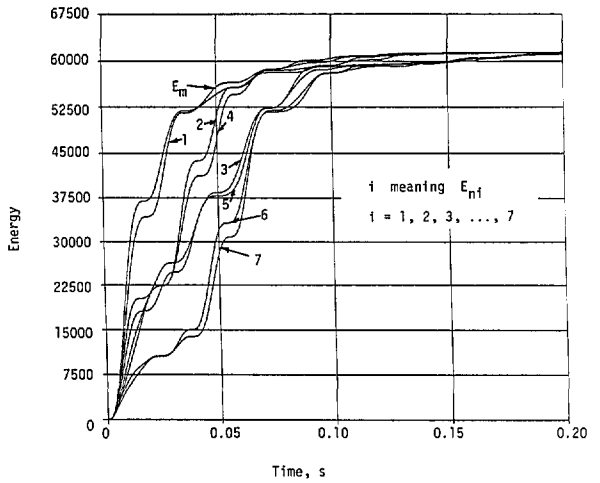

Fig. 15. Energy contents of the helicopter whose approximate cw magnitude response is given in Fig. 10.

7. Conclusions

We have used a simple method known in classical network theory to determine the complete characteristics for an unknown linear system from a given cw magnitude response only. These characteristics include possible different transfer functions, their phases, and the corresponding impulse responses. Only one transfer function is minimum phase. The main achievement is to deduce an approximate squared-magnitude function in the form of a ratio of two even polynomials based on the outstanding features in the given magnitude response, such as resonant frequencies and bandwidths. The remaining procedures for obtaining the complete system characteristics are exact. Four examples, three simulations and one using measured data, have been given to illustrate the proposed method. We have written software that greatly facilitates application of this technique. It first performs numerical calculations necessary to obtain the system transfer functions from the measured magnitude-frequency input data, and then gives impulse responses. We also have shown that the minimum-phase case, through its associated impulse response and energy content, constitutes the most pessimistic estimate as far as the initial threat to the system is concerned.

Acknowledgments

We acknowledge with gratitude the partial support provided by the Naval Sea Systems Command (NAVSEA), and appreciate the interest and discussions of the problem under study with Vincent Paschke of NAVSEA and Robert Amadori of Naval Surface Warfare Center (NSWC).

8. References

[1] F. M. Reza, and S. Seely, Modern Network Analysis, McGraw-Hill, New York (1959).
[2] A. Papoulis, The Fourier Integral and its Applications, McGraw-Hill, New York (1962).
[3] H. W. Bode, Network Analysis and Feedback Amplifier Design, Van Nostrand, Princeton, NJ (1945).
[4] E. A. Guillemin, The Mathematics of Circuit Analysis, John Wiley & Sons, New York (1949).
[5] A. J. Berkhout, Shell Petroleum Report on the minimum phase criterion of sampled signals, State of Brunei (1987).
[6] F. M. Tesche, EMC Zurich Symposium, (1989) p. 191.
[7] F. M. Tesche, IEEE Trans. EMC **34** (1992) p. 259.
[8] N. Balabanian, Network Synthesis, Prentice-Hall, Englewood Cliffs, NJ (1958).
[9] M. E. Van Valkenburg, Network Analysis, Prentice-Hall, Englewood Cliffs, NJ (1959).
[10] M. F. Gardner, and J. L. Barnes, Transients in Linear Systems, Vol. I, (John Wiley & Sons, New York (1956).
[11] D. K. Cheng, Analysis of Linear Systems, Addison Wesley, Reading, MA (1959).
[12] A. V. Oppenheim, and R. W. Schafer, Digital Signal Processing, Prentice-Hall, New York (1975).
[13] I. S. Gradshteyn, and I. M. Ryzhik, Tables of Integrals, Series, and Products, John Wiley & Sons, New York (1956).
[14] M. T. Ma, and J. W. Adams, Natl. Inst. Stand. Technol. Technical Note 1349, (1991).
[15] R. A. McConnell, IEEE National Symp. on EMC **54** (1989) p. 54.

About the authors: M. T. Ma and J. W. Adams are with the Electromagnetic Fields Division, NIST Electronics and Electrical Engineering Laboratory. The National Institute of Standards and Technology is an agency of the Technology Administration, U.S. Department of Commerce.

Volume 98, Number 3, May-June 1993
Journal of Research of the National Institute of Standards and Technology

[J. Res. Natl. Inst. Stand. Technol. 98, 321 (1993)]

X-Ray Diffraction Line Broadening: Modeling and Applications to High-T_c Superconductors

Volume 98 Number 3 May-June 1993

Davor Balzar[1]

National Institute of Standards and Technology,
Boulder, CO 80303-3328

A method to analyze powder-diffraction line broadening is proposed and applied to some novel high-T_c superconductors. Assuming that both size-broadened and strain-broadened profiles of the pure-specimen profile are described with a Voigt function, it is shown that the analysis of Fourier coefficients leads to the Warren-Averbach method of separation of size and strain contributions. The analysis of size coefficients shows that the "hook" effect occurs when the Cauchy content of the size-broadened profile is underestimated. The ratio of volume-weighted and surface-weighted domain sizes can change from ~1.31 for the minimum allowed Cauchy content to 2 when the size-broadened profile is given solely by a Cauchy function. If the distortion coefficient is approximated by a harmonic term, mean-square strains decrease linearly with the increase of the averaging distance. The local strain is finite only in the case of pure-Gauss strain broadening because strains are then independent of averaging distance. Errors of root-mean-square strains as well as domain sizes were evaluated. The method was applied to two cubic structures with average volume-weighted domain sizes up to 3600 Å, as well as to tetragonal and orthorhombic $(La\text{-}Sr)_2CuO_4$, which exhibit weak line broadenings and highly overlapping reflections. Comparison with the integral-breadth methods is given. Reliability of the method is discussed in the case of a cluster of the overlapping peaks. The analysis of La_2CuO_4 and $La_{1.85}M_{0.15}CuO_4$(M = Ca, Ba, Sr) high-T_c superconductors showed that microstrains and incoherently diffracting domain sizes are highly anisotropic. In the superconductors, stacking-fault probability increases with increasing T_c; microstrain decreases. In La_2CuO_4, different broadening of (h00) and (0k0) reflections is not caused by stacking faults; it might arise from lower crystallographic symmetry. The analysis of Bi-Cu-O superconductors showed much higher strains in the [001] direction than in the basal a-b plane. This may be caused by stacking disorder along the c-axis, because of the two-dimensional weakly bonded BiO double layers. Results for the specimen containing two related high-T_c phases indicate a possible mechanism for the phase transformation by the growth of faulted regions of the major phase.

Key words: diffraction line broadening; lattice defects; profile fitting; superconductors; Voigt function; Warren-Averbach analysis; x-ray diffraction.

Accepted: January 25, 1992

Contents

[1] Visiting scientist on leave from the Department of Physics, Faculty of Metallurgy, University of Zagreb, Sisak, Croatia.

Glossary

a, b, c, m, m',	General constants
$U, V, W,$	General constants
U', V', W'	General constants
i, x, z	General variables
A	Fourier coefficient
a_3	Edge of orthorhombic cell, orthogonal to diffracting planes
D	Domain size orthogonal to diffracting planes
d	Interplanar spacing
e	Upper limit of strain
FWHM	Full width at half maximum of profile
f, F	Pure-specimen (physically) broadened profile and its Fourier transform
g, G	Instrumentally broadened profile and its Fourier transform
h, H	Observed broadened profile and its Fourier transform
hkl	Miller indices
I	Intensity
J_c	Critical superconducting current density
K	Scherrer constant
k	$\beta_C/(\pi^{1/2}\beta_G)$, characteristic integral-breadth ratio of a Voigt function
L	na_3, column length (distance in real space) orthogonal to diffracting planes
l	Order of reflection
MSS	Mean-square strains
N	Average number of cells per column
n	Harmonic number
p	Column-length distribution function
R	Relative error
RMSS	Root-mean-square strains
s	$2\sin\theta/\lambda = 1/d$, variable in reciprocal space
T_c	Critical superconducting transition temperature
w	Observation weight
Z	Displacement of two cells in a column
α	Stacking-fault probability
α'	Twin-fault probability
β	$\beta(2\theta)\cos\theta_0/\lambda$, integral breadth in units of s ($Å^{-1}$)
γ	Geometrical-aberration profile
δ	Fraction of oxygen atoms missing per formula unit
$\langle\epsilon^2(L)\rangle$	Mean-square strain, orthogonal to diffracting planes, averaged over the distance L
η	"Apparent strain"
θ	Bragg angle
θ_0	Bragg angle of $K\alpha_1$ reflection maximum
λ	X-ray wavelength
σ	Span of profile in real space
ω	Wavelength-distribution profile

Superscripts

D Denotes the distortion-related parameter
S Denotes the size-related parameter

Subscripts

C Denotes Cauchy component of Voigt function
D Denotes distortion-related parameter
f Denotes pure-specimen (physically) broadened profile
G Denotes Gauss component of Voigt function
g Denotes instrumentally broadened profile
h Denotes observed broadened profile
S Denotes size-related parameter
s Denotes surface-weighted parameter
v Denotes volume-weighted parameter
wp Denotes weighted-residual error

Operators

$\star$ Convolution: $g(x)\star f(x) = \int g(z)f(x-z)\mathrm{d}z$

1. Introduction

X-ray diffraction is one of the oldest tools used to study the structure of matter. In 1912, Laue [1] demonstrated in a single experiment that crystals consist of regularly repeating elementary building blocks, and that x rays show wave nature. Since then, x-ray diffraction has become one of the basic and the most widely used methods for characterization of a broad range of materials.

1.1 Powder X-Ray Diffraction

Many materials are not available in a monocrystal form. Moreover, powders and bulk materials are more easily obtainable, practical, and less expensive. A powder-diffraction experiment requires an order-of-magnitude shorter time than a monocrystal experiment. Thus, powder diffraction is used very often. However, because data are of lower quality and peaks are generally highly overlapped at higher diffracting angles, until 25 years ago powder diffraction was mostly used for qualitative phase analysis. Through advances by Rietveld [2, 3], powder-diffraction patterns become used in structure analysis, so-called structure (Rietveld) refinement. Development of fast on-line computer-controlled data acquisition has allowed a quick analysis of the whole diffraction pattern. Table 1 summarizes uses of different diffraction line-profile parameters in various types of analyses (after Howard and Preston [4]). We shall focus on line-profile analysis to obtain information about microstructural properties of materials: microstrains in the lattice and size of incoherently diffracting domains in crystals.

Table 1. Use of diffraction line-profile parameters

Position	Intensity	Shape	Shift	Method	Identification
√				Indexing	Cell parameters
√	√			Phase analysis	Identification and quantity
			√	Peak-shift analysis	Internal strain (residual stress)
√		√		Profile analysis	Microstrain, crystallite size, lattice defects
√	√	√		Structure refinement	Atomic positions, Debye-Waller factors, others

1.2 Diffraction-Line Broadening

Diffraction from crystal planes occurs at well-defined angles that satisfy the Bragg equation

$$\lambda = 2d_{hkl}\sin\theta_{hkl}. \quad (1)$$

Theoretically, intensity diffracted from an infinite crystal should consist of diffraction lines without width (Dirac delta functions) at some discrete diffraction angles. However, both instrument and specimen broaden the diffraction lines, and the observed line profile is a convolution of three functions [5, 6]

$$h(2\theta) = [(\omega\star\gamma)\star f]\,(2\theta) + \text{background}. \quad (2)$$

Wavelength distribution and geometrical aberrations are usually treated as characteristic for the particular instrument (instrumental profile):

$$g(2\theta) = (\omega\star\gamma)\,(2\theta). \quad (3)$$

To obtain a specimen's microstructural parameters, the specimen (physically) broadened profile f must be extracted from the observed profile h.

Origins of specimen broadening are numerous. Generally, any lattice imperfection will cause

additional diffraction-line broadening. Therefore, dislocations, vacancies, interstitials, substitutions, and similar defects manifest themselves through the lattice strain. If a crystal is broken into smaller incoherently diffracting domains by dislocation arrays, stacking faults, twins, or any other extended imperfections, then domain-size broadening occurs.

1.3 Superconductivity and Defects

Since discovery of the ~90 K superconductor $YBa_2Cu_3O_{7-\delta}$ [7], it became clear that the novel superconductivity relates closely to defects in structure. Both point and extended defects relate closely to the physical properties of superconductors [8, 9]. Defects play an important role both in the critical superconducting transition temperature T_c [10] and in the critical current density J_c [11]. Some theories also connect T_c with lattice distortion [12], with strains around dislocations [13], and with interaction of current carriers and the elastic-strain field [14].

The T_c of $YBa_2Cu_3O_{7-\delta}$, for instance, depends strongly on the oxygen stoichiometry, that is, number of oxygen vacancies in the charge-reservoir layers and their arrangement (see Jorgensen [15] and references therein). Superconductivity in La_2CuO_4 appears either by the partial substitution of La with Sr, Ba, Ca [16, 17], or by the introduction of interstitial oxygen defects in the La_2O_2 layer [18]. Some substitutions, especially on Cu sites, destroy the superconductivity.

For classical superconductors, J_c can be drastically increased by introducing defects to pin magnetic flux vortices. The layered structure of high-T_c cuprates causes the vortices to be pinned in the form of pancakes, rather than long cylinders [19]. Because of relatively small coherence length of vortices, pinning can not be increased in the classical way by introducing second-phase precipitates. Instead, submicroscopic lattice defects caused by local stoichiometry fluctuations, vacancies, substitutions, Guinier-Preston zones, and the strain field of small coherent precipitates are much more effective. Especially in highly anisotropic Tl-based and Bi-based cuprates, substitutions are very successful. Even a 5% Mg for Ba substitution in $Tl_2Ba_2CaCu_2O_8$ increases J_c by 25% [20].

1.4 Purpose of the Study

We know that defects have a very important role in novel high-T_c superconductivity. Defects can be characterized and quantified by analyzing the x-ray diffraction broadening. Basically, there are two approaches:

(i) The Stokes deconvolution method [21] combined with the Warren and Averbach analysis [22] give the most rigorous and unbiased approach because no assumption about the analytical form of diffraction-peak shape is required. However, when peaks overlap and specimen broadening is comparable with the instrumental broadening, the Stokes method gives unstable solutions and large errors or can not be performed at all. To obtain reliable results, proper corrections have to account for truncation, background, sampling, and the standard's errors [23].

(ii) The simplified integral-breadth methods (summarized by Klug and Alexander [24]) are more convenient and easier to use, but they require that size and strain broadening are modeled by either Cauchy or Gauss functions. Experience has shown, however, that in most cases both size and strain profiles can not be satisfactorily represented with either function. However, there is some theoretical and experimental evidence that the effect of small-domain-size broadening produces long profile tails of the Cauchy function, and that the lattice-strain distribution is more Gauss-like. Langford [25, 26] used the convolution of Cauchy and Gauss functions (Voigt function) to model specimen broadening. However, the results obtained by the integral-breadth and Warren-Averbach analyses are usually not comparable; the first methods give volume-weighted domain sizes and upper limit of strain; the second gives surface-weighted domain sizes and mean-square strain averaged over some distance perpendicular to diffracting planes.

Unfortunately, most high-T_c superconductors show weak peak broadening (because of high annealing temperatures) and strong peak overlapping (because of relatively complicated crystal structures), which makes it very difficult to apply the Stokes deconvolution method to extract pure specimen broadening. The aim in this study is twofold:

(i) To develop a reliable method for analysis of a pattern with highly overlapping reflections and weak structural broadening, and to compare it with the previously described approaches. It will be shown that the Voigt-function modeling of the specimen broadening concurs with the Warren-Averbach approach.

(ii) To apply the method to the same high-T_c superconductors and conclude how much information about defects can be extracted from analysis of the x-ray diffraction broadening.

2. Previous Studies

2.1 Size and Strain Broadening

Some important methods to extract specimen size and strain broadening and information about domain sizes and strains will be reviewed briefly. An excellent review about Fourier methods and integral-breadth methods is given by Klug and Alexander [24]. A survey of single-line methods was authored by Delhez, de Keijser, and Mittemeijer [27]. The use of variance (reduced second moment of the line profile) in the analysis of broadening will not be treated here. Wilson described the contributions to variance by crystallite size [28] and strain [29].

2.1.1 Determination of the Pure Specimen-Broadened Profile As mentioned in Sec. 1.2, before the specimen's size and strain broadening can be obtained, the observed profile must be corrected for instrumental broadening. Most used methods are the Fourier-transform deconvolution method [30, 21] and simplified integral-breadth methods that rely on some assumed analytical forms of the peak profiles. The iterative method of successive foldings [31, 32] is not used extensively, and will not be considered here.

Deconvolution Method of Stokes From Eqs. (2) and (3), it follows that deconvolution can be performed easily in terms of Fourier transforms of respective functions:

$$F(n)=\frac{H(n)}{G(n)}. \tag{4}$$

Hence, the physically broadened profile f is retrieved from the observed profile h without any assumption on the peak-profile shape (see Fig. 1). This method is the most desirable approach because it is totally unbiased. However, because of the deconvolution process, there are many problems. Equation (4) may not give a solution if the Fourier coefficients of the f profile do not vanish before those of the g profile. Furthermore, if physical broadening is small compared with instrumental broadening, deconvolution becomes too unstable and inaccurate [33, 34]. If the h profile is 20% broader than the g profile, this gives an upper limit of about 1000 Å for the determination of effective domain size [34]. Regardless of the degree of broadening, deconvolution produces unavoidable profile-tail ripples because of truncation effects. To obtain reliable results, these errors have to be corrected, along with errors of incorrect background, sampling, and the standard specimen [23, 35, 36]. The largest problem, however, is peak overlapping. If the complete peak is not separated, the only possible solution is to try to reconstruct the missing parts. That would require some assumption on the peak-profile shape, that is introduction of bias into the method. The application of the Stokes method is therefore limited to materials having the highest crystallographic symmetry.

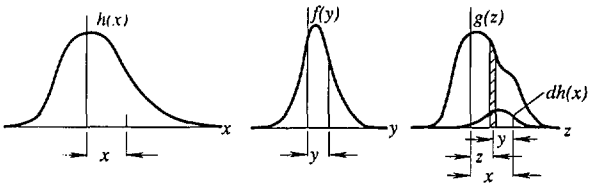

Fig. 1. Observed profile h is a convolution of the instrumental profile g with the specimen profile f. Adapted from Warren [59].

Integral-Breadth Methods The basic assumption of these methods is that diffraction profiles can be approximated with some analytical function. In the beginning, two commonly used functions were Gauss

$$I(x)=I(0)\exp\left[-\pi\frac{x^2}{\beta_G^2}\right] \tag{5}$$

and Cauchy

$$I(x)=I(0)\frac{1}{\frac{\beta_C^2}{\pi^2}+x^2}. \tag{6}$$

From the convolution integral, it follows easily that

$$\beta_{hC}=\beta_{gC}+\beta_{fC} \tag{7}$$

for Cauchy profiles, and

$$\beta_{hG}^2=\beta_{gG}^2+\beta_{fG}^2 \tag{8}$$

for Gauss profiles. However, the observed x-ray diffraction line profiles can not be well represented with a simple Cauchy or Gauss function [24, 37]. But they are almost pure Cauchy at highest angles because the dominant cause of broadening becomes the spectral distribution in radiation [24]. Different geometrical aberrations of the instrument are difficult to describe with simple analytical functions. In the case of closely Gaussian broadening of γ, following Eq. (3), the instrumental line profile can be best described by a convolution of Cauchy and Gauss functions, which is the Voigt

function. Experience shows that the Voigt function [38] (or its approximations, pseudo-Voigt [39, 40] and Pearson-VII [41, 42]) fits very well the observed peak profiles [25, 43, 37]. The Voigt function is usually represented following Langford [25]

$$I(x)=I(0)\left(\frac{\beta}{\beta_C}\right)\mathrm{Re}\left[\mathrm{erfi}\left(\frac{\pi^{1/2}x}{\beta_G}+ik\right)\right]. \quad (9)$$

Here, the complex error function is defined as

$$\mathrm{erfi}(z)=\exp(-z^2)\,[1-\mathrm{erf}(-iz)]. \quad (10)$$

Its evaluation can be accomplished using Sundius [44] or Armstrong [45] algorithms with eight-digit accuracy. Useful information about the Voigt function can be found in papers of Kielkopf [46], Asthana and Kiefer [47], and de Vreede et al. [48]. Figure 2 presents a Voigt function for different values of Cauchy and Gauss integral breadths.

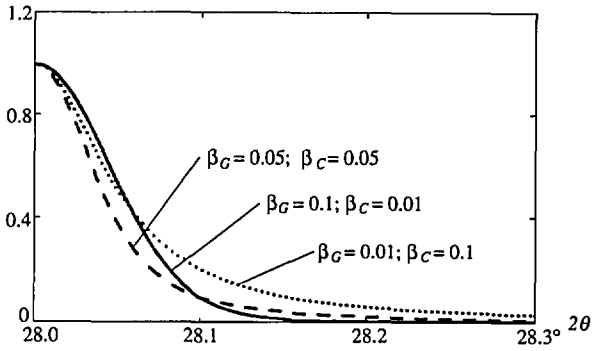

Fig. 2. Voigt functions for different values of Cauchy and Gauss integral breadths. Adapted from Howard and Preston [4].

Integral breadth of the Voigt function is expressed through its constituent integral breadths [49]

$$\beta=\beta_G\frac{\exp(-k^2)}{\mathrm{erfc}(k)}. \quad (11)$$

Here, erfc denotes the complementary error function.

Because convolution of two Voigt functions is also a Voigt function, integral breadths are easily separable conforming to Eqs. (7) and (8).

2.1.2 Separation of Size and Strain Broadening After removing the instrumental broadening from the observed line profile, it is possible to analyze the pure-specimen (physically) broadened line profile, to consider the origins and amount of broadening.

In 1918 Scherrer [50] recognized that breaking the crystal into domains smaller than ~1000 Å causes diffraction-line broadening

$$\langle D\rangle_v=\frac{K\lambda}{\beta(2\theta)\cos\theta}. \quad (12)$$

The constant K depends on the crystallite shape [51,52,53,54,55,56], but generally is close to unity. The main characteristic of size broadening is that it is independent of the reflection order, that is, independent of diffraction angle.

Most of the work on x-ray diffraction line broadening was done on metals and alloys. It is widely accepted that plastic deformation in metals produces dislocation arrays, which divide crystallites into much smaller incoherently scattering domains. These dislocations produce strains within the domains, causing strain broadening. It was elaborated in Sec. 1.2 that any lattice imperfection (vacancies, interstitials, and substitutions) would broaden the diffraction peaks. These effects would be interpreted in the frame of this theory as a strain broadening, too. Stokes and Wilson [57] defined "apparent strain" as

$$\eta=\beta(2\theta)\cot\theta. \quad (13)$$

Strain broadening is angle dependent. Therefore, the angle dependence of the line broadening gives a possibility to distinguish between contributions of size and strain. However, when we speak of size and strain broadening, they may include other contributions. For instance, stacking faults and twins will contribute to broadening similar to size effects.

Warren-Averbach Method This method was developed originally for plastically deformed metals, but since its introduction [58, 22] it found successful application to many other materials. The method is extensively described in Warren's publications [59, 60]. Each domain is represented by columns of cells along the a_3 direction [61] (see Fig. 3). The crystal has orthorhombic axes with the direction a_3 normal to the diffracting planes ($00l$). The experimentally observable diffraction power may be expressed as a Fourier series

$$I(2\theta)=\frac{c}{\sin^2\theta}\sum_{n=-\infty}^{\infty}A_n\exp(2\pi i n a_3 s). \quad (14)$$

Here, experimentally measurable coefficients A_n are

$$A_n=\frac{N_n}{\langle D\rangle_s}\langle\exp(2\pi i l Z_n)\rangle. \quad (15)$$

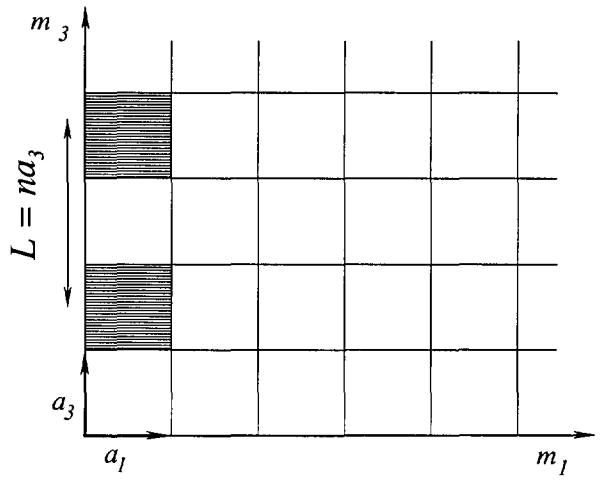

Fig. 3. Representation of the crystal in terms of columns of cells along the a_3 direction [59].

The A_n coefficients are the product of two terms. The first term depends only on the column length (size coefficient); the second depends only on distortion in domains (distortion coefficient):

$$A_n = A_n^S A_n^D . \tag{16}$$

$$A_n^S = \frac{N_n}{\langle D \rangle_s}; A_n^D = \langle \exp(2\pi i l Z_n) \rangle. \tag{17}$$

It is more convenient to express the distortion coefficient in terms of the strain component. If $L = na_3$ is the undistorted distance between a pair of cells along direction a_3, and distortion changes distance by $\Delta L = a_3 Z_n$, the component of strain in the a_3 direction (orthogonal to reflecting planes) averaged over distance L can be defined as $\epsilon(L) = \Delta(L)/L$. Because $a_3/l = d$, interplanar spacing, the distortion coefficient can be rewritten

$$A^D(L) = \langle \exp(2\pi i L \epsilon(L)/d) \rangle . \tag{18}$$

To obtain the strain component, it is necessary to approximate the exponential term. For not too large L

$$\langle \exp(2\pi i L \epsilon(L)/d \rangle$$

$$\approx \exp(-2\pi^2 L^2 \langle \epsilon^2(L) \rangle / d^2). \tag{19}$$

This relationship is exact if the distributions of $\epsilon(L)$ for all L values follow the Gauss function and is generally true as far as terms in $\epsilon^3(L)$ because these distributions are usually sufficiently symmetrical [57]. Now, Eq. (16) can be approximated as

$$\ln A(L) = \ln A^S(L) - (2\pi^2 \langle \epsilon^2(L) \rangle L^2/d^2). \tag{20}$$

Warren and Averbach [22] derived this relationship in a similar way. It separates size and strain contributions to the broadening, and allows for their simultaneous evaluation.

If the size coefficients are obtained by applications of Eq. (20), it is possible to evaluate the average surface-weighted domain size and the surface-weighted column-length distribution function [59]:

$$\left(\frac{dA^S(L)}{dL}\right)_{L \to 0} = -\frac{1}{\langle D \rangle_s} ; \tag{21}$$

$$p_s(L) \propto \frac{d^2 A^S(L)}{dL^2} . \tag{22}$$

Figure 4 shows how $\langle D \rangle_s$ can be obtained from both the size coefficients $A^S(L)$ and the column-length distribution function.

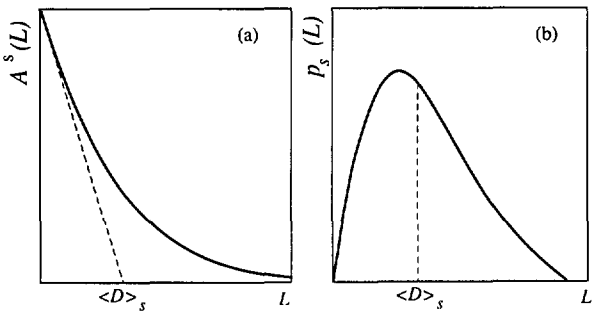

Fig. 4. Surface-weighted domain size is determined: (a) by the intercept of the initial slope on the L-axis; (b) as a mean value of the distribution function.

Multiple-Line Integral-Breadth Methods To separate size and strain broadening by using integral breadths, it is necessary to define the functional form for each effect. In the beginning, size and strain contributions were described by Cauchy or Gauss functions. Using Eqs. (12) and (13) on the s scale, and additive relations for the integral breadths following Eqs. (7) and (8)

$$\beta = \frac{1}{\langle D \rangle_v} + 2es \qquad \text{(Cauchy-Cauchy)}, \tag{23}$$

$$\beta = \frac{1}{\langle D \rangle_v} + \frac{4e^2 s^2}{\beta} \qquad \text{(Cauchy-Gauss)}, \tag{24}$$

$$\beta^2=\frac{1}{\langle D\rangle_v^2}+4e^2s^2 \qquad \text{(Gauss-Gauss)}. \qquad (25)$$

Here, $e=\eta/4\approx\Delta d/d$ is the upper limit for a strain. Equation (24) uses the Halder and Wagner [62] parabolic approximation for the integral breadth of the Voigt function expressed by Eq. (11) :

$$\frac{\beta_C}{\beta}=1-\left(\frac{\beta_G}{\beta}\right)^2. \qquad (26)$$

Experience shows, however, that neither Cauchy nor Gauss functions can model satisfactorily size or strain broadening in a general case. Langford [26] introduced the so-called multiple-line Voigt-function analysis. Both size-broadened and strain-broadened profiles are assumed to be Voigt functions. Using Eqs. (12) and (13), it follows symbolically for Cauchy and Gauss parts that

$$\beta_C=\beta_{SC}+\beta_{DC}s\ ; \qquad (27)$$

$$\beta_G^2=\beta_{SG}^2+\beta_{DG}^2s^2\,. \qquad (28)$$

This approach disagrees with the Warren-Averbach analysis, that is, the two methods give different results (see Sec. 4.4) [63, 64].

Single-Line Methods There are cases where only the first order of reflection is available or higher-order reflections are severely suppressed (extremely deformed materials, multiphase composites, catalysts, and oriented thin films). Many methods exist to separate size and strain broadening from only one diffraction peak. However, it was stated in Sec. 2.1.2 that the different size and strain broadening angle dependence is a basis for their separation; hence, using only one diffraction line introduces a contradiction. Consequently, single-line methods should be used only when no other option exists. The single-line methods can be divided in two main parts: Fourier-space and real-space methods. Fourier-space methods are based on the Warren-Averbach separation of size and strain broadening following Eq. (20). The functional form of $\langle E^2(L)\rangle$ is assumed either to be constant [65,66,67,68], or assumed to depend on L as $\langle\epsilon^2(L)\rangle=c/L$ [69,70,71,72]. Then, Eq. (20) can be fitted to few points of $A(L)$ for the small averaging distance L, to obtain size and strain parameters. All Fourier-space methods have the serious problem that the Fourier coefficients $A(L)$ are usually uncertain for small L, because of the so-called "hook" effect [60] (see Sec. 4.2). Zocchi [73] suggested that fitting the straight line through the first derivatives of the Fourier coefficients, instead of through the coefficients themselves, would solve the "hook"-effect problem.

All real-space methods [74,75,76] are based on the assumption that the Cauchy function determines size and that the Gauss function gives strain. The most widely used method of de Keijser et al. [76] gives size and strain parameters from Cauchy and Gauss parts of the Voigt function, respectively:

$$\langle D\rangle_v=\frac{1}{\beta_C}; \qquad (29)$$

$$e=\frac{\beta_G}{2s}\,. \qquad (30)$$

2.2 Diffraction-Line-Broadening Analysis of Superconductors

In this field, very few studies exist. Williams et al. [77] reported isotropic strains in $YBa_2Cu_3O_{7-\delta}$ powder by the simultaneous Rietveld refinement of pulsed-neutron and x-ray diffraction data. Using a GSAS Rietveld refinement program [78], both size and strain broadening were modeled with the Gauss functions for the neutron-diffraction data [79, 80], and with the Cauchy functions for the x-ray diffraction data (modified method of Thompson, Cox, and Hastings [81]). Interestingly, both the neutron and x-ray data gave identical values for the isotropic strain (0.23%) and no size broadening. Singh et al. [82] studied internal strains in $YBa_2Cu_3O_{7-\delta}$ extruded wires by pulsed-neutron diffraction. They separated size and strain parameters by means of Eq. (25) (Gauss-Gauss approximation). Size broadening was found to be negligible, but (isotropic) microstrains range from 0.05% for the coarse-grained material to 0.3% for the fine-grained samples. Eatough, Ginley, and Morosin [83] studied $Tl_2Ba_2Ca_2Cu_3O_{10}$ (Tl-2223) and $Tl_2Ba_2CaCu_2O_8$ (Tl-2212) superconducting thin films by x-ray diffraction. Using the Gauss-Gauss approximation, they found strains of 0.14–0.18% in both phases, and domain sizes of 1200–1400 Å for Tl-2212, but 500 Å for Tl-2223.

We are aware of only two more unpublished studies [84, 85] involving size-strain analysis in high-T_c superconductors. The probable reason is that any analysis is very difficult because of weak line broadening and overlapping reflections. This

precludes application of reliable analysis, such as the Stokes deconvolution method with the Warren-Averbach analysis of the broadening. Instead, simple integral-breadth methods are used, which gives generally different results for each approach. Moreover, for x-ray diffraction broadening, application of the Gauss-Gauss approximation does not have any theoretical merit, although reasonable values, especially of domain sizes, may be obtained [86]. We showed [87,88,89] that reliable diffraction-line-broadening analysis of superconductors can be accomplished and valuable information about anisotropic strains and incoherently diffracting domain sizes obtained.

3. Experiment

3.1 Materials

The materials used for this study were tungsten and silver commercially available powders with nominal grain sizes 4–12 μm, $La_{2-x}Sr_xCuO_4$($x=0$, 0.06, 0.15, 0.24) powders, $La_{1.85}M_{0.15}CuO_4$(M = Ca, Ba) powders, $Bi_2Sr_2CaCu_2O_8$ (Bi-2212) sinter, $(BiPb)_2Sr_2Ca_2Cu_3O_{10}$(Bi,Pb-2223) sinter, and $(BiPb)_2(SrMg)_2(BaCa)_2Cu_3O_{10}$ (Bi,Pb,Mg,Ba-2223) sinter.

Powders with nominal compositions $La_{2-x}Sr_xCuO_4$($x=0$, 0.06, 0.15, 0.24) and $La_{1.85}M_{0.15}CuO_4$(M = Ca, Ba) were prepared at the National Institute of Standards and Technology, Boulder, Colorado, by A. Roshko, using a freeze-drying acetate process [90]. Acetates of the various cations were assayed by mass by calcining to the corresponding oxide or carbonate. The appropriate masses of the acetates for the desired compositions were dissolved in deionized water. The acetate solutions were then sprayed through a fine nozzle into liquid nitrogen to preserve the homogeneous cation distributions. Frozen particles were transferred to crystallization dishes and dried in a commercial freeze dryer, to a final temperature of 100 °C. After drying, the powders, except the $La_{1.85}Ba_{0.15}CuO_4$, were calcined in alumina (99.8%) crucibles at 675 °C for 1 h in a box furnace with the door slightly open to increase ventilation. Because $BaCO_3$ is difficult to decompose, the $La_{1.85}Ba_{0.15}CuO_4$ was calcined under a vacuum of 2 Pa at 800 °C for 4 h, then cooled slowly in flowing oxygen (2 °C/min). The calcined powders were oxidized in platinum-lined alumina boats in a tube furnace with flowing oxygen at 700 °C. After 3 h at 700 °C the powders were pushed to a cold end of the furnace tube where they cooled quickly (20 °C/s) while still in flowing oxygen.

The cylindrical specimens (23 mm in diameter and 9 mm thick) of Bi-2212, Bi,Pb-2223, and Bi,Pb,Mg,Ba-2223 were prepared at the National Research Institute for Metals, Tsukuba, Japan, by K. Togano [91]. Starting oxides and carbonates were: Pb_3O_4, Bi_2O_3, CuO, $SrCO_3$, $MgCO_3$, and $BaCO_3$. They were calcinated in air at 800 °C for 12 h. Powders were then pressed and sintered in 8% oxygen-92% argon mixture at 835 °C for 83 h. Specimens were furnace cooled to 750 °C, held for 3 h in flowing oxygen, and then furnace cooled in oxygen to room temperature.

3.1.1 Preparation of Specimens for X-ray Diffraction The bulk specimens were surface polished, if necessary, and mounted in specimen holders. Coarse-grained powders of $La_{2-x}Sr_xCuO_4$ ($x=0$, 0.06, 0.15, 0.24) and $La_{1.85}M_{0.15}CuO_4$ (M = Ca, Ba) were ground with a mortar and pestle in toluene and passed through a 635-mesh sieve (20-μm nominal opening size). Silver and tungsten powders were dry ground with a mortar and pestle. All powders were mixed with about 30% silicone grease and loaded into rectangular cavities or slurried with amyl acetate on a zero-background quartz substrate.

3.2 Measurements

X-ray-diffraction data were collected using a standard two-circle powder goniometer in Bragg-Brentano parafocusing geometry [92, 93] (see Fig. 5). A flat sample is irradiated at some angle incident to its surface, and diffraction occurs only from crystallographic planes parallel to the specimen surface. The goniometer had a vertical θ–2θ axis and 22 cm radius. Cu$K\alpha$ radiation, excited at 45 kV and 40 mA, was collimated with Soller slits [94] and a 2 mm divergence slit. Soller slits in the diffracted beam, 0.2 mm receiving slit and Ge solid-state detector were used in a step-scanning mode (0.01°/10 s for a standard specimen, 0.02°–0.05°/30–80 s for other specimens, depending on the amount of broadening).

3.3 Data Analysis

The diffractometer was controlled by a computer, and all measurements were stored on hard disc. Data were transferred to a personal computer for processing.

We used computer programs for most calculations. X-ray diffraction patterns were fitted with the program SHADOW [95]. This program allows a choice of the fitting function and gives refined positions of the peak maximums, intensities, and function-dependent parameters. It also has the

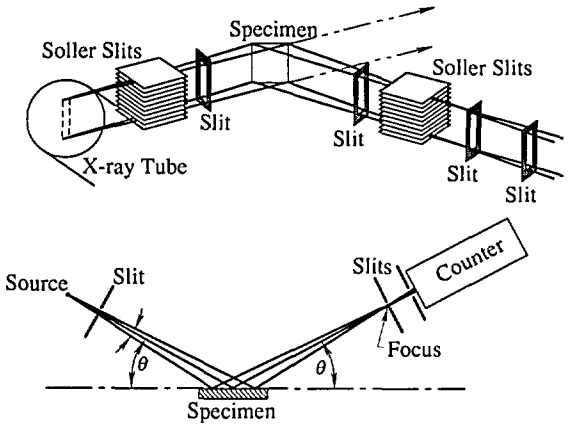

Fig. 5. Optical arrangement of an x-ray diffractometer. *Adapted from Klug and Alexander [24].*

ability to convolute the predefined instrumental profile with the specimen function to match the observed pattern. Choice of the specimen function includes Gauss and Cauchy functions. We added the ability to model the specimen broadening with an exact Voigt function and implemented SHADOW on a personal computer. In the fitting procedure, for every peak in the pattern, the program first generates the instrumental profile at the required diffraction angle. The instrumental profile is determined from prior measurements on a well-annealed standard specimen (see Sec. 5.1). Then it assumes parameters of the specimen profile. For an exact Voigt function, parameters are peak position, peak intensity, and Cauchy and Gauss integral breadths of the Voigt function. By convoluting the instrumental profile with the specimen profile, and adding a background, the calculated pattern is obtained [Eq. (2)]. Parameters of the specimen profile are varied until the weighted least-squares error of calculated and observed patterns Eq. (59), reaches a minimum. This process avoids the unstable Stokes deconvolution method. It is possible that the refinement algorithm is being trapped in a false minimum [96], but it can be corrected by constraining some parameters. Refined parameters of the pure-specimen profile are input for the size-strain analysis of the broadening. A program for this analysis was written in Fortran.

Lattice parameters of powder specimens were calculated by the program NBS*LSQ85, based on the method of Appleman and Evans [97]. A program in Fortran was written to apply corrections to observed peak maximums by using NIST standard reference material 660 LaB_6 as an external standard. Lattice parameters of bulk specimens were determined by the Fortran program, which uses a modified Cohen's method [98,99,100] to correct for systematic diffractometer errors. Lattice parameters were also calculated by the Rietveld refinement programs GSAS [78] and DBW3.2S [101, 102].

4. Methodology

When instrumental and specimen contributions to the observed line profile must be modeled separately, adopting a specimen function is a critical step. Yau and Howard [103, 104] used Cauchy, and Enzo et al. [105] pseudo-Voigt functions. Benedetti, Fagherazzi, Enzo, and Battagliarin [106] showed that modeling the specimen function with the pseudo-Voigt function gives results comparable to those of the Stokes deconvolution method when combined with the Warren-Averbach analysis of Fourier coefficients. De Keijser, Mittemeijer, and Rozendaal [107] analytically derived domain sizes and root-mean-square strains for small averaging distance L in the case of the Voigt and related functions.

The aim here is to study more thoroughly the consequences of assumed Voigt specimen function on the size-strain analysis of the Fourier coefficients of the broadened peaks. It is shown that some experimentally observed interrelations between derived parameters (particularly volume-weighted and surface-weighted domain sizes) and their behavior (the "hook" effect and dependence of mean-square strains on the averaging distance) can be explained by this simple assumption. Moreover, the discrepancy between the integral-breadth methods and Warren-Averbach analysis results from different approximations for the strain broadening and the background experimental errors.

4.1 Separation of Size and Strain Broadenings

The normalized Fourier transform of a Voigt function is easily computable [46]:

$$A_n = \exp\left[-2n\frac{\beta_C(2\theta)}{\sigma(2\theta)} - \pi n^2 \frac{\beta_B^2(2\theta)}{\sigma^2(2\theta)}\right]. \quad (31)$$

It is convenient to express Fourier coefficients in terms of distance L, by immediately making the approximation $\Delta(2\theta) = \lambda \Delta s/\cos\theta_0$:

$$A(L) = \exp[-2L\beta_C - \pi L^2 \beta_G^2]. \quad (32)$$

Equation (32) is a good approximation even for large specimen broadening. Even for a profile span of $\Delta(2\theta) = 80°$, the error made by replacing this interval by an adequate $\Delta(\sin\theta)$ range is 2%. However, strictly speaking, the profile will be asymmetrical in reciprocal space, and Fourier-interval limits will not correspond to the $2\theta_1$ and $2\theta_2$ peak-cutoff values in real space. It is important to keep Fourier interval limits identical for all multiple-order reflections; otherwise serious errors in the subsequent analysis will occur [108]. If higher accuracy for a considerable broadening is desired, profile fitting can be accomplished in terms of the reciprocal-space variable s, instead of in a real 2θ space.

Assuming that only the Cauchy function determines domain size $[A^S(L) = \exp(-L/\langle D\rangle_s)]$ and only the Gauss function gives root-mean-square strain (RMSS) $[A^D(L) = \exp(-2\pi^2 L^2\langle\epsilon^2\rangle/d^2)]$, Eq. (32) leads to the Warren-Averbach [Eq. (20)] for the separation of size and strain contribution [62]. Experience shows that Cauchy and Gauss functions can not satisfactory model specimen broadening. Balzar and Ledbetter [64] postulate that the specimen function includes contributions of size and strain effects, both approximated with the Voigt functions. Because the convolution of two Voigt functions is also a Voigt function, Cauchy and Gauss integral breadths of the specimen profile are easily separable:

$$\beta_C = \beta_{SC} + \beta_{DC}; \tag{33}$$

$$\beta_G^2 = \beta_{SG}^2 + \beta_{DG}^2 . \tag{34}$$

Langford [26] separated the contributions from size and strain broadening in a similar way. (See Eqs. (27) and (28).) Note, however, that Eqs. (33) and (34) do not define size and strain angular order-dependence.

Because Fourier coefficients are a product of a size and a distortion coefficient, from Eqs. (32), (33), and (34), we can obtain the separation of size and strain contributions to the pure specimen broadening:

$$A^S(L) = \exp(-2L\beta_{SC} - \pi L^2\beta_{SG}^2); \tag{35}$$

$$A^D(L) = \exp(-2L\beta_{DC} - \pi L^2\beta_{DG}^2) . \tag{36}$$

Wang, Lee, and Lee [109] modeled the distortion coefficient, and Selivanov and Smislov [110] modeled the size coefficient in the same way.

To obtain size and distortion coefficients, at least two reflections from the same crystallographic-plane family must be available.

4.2 Size Coefficient

Surface-weighted domain size is calculated from the size coefficients following Eq. (21). From Eq. (35) we obtain

$$\langle D\rangle_s = \frac{1}{2\beta_{SC}} . \tag{37}$$

Therefore, surface-weighted domain size depends only on the Cauchy part of the size-integral breadth.

The second derivative of the size coefficients is proportional to the surface-weighted column-length distribution function, Eq. (22). The volume-weighted column-length distribution function follows similarly [111]:

$$p_v(L) \propto L\frac{d^2A^A(L)}{dL^2} . \tag{38}$$

By differentiating Eq. (35) twice, we obtain

$$\frac{d^2A^S(L)}{dL^2} = [(2\pi L\beta_{SG}^2 + 2\beta_{SC})^2 - 2\pi\beta_{SG}^2 A^S(L) . \tag{39}$$

Because the column-length distribution function should always be positive [59], the Cauchy part must dominate. Inspection of Eq. (39) shows that for small L we must require

$$\beta_{SC} \geq \sqrt{\frac{\pi}{2}}\beta_{SG} . \tag{40}$$

Otherwise, the "hook" effect will occur in the plot of size coefficients $A^S(L)$ versus L, that is, the plot will be concave downward for small L (Fig. 6). The "hook" effect is usually attributed to experimental errors connected with the truncation of the line profiles, and consequently overestimation of background [59]. This is a widely encountered problem in the Fourier analysis of line broadening. It results in overestimation of effective domain sizes and underestimation of the RMSS [36]. Some authors [106] claim that the preset specimen-broadening function eliminates the "hook" effect. However, Eq. (39) shows that, effectively, too high

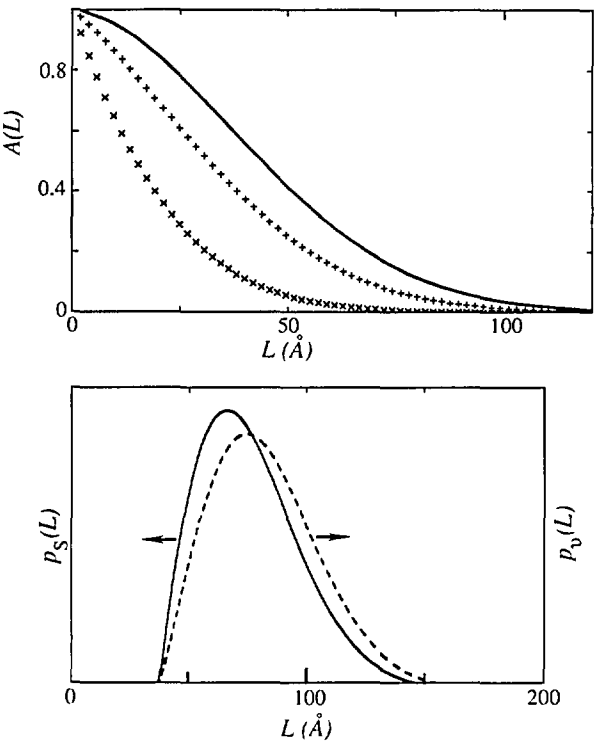

Fig. 6. (upper) The "hook" effect of the size coefficients A^S (full line) at small L; (lower) it causes negative values (set to zero) of the column-length distribution functions.

background causes underestimation of the Cauchy content of the Voigt function, because the long tails are truncated prematurely. It has to be mentioned that Wilkens [112] proposed tilted small-angle boundaries to be the source of the "hook" effect. Liu and Wang [113] defined a minimum particle size present in a specimen, depending on the size of the "hook" effect. Figure 6 shows that negative values of the column-length distribution functions (set to zero), do not affect the shape, but shift the entire distribution toward larger L values.

Note also that the surface-weighted column-length distribution function $p_s(L)$ will usually have a maximum at $L=0$; but for the particular ratio of integral breadths, determined by Eq. (40), it can be zero. The volume-weighted column-length distribution function $p_v(L)$ will always have a maximum for $L \neq 0$.

If the column-length distribution functions are known, it is possible to evaluate mean values of respective distributions:

$$\langle D\rangle_{s,v} = \frac{\int_0^\infty L p_{s,v}(L)\,dL}{\int_0^\infty p_{s,v}(L)\,dL}. \qquad (41)$$

Integrals of this type can be evaluated analytically [114]:

$$\int_0^\infty x^m \exp(-bx^2-cx)\,dx = \frac{(-1)^m}{2}\sqrt{\frac{\pi}{b}}\,\frac{\partial^m}{\partial c^m}\left[\exp\left(\frac{c^2}{4b}\right) erfc\left(\frac{c}{2\sqrt{b}}\right)\right]. \qquad (42)$$

Surface-weighted domain size $\langle D\rangle_s$ must be equal to the value obtained from Eq. (37). The volume-weighted domain size follows:

$$\langle D\rangle_v = \frac{\exp(k)^2}{\beta_{SG}}\,\mathrm{erfc}(k) = \frac{1}{\beta^S}. \qquad (43)$$

Using Eqs. (37) and (43), we can evaluate the ratio of domain sizes:

$$\frac{\langle D\rangle_v}{\langle D\rangle_s} = 2\sqrt{\pi}k\exp(k^2)\mathrm{erfc}(k). \qquad (44)$$

Theoretically, k can change from zero to infinity. However, the minimum value of k is determined by Eq. (40):

$$1/\sqrt{2} \le k < \infty. \qquad (45)$$

Hence, the ratio of domain sizes can change in a limited range (see also Fig. 7):

$$1.31 \approx \sqrt{2\pi e}\,\mathrm{erfc}\left(\frac{1}{\sqrt{2}}\right) \le \frac{\langle D\rangle_v}{\langle D\rangle_s} < 2. \qquad (46)$$

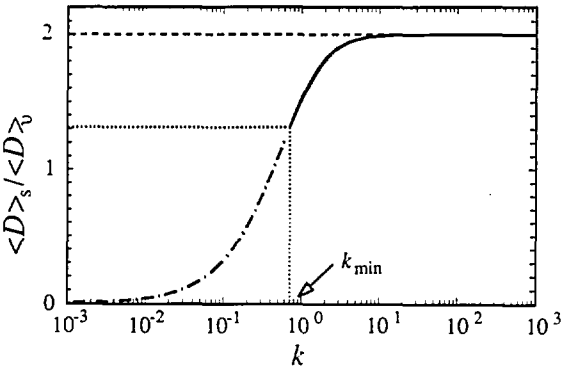

Fig. 7. The ratio of volume-weighted and surface-weighted domain sizes as a function of the characteristic ratio of Cauchy and Gauss integral breadths k.

It may be noted that most experiments give the ratio $\langle D\rangle_v/\langle D\rangle_s$ in this range (see for instance review by Klug and Alexander [24]). When k goes to infinity the size broadening is given only by the Cauchy component and $\langle D\rangle_v = 2\langle D\rangle_s$. This is a case of pure Cauchy size broadening, described by Halder and Wagner [62] and de Keijser, Mittemeijer and Rozendaal [107]. It is possible to imagine a more complicated column-length distribution function [27] than Eq. (39), which would allow even larger differences between surface-weighted and volume-weighted domain sizes. However, we are not aware of any study reporting a difference larger than 100%.

4.3 Distortion Coefficient

In Sec. 2.1.2 it was shown that the distortion coefficient can be approximated by the exponential

$$A^D(L) = \exp(-2\pi^2 s^2 L^2 \langle \epsilon^2(L)\rangle) . \quad (47)$$

Comparing with Eq. (36), we can write

$$\langle \epsilon^2(L)\rangle = \frac{1}{s^2}\left(\frac{\beta_{DG}^2}{2\pi} + \frac{\beta_{DC}}{\pi^2}\frac{1}{L}\right). \quad (48)$$

Therefore, mean-square strains (MSS) decrease linearly with averaging distance L. This behavior is usually observed in the Warren-Averbach analysis. Rothman and Cohen [115] showed that such behavior would be expected of strains around dislocations. Adler and Houska [116], Houska and Smith [117], and Rao and Houska [118] demonstrated for a number of materials that MSS can be represented by a sum of two terms, given by Cauchy and Gauss strain-broadened profiles.

However, for $\beta_{DC}=0$, the MSS are independent of L:

$$\langle \epsilon^2\rangle^{1/2} = \frac{\beta_{DG}(2\theta)}{2\sqrt{2\pi}}\cot\theta = \frac{2}{\sqrt{2\pi}}e , \quad (49)$$

where the upper limit of strain e is defined as $\eta/4$ (see Sec. 2.1.2). This is a limiting case of pure-Gauss strain broadening, described by de Keijser, Mittemeijer and Rozendaal [107].

4.4 Discussion

To calculate domain sizes and strain, it is necessary to define size and distortion integral-breadths angular order-dependence. From Eq. (43) it follows that the domain size $\langle D\rangle_v$ is always independent of the order of reflection:

$$\beta_{SC} = \text{const.}; \quad \beta_{SG} = \text{const.} \quad (50)$$

However, from Eq. (48) we find

$$\frac{\beta_{DC}}{s^2} = \text{const.}; \quad \frac{\beta_{DG}}{s} = \text{const.} \quad (51)$$

An important consequence is that "apparent strain" η will be independent of angle of reflection only in the case of pure-Gauss strain broadening because β_{DC} and β_{DG} depend differently on the diffraction angle. If we compare Eq. (51) with the multiple-line Voigt-function analysis [26], given by Eqs. (27) and (28), it is evident that they disagree. Therefore, recombination of constituent integral breadths β_{DC} and β_{DG} to Voigt strain-broadened integral breadth β^D and the subsequent application of Eq. (49) to calculate strain [26, 119] will concur with the Fourier methods if strain broadening is entirely Gaussian and for the asymptotic value of MSS ($\langle\epsilon^2(\infty)\rangle$). However, neither volume-weighted domain sizes $\langle D\rangle_v$ will agree, although they are defined identically in both approaches, because size-broadened and strain-broadened integral breadths are dependent variables.

If at least two orders of reflection (l and $l+1$) of the same plane (hkl) are available, using Eqs. (50) and (51) we can solve Eqs. (33) and (34):

$$\beta_{SC} = \frac{s^2(l+1)\beta_C(l) - s^2(l)\beta_C(l+1)}{s^2(l+1) - s^2(l)} \quad (52)$$

$$\beta_{SG}^2 = \frac{s^2(l+1)\beta_G^2(l) - s^2(l)\beta_G^2(l+1)}{s^2(l+1) - s^2(l)} \quad (53)$$

$$\beta_{DC} = \frac{s^2(l)}{s^2(l+1) - s^2(l)}\left[\beta_C(l+1) - \beta_C(l)\right] \quad (54)$$

$$\beta_{DG}^2 = \frac{s^2(l)}{s^2(l+1) - s^2(l)}\left[\beta_G^2(l+1) - \beta_G^2(l)\right]. \quad (55)$$

If we substitute these expressions into Eqs. (35) and (36), we see that this approach leads exactly to the Warren-Averbach Eq. (20) for two orders of reflections. This is expected because the distortion coefficient is approximated with the exponential (47)]. Delhez, de Keijser, and Mittemeijer [23] argued that, instead of Eq. (20), the following relation would be more accurate:

$$A(L) = A^s(L)\,(1 - 2\pi^2\langle\epsilon^2(L)\rangle L^2/d^2). \quad (56)$$

These two approximations differ with fourth-order terms in the power-series expansion. In terms of this approach, Eq. (48) has to be rewritten:

$$\langle \epsilon^2(L) \rangle = \frac{1-\exp(-2L\beta_{DC}-\pi L^2\beta_{DG}^2)}{2\pi^2 s^2 L^2}. \quad (57)$$

This means that even if the strain-broadened profile is given entirely by the Gauss function, the MSS depend on distance L (see Fig. 8). In this approximation no simple relation for the distortion integral-breadths angular order-dependence exists. For not so large L, however, Eq. (51) holds, and approximations from Eqs. (20) and (56) do not differ much (see Fig. 8).

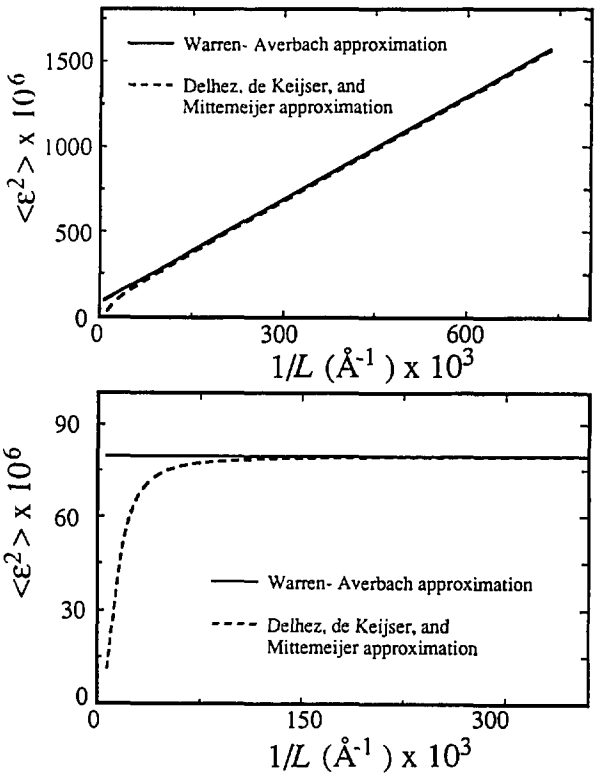

Fig. 8. Mean-square strains $\langle \epsilon^2(L) \rangle$ for two approximations of the distortion coefficient: (upper) Voigt strain broadening; (lower) pure-Gauss strain broadening.

Generally, it was shown that in the size-broadened profile the Cauchy part must dominate. No similar requirement for the strain-broadened profile exists. However, experience favors the assumption that it has to be more of Gauss-type. The Warren-Averbach approach is exact if strain broadening is purely Gaussian, so Eqs. (20) and (48) are better approximations as strain profile is closer to the Gauss function. In any case, both approaches, given by Eqs. (20) and (56), are good up to the third power in strain, and the Warren-Averbach relation [Eq. (20)] does not assume that MSS are independent of distance L [27]; it also represents a harmonic approximation.

If at least two orders of reflection from the same plane (*hkl*) are available, we can use Eqs. (52), (53), (54), and (55) to calculate size-related and strain-related integral breadths. Subsequent application of Eqs. (37), (43), and (48) gives directly domain sizes $\langle D \rangle_s$ and $\langle D \rangle_v$, and mean-square strains $\langle \epsilon^2(L) \rangle$. This approach is more straightforward and much simpler than the original Warren-Averbach analysis. Great care should be given to the possible systematic errors. The easiest way to observe the "hook" effect is to plot column-length distribution functions as a function of averaging distance L. If they show negative values for small L (see Fig. 6), all derived parameters will be in error. This is because (i) only the positive values of the column-length distribution functions are numerically integrated or (ii) the intercept on the L-axis of the linear portion of the A^S vs L curve is taken (see Fig. 4), always larger values of domain sizes will be obtained than by the application of Eqs. (37) and (43). Therefore, we conclude that the discrepancy between integral-breadth and Fourier methods is always present by the appearance of the "hook" effect in the A^S vs L curve. An analogous discrepancy exists between integral-breadth and variance methods [119]. In such cases, correction methods for truncation can be applied [35, 119, 120], but the best procedure is to repeat the pattern fitting with the correct background.

In the Fourier analysis it is usually observed that the mean-square strains diverge as the averaging distance L approaches zero. This also follows from Eqs. (48) and (57). However, because the MSS dependence on distance L is not defined in Warren-Averbach analysis, it was suggested [27, 107, 121] that local strain can be obtained by taking the second derivative of the distortion coefficient, or by a Taylor-series expansion of local strain. Therefore, we obtain from Eq. (36):

$$\langle \epsilon^2(0) \rangle = \frac{1}{s^2}\left(\frac{\beta_{DG}^2}{2\pi} - \frac{\beta_{DC}^2}{\pi^2}\right). \quad (58)$$

It is evident that this relation is wrong. It holds only for a special case of pure-Gauss strain-broadened profile, when the MSS are equal for any L. Otherwise, if the Cauchy function contributes to

strain broadening, all derivatives of strain in $L=0$ are infinite, and local strain can not be defined. If the main origin of strains is dislocations [115], strains are defined after some distance from the dislocation (cutoff radius) to be finite. Averaging strains over a region smaller than the Burgers vector is probably not justified. For instance, Eq. (48) gives, even for a small averaging distance, $L=1$ Å, and considerable strain broadening ($\beta_{DG}(2\theta)=\beta_{DC}(2\theta)=10°$), root-mean-square strain $\langle\epsilon^2(L=1\text{ Å})\rangle^{1/2}\approx 0.2$, that is, about the elastic limit.

4.5 Random Errors of Derived Parameters

Errors in size and strain analysis of broadened peaks are relatively difficult to evaluate. Following Langford [26], sources of the systematic errors include choice of standard specimen, background, and type of analytical function used to describe the line profiles. The first two errors should be minimized in the experimental procedure. Errors caused by inadequate choice of specimen function would systematically affect all derived results, but they can not be evaluated. Random errors caused by counting statistics have been computed by Wilson [122, 123, 124] and applied to the Stokes deconvolution method by Delhez, de Keijser, and Mittemeijer [23], as well as by Langford [26] and de Keijser et al. [76] using single-line Voigt-function analysis. Nevertheless, the approximate error magnitude can be calculated from estimated standard deviations (e.s.d.) of the parameters refined in the fitting procedure. In the program SHADOW, the weighted least-squares error is minimized:

$$R_{wp}=\frac{RES}{\sum_{i=1}^{m} w_i I_i^2(\text{obs})}\,. \tag{59}$$

Here

$$RES=\sum_{i=1}^{m} w_i[I_i(\text{obs})-I_i(\text{cal})]^2 \tag{60}$$

and weights are the reciprocal variances of the observations:

$$w_i=1/I_i(\text{obs})\,. \tag{61}$$

Each line profile has four parameters varied independently: position, intensity, and Cauchy and Gauss integral breadths of the Voigt profile. In least-squares refinement, e.s.d.'s are computed as

$$\sqrt{b_{ii}\frac{RES}{m-m'}}\,. \tag{62}$$

Here b_{ii} are diagonal elements of the inverse matrix of the equation coefficients, m is the number of observations, and m' is the number of refined parameters. The main source of errors is integral breadths. Errors in peak position, peak intensity, and background are much smaller and can be neglected in this simple approach. For two independent variables, β_G and β_C, covariance vanishes, and from Eqs. (37) and (38), for the two orders of reflection, l and $l+1$, it follows that

$$R^2(\langle D\rangle_s)=$$

$$\frac{s^4(l+1)\beta_C^2(l)R^2(\beta_C(l))+s^4(l)\beta_C^2(l+1)R^2(\beta_C(l+1))}{[s^2(l+1)\beta_C(l)-s^2(1)\beta_C(l+1)]^2}\,; \tag{63}$$

$$R^2(\langle\epsilon^2(L)\rangle^{1/2})=$$

$$\frac{\beta_C^2(l)R^2(\beta_C(l))+\beta_C^2(l+1)R^2(\beta_C(l+1))}{\{2[\beta_C(l+1)-\beta_C(l)]+\pi L[\beta_G^2(l+1)-\beta_G^2(l)]\}^2}$$

$$+\frac{\pi^2L^2[\beta_G^4(l)R^2(\beta_G(l))+\beta_G^4(l+1)R^2(\beta_G(l+1))]}{\{2[\beta_C(l+1)-\beta_C(l)+\pi L[\beta_G^2(l+1)-\beta_G^2(l)]\}^2}\,. \tag{65}$$

Here $R(x)$ are "relative standard deviations." The error in $\langle D\rangle_v$ would be complicated to evaluate, but because $1.31\langle D\rangle_s\le\langle D\rangle_v<2\langle D\rangle_s$, Eq. (63) gives a good estimation for the error in $\langle D\rangle_v$ as well. Alternatively, to see how errors depend on the Fourier coefficients, errors can be estimated from the Warren-Averbach relationship [Eq. (20)] (86). From Eq. (32) it follows that

$$R^2(A(L))=4\pi^2L^4\beta_G^4(s)R^2(\beta_G(2\theta))+$$

$$4L^2\beta_C^2(s)R^2(\beta_C(2\theta))\,. \tag{66}$$

Errors in root-mean-square strains and domain sizes are

$$R^2(\langle\epsilon^2(L)\rangle^{1/2})=$$

$$\frac{R^2(A(L,l))+R^2(A(L,l+1))}{4\ln^2\frac{A(L,l)}{A(L,l+1)}}\,; \tag{67}$$

$$R^2(\langle D\rangle_s)=\left(\frac{A^S(L)}{1-A^S(L)}\right)^2$$

$$\frac{s^4(l+1)R^2(A(L,l))+s^4(l)R^2(A(L,l+1))}{[s^2(l+1)-s^2(l)]^2}\ . \quad (68)$$

Here, $\langle D\rangle_s$ is approximately defined with $A^S(L)=1-L/\langle D\rangle_s$. Errors in Fourier coefficients increase with L, while factors in Eqs. (67) and (68) lower the errors for large L. In general, errors of domain sizes and strains are of the same order of magnitude as errors of integral breadths [86].

5. Application

5.1 Correction for Instrumental Broadening

Before specimen broadening is analyzed, instrumental broadening must be determined. This is accomplished by carefully measuring diffraction peaks of some well-annealed "defect-free" specimen. It is then assumed that its broadening may be attributed only to the instrument. The usual procedure is to anneal the specimen. However, in some instances that is not possible, because either the material undergoes an irreversible phase transition on annealing, or the number of defects can not be successfully decreased by annealing. Another possibility is to measure the whole diffraction pattern of the material showing the minimal line broadening, and then to synthesize the instrumental profile at the needed diffraction angle. This approach requires the modeling of the angle dependence of the instrumental (standard) parameters. Cagliotti, Paoletti, and Ricci [125] proposed the following function to describe the variation of the full width at the half maximum of profile with the diffraction angle:

$$\mathrm{FWHM}^2(2\theta)=U\tan^2\theta+V\tan\theta+W. \quad (69)$$

Although this function was derived for neutron diffraction, it was confirmed to work well also in x-ray diffraction case [126, 127]. A more appropriate function for the x-ray angle-dispersive powder diffractometer, based on theoretically predicted errors of some instrumental parameters [128] may be the following [129]:

$$\mathrm{FWHM}^2(2\theta)=W+V\sin^2 2\theta+$$

$$U\tan^2\theta+U'\cot^2\theta. \quad (70)$$

This function may better model the increased axial divergency at low angles and correct for the specimen transparency [129]. However, contrary to the requirement on the specimen function, most important for the instrumental function is to correctly describe the angular variation of parameters, regardless of its theoretical foundation.

When specimen broadening is modeled with a Voigt function, the simplest way to correct for the instrumental broadening is by fitting the line profiles with the Voigt function, too. Cauchy and Gauss integral breadths of the specimen-broadened profile are then easily computable by Eqs. (7) and (8). However, because the instrumental broadening is asymmetric [24], modeling with the symmetric Voigt function can cause a fictitious error distribution, resulting in errors of strain up to 35% [76]. Another approach is to model the instrumental-broadening angle dependence by fitting the profile shapes of a standard specimen with some asymmetrical function; split-Pearson-VII [95] or pseudo-Voigt convoluted with the exponential function [105]. The instrumental function can then be synthesized at any desired angle of diffraction and convoluted with the assumed specimen function to match the observed profile by means of Eq. (2).

In the program SHADOW, instrumental parameters are determined by fitting the split-Pearson VII function (see Fig. 9) to line profiles of a standard specimen:

$$I(x)=I(0)\frac{1}{\left(1+\frac{x^2}{mc^2}\right)^m}\ , \quad (71)$$

with

$$c=\frac{\beta\Gamma(m)}{\sqrt{m\pi}\,\Gamma(m-1/2)}\ . \quad (72)$$

Here, $m=1$ or $m=\infty$ yields a Cauchy or Gauss function, respectively. Refined full widths at half maximum (FWHM) and shape factors m for both low-angle and high-angle sides of the profiles are fitted with second-order polynomials. To fit the FWHM, we used Eq. (69), and for the shape factors

$$m(2\theta)=U'(2\theta)^2+V'(2\theta)+W'. \quad (73)$$

The resulting coefficients U, V, W, U', V', and W' permit synthesis of the asymmetrical instrumental line profile at any desired angle.

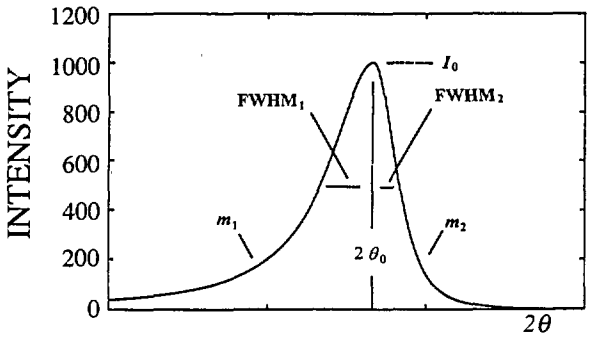

Fig. 9. A split-Pearson VII profile. The two half profiles have same peak position and intensity. Adapted from Howard and Preston [4].

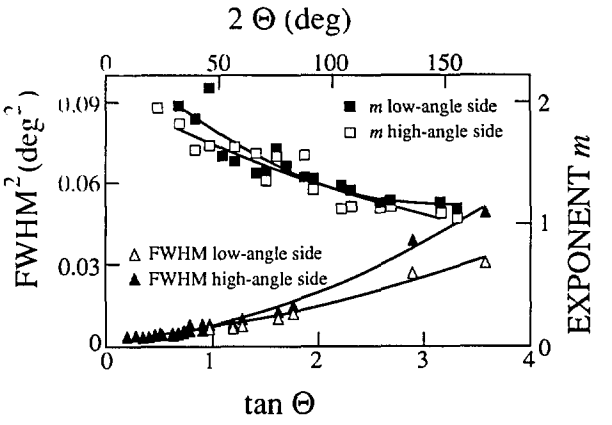

Fig. 10. Refined FWHMs and shape factors (exponents) m for low-angle and high-angle sides of LaB_6 line profiles. Second-order polynomials were fitted through points.

The basic requirement on the standard specimen is, however, to show as small a line broadening as possible. To minimize physical contributions to the line broadening of the standard specimen, a few moments were emphasized as follows. Because diffraction-line width depends strongly on degree of annealing, it is preferable to use some reference powder-diffraction standard. Furthermore, asymmetry in the peak profiles is introduced by axial divergence of the beam, flat specimen surface, and specimen transparency [24]. Choosing a standard specimen with low absorption coefficient would cause transparency effects to dominate. If the studied specimen has a large absorption coefficient (compared to the standard), this might produce a fictitious size contribution and errors in microstrains. All of the specimens studied have absorption coefficients exceeding 1000 cm^{-1}, so a NIST standard reference material 660 LaB_6 was chosen to model the instrumental broadening ($\mu = 1098$ cm^{-1}). According to Fawcett et al. [130], LaB_6 showed the narrowest lines of all studied compounds. Furthermore, LaB_6 has a primitive cubic structure (space group $Pm\bar{3}m$) resulting in relatively large number of peaks equally distributed over 2θ. This allows for better characterization and lower errors of FWHMs and shape factors of split-Pearson VII functions (Fig. 10).

5.2 Applicability of the Method

To study the applicability of method described in Sec. 4, we first studied simple cubic-structure materials such as silver and tungsten. Tungsten has very narrow line profiles, allowing us to obtain the upper limit of domain sizes that can be studied. Silver is easily deformed, which provides a possibility to apply the method to broad line profiles. To test the case of relatively complicated patterns and weak line broadening, the method was also applied to $La_{1.85}Sr_{0.15}CuO_4$ and La_2CuO_4 powders. In this section only the mechanical aspects of the line broadening are discussed. Discussion about the origins of broadening of superconductors can be found in Sec. 6.

5.2.1 Silver and Tungsten Powders Figure 11 shows observed and refined peaks of tungsten untreated and silver ground powders. In Table 2 are listed results of fitted pure-specimen Voigt profiles for silver and tungsten specimens; Table 3 and Fig. 12 give results of the line-broadening analysis. Untreated tungsten powder shows relatively weak broadening. Instrumental profile FWHMs at angle positions of (110) and (220) tungsten lines are 0.059° and 0.081°, respectively, close to values measured for tungsten: 0.065° and 0.100°. Results in Table 3 reveal that small broadening is likely caused by domain sizes, because microstrains have negligible value. This pushes the limit for measurable domain sizes probably up to 4500–5000 Å. However, one must be aware that weak specimen broadening implies higher uncertainty of all derived parameters. Moreover, the choice of the instrumental standard becomes more crucial.

Both silver and tungsten line profiles become more Cauchy-like after grinding, which probably increases dislocation density in the crystallites. This is consistent with the presumption that small crystallites and incoherently diffracting domains separated by dislocations within grains affect the tails of the diffraction-line profiles [60, 115]. Figure 13 illustrates the dependence of MSS on the reciprocal of the averaging distance L.

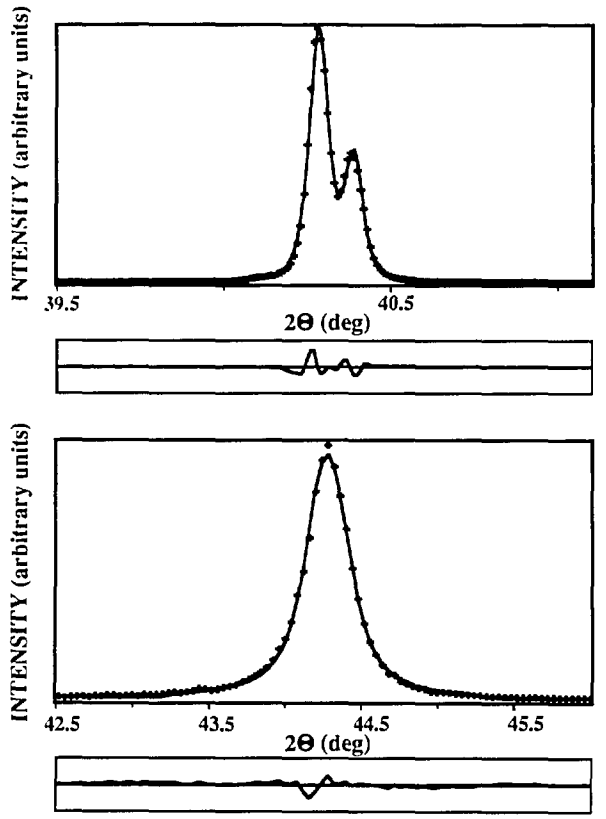

Fig. 11. Observed points (pluses), refined pattern (full line), and difference pattern (below): (110) W untreated (upper); (200) Ag ground (lower).

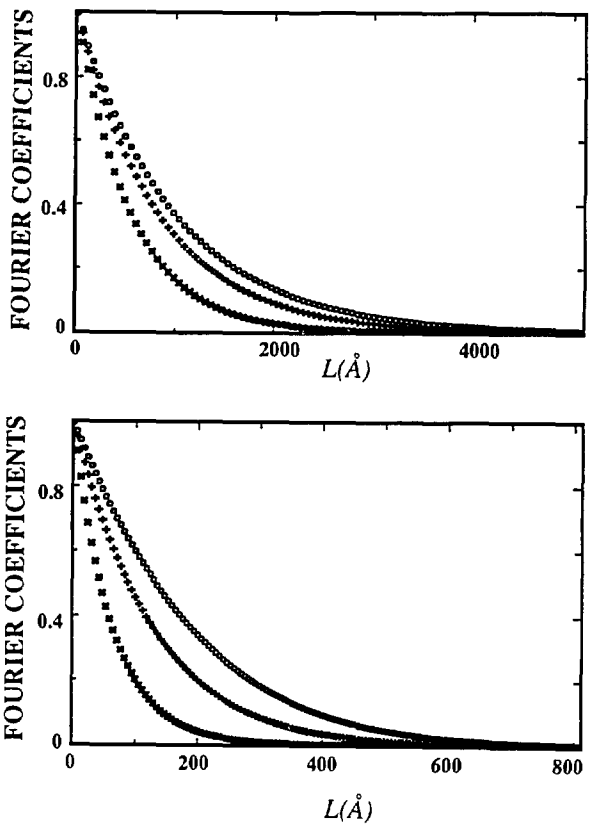

Fig. 12. Fourier coefficients for the first- (pluses) and second-order (crosses) reflection, and size coefficients (circles): [111] Ag untreated (upper); [100] Ag ground (lower).

Table 2. Parameters of the pure-specimen Voigt function, as obtained from profile-fitting procedure for tungsten and silver powders

Specimen	*hkl*	$2\theta_0$(°)	β_C(°)	β_G(°)	FWHM(°)	R_{wp}(%)
W untreated	110	40.28	0.0065(7)	0.020(2)	0.021	9.0
	220	87.05	0.0301(6)	$<10^{-5}$	0.019	4.4
W ground	110	40.29	0.100(2)	0.038(4)	0.080	9.0
	220	87.05	0.222(3)	0.069(6)	0.166	4.2
Ag untreated	111	38.06	0.056(1)	$<10^{-5}$	0.036	10.5
	222	81.51	0.105(4)	0.0008(21)	0.067	9.7
	200	44.25	0.118(2)	$<10^{-5}$	0.075	10.5
	400	97.86	0.274(21)	$<10^{-5}$	0.175	12.2
Ag ground	111	38.07	0.175(3)	0.038(12)	0.121	9.9
	222	81.51	0.410(26)	$<10^{-5}$	0.261	14.5
	200	44.24	0.365(10)	0.076(29)	0.250	9.9
	400	97.83	1.079(82)	$<10^{-5}$	0.687	14.5

Table 3. Microstructural parameters for tungsten and silver powders

Specimen	Direction	$\langle D\rangle_s$(Å)	$\langle D\rangle_v$(Å)	$\langle\epsilon^2(a_3)\rangle^{1/2}$	$\langle\epsilon^2(\langle D\rangle_v/2)\rangle^{1/2}$
W untreated	[110]	3200(200)	3500(200)	0.00038	0.00008(2)
W ground	[110]	620(20)	1030(30)	0.0023	0.00054(2)
Ag untreated	[111]	1000(20)	2000(20)	0.0010	0.00024(1)
	[100]	510(20)	1030(20)	0.0022	0.00047(5)
Ag ground	[111]	380(20)	650(20)	0.0047	0.00095(7)
	[100]	210(10)	350(20)	0.0100	0.00180(14)

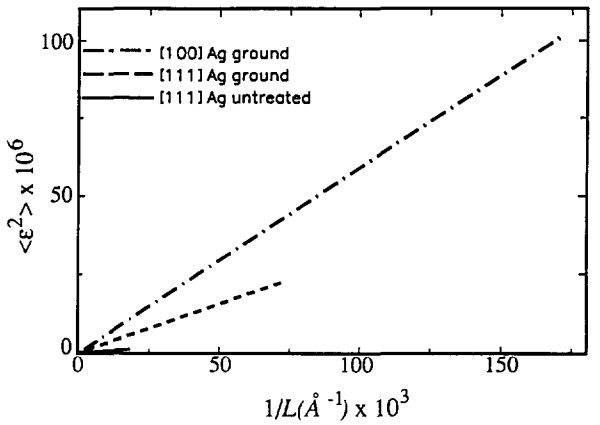

Fig. 13. Mean-square strains $\langle\epsilon^2\rangle$ as a function of $1/L$.

Errors in integral breadths allow estimation of errors in strain and size parameters (Sec. 4.5), but in some cases the refinement algorithm gives unreliable errors of integral breadths. When a particular parameter is close to the limiting value (for instance, 10^{-5} degrees has been put as the minimum value for integral breadths), errors become large. However, in Eqs. (63), (65), (66), (67), and (68), only the product of integral breadth and accompanying error is significant, which is roughly equal for Cauchy and Gauss parts. Errors of domain sizes and strains are of the same order of magnitude as errors of integral breadths.

The possible source of systematic error is potential inadequacy of Voigt function to accurately describe specimen broadening. This effect can not be evaluated analytically; but it would affect all derived parameters, especially the column-length distribution functions. The logical relationship between values of domain sizes (see Table 3) for different degrees of broadening indicates that possible systematic errors can not be large.

Equation (41) allows computation of volume-weighted and surface-weighted average domain sizes if respective column-length distribution functions can be obtained. Figure 14 gives surface-weighted and volume-weighted average column-length distribution functions following Eqs. (39) and (38). Width of the distribution function determines the relative difference between $\langle D\rangle_s$ and $\langle D\rangle_v$. The broader the distribution, the larger the differences, because small crystallites contribute more to the surface-weighted average. That is much more evident comparing the surface-weighted column-length distribution with the volume-weighted. If they have similar shape and maximum position, as in Fig. 15, differences are small. Conversely, if the surface-weighted distribution function has a sharp maximum toward smaller sizes, differences are larger (see Fig. 14). The difference between $\langle D\rangle_s$ and $\langle D\rangle_v$, and the actual mean dimension of the crystallites in a particular direction, also depends strongly on the average shape of the crystallites [52, 131, 132].

If experimental profiles are deconvoluted by the Stokes method, even for considerable specimen broadening, size coefficients A^S usually oscillate at larger L values [59, 106], preventing computation of the column-length distribution function. Few techniques were used to deal with this problem: successive convolution unfolding method [32, 133], smoothing, and iterative methods [134, 135, 136, 137]. Figures 14 and 15 show very smooth column-length distribution functions. However, they follow from size coefficients A^S that depend on the accuracy of the approximation for the distortion coefficient, given by Eq. (47). Equation (47) is exact if the strain distribution is Gaussian, but in general holds only for small harmonic numbers n, if strain broadening is not negligible.

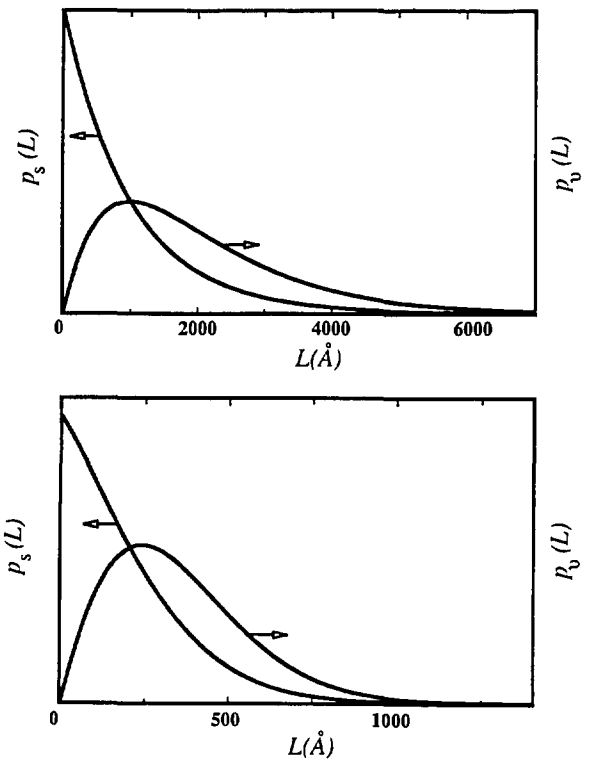

Fig. 14. Surface-weighted and volume-weighted column-length distribution functions, normalized on unit area: [111] Ag untreated (upper); [100] Ag ground (lower).

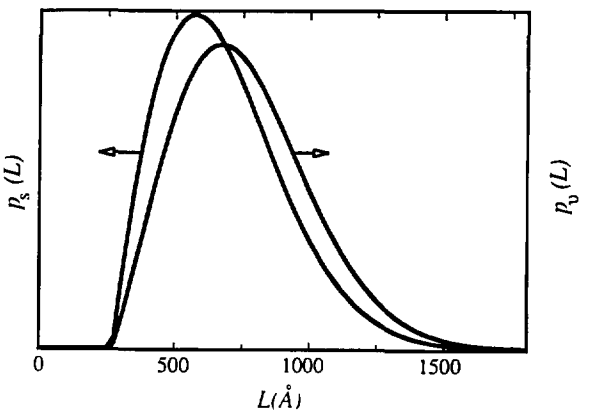

Fig. 15. Surface-weighted and volume-weighted column-length distribution functions for [010] La_2CuO_4, normalized on unit area.

5.2.2 $La_{2-x}Sr_xCuO_4$ Powders To test the applicability of the discussed method to more complicated patterns, two compounds with lower crystallographic symmetry were studied. $La_{1.85}Sr_{0.15}CuO_4$ has a tetragonal K_2NiF_4-type structure, space group $I4/mmm$. La_2CuO_4 is orthorhombic at room temperature. Both compounds show slight line broadening and relatively highly overlapping peaks (see Fig. 16), which makes it very difficult, if not impossible, to perform a Stokes analysis.

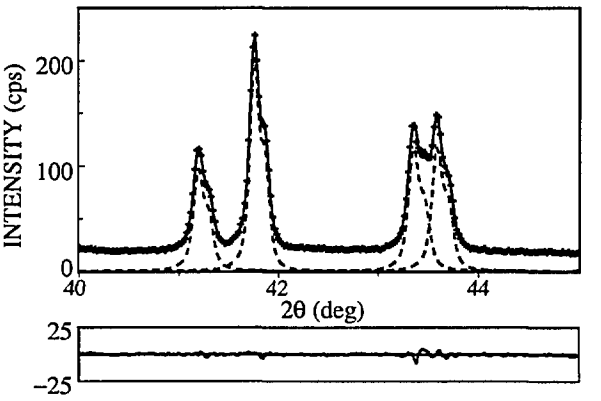

Fig. 16. Observed points (pluses), refined pattern (full line), convoluted profiles (dashed line), and difference plot (below) for part of La_2CuO_4 pattern.

Tables 4 and 5 list results from the fitting procedure and the analysis of specimen-broadened integral breadths. There are no qualitative differences in results for tungsten and silver powders. However, average errors are higher, as expected because of overlapping peaks, while weighted errors R_{wp} are surprisingly smaller. This fact illustrates the unreliability of R_{wp} when only a segment of the pattern is being refined, because it depends on the number of counts accumulated in points, as well as on the 2θ range of the refinement.

Figures 17 and 18 represent Fourier coefficients of $La_{1.85}Sr_{0.15}CuO_4$ [110] and La_2CuO_4 [010] directions. In the second plot, the $A^S(L)$-versus-L plot shows a concave-downward part near $L=0$, the so-called "hook" effect. It was shown in Sec. 4.2 that the "hook" effect originates because of underestimation of background, connected with the truncation of profiles. In the profile refinement, all peaks separated less than 4° 2θ have been included in the refinement region to avoid possible overlapping of peak tails, and specimen profiles have been truncated below 0.1 % of the maximum intensity. However, because the polynomial background was determined prior to profile refinement, it may be overestimated for complicated patterns containing many overlapping peaks. If background is refined with other profile parameters, undesirable correlation with integral breadths occurs.

Table 4. Parameters of the pure-specimen Voigt function, as obtained from profile-fitting procedure for $La_{2-x}Sr_xCuO_4$ powders

Specimen	*hkl*	$2\theta_0(°)$	$\beta_C(°)$	$\beta_G(°)$	FWHM(°)	$R_{wp}(\%)$
$La_{1.85}Sr_{0.15}CuO_4$	004	26.95	0.046(4)	0.024(8)	0.042	3.4
	006	40.92	0.083(5)	$<10^{-5}$	0.053	6.2
	110	33.52	0.110(5)	$<10^{-5}$	0.070	12.5
	220	70.46	0.171(9)	$<10^{-5}$	0.109	4.3
La_2CuO_4	004	27.13	0.061(8)	0.045(9)	0.067	3.9
	006	41.19	0.124(7)	$<10^{-5}$	0.079	7.7
	020	33.16	0.074(10)	0.078(10)	0.102	2.9
	040	69.57	0.210(30)	0.026(81)	0.135	2.9
	200	33.45	0.074(8)	0.061(10)	0.087	6.9
	400	70.28	0.130(10)	0.023(95)	0.089	2.9

Table 5. Microstructural parameters for $La_{1.85}Sr_{0.15}CuO_4$ and La_2CuO_4 powders

Specimen	Direction	$\langle D\rangle_s$(Å)	$\langle D\rangle_v$(Å)	$\langle\epsilon^2(a_3)\rangle^{1/2}$	$\langle\epsilon^2(\langle D\rangle_v/2)\rangle^{1/2}$
$La_{1.85}Sr_{0.15}CuO_4$	[001]	1700(300)	2000(200)	0.0024	0.00049(9)
	[110]	470(20)	940(20)	0.0017	0.00044(6)
La_2CuO_4	[001]	1100(100)	1200(100)	0.0038	0.0008(1)
	[010]	680(50)	760(50)	0.0033	0.0007(2)
	[100]	680(50)	810(50)	0.0016	0.0003(3)

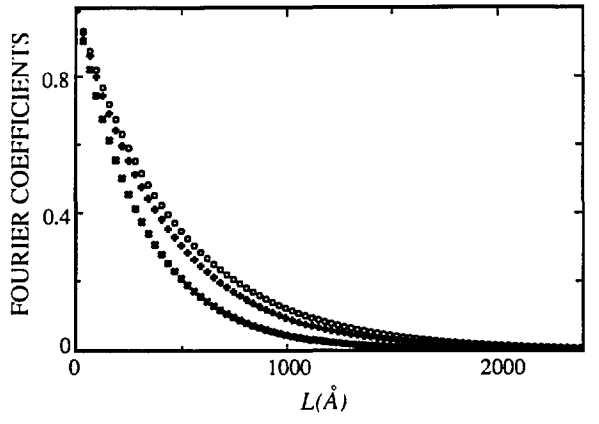

Fig. 17. Fourier coefficients for the first- (pluses) and second-order (crosses) reflection, and size coefficients (circles) for [110] $La_{1.85}Sr_{0.15}CuO_4$.

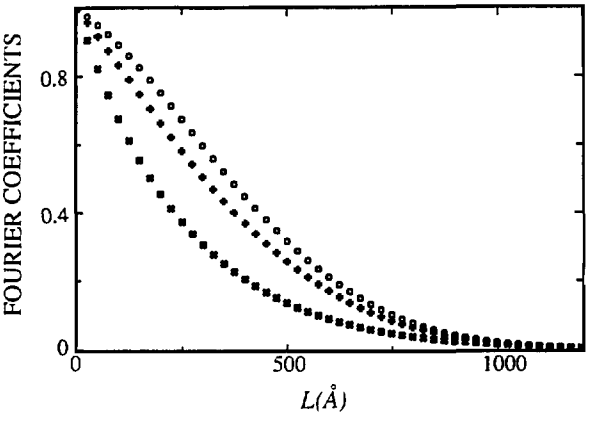

Fig. 18. Fourier coefficients for first- (pluses) and second-order (crosses) reflection, and size coefficients (circles) for [010] La_2CuO_4.

5.3. Comparison with the Integral-Breadth Methods

Knowing the specimen integral breadths, simplified methods can be applied. In Sec. 2.1.2 we reviewed multiple-line and single-line integral-breadth methods. We shall compare the simplified multiple-line methods [Eqs. (23), (24), and (30)] and the single-line method [76] [Eqs. (29) and (30)] with results obtained for silver, tungsten, and $La_{2-x}Sr_xCuO_4$ powders (Tables 3 and 5). We did not compare with the multiple-line Voigt-function method [26] because it was shown in Sec. 4.4 that it is incompatible with the Warren-Averbach analysis. In Table 6, integral breadth β_I was computed according to Eq. (11). This value was compared with β_A, integral breadth computed from Fourier coefficients [58]:

$$\beta_A = \frac{1}{a_3 \sum_{L=-\infty}^{\infty} A(L)} . \qquad (74)$$

Results obtained by the Warren-Averbach analysis are significantly smaller for both size and strain. Integral-breadth methods give the upper limit for strain, so comparison is limited. Considering the approximation $e = 1.25\langle \epsilon^2(L)\rangle^{1/2}$ [138] with $L = \langle D\rangle_v/2$ or $L = \langle D\rangle_s/2$, strains resemble more closely than crystallite sizes. It must be noted, however, that this approximation makes sense only in the case of pure-Gauss strain broadening. Benedetti et al. [106] reported excellent agreement for both size and strain using Warren-Averbach and Cauchy-Gauss [Eq. (24)] methods. Results from Table 6, on the contrary, indicate that the Gauss-Gauss approximation gives values closest to the Warren-Averbach method for crystallite sizes, whereas the Cauchy-Gauss and especially the Cauchy-Cauchy approximation tend to give too large values. For strain, the trend is opposite. The Cauchy-Cauchy approximation resembles most

Table 6. Comparison of results obtained with the integral-breadth methods: Cauchy-Cauchy (C-C), Cauchy-Gauss (C-G), Gauss-Gauss (G-G), and single-line (S-L) analysis

Specimen	*hkl*	$\beta_I \times 10^3$ (Å^{-1})	$\beta_A \times 10^3$ (Å^{-1})	$\langle D\rangle_v$ (Å)	$\langle D\rangle_v$(Å) C-C	C-G	G-G	S-L	$\langle \epsilon^2(\langle D\rangle_v/2)\rangle^{1/2} \times 10^3$	$e \times 10^3$ C-C	C-G	G-G	S-L
W untreated	110	0.259	0.259	3500	3700	3810	3810	14500	0.08	−0.01	−0.03	−0.05	0.24
	220	0.247	0.247					4040					0[a]
W ground	110	1.25	1.25	1030	2240	1450	1220	940	0.54	0.90	0.93	1.05	0.45
	220	2.04	2.05					550					0.32
Ag untreated	111	0.600	0.600	2000	3340	2390	2190	1670	0.24	0.35	0.39	0.95	0[a]
	222	0.901	0.900					1110					0[a]
	200	1.24	1.24	1030	2270	1470	1230	810	0.47	0.82	0.85	0.95	0[a]
	400	2.04	2.04					490					0[a]
Ag ground	111	1.98	2.00	650	2080	1240	910	530	0.95	1.79	1.82	1.97	0.48
	222	3.52	3.52					280					0[a]
	200	4.03	4.06	350	9380	4780	1320	260	1.80	4.05	4.05	4.08	0.82
	400	8.03	8.03					120					0[a]
$La_{1.85}Sr_{0.15}CuO_4$	004	0.657	0.650	2000	5230	3290	2660	1970	0.49	0.76	0.78	0.88	0.44
	006	0.881	0.880					1140					0[a]
	110	1.19	1.19	940	1240	1000	970	840	0.44	0.52	0.64	0.80	0[a]
	220	1.58	1.58					630					0[a]
La_2Cu_4	004	0.988	0.998	1200	2980	1940	1630	1490	0.8	1.07	1.12	1.27	0.81
	006	1.32	1.31					760					0[a]
	020	1.43	1.42	760	1200	910	860	1240	0.7	0.79	0.90	1.10	1.14
	040	1.98	2.00					510					0.16
	200	1.26	1.24	810	810	810	810	1250	0.3	0.02	0.11	0.15	0.89
	400	1.25	1.26					830					0.14

[a] Not possible to evaluate because of too small Gauss integral breadth.

closely a Warren-Averbach method. These results concur with the Klug and Alexander [24] comparison of the published size and strain values obtained by Warren-Averbach (Stokes) and integral-breadth methods. However, for x-ray diffraction, the Cauchy-Gauss assumption for the size-strain broadening is theoretically and experimentally more favored than the other two models. The fact that the Gauss-Gauss method for crystallite size and the Cauchy-Cauchy method for strain give more realistic results may mean that the presumption that size and strain broadening are exclusively of one type is an oversimplification.

The single-line method seems much less reliable. If Gaussian breadth is very small, no information about strain is obtained. Moreover, second-order reflections give much lower values of both size and strain than do basic reflections. However, if multiple reflections are not available, the single-line method can give satisfactory estimations.

5.4 Reliability of Profile Fitting

The profile fitting of a cluster of even severely overlapping peaks can be accomplished with a low error and excellent fit of total intensity. But how reliable is information obtained about separate peaks in the cluster? In the fitting procedure, it is possible to put constraints on the particular profile parameter to limit intensity, position, and width of the peak. If anisotropic broadening or different phases are present, constraints may not be realistic. Morever, acceptable results can be obtained even using a different number of profiles in refinement [4]. Hence, the first condition for the successful application of this method is knowledge of actual phases present in the sample and their crystalline structures.

In this regard, two powders were measured: orthorhombic $La_{1.94}Sr_{0.06}CuO_4$ has a slightly distorted K_2NiF_4-type structure (space group *Bmab*, $a = 5.3510(2)$ Å, $b = 5.3692$ Å(2), $c = 13.1931(7)$ Å) and tetragonal $La_{1.76}Sr_{0.24}CuO_4$ (space group *I4/mmm* $a = 3.7711(3)$ Å, $c = 13.2580(8)$ Å). Data were collected for each specimen separately and for a specimen obtained by mixing the same powders. Because diffracted intensity of each phase was lower for the mixture, counting time was proportionally increased to obtain roughly the same counting statistics. Figure 19 shows two partially separated orthorhombic (020), (200) and (040), (400) peaks, overlapped with tetragonal (110) and (220) reflections. During the profile fitting of the mixed powders, (200) orthorhombic peak tended to "disappear" on account of neighboring (020) and (110) reflections. Its intensity was constrained to vary in range ±30 % of (020) peak intensity, which can be justified if the crystallographic structure is known.

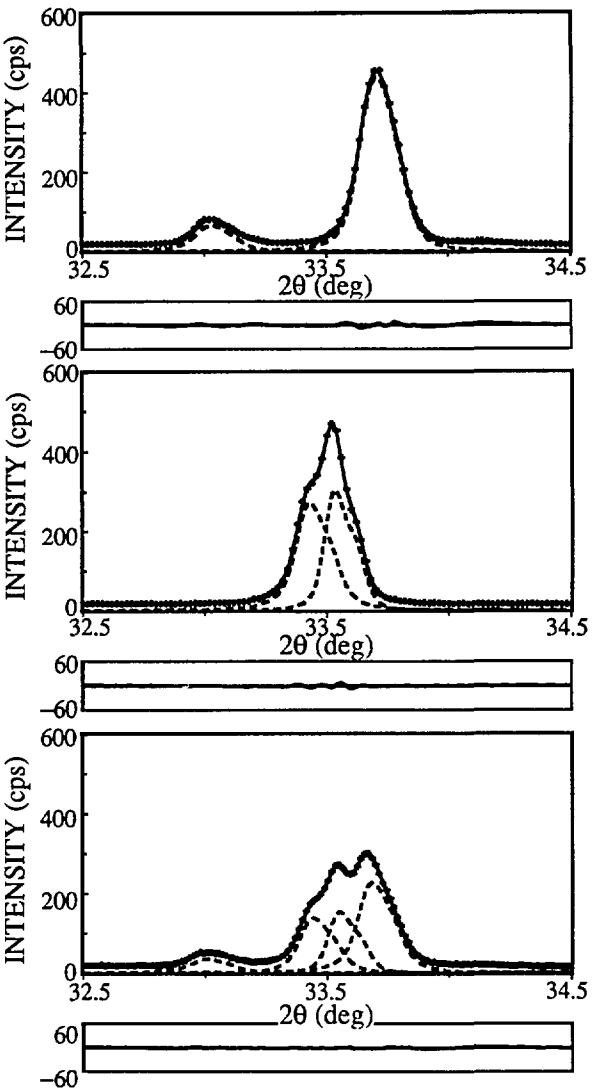

Fig. 19. (upper) $La_{1.76}Sr_{0.24}CuO_4$ (110) peak; (middle) $La_{1.94}Sr_{0.06}CuO_4$ (020) and (200) peaks; (lower) (110), (020), and (200) peaks.

Table 7 contains results of fitted specimen-Voigt functions, as well as size and strain values obtained by the analysis of broadening. Comparing integral breadths of the starting and mixed powders, some profiles change from more Cauchy-like to Gauss-like and vice versa. This is especially evident for the (400) reflection, meaning that accurate determination of the profile tails is indeed affected in the cluster of overlapping peaks. However, integral breadth does not change significantly, so results of

Table 7. Comparison between two specimens run separately and mixed together

Specimen	*hkl*	$2\theta_0$(°)	β_C(°)	β_G(°)	$\langle D\rangle_s$(Å)	$\langle D\rangle_v$(Å)	$\langle\epsilon^2(\langle D\rangle_v/2)\rangle^{1/2}\times10^3$
$La_{1.76}Sr_{0.24}CuO_x$	110	33.69	0.058(6)	0.094(7)	780(60)	850(60)	1.0(1)
	220	70.73	0.22(2)	0.13(2)			
$La_{1.94}Sr_{0.06}CuO_4$	020	33.42	0.084(9)	0.55(14)	500(90)	1000(200)	0.7(1)
	040	70.12	0.10(2)	0.14(1)			
	200	33.53	0.0216(85)	0.061(8)	1100(100)	1200(100)	0.3(1)
	400	70.40	0.026(11)	0.088(8)			
Mix	110	33.67	0.083(21)	0.064(14)	800(300)	1200(300)	0.8(3)
$La_{1.76}Sr_{0.24}CuO_4$	220	70.72	0.19(7)	0.13(4)			
+	020	33.43	0.066(35)	0.070(23)	800(300)	1000(300)	0.7(4)
$La_{1.94}Sr_{0.06}CuO_4$	040	70.12	0.116(93)	0.13(5)			
	200	33.54	0.024(156)	0.071(61)	900(700)	1000(600)	0.4(12)
	400	70.41	0.11(2)	0.003(320)			

the multiple-line methods are not much influenced. On the contrary, the single-line method gives quite different results. This may support the conclusion of Suortti, Ahtee, and Unonius [43] that the Voigt function fails to account properly for size and strain broadening simultaneously if only Cauchy integral breadth determines crystallite size.

Table 7 shows that the results of Warren-Averbach analysis of starting and mixed powders agree in the range of standard deviations. However, errors are much larger, especially for the hidden (200)–(400) reflections. From Eq. (62) it follows that more counts (longer counting times) and more observables (smaller step-size) would lower standard deviations. Therefore, in the case of highly overlapping patterns, to obtain desirable accuracy, much longer measurements are needed, although that will not change the fact that higher overlapping implies intrinsically higher errors of all refinable parameters. To further minimize possible artifacts of the fitting procedure, it is desirable to include in the analysis as many reflections in the same crystallographic direction as possible.

5.5 Remarks

By modeling the specimen size and strain broadening with the simple Voigt function, it is possible to obtain domain sizes and strains that agree with experiment and show a logical interrelationship. Furthermore, the Voigt function shows the correct $1/\Delta(2\theta)^2$ asymptotic behavior of peak tails, as expected from kinematical theory [139]. However, if the specimen profile is significantly asymmetric (because of twins and extrinsic stacking faults [140, 59]) or the ratio FWHM/β is not intermediate to the Cauchy ($2/\pi$) and Gauss ($2(\ln 2/\pi)^{1/2}$) functions, then the Voigt function can not be applied [25]. Suortti, Ahtee, and Unonius [43] found good overall agreement by fitting the Voigt function to the pure-specimen profiles of a Ni powder, deconvoluted by the instrumental function. However, more accurate comparison is limited because of unavoidable deconvolution ripples of specimen profiles. Furthermore, the Voigt function might not be flexible enough to model a wide range of specimen broadening, as well as the different causes of broadening. Therefore, the question whether the Voigt function can satisfactorily describe complex specimen broadening over the whole 2θ range in a general case needs further evaluation.

This method of Fourier analysis, with the assumed profile-shape function, is most useful in cases when the classical Stokes analysis fails; therefore when peak overlapping occurs and specimen broadening is comparable to instrumental broadening. It was shown that for a high degree of peak overlapping, the fitting procedure can give unreliable results of Gauss and Cauchy integral breadths; that is, the peak can change easily from predominantly Cauchy-like to Gauss-like, and contrary. This can lead to illogical values of size-integral and strain-integral breadths, according to Eqs. (52), (53), (54), and (55), and to irregularities in the behavior of Fourier coefficients for large L. Simultaneously, if the size-broadened profile has a large Gauss-function contribution, the "hook" effect will occur. However, volume-weighted domain sizes $\langle D\rangle_v$ and MSS $\langle\epsilon^2(L)\rangle$ for small L are much less affected, because they rely on both Cauchy and Gauss parts of the broadened profile. Any integral-breadth method that attempts to describe the size and strain broadening exclusively by a Cauchy or Gauss function, in this case, fails completely. For specimens with lower crystallographic symmetry,

when many multiple-order reflections are available, but the peaks are overlapped, it is therefore desirable to include in the analysis as many reflections as possible, to minimize the potential artifacts of the fitting process.

6. Analysis of Superconductors

6.1 $(La\text{-}M)_2CuO_4$ Superconductors

Bednorz and Müller [16] found the first high-temperature oxide superconductor in the La-Ba-Cu-O system. Soon after, substituting Ba with Sr and Ca, Kishio et al. [17] found superconductivity in two similar compounds. Later, many compounds with much higher transition temperatures (T_c) were found. The $(La\text{-}M)_2CuO_4$ system remains favorable for study because the cation content, responsible for the superconductivity, is easier to control and measure than the oxygen stoichiometry. Also, this system provides a wide range of substitutional cation solubility in which the tetragonal K_2NiF_4-type structure is maintained. Compared with much-studied Y-Ba-Cu-O, this structure is simpler because it contains only one copper-ion site and two oxygen-ion sites.

The undoped compound La_2CuO_4 is orthorhombic at room temperature. It becomes superconducting either with cation substitution on La sites or increased oxygen content to more than four atoms per formula unit. Doping with divalent cations increases the itinerant hole carriers in the oxygen-derived electron band [141], which probably causes the superconductivity. However, different dopants influence the transition temperature T_c. Although the unit-cell c-parameter simply reflects ionic dopant size [142], the in-plane unit-cell parameter (and accordingly the Cu-O bond length) correlates with T_c for different dopants and for different doping amounts [142, 143].

$La_{1.85}M_{0.15}CuO_4$ (M = Ba, Ca, Sr) have a tetragonal K_2NiF_4-type structure, space group *I4/mmm* with four atoms in the asymmetric unit [117]. One site is occupied with La, partially substituted with dopant ions (Fig. 20). La_2CuO_4 is orthorhombic at room temperature. The best way to correlate these two structures is to describe La_2CuO_4 in space group *Bmab*; the *c* axis remains the same, tetragonal [110] and [1$\bar{1}$0] directions become [010] and [100] orthorhombic axes, and size of the unit cell is doubled [144].

Figure 21 shows parts of the x-ray diffraction patterns, observed and refined, of $La_{1.85}M_{0.15}CuO_4$ (M = Sr, Ba, Ca) and La_2CuO_4. Refined lattice parameters are given in Table 8. Table 9 shows results of the line-broadening analysis. Relatively

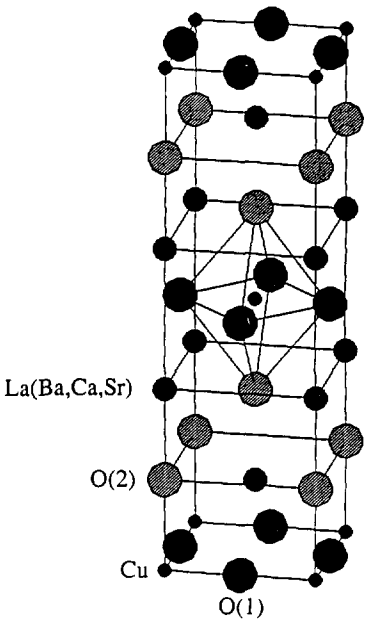

Fig. 20. Crystal structure of $(La\text{-}M)_2CuO_4$ showing one unit cell.

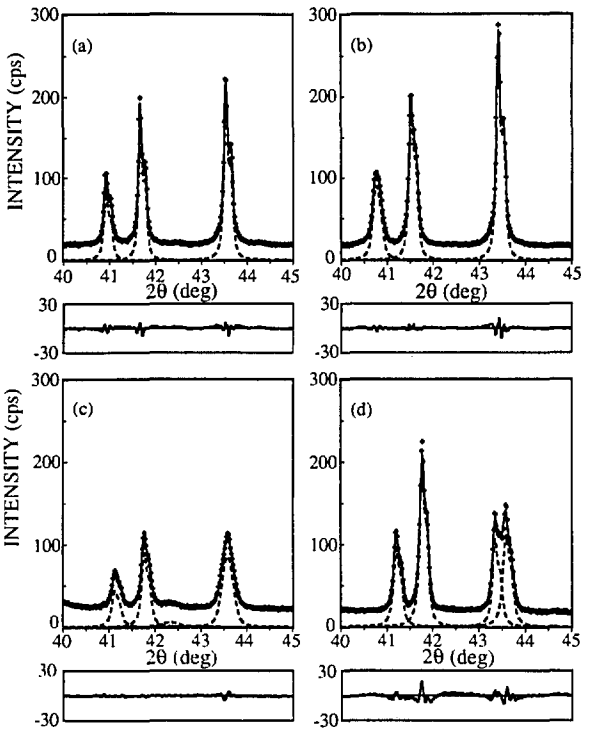

Fig. 21. Diffraction patterns of $La_{1.85}M_{0.15}CuO_4$ specimens: (a) M = Sr; (b) M = Ba; (c) M = Ca; (d) M = La.

Table 8. Lattice parameters and T_c at zero resistivity (Ac method at 10 Ma current)

Specimen	a(Å)	b(Å)	c(Å)	T_c(K)
$La_{1.85}Sr_{0.15}CuO_4$	3.77814(7)		13.231(2)	36
$La_{1.85}Ba_{0.15}CuO_4$	3.7846(2)		13.288(4)	28
$La_{1.85}Ca_{0.15}CuO_4$	3.7863(7)		13.17(2)	19
La_2CuO_4	5.3558(2)	5.4053(2)	13.1451(8)	

Table 9. Results of line-broadening analysis for $(La\text{-}M)_2Cu_4$ specimens

Specimen	hkl	β_C(°)	β_G(°)	$\langle D\rangle_s$(Å)	$\langle D\rangle_v$(Å)	$\langle\epsilon^2(\langle D\rangle_v/2)\rangle^{1/2}$
$La_{1.85}Sr_{0.15}CuO_4$	004	0.046(4)	0.024(8)	1700(300)	2000(200)	0.00049(9)
	006	0.083(5)	$<10^{-5}$			
	110	0.110(5)	$<10^{-5}$	470(20)	940(20)	0.00044(6)
	220	0.171(9)	$<10^{-5}$			
$La_{1.85}Ba_{0.15}CuO_4$	004	0.049(6)	0.076(6)	1100(200)	1100(100)	0.0011(2)
	006	0.110(7)	0.089(9)			
	110	0.087(4)	0.00042(6)	560(20)	1110(20)	0.00024(5)
	220	0.116(3)	$<10^{-5}$			
$La_{1.85}Ca_{0.15}CuO_4$	004	0.120(13)	0.032(22)	440(70)	780(90)	0.0007(4)
	006	0.146(12)	0.033(27)			
	110	0.045(25)	0.200(19)	340(30)	360(20)	0.0013(2)
	220	0.343(22)	$<10^{-5}$			
La_2CuO_4	004	0.061(8)	0.045(9)	1100(100)	1200(100)	0.0008(1)
	006	0.124(7)	$<10^{-5}$			
	020	0.074(10)	0.078(10)	680(50)	760(50)	0.0007(2)
	040	0.210(30)	0.026(81)			
	200	0.074(8)	0.061(10)	680(50)	810(50)	0.0003(3)
	400	0.130(10)	0.023(95)			

weak peak broadening was observed, which can not be attributed to the proximity of the phase transformation; $La_{1.85}Sr_{0.15}CuO_4$ is tetragonal down to $\approx$170 K [145], $La_{1.85}Ba_{0.15}CuO_4$ to 140 K [146, 147], and $La_{1.85}Ca_{0.15}CuO_4$ to 130 K [148]. Another possible reason for peak broadening might be continuous compositional variations in dopant content. The scanning Auger microprobe analysis of $La_{2-x}Sr_xCuO_4$ compounds [149] showed that grain-boundary segregation of Sr is weak and limited to a narrow region near the grain surface. In the case of the separation of two phases with different Sr content and similar lattice parameters, asymmetry of some reflections would be observed [150]. Moreover, in the case of compositional inhomogeneity, microstrains $\langle\epsilon^2(L)\rangle$ would be roughly independent of the averaging distance L in the grains [151]; therefore distribution of strains would be Gaussian. For all specimens, microstrain behavior is identical; it decreases linearly with distance L. Rothman and Cohen [115] showed that such behavior of microstrains is caused by dislocations that might arise during grinding. Assuming the same applied stress, microstrain would be approximately inversely proportional to the elastic moduli of these materials. If mean microstrain is defined as the arithmetic average of strains for the [001] and [110] directions, results agree with values of the Young's moduli for polycrystalline La_2CuO_4, $La_{1.85}M_{0.15}CuO_4$ (M = Sr, Ba, Ca) [152]. However, other factors may contribute to the microstrain. Coordination-6 ionic radii of La^{3+}, Sr^{2+}, Ba^{2+}, Ca^{2+} are 1.06, 1.16, 1.36, 1.00 Å, respectively [153]. Substitution of La^{3+} with ions of different sizes affects the lattice parameter [142] and may cause much larger strains in the [001] direction when some of the ions are replaced with Ba^{2+} than with Sr^{2+}, in accord with results in Table 9. Substitution of Ca^{2+} ions produces an entirely different effect; microstrains in the [110] direction are larger. This may be explained by

comparing effects of substitutional ions on the unit-cell a-parameter. The Ba-doped specimen has a larger a-parameter than the Sr-doped, but the Ca-doped a-parameter is largest, although Ca^{2+} has the smallest ionic size. This should increase the cell distortion in the a-b plane.

Table 9 reveals high anisotropy in these materials, consistent with other physical properties such as thermal expansion [154] and upper critical magnetic field [155]. Differences of domain sizes might arise from a layered structure in the [001] direction and consequently easy incorporation of stacking faults between regularly stacked layers. The stacking-fault and twin-fault probabilities can be estimated from the average surface-weighted domain sizes [59]:

$$\frac{1}{\langle D\rangle_s^{[hkl]}} = \frac{1}{\langle D\rangle} + c^{[hkl]}\,\mathrm{fun}(\alpha,\alpha'). \qquad (75)$$

Here, $c^{[hkl]}$ is a constant for the particular $[hkl]$ direction, and fun(α, α') a linear combination of stacking-fault probability and twin-fault probability α'. The exact form of Eq. (75) was derived only for the cubic and hexagonal crystal structures. On condition that the "true" domain dimension D is isotropic or so large that the second term of Eq. (75) dominates, a linear function of stacking-fault and twin-fault probability is

$$\mathrm{fun}(\alpha,\alpha') = c\left(\frac{1}{\langle D\rangle_s^{[110]}} - \frac{1}{\langle D\rangle_s^{[001]}}\right). \qquad (76)$$

Here, c denotes a constant that depends only on geometrical factors and is the same for all three doped compounds.

Figure 22 shows a possible correlation between T_c and fault-defect probabilities computed from. TEM observations of $La_{2-x}Sr_xCuO_4$ revealed that stacking-fault density increased with Sr content up to $x = 0.15$ [156]. That study suggests that a shear mechanism forming the fault-boundary dislocations implies oxygen vacancies and/or cation deficiency. We did not measure oxygen content, but neutron-diffraction studies showed that oxygen deficiency starts to appear at much higher Sr content [157]. However, the increase of fault probability with the simultaneous decrease of microstrain in Fig. 22 supports the assumption that defects are introduced to accommodate lattice strains [156]. A similar increase in T_c was found in $Y_2Ba_4Cu_8O_{20-\delta}$ thin films [158]. Compounds with asymmetric broadened and shifted peaks showed higher T_c, which was attributed to stacking faults. Although extrinsic stacking faults may cause asymmetric peak broadening [140], it is probably caused by twinning. Twinning in La-M-Cu-O materials is less abundant than in Y-Ba-Cu-O compounds, but it was observed in $(La\text{-}Sr)_2CuO_4$ monocrystals on (110) planes [159]. In the profile-fitting procedure, peak asymmetry is incorporated only in the instrumental function; therefore we could not model asymmetric peak broadening. However, any significant asymmetry of the specimen profile would cause an uneven fit of low-angle and high-angle sides of peaks, which was not observed. This gives much more importance to stacking faults in Eq. (76).

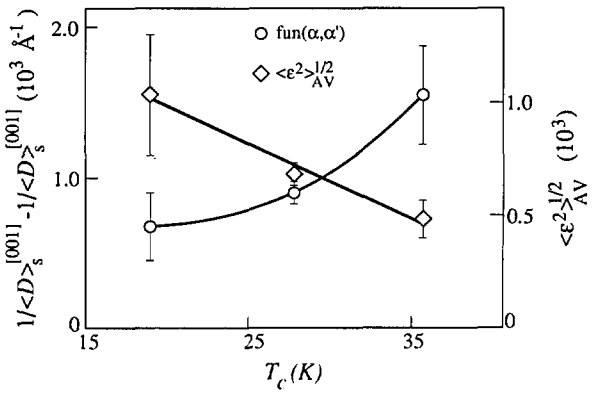

Fig. 22. Arithmetic average of [110] and [001] root-mean-square strains and linear function of stacking-fault and twin-fault probabilities as a function of T_c.

In Fig. 22, average microstrains, defined as the arithmetic average of [001] and [110] directions, correlate inversely with T_c. However, we did not find a correlation of T_c and microstrains in a particular direction. [001] microstrains simply reflect difference in size of dopant and host La^{3+} ions (see Table 9).

In La_2CuO_4, ($0k0$) reflections are significantly broader than ($h00$). This has also been observed in low-temperature orthorhombic $La_{1.85}Sr_{0.15}CuO_4$ and $La_{1.85}Ba_{0.15}CuO_4$ [160], and explained by either stacking faults or possible lower symmetry. Our results reveal that domain sizes $\langle D\rangle_s$ have identical values for [010] and [100] directions (Table 9). From Eq. (76), it follows that stacking-fault probabilities in these directions have the same values. However, microstrains in the [010] direction are roughly twice as large as in the [100] direction, which is responsible for the different broadening. In the case of doped La_2CuO_4 compounds, different microstrains might be caused by oxygen

vacancies ordered along one direction in the *a-b* plane, similar to effects found in $YBa_2Cu_3O_{7-\delta}$. However, undoped La_2CuO_4 is not expected to have significant oxygen deficiency. Other possibilities are lower crystallographic symmetry and/or La vacancies, although they were not reported for this system, but La deficiency was found in an La_2CoO_4 compound [161].

We can conclude that lattice strains and incoherently diffracting domain sizes confirm high anisotropy in these materials. This simple approach, however, does not allow unambiguous identification of the strain's origin. Probably, the strains originate from dislocations and from different sizes of host and dopant ions. Domain sizes of all compounds are larger in the *c*-direction than in the *a-b* plane. This indicates existence of stacking faults and twins. However, because estimated errors are relatively large and only three materials were studied, the possible connection between stacking faults and T_c needs further study.

6.2 Bi-Cu-O Superconductors

Among the high-T_c superconductors, the Bi-Cu-O compounds appear intriguing, especially because their incommensurate structure modulation remains incompletely understood [162, 163]. The crystal structure consists of perovskite-like $SrO\text{-}(CuO_2Ca)_{m-1}\text{-}CuO_2\text{-}SrO$ layers separated by NaCl-like BiO double layers (see Fig. 23 [164]). The number m of CuO_2 layers alters the superconducting transition temperature T_c (for $m = 1, 2$, and 3, $T_c \approx 10$, 90, and 110 K, respectively). This two-dimensional layered structure makes these materials highly anisotropic and favours the creation of defects.

Bulk sintered specimens showed relatively weak peak broadening. Moreover, the diffraction patterns contained many overlapping peaks because the compound crystallizes in an orthorhombic low-symmetry space group $A2aa$ [165], and incommensurate modulation gives superlattice reflections. All patterns revealed a strong [00l] texture (Fig. 24), making reflections other than (00l) difficult to analyze. The lattice parameters vary depending on the exact compound stoichiometry and processing history, but characteristically they have almost identical *a* and *b* parameters, and large *c* parameter: $a = 5.4095$ Å, $b = 5.4202$ Å, $c = 30.9297$ Å for $Bi_2Sr_2CaCu_2O_8$ (Bi-2212) [166] and $a = 5.392$ Å, $b = 5.395$ Å, $c = 36.985$ Å for $(BiPb)_2Sr_2Ca_2Cu_3O_{10}$ (Bi,Pb-2223) [165]. Thus, we treated $(h00)$ and $(0k0)$ reflections as single peaks. Table 10 gives the results for three specimens: Bi-2212, $(BiPb)_2(SrMg)_2(BaCa)_2Cu_3O_{10}$ (Bi,Pb,Mg,Ba-2223), which were one-phase specimens, and Bi,Pb-2223, containing approximately equal amounts of 2212 and 2223 phases. The in-plane lattice parameters of 2212 and 2223 phases differ little, hence only the $[00l]$ directions of the mixed-phase specimen were evaluated.

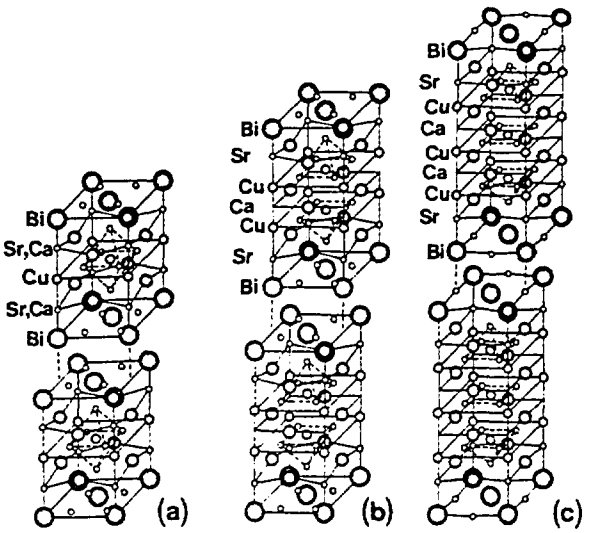

Fig. 23. Average crystal structure of $Bi_2Sr_2Ca_{m-1}Cu_mO_{4+2m}$ for: (a) $m = 1$; (b) $m = 2$; (c) $m = 3$ [164].

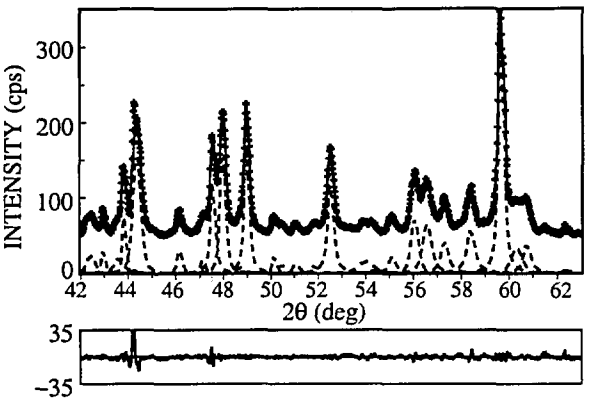

Fig. 24. Part of Bi,Pb,Mg,Ba-2223 refined pattern. There are 48 fundamental reflections in this region.

Interpretation of the results in the case of these complicated compounds must be considered carefully. Microstrains are probably caused by dislocation arrays. However, substitution of different-sized ions and vacancies would also contribute to the strains, as would other kinds of disorder, especially

Table 10. Results of line-broadening analysis for Bi-Cu-O supreconductors

Specimen	Phase	*hkl*	β_C (°)	β_G (°)	$\langle D\rangle_s$ (Å)	$\langle\epsilon^2(\langle D\rangle_s/2)\rangle^{1/2}$
Bi-2212	2212	008	0.163(8)	0.01(6)	420(80)	0.0021(6)
		00.12	0.22(3)	0.05(6)		
		020+200	0.104(4)	$<10^{-5}$	580(30)	0.0007(1)
		040+400	0.18(2)	0.0004(6300)		
Bi,Pb,Mg,Ba-2223	2223	00.10	0.097(1)	0.0002(1700)	770(60)	0.0012(1)
		00.20	0.21(2)	0.007(150)		
		020+200	0.12(27)	0.13(10)	380(430)	0.0009(71)
		040+400	0.15(95)	0.21(33)		
Bi,Pb-2223	2212	008	0.23(2)	0.002(350)	220(30)	0.0013(26)
		00.12	0.25(5)	0.001(1000)		
	2223	00.10	0.22(8)	0.092(67)	230(190)	0.0012(197)
		00.20	0.23(99)	0.18(47)		

stacking faults and twins. Table 10 shows larger strains in the [001] direction that in the basal plane. This can be explained by stacking disorder along the *c*-axis, which was frequently observed in electron-diffraction patterns as streaking [167, 168]. Easy incorporation of stacking faults is possible because of the two-dimensional weak-bonded layers (BiO double layers are spaced about 3 Å apart). The difference in microstrain between in-plane and the *c*-direction is much smaller for the Bi,Pb,Mg,Ba-2223 phase, probably because Pb lowers the faulting by stabilizing the higher-T_c 2223 phase [167]. For the Bi,Pb-2223 specimen, with two phases, there are two possibilities: Either the specimen consists mainly of a mix of two kinds of one-phase grains, or both phases occur within the same grains. The second possibility was confirmed experimentally [169, 170], and our results concur because microstrain in the 2212 phase is much smaller than in the one-phase Bi-2212 specimen. Processing conditions and cation content probably favour development of the macroscopic intergrowth of both phases within the grains; that is, microscopic defects grow to sufficiently large regions to give a diffraction pattern of another phase with the different number of CuO_2 layers. As a result, strain is relieved, and both strains and domain sizes, being quite different in one-phase specimens, tend to equalize.

For the Bi-Cu-O specimens, the mean surface-weighted domain sizes are generally smaller than for $(La\text{-}M)_2CuO_4$ compounds. Therefore, the computation of the stacking- and twin-fault probabilities by using Eq. (75) may be wrong. It would be very instructive to compare the different broadening of satellite and fundamental reflections, which indicates a more pronounced stacking disorder in the modulated structure [171].

In summary, we found that for both Bi-2212 and Bi,Pb,Mg,Ba-2223 superconductors, the *c*-axis strain exceeds the in-plane strain. The Bi,Pb-2223 specimen, containing both 2212 and 2223 phases within the single grains, shows smaller incoherently diffracting domains and lower c-axis strain than the one-phase specimens. This fact may direct us toward the mechanism of the second-phase formation in these materials.

6.3 Remarks

It was shown that this particular method of the line-broadening analysis can give information about the size of incoherently diffracting domains and lattice strains in $(La\text{-}M)_2CuO_4$ and Bi-Cu-O superconductors. Moreover, results show high anisotropy of both size and strain parameters, as one may expect, because of the layered structure of all superconducting cuprates. Generally, structural line broadening is not large; that is a result of relatively large domain sizes (200–2000 Å) and small strains (0.02%–0.2%). It is interesting to compare these values with the published results for $YBa_2Cu_3O_{7-\delta}$ (isotropic strains of 0.23% [77] and 0.05%–0.3% [82]). Although the different materials were studied, they seem too large, especially because they are the average of strains in different directions.

The main drawback of the line-broadening theory is the uncertainty about the origins of the line broadening; that is, it is difficult to distinguish the main effects responsible for the broadening. For

the novel superconductors, particularly, the numerous defects (substitutions, vacancies, stacking faults, dislocations, and similar) can occur simultaneously, which makes it very difficult to determine their individual contributions. Furthermore, the crystal structures of most novel superconductors are relatively complicated. The average structure has mostly a slightly distorted tetragonal symmetry; very similar a and b lattice parameters, and a large c parameter, but $c \approx 3b$ for $YBa_2Cu3O_{7-\delta}$, for instance. This results in a large number of overlapping peaks, and consequently in large errors of all results. This showed especially in the case of Bi-Cu-O superconductors (see Table 10). Following the discussion of reliability of profile fitting in Sec. 5.4, it would be desirable to include more than two reflections in the analysis of broadening, but higher-order peaks are usually too weak and overlapped. One way to partially solve this problem would be a whole pattern fitting [172, 173] and Rietveld structure refinement [2, 3] in terms of size and strain parameters. This requires an accurate preset function to model specimen broadening and precise definition of angular dependence of size and strain parameters. The Rietveld programs that model the line broadening in terms of size and strain parameters are based either on the simplified integral-breadth methods [78, 95] or on the single-line method [174].

7. Conclusions

A method for analyzing the pure-specimen (structural) broadening of x-ray diffraction line profiles is proposed. By modeling the specimen size and strain broadenings with the simple Voigt function, it is possible to obtain domain sizes and strains that agree with experiment and show a logical interrelationship. Furthermore, some common consequences and problems in the Fourier-method analysis follow easily. The specimen function is convoluted with the instrumental function to match the observed x-ray diffraction-line profile. This avoids the Stokes deconvolution method, thus allowing analysis of patterns with highly overlapping peaks and weak structural broadening. Therefore, the method was applied to some novel high-T_c superconductors. We reached the following conclusions:

(i) Surface-weighted domain size depends only on the Cauchy integral breadth of the size-broadened profile.

(ii) The "hook" effect occurs when the Cauchy-content of the size-broadened profile is underestimated, that is, for $\beta_{SC} < (\pi/2)^{1/2}\beta_{SG}$. Usually this happens when the background is estimated too high, so the long tails of the Cauchy function are prematurely cut off.

(iii) It also follows from conclusion (ii) that the volume-weighted domain size can not be more than twice the surface-weighted domain size (limiting value $\langle D\rangle_v = 2\langle D\rangle_s$ is obtained for the pure-Cauchy size-broadened profile). Minimum value for $\langle D\rangle_v / \langle D\rangle_s$ should not be less than ~ 1.31.

(iv) If the distortion coefficient is approximated with a harmonic term, this leads exactly to the Warren-Averbach method of separation of size and strain broadenings.

(v) In that case, mean-square strains decrease linearly with the distance L.

(vi) It is possible to evaluate local strain ($\langle \epsilon^2(0)\rangle^{1/2}$) only in the case of pure-Gauss strain broadening. Then, root-mean-square strain is independent of the distance L and related to the upper limit of strain obtained from the integral breadth of the strain-broadened profile.

(vii) If strain broadening is not described exclusively with the Gauss function, the multiple-line Voigt integral breadth and Warren-Averbach analyses can not give the same results for volume-weighted domain size, although $\langle D\rangle_v$ is defined identically in both approaches, because the "apparent strain" $\eta = \beta^D(2\theta)\cot\theta$ is not angular-independent.

(viii) Smooth size coefficients give column-length distribution functions without oscillations and make possible a computation of volume-weighted average domain sizes up to ~ 5000 Å.

(ix) Comparison with the simplified integral-breadth methods, in most cases, has shown not large, but systematic discrepancy of results, indicating that size and strain broadening can not be accurately modeled by a single Cauchy or Gauss function. Moreover, the application of the single-line method is much less reliable, and it should not be used where multiple reflections are available.

(x) The knowledge of all phases present in the sample and their crystallographic structure is required to successfully fit a cluster of overlapping peaks. Although it is very difficult to accurately determine the Cauchy-Gauss ratio of an overlapped peak, final results of domain size and strain are much less affected. Therefore, connecting the crystallite size exclusively with the Cauchy content and strain with the Gauss content of a specimen profile might be doubtful.

(xi) Evaluated errors of domain sizes and strains increase substantially with the degree of

peak overlapping. Hence, for complicated patterns, very accurate measurements are necessary and one needs to analyze as many reflections in the same crystallographic direction as possible.

(xii) Line-broadening analysis of $(La\text{-}M)_2CuO_4$ and Bi-Cu-O compounds confirms high anisotropy in these materials.

(xiii) Strains in $(La\text{-}M)_2CuO_4$ probably originate from dislocations and from different sizes of host and dopant ions.

(xiv) Stacking-fault probability in $(La\text{-}M)_2CuO_4$ (M=Ba, Ca, Sr) increases with increasing T_c, whereas the average strain decreases.

(xv) In La_2CuO_4, different broadening of $(h00)$ and $(0k0)$ reflections is not caused by stacking faults.

(xvi) All Bi-Cu-O superconductors show larger strain in the c-direction than in the a-b plane, which can be explained by stacking disorder along the [001] direction.

(xvii) In the specimen with approximately equal amounts of Tl-2212 and Tl,Pb-2223 phases, it is likely that a secondary phase develops by the growth of the microscopic faulted regions of the primary phase.

Acknowledgments

I am thankful to Dr. Harry McHenry for his support and especially to Dr. Hassel Ledbetter for his wise guidance and most useful help during my stay at NIST. I am also indebted to my home institution, the Faculty of Metallurgy of the University of Zagreb, for allowing me the leave of absence at NIST

8. References

[1] W. Friedrich, P. Knipping, and M. v. Laue, Ann. Physik, **41**, 971 (1912).
[2] H. M. Rietveld, Acta Cryst. **22**, 151 (1967).
[3] H. M. Rietveld, J. Appl. Cryst. **2**, 65 (1969).
[4] S. A. Howard and K. D. Preston, in Modern Powder Diffraction, Vol. 20, The Mineralogical Society of America, Washington, DC (1989) p. 217.
[5] D. Taupin, J. Appl. Cryst. **6**, 266 (1973).
[6] T. C. Huang and W. Parrish, Appl. Phys. Lett. **27**, 123 (1975).
[7] M. K. Wu, J. R. Ashburn, C. J. Torng, P. H. Hor, R. L. Meng, L. Gao, Z. J. Hwang, Y. Q. Wang, and C. W. Chu, Phys. Rev. Lett. **58**, 908 (1987).
[8] D. Shi, MRS Bull. **16**, 37 (1991).
[9] D. Larbalestier, Phys. Today **44**, 74 (1991).
[10] J. C. Phillips, Phys. Rev. B **45**, 12647 (1992).
[11] B. Raveau, Phys. Today **45**, 53 (1992).
[12] A. J. Millis and K. M. Rabe, Phys. Rev. B **38**, 8908 (1988).
[13] F. Guinea, Europhys. Lett. **7**, 549 (1988).
[14] C. P. Dhard and P. Singh, in Proc. Int. Symp. High-Temp. Supercond., Jaipur, India, Oxford & IBH Publishing, New Delhi (1988) p. 271.
[15] J. D. Jorgensen, Phys. Today **44**, 34 (1991).
[16] J. G. Bednorz and K. A. Müller, Z. Phys. B **64**, 189 (1986).
[17] K. Kishio, K. Kitazawa, S. Kaube, I. Yasuda, N. Sugii, H. Takagi, S. Uchida, K. Fueki, and S. Tanaka, Chem. Lett. 429 (1987).
[18] J. D. Jorgensen, B. Dabrowski, S. Pei, D. G. Hinks. L. Soderholm, B. Morosin, J. E. Venturini, and D. S. Ginley, Phys. Rev. B **38**, 11337 (1988).
[19] J. R. Clem, Phys. Rev. B **43**, 7837 (1991).
[20] M. Paranthaman, M. Földeáki, D. Balzar, H. Ledbetter, A. J. Nelson, and A. M. Hermann, submitted to Phys. Rev. B.
[21] A. R. Stokes, Proc. Phys. Soc. Lond. **61**, 382 (1948).
[22] B. E. Warren and B. L. Averbach, J. Appl. Phys. **23**, 497 (1952).
[23] R. Delhez, Th. H. de Keijser, and E. J. Mittemeijer, in Accuracy in Powder Diffraction, S. Block and C. R. Hubbard, eds., Natl. Bur. Stand. (U.S.) Special Publication 567 (1980) p. 213.
[24] H. P. Klug and L. E. Alexander, X-ray Diffraction Procedures, 2nd Edition, John Wiley, New York (1974) p. 661.
[25] J. I. Langford, J. Appl. Cryst. **11**, 10 (1978).
[26] J. I. Langford, in Accuracy in Powder Diffraction, S. Block and C. R. Hubbard, eds., Natl. Bur. Stand. (U.S.) Special Pubication 567 (1950) p. 255.
[27] R. Delhez, Th. H. de Keijser, and E. J. Mittemeijer, Fresenius Z. Anal. Chem. **312**, 1 (1982).
[28] A. J. C. Wilson, Proc. Phys. Soc. Lond. **80**, 286 (1962).
[29] A. J. C. Wilson, Proc. Phys. Soc. Lond. **81**, 41 (1963).
[30] L. P. Smith, Phys. Rev. **46**, 343 (1934).
[31] H. C. Burger and P. H. van Cittert, Z. Phys. **79**, 722 (1932).
[32] S. Ergun, J. Appl. Cryst. **1**, 19 (1968).
[33] R. Croche and L. Gatineau, J. Appl. Cryst. **10**, 479 (1977).
[34] L. H. Schwarz and J. B. Cohen, Diffraction from Materials, Academic Press, New York (1977) p. 391.
[35] R. Delhez, Th. H. de Keijser, E. J. Mittemeijer, and J. I. Langford, J. Appl. Cryst. **19**, 459 (1986).
[36] R. Delhez, Th. H. de Keijser, E. J. Mittemeijer, and J. I. Langford, Aust. J. Phys. **41**, 213 (1988).
[37] R. A. Young and D. B. Wiles, J. Appl. Cryst. **15**, 430 (1982).
[38] W. Voigt, Stizungsber. K. Bayer. Akad. Wiss. **42**, 603 (1912).
[39] E. E. Whiting, J. Quant. Spectrosc. Radiat. Transfer **8**, 1379 (1968).
[40] G. K. Wertheim, M. A. Butler, K. W. West, and D. N. E. Buchanan, Rev. Sci. Instrum. **11**, 1369 (1974).
[41] M. M. Hall Jr., V. G. Veeraraghavan, H. Rubin, and P. G. Winchell, J. Appl. Cryst. **10**, 66 (1977).
[42] A. Brown and J. W. Edmonds, Adv. X-Ray Anal. **23**, 361 (1980).
[43] P. Suortti, M. Ahtee, L. Unonius, J. Appl. Cryst. **12**, 365 (1979).
[44] T. Sundius, J. Raman Spectrosc. **1**, 471 (1973).
[45] B. H. Armstrong, J. Quant. Spectrosc. Radiat. Transfer **7**, 61 (1967).
[46] J. F. Kielkopf, J. Opt. Soc. Am. **63**, 987 (1973).
[47] B. P. Asthana and W. Kiefer, Appl. Spectr. **36**, 250 (1982).

[48] J. P. M. de Vreede, S. C. Mehrotra, A. Tal, and H. A. Dijkerman, Appl. Spectr. **36**, 227 (1982).
[49] F. R. L. Schoening, Acta Cryst. **18**, 975 (1965).
[50] P. Scherrer, Gött. Nachr. **2**, 98 (1918).
[51] A. R. Stokes and A. J. C. Wilson, Proc. Cambridge Philos. Soc. **38**, 313 (1942).
[52] A. J. C. Wilson, X-Ray Optics, 2nd edition, Methuen, London (1962).
[53] S. Lele and T. R. Anantharaman, Proc. Indian Acad. Sci. Sect. A **64**, 261 (1966).
[54] D. Louër, D. Weigel, and J. I. Langford, J. Appl. Cryst. **5**, 353 (1972).
[55] A. J. C. Wilson, J. Appl. Cryst. **2**, 181 (1969).
[56] J. I. Langford and A. J. C. Wilson, J. Appl. Cryst. **11**, 102 (1978).
[57] A. R. Stokes and A. J. C. Wilson, Proc. Phys. Soc. Lond. **56**, 174 (1944).
[58] B. E. Warren and B. L. Averbach, J. Appl. Phys. **21**, 595 (1950).
[59] B. E. Warren, X-Ray Diffraction, Addison-Wesley, Reading, Massachusetts (1969) p. 264.
[60] B. E. Warren, in Progress in Metal Physics, Vol. 8, Pergamon Press, London, (1959) p. 146.
[61] F. Bertaut, C. R. Acad. Sci. Paris **228**, 187 (1949).
[62] N. C. Halder and C. N. J. Wagner, Acta Cryst. **20**, 312 (1966).
[63] D. Balzar and H. Ledbetter, in Proceedings of the Accuracy in Powder Diffraction II, Natl. Inst. Stand. Technol. (1992) p. 37.
[64] D. Balzar and H. Ledbeter, J. Appl. Cryst. **26**, (1993) in press.
[65] J. N. Eastabrook and A. J. C. Wilson, Proc. Phys. Soc. Lond. B **65**, 67 (1952).
[66] R. S. Smith, IBM J. Res. Develop. **4**, 205 (1960).
[67] B. Y. Pines and A. F. Sirenko, Soviet Physics Cryst. **7**, 15 (1962).
[68] G. B. Mitra and N. K. Misra, Acta Cryst. **22**, 454 (1967).
[69] A. Gangulee, J. Appl. Cryst. **7**, 434 (1974).
[70] J. Mignot, D. Rondot, Acta Met. **23**, 1321 (1975).
[71] J. Mignot and D. Rondot, Acta Cryst. A **33**, 327 (1977).
[72] R. K. Nandi, H. K. Kuo, W. Schlosberg, G. Wissler, J. B. Cohen, and B. Crist Jr., J. Appl. Cryst. **17**, 22 (1984).
[73] M. Zocchi, Acta Cryst. A **36**, 164 (1980).
[74] P. Ramarao and T. R. Anantharaman, Trans. Ind. Ins. Metals **18**, 181 (1965).
[75] R. K. Nandi and S. P. Sen Gupta, J. App. Cryst. **11**, 6 (1978).
[76] Th. H. de Keijser, J. I. Langford, E. J. Mittemeijer, and B. P. Vogels, J. Appl. Cryst. **15**, 308 (1982).
[77] A. Williams, G. H. Kwei, R. B. Von Dreele, A. C. Larson, I. D. Raistrick, and D. L. Bish, Phys. Rev. B **37**, 7960 (1988).
[78] A. C. Larson and R. B. Von Dreele, Los Alamos National Laboratory Report No. LA-UR-86-748 (1988).
[79] J. D. Jorgensen, D. H. Johnson, M. H. Mueller, J. G. Worlton, and R. B. Von Dreele, in Proceedings of the Conference on Diffraction Profile Analysis, Cracow, Poland (1978) p. 20.
[80] R. B. Von Dreele, J. D. Jorgensen, and C. G. Windsor, J. Appl. Cryst. **15**, 581 (1982).
[81] P. Thompson, D. E. Cox, and J. B. Hastings, J. Appl. Cryst. **20**, 79 (1987).
[82] J. P. Singh, R. A. Guttschow, D. S Kupperman, J. T. Dusek, and R B. Poeppel, in High Temperature Superconducting Compounds III, S. Whang, A. Gupta, and E. Collings, eds., TMS, AIME, Warrendale (1991) p. 281.
[83] M. O. Eatough, D. S Ginley, and B. Morosin, Adv. X-Ray Anal. **33**, 145 (1990).
[84] E. J. Peterson, P. J. Kung, R. E Muenchausen, and D. M. Smith, in Proceedings of the 41st Annual Denver Conference on Applications of X-Ray Analysis, Colorado Springs, Colorado (1992) p. 74.
[85] M. Rand, J. I. Langford, and J. S. Abell, submitted to J. Cryogenics (1992).
[86] D. Balzar, J. Appl. Cryst. **25**, 559 (1992).
[87] D. Balzar, H. Ledbetter, and A. Roshko, Physica C **185-189**, 871 (1991).
[88] D. Balzar and H. Ledbetter, J. Mater. Sci. Lett. **11**, 1419 (1992).
[89] D. Balzar, H. Ledbetter, and A. Roshko, Pow. Diffr. **8**, (1993), in press.
[90] S. Johnson, M. Gusman, D. Rowcliffe, T. Geballe, and J. Sun, Adv. Ceram. Mater. **2**, 337 (1987).
[91] H. Ledbetter, S. A. Kim, R. B. Goldfarb, and K. Togano, Phys. Rev. B **39**, 9689 (1989).
[92] H. Friedman, Electronics 132 (1945).
[93] W. Parrish (ed.), in Advances in X-Ray Diffractometry and X-Ray Spectrography, Centrex Publishing Company, Eindhoven, The Netherlands (1962).
[94] W. Soller, Phys. Rev. **24**, 158 (1924).
[95] S. A. Howard, R. L. Snyder, J. Appl. Cryst. **22**, 238 (1989).
[96] G. H. Stout and L. H. Jensen, X-Ray Structure Determination, 2nd edition, Wiley, New York (1989) p. 373.
[97] D. E. Appleman and T. Evans, Jr., Final Report 92-14, U.S. Geological Survey, Washington, DC (1973). Available as NTIS Document No. PB-216188.
[98] M. U. Cohen, Rev. Sci. Instrum. **6**, 68 (1935).
[99] M. U. Cohen, Rev. Sci. Instrum. **7**, 155 (1936).
[100] M. H. Mueller, L. Heaton, and K. T. Miller, Acta Cryst. **13**, 828 (1960).
[101] R. A. Young, P. E. Mackie, and R. B. Von Dreele, J. Appl. Cryst. **10**, 262 (1977).
[102] D. B. Wiles and R. A. Young, J. Appl. Cryst. **14**, 149 (1981).
[103] J. K. Yau and S. A. Howard, J. Appl. Cryst. **22**, 244 (1989).
[104] S. A. Howard, J. K. Yau, and H. U. Anderson, J. Appl. Phys. **65**, 1492 (1989).
[105] S. Enzo, G. Fagherazzi, A. Benedetti, and S. Poilizzi, J. Appl. Cryst. **21**, 536 (1988).
[106] A. Benedetti, G. Fagherazzi, S. Enzo, and M. Battagliarin, J. Appl. Cryst. **21**, 543 (1988).
[107] Th. H. de Keijser, E. J. Mittemeijer, and H. C. F. Rozendaal, J. Appl. Cryst. **16**, 309 (1983).
[108] Y. Zhang, J. M. Stewart, C. R. Hubbard, and B. Morosin, Adv. X-Ray Anal. **33**, 373 (1990).
[109] Y. Wang, S. Lee, and Y. Lee, J. Appl. Cryst. **15**, 35 (1982).
[110] V. N. Selivanov and E. F. Smislov, Zavod. Lab. **57**, 28 (1991).
[111] A. Guinier, X-Ray Diffraction, W. H. Freeman, San Francisco (1963) p. 139.
[112] M. Wilkens, J. Appl. Cryst. **12**, 119 (1979).
[113] D. Liu and Y. Wang, Pow. Diffr. **2**, 180 (1987).
[114] A. P. Prudnikov, Yu. A. Brychkov, and O. I. Marichev, Integrals and Series, Vol. 1, Gordon and Breach, Amsterdam, The Netherlands (1986) p. 344.

[115] R. L. Rothman and J. B. Cohen, J. Appl. Phys. **42**, 971 (1971).
[116] T. Adler and C. R. Houska, J. Appl. Phys. **50**, 3282 (1979).
[117] C. R. Houska and T. M. Smith, J. Appl. Phys. **52**, 748 (1981).
[118] S. Rao and C. R. Houska, Acta Cryst. A **42**, 14 (1986).
[119] J. I. Langford, R. Delhez, Th. H. de Keijser, and E. J. Mittemeijer, Aust. J. Phys. **41**, 173 (1988).
[120] J. I. Langford, J. Appl. Cryst. **15**, 315 (1982).
[121] M. J. Turunen, Th. H. de Keijser, R. Delhez, and N. M. van der Pers, J. Appl. Cryst. **16**, 176 (1983).
[122] A. J. C. Wilson, Acta Cryst. **23**, 888 (1967).
[123] A. J. C. Wilson, Acta Cryst. A **24**, 478 (1968).
[124] A. J. C. Wilson, Acta Cryst. A **25**, 584 (1969).
[125] G. Gagliotti, A. Paoletti, and F. P. Ricci, Nucl. Instrum. **3**, 223 (1958).
[126] J. I. Langford, R. J. Cernik, and D. Louër, J. Appl. Cryst. **24**, 913 (1991).
[127] J. I. Langford, in Accuracy in Powder Diffraction II, preprint.
[128] A. J. C. Wilson, Mathematical Theory of X-Ray Powder Diffractometry, Centrex, Eindhoven, The Netherlands (1963).
[129] J. I. Langford, Prog. Cryst. Growth and Charact. **14**, 185 (1987).
[130] T. G. Fawcett, C. E. Crowder, S. J. Brownell, Y. Zhang, C. R. Hubbard, W. Schreiner, G. P. Hamill, T. C. Huang, E. Sabino, J. I. Langford, R. Hamilton, and D. Louër, Pow. Diffr. **3**, 209 (1988).
[131] W. L. Smith, J. Appl. Cryst. **9**, 187 (1976).
[132] J. I. Langford and D. Louër, J. Appl. Cryst. **15**, 20 (1982).
[133] Fl. Popescu and L. Benes, Acta Cryst. A **33**, 323 (1977).
[134] P. Păuşeşcu, R. Mănăilă, M. Popescu, and E. Jijovici, J. Appl. Cryst. **7**, 281 (1974).
[135] P. F. Bley, Y. Calvayrac, and M. Fayard, J. Appl. Cryst. **7**, 493 (1974).
[136] B. Moraweck, Ph. de Montgolfier, and A. J. Renouprez, J. Appl. Cryst. **10**, 191 (1977).
[137] A. Le Bail and D. Louër, J. Appl. Cryst. **11**, 50 (1978).
[138] D. R. Buchanan, R. L. McCullough, and R. L. Miller, Acta Cryst. **20**, 922 (1966).
[139] P. Suortti and L. D. Jennings, Acta Cryst. A **33**, 1012 (1977).
[140] J. B. Cohen and C. N. J. Wagner, J. Appl. Phys. **33**, 2073 (1962).
[141] A. Bianconi, J. Budnick, A. M. Flank, A. Fontaine, P. Lagarde, A. Marcelli, H. Tolentino, B. Chamberland, C. Michel, B. Raveau, and G. Demazeau, Phys. Lett. A **127**, 285 (1988).
[142] K. Fueki, K. Kitazawa, K. Kishio, T. Hasegawa, S. Uchida, H. Takagi, and S. Tanaka, in Chemistry of High-Temperature Superconductors, D. L. Nelson, M. S. Whittingham, and T. F. George, eds., American Chemical Society (1987) p. 38.
[143] T. Fujita, Y. Aoki, Y. Maeno, J. Sakurai, H. Fukuba, and H. Fujii, J. Appl. Phys. **26**, L368 (1987).
[144] R. M. Hazen, in Physical Properties of High-T_c Superconductors, Vol. 2, D. M. Ginsberg, ed., World Scientific, Singapore (1990) p. 121.
[145] J. B. Torrance, A. Bezinge, A. I. Nazzal, T. C. Huang, S. P. Parkin, D. T. Keane, S. J. LaPlaca, P. M. Horn, and G. A. Held, Phys. Rev. B **40**, 8872 (1989).
[146] J. D. Axe, A. H. Moudden, D. Hohlwein, D. E. Cox, K. M. Mohanty, A. R. Moodenbaugh, and Y. Xu, Phys. Rev. Lett. **62**, 2751 (1989).
[147] T. Suzuki and T. Fujita, Physica C **159**, 111 (1989).
[148] T. Fujita and Y. Maeno, in Superconducting Materials, JJAP, Series 1 (1988) p. 34.
[149] A. Roshko and Y.-M. Chiang, J. Appl. Phys. **66**, 3710 (1989).
[150] D. E. Cox, S. C. Moss, R. L. Meng, P. H. Hor, and C. W. Chu, J. Mater. Res. **3**, 1327 (1988).
[151] B. Crist and J. B. Cohen, J. Polym. Sci. **17**, 1001 (1979).
[152] H. Ledbetter, S. Kim, and A. Roshko, Z. Phys. B **89**, 275 (1992).
[153] R. D. Shannon and C. T. Prewitt, Acta Cryst. B **25**, 925 (1969).
[154] M. Lang, H. Spille, F. Steglich, Y. Hidaka, T. Murakami, and Y. Endoh, Physica C **162-164**, 1037 (1989).
[155] Y. Hidaka and T. Murakami, Phase Trans. **15**, 241 (1989).
[156] P. L. Gai and E. M. McCarron, Science **247**, 553 (1990).
[157] T. Kamiyama, I. Izumi, H. Asano, H. Takagi, S. Uchida, Y. Tokura, E. Takayama-Muromachi, M. Matsuda, K. Yamada, Y. Endoh, and Y. Hidaka, Physica C **172**, 120 (1990).
[158] A. Kapitulnik, Physica C **153–155**, 520 (1988).
[159] L. A. Muradyan, V. N. Molchanov, R. A. Tamazyan, and V. I. Simonov, Physica C **162–164**, 536 (1989).
[160] P. Day, M. Rosseinsky, K. Prassides, W. I. F. David, O. Moze, and A. Soper, J. Phys. C **20**, L429 (1987).
[161] J. T. Lewandowski, R. A. Beyerlein, J. M. Longo, and R. A. McCauley, J. Amer. Ceram. Soc. **69**, 699 (1986).
[162] R. Ramesh, G. van Tendeloo, G. Thomas, S. M. Green, Y. Mei, C. Jiang, and H. L. Luo, Appl. Phys. Lett. **53**, 2220 (1988).
[163] J. Schneck, L. Pierre, J. C. Tolédano, and C. Daguet, Phys. Rev. B **39**, 9624 (1989).
[164] O. Eibl, Physica C **168**, 215 (1990).
[165] W. Carrilo-Cabrera and W. Göpel, Physica C **161**, 373 (1989).
[166] P. Bordet, J. J. Capponi, C. Chaillout, J. Chenavas, A. W. Hewat, E. A. Hewat, J. L. Hodeau, M. Marezio, J. L. Tholence, and D. Tranqui, Physica C **156**, 189 (1988).
[167] R. Ramesh, K. Remschnig, J. M. Tarascon, and S. M. Green, J. Mater. Res. **6**, 278 (1991).
[168] Z. Hiroi, Y. Ikeda, M. Takano, and Y. Bando, J. Mater. Res. **6**, 435 (1991).
[169] Y. Inoue, M. Hasegawa, Y. Shichi, I. Munakata, M. Yamanaka, S. Hiyama, and O. Nittono, J. Mater. Res. **5**, 737 (1990).
[170] R. Ramesh, B. G. Bagley, J. M. Tarascon, S. M. Green, M. L. Rudee, and H. L. Luo, J. Appl. Phys. **67**, 379 (1990).
[171] X. B. Kan, J. Kulik, P. C. Chow, S. C. Moss, Y. F. Yan, J. H. Wang, and Z. X. Zhao, J. Mater. Res. **5**, 731 (1990).
[172] G. S. Pawley, J. Appl. Cryst. **13**, 630 (1980).
[173] H. Toraya, J. Appl. Cryst. **19**, 440 (1986).
[174] L. Lutterotti and P. Scardi, J. Appl. Cryst. **23**, 246 (1990).

About the author: Davor Balzar is with Faculty of Metallurgy of the University of Zagreb, Sisak, Croatia and was a Guest Researcher at NIST. The National Institute of Standards and Technology is an agency of the Technology Administration, U.S. Department of Commerce.

Volume 98, Number 3, May–June 1993
Journal of Research of the National Institute of Standards and Technology

[J. Res. Natl. Inst. Stand. Technol. 98, 355 (1993)]

Evaluation of Serum Volume Losses During Long-Term Storage

Volume 98 | Number 3 | May–June 1993

Neal E. Craft, Katherine S. Epler, Therese A. Butler, Willie E. May, and Regina G. Ziegler[1]

National Institute of Standards and Technology,
Gaithersburg, MD 20899-0001

Aliquots of serum collected in a large case-control study of cervical cancer were stored at −70 °C for up to 4 years during implementation of the study. When 500 μL serum aliquots were thawed in preparation for carotenoid and vitamin A assays, volumes were noticeably variable and fell below 500 μL in the majority of the samples. We were concerned about evaporation/sublimation during storage of the samples because loss of water would concentrate the analytes of interest. We evaluated the use of density and sodium ion concentration measurements to confirm its occurrence. We found that serum density was an unreliable indicator of extent of volume loss since the anticipated increases in density due to evaporation were of the same magnitude as inter-individual variation in serum density. In contrast, Na^+ concentration is tightly regulated and would rise if water had been lost from the samples. In a representative sample of serum aliquots from the case-control study, 24 of 25 vials contained less than 500 μL of serum. The mean sodium ion concentration (138.1 ± 3.6 mmol/L) was within the normal range for human serum of 136–145 mmol/L, and no correlation was observed between serum volume and Na^+ concentration. These results strongly suggest that the observed low volumes were not due to evaporative losses. Instead, the variably low volumes of serum aliquots were probably due to pipetting errors in the initial aliquotting resulting from the use of air-displacement pipettes.

Key words: density; long-term storage; serum; sodium; sublimation; volume loss.

Accepted: January 11, 1993

1. Introduction

To study the determinants of disease in human populations, epidemiologists are increasingly relying on biochemical measurements in human tissues, such as blood, to complement information obtained by interviews. "Molecular epidemiology" requires reliable methods for sampling and storing biological materials collected from large numbers of individuals in the field. For example, in a prospective epidemiologic study, blood may be collected from a healthy group of people, and the cohort followed over time. When a sufficient number of diagnoses or deaths have occurred in the cohort, which may require many years, the blood samples collected earlier can be compared for the cases and a subset of the non-cases matched to the cases. Aliquots of the stored blood are thawed and assayed for molecules of interest, such as nutrients, hormones, viral markers, putative carcinogens, etc.

[1] Environmental Epidemiology Branch, Epidemiology and Biostatistics Program, Division of Cancer Etiology, National Cancer Institute, Bethesda, MD 20892.

Alternatively, in a retrospective epidemiologic study, patients with a particular disease are identified, comparable controls are selected, and blood samples can be collected and compared for the cases and controls. Aliquots of the blood often need to be stored for several years until sufficient numbers of subjects are identified so that assays can be run consecutively on all samples with tight quality control. In both types of epidemiologic studies, blood is often collected under non-optimal conditions, such as at the home, workplace, or neighborhood clinic, to maximize subject participation.

In a large case-control study of cervical cancer conducted in five areas of the United States [1,2], blood to be assayed for micronutrients believed to be involved in the etiology of this cancer was collected from 1023 subjects. Blood was drawn at least 6 mo after completion of surgery or other treatment for cervical cancer to allow dietary patterns, appetite, and metabolism to revert to normal. Aliquots of serum were prepared, mixed with any reagents necessary to stabilize analytes of interest, and stored at −70 °C for up to 4 yr while the study was being conducted. When 500 μL serum aliquots were defrosted in preparation for carotenoid and vitamin A assays, volumes were noticeably variable and tended to be less than 500 μL in the majority of the samples. We were concerned about evaporation/sublimation during storage because a loss of water would have concentrated the analytes. Other workers have reported losses from polypropylene bottles to be 0.26% [3] and 0.27% [4] per year at room temperature. This low percentage can be of significance when very small initial sample volumes are involved. Such samples would have a much higher relative surface area than larger volumes would have. Another group of workers has discussed evaporative losses from open autosampler cups, and has expressed surprise that the clinical literature has failed to discuss this problem fully [5]. Here we describe the use of serum density and sodium ion (Na^+) concentration to determine whether evaporative volume loss occurred from polypropylene cryovials during long-term storage at −70 °C.

2. Materials and Methods

2.1 Specimens

Twenty-five of the samples were 500 μL aliquots of serum from subjects in a case-control study of cervical cancer (study samples). Blood had been collected from the participating subjects by a single trained phlebotomist. After centrifugation serum was aliquoted with a 0.1 to 1.0 mL adjustable-volume, air-displacement pipet into 1.2 mL polypropylene cryovials with inside-thread screw stoppers and silicone gaskets. The samples had been stored in a −70 °C frost-free freezer for 4–5 yr prior to this analysis. In addition, ten samples were tested from each of two serum pools (QC1 and QC2), prepared with known amounts of specific micronutrients to monitor quality control. Approximately 500 μL of each of the QC pools had been aliquoted with an automatic dispenser into similar 1.2 mL cryovials and stored at −70 °C for 4 yr prior to this analysis. One individual aliquotted the study samples; a second individual aliquotted the QC samples. The QC samples were included in this volume-loss study because each set came from one serum pool. Therefore, the parameter being measured, either density or Na^+ concentration, should have been the same for each of the ten samples in the set if no evaporation or sublimation had occurred. If, however, such a loss had occurred, the differences between results for these samples would have been noticeable since the volumes of serum in these cryovials were also variable, suggesting that if evaporation/sublimation had indeed occurred, it had not been at the same rate for all cryovials.

2.2 Density

Serum samples were thawed at room temperature with screw caps on and were then centrifuged at $1000 \times g$ for 5 min to force condensation on the cap down to the bottom of the tube. Sample volumes were measured to ±1% using a calibrated 500 μL gas-tight syringe. Each sample was weighed to ±2 mg using an electronic balance. The density of each serum sample was calculated by dividing the weight by the volume.

2.3 Sodium Ion Concentration

Na^+ concentration was determined by flame atomic emission spectroscopy (FAES) using a modification of the NIST reference method for the determination of sodium in serum [6]. Briefly, the samples were gently mixed, and a 200 μL aliquot of each sample was diluted 1:100 with KCl diluent (4.5 mmol/L). Following calibration and method verification using NIST SRM 909: Freeze-dried Human Serum, Na^+ was measured by FAES at 589 nm. The precision of the method is estimated at ±1% with a bias of less than 1.5%.

2.4 Statistical Analysis

Linear regression analysis was performed with the data from the cervical cancer samples to determine the correlation coefficients (r) for density vs volume and Na^+ concentration vs volume. Differences in volume, density, and Na^+ concentration among the three groups of samples were determined by analysis of variance using General Linear Models[2] (SAS, Cary, NC) [7].

3. Results

3.1 Serum Volume and Density

The volume of 24 of the 25 study samples was less than 500 μL, ranging from 305 to 470 μL. This range as well as the mean density, Na^+ range, and mean Na^+ concentrations are provided in Table 1. Twenty-five percent of the samples contained less than 406 μL; 50%, less than 430 μL; and 75%, less than 465 μL. By contrast, the volume of the 10 QC1 samples ranged from 495 to 515 μL; and the 10 QC2 samples ranged from 410 to 440 μL. The mean volumes were significantly different ($p < 0.001$) among the three groups. The correlation coefficient between density and volume was −0.296 for the study samples (Fig. 1). QC sera were not included in the linear regression analysis since they are aliquots of the same sera, and the QC sera were not necessarily representative of normal sera.

3.2 Sodium Ion Concentration

The Na^+ concentrations for the 10 QC1 samples were essentially the same (146.6 ± 1.3 mmol/L); likewise the QC2 samples were not different from each other (140.4 ± 1.3 mmol/L). The mean of the QC2 group was within the normal range of human serum Na^+ concentrations of 136–145 mmol/L [8]. The mean Na^+ concentration of QC1 was approximately 1% above the normal range. The range of Na^+ concentrations in the samples from the 25 case-control study subjects was wider (127.4–142.9 mmol/L) than the range for either QC series; the mean concentration (138.1 ± 3.6 mmol/L) was within the normal range. As illustrated in Fig. 2, no correlation ($r = 0.095$) was found between Na^+ concentration and volume in the study samples.

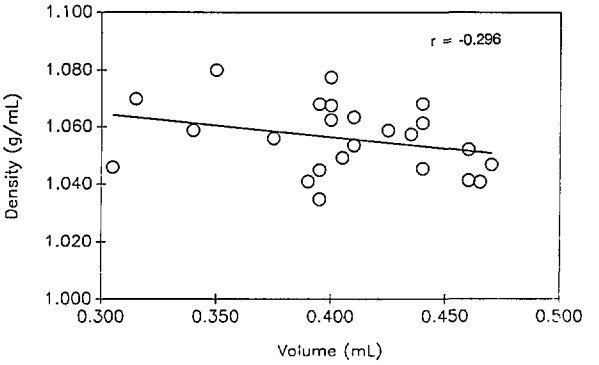

Fig. 1. Scatterplot of density and volume for 25 serum samples stored at −70 °C for 4–5 yr, from participants in a case-control study of cervical cancer.

4. Discussion

We investigated the cause of apparent volume losses during long-term serum sample storage at −70 °C by measuring density and Na^+ concentration. In preliminary studies of the density of lyophilized sera reconstituted with graded volumes of water, we were able to establish a linear relationship between density and volume over the range of 60 to 100% of the original serum volume. However, density is not a very sensitive indicator of volume loss in serum since the concentration of

Table 1. Volumes actually present in the cryovials, mean density, and the mean and range of the Na^+ concentration

	Density (g/mL)	Volume (μL)	Na^+ Range (mmol/L)	Na^+ (mmol/L)
Study samples	1.056 ± 0.012	305 to 470	127.4 – 142.9	138.1 ± 3.6
QC1	1.051 ± 0.007	495 to 515	144.6 – 147.7	146.6 ± 1.3
QC2	1.052 ± 0.013	410 to 440	138.9 – 142.8	140.4 ± 1.3
Expected		500	136 – 145	

[2] Certain commercial equipment, instruments, or materials are identified in this paper to specify adequately the experimental procedure. Such identification does not imply recommendation or endorsement by the National Institute of Standards and Technology, nor does it imply that the materials or equipment identified are necessarily the best available for the purpose.

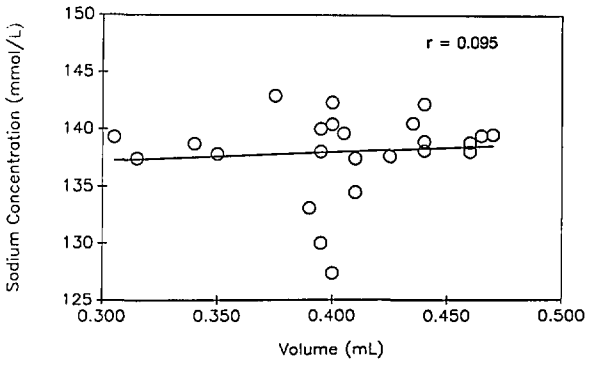

Fig. 2. Scatterplot of Na^+ concentration and volume for the same 25 samples described in Fig. 1.

serum solutes is low and thus the density of serum does not differ greatly from the water that may be evaporating from it. A 20% change in serum volume was required to produce a 1% change in density. The density of normal serum varies by 1–2% [8], which makes density an unreliable measure of evaporative volume loss.

The density of the study samples varied from 1.035 to 1.078 g/mL. This ±2% range in density would be equivalent to ±40% differences in volume, (i.e., 4% change in density=80% change in volume). There was a slight inverse correlation ($r = -0.296$) between density and volume in the study samples, which might indicate minor evaporation or sublimation losses. The occurrence of serum volume losses during storage of samples is a plausible explanation for the increases in measured concentrations of serum retinol reported by Parkinson and Gal [9].

Serum Na^+ concentration is very tightly regulated [8,10]. Since Na^+ concentration varies inversely and proportionately with volume loss, the measurement of Na^+ concentration could provide a sensitive means of determining whether consistently low serum volumes might be due to actual volume loss during storage or to pipetting errors. Due to the stability of inorganic ions, this approach also offered a possible means of correcting for volume losses in stored serum samples if such losses occurred. The absence of correlation between Na^+ concentration and volume (Fig. 2) does not support the hypothesis that evaporation or sublimation caused the reduced sample volumes. Among the study samples, only four had Na^+ concentrations outside the normal range. The Na^+ concentrations for all four study samples were lower than the norm, again refuting the possibility that evaporative losses might be responsible for low sample volumes. Thus, pipetting errors were probably responsible for the range of volumes observed.

The mean volume of the QC1 samples was not significantly less than the expected 500 μL, and the mean Na^+ concentration was only slightly above the normal range indicating that volume losses had not occurred in this group of sera. The mean volume of the QC2 samples was significantly less than the expected 500 μL, but the volumes fell within a narrow range. In spite of the low volumes, the mean Na^+ concentration of these sera was also normal. Had the 17% reduction in volume been due to evaporative losses, the Na^+ concentration would have been elevated by a corresponding 17%. In another set of QC2 samples used in a preliminary study the Na^+ concentration was similar and the mean volume was very close to the expected 500 μL. These results may indicate that the dispensing pipette had been incorrectly calibrated for a portion of the QC2 samples.

This exercise indicates that the variably low volumes observed in this study were not due to sample evaporation or sublimation during storage. It also indicates that accurate dispensing, assumed to occur in such studies, may not take place. In some studies aliquotting may not be crucial, e.g., when an accurately measured aliquot is subsequently removed and used for analysis. However, in other studies, dispensing of accurate volumes is critical. Such is the case when an aliquot of serum is added to a measured volume of a solution designed to stabilize the analyte of interest, e.g., the addition of metaphosphoric acid to sera to be analyzed for vitamin C. Unless a tightly regulated serum component, such as Na^+, is measured to normalize the measurements, a sizeable error could occur. This potential source of error could be greatly reduced if positive-displacement pipettes were used to aliquot viscous fluids such as serum. Air-displacement pipettes are designed for accurate and precise measurement of solutions with a density and viscosity similar to water. However, with viscous fluids, air-displacement pipettes fill and expel incompletely. Errors resulting from incomplete expulsion can be minimized by reversed-mode pipetting, but this is not as convenient as using a positive-displacement pipette. The piston in a positive-displacement pipette comes into contact with the sample, wiping the inside of the plastic pipette tip and making expulsion complete. Because of this contact, the piston must be rinsed or replaced to eliminate carryover errors. Variation in these mass-produced pistons causes the positive-displacement

pipette to be inherently less precise than air-displacement pipettes, because the piston in the air-displacement pipette is permanent. Nevertheless the positive-displacement pipette is more accurate and precise than the air-displacement pipette when measuring viscous solutions.

In summary, using serum Na^+ concentrations, we have established that variable low volumes observed during long-term sample storage were not due to evaporation or sublimation but were more likely due to pipetting errors that occurred during the initial sample preparation.

Acknowledgments

This work was supported in part by the National Cancer Institute, Division of Cancer Etiology, agreement #Y01-CP9-0513. We thank Dr. Stephen Wise for his helpful suggestions during the preparation of the manuscript.

5. References

[1] R. G. Ziegler, L. A. Brinton, R. F. Hamman, H. F. Lehman, R. S. Levine, K. Mallin, S. A. Norman, J. F. Rosenthal, A. C. Trumble, and R. N. Hoover, Am. J. Epidemiol. **132**, 432 (1990).
[2] R. G. Ziegler, C. J. Jones, L. A. Brinton, S. A. Norman, K. Mallin, R. S. Levine, H. F. Lehman, R. F. Hamman, J. F. Rosenthal, A. C. Trumble, and R. N. Hoover, Cancer Causes Control **2**, 17 (1991).
[3] G. J. Curtis, J. E. Rein, and S. S. Yamamura, Anal. Chem. **45**, 996 (1973).
[4] J. R. Moody and R. M. Lindstrom, Anal. Chem. **49**, 2264 (1977).
[5] C. A. Burtis, J. M. Begovich, and J. S. Watson, Clin. Chem. **21**, 1907 (1975).
[6] R. A. Velapoldi, R. C. Paule, R. Schaffer, J. Mandel, and J. R. Moody, Natl. Bur. Stand. (U.S.) Special Publication 260-60, 1978.
[7] SAS user's guide, J. T. Helwig and K. A. Council, eds., SAS Institute, Inc., Cary, NC (1982).
[8] Harper's Biochemistry, R. K. Murray, D. K. Granner, P. A. Mayes, and V. W. Rodwell, eds., Appleton and Lange, Norwalk, CT (1988).
[9] C. Parkinson and I. Gal, Clin. Chim. Acta **40**, 83 (1972).
[10] E. K. Harris, P. Kanofsky, G. Shakarji, and E. Cotlove, Clin. Chem. **16**, 1022 (1970).

About the authors: *Neal E. Craft is a biologist and Katherine S. Epler is a chemist in the Organic Analytical Research Division; Therese A. Butler is a chemist in the Inorganic Analytical Research Division; and Willie E. May is the Chief of the Organic Analytical Research Division of the NIST Chemical Science and Technology Laboratory. Regina G. Ziegler is a nutritional epidemiologist in the Division of Cancer Etiology of the Environmental and Epidemiology Branch at the National Cancer Institute. The National Institute of Standards and Technology is an agency of the Technology Administration, U.S. Department of Commerce.*

Volume 98, Number 3, May–June 1993
Journal of Research of the National Institute of Standards and Technology

[J. Res. Natl. Inst. Stand. Technol. 98, 361 (1993)]

Dependence of Quantized Hall Effect Breakdown Voltage on Magnetic Field and Current

Volume 98 Number 3 May–June 1993

M. E. Cage

National Institute of Standards and Technology,
Gaithersburg, MD 20899-0001

When large currents are passed through a high-quality quantized Hall resistance device the voltage drop along the device is observed to assume discrete, quantized states if the voltage is plotted versus the magnetic field. These quantized dissipative voltage states are interpreted as occurring when electrons are excited to higher Landau levels and then return to the original Landau level. The quantization is found to be, in general, both a function of magnetic field and current. Consequently, it can be more difficult to verify and determine dissipative voltage quantization than previously suspected.

Key words: breakdown; inter-Landau level scattering; quantized dissipation; quantized voltage states; quantum Hall effect; two-dimensional electron gas.

Accepted: March 30, 1993

1. Introduction

The integer quantum Hall effect [1] occurs when current is passed through a two-dimensional electron gas (2DEG) formed in a semiconductor device which is cooled to very low temperatures in the presence of a large magnetic field. The Hall resistance R_H of the ith plateau of a fully quantized 2DEG assumes the values $R_H(i)=h/(e^2i)$, where h is the Planck constant, e is the elementary charge, and i is an integer. In high-quality devices the current flow within the 2DEG is nearly dissipationless in the plateau regions for currents around 25 μA. At high currents, however, energy dissipation can suddenly appear in these devices [2,3]. This is called breakdown of the quantum Hall effect.

The dissipative breakdown voltage V_x can be detected by measuring voltage differences between potential probes placed on either side of the device in the direction of current flow. Cage et al. [3] had found that there is a distinct set of dissipative V_x states in wide samples, with transient switching observed on microsecond time scales among those states. Bliek et al. [4] proposed the existence of a new quantum effect to explain the breakdown structures in their curves of V_x versus magnetic field for samples with narrow constrictions. Their phenomenological model presumed that the structures were quantized in resistance, rather than voltage. Cage et al. [5] then found that, in wide samples, the distinct states are quantized in voltage. Hein et al. [6] have now observed dissipative voltages during breakdown of the quantum Hall effect in wide samples, but did not confirm that these voltage states are quantized. We show in this paper that the voltage is indeed quantized, but that the quantization is more complicated than previously suspected because, in general, it is a function of both the magnetic field and the current. Some of the data presented here were described with less detail in an earlier paper [7].

2. Experiment

2.1 Sample

Our sample is a GaAs/$Al_xGa_{1-x}As$ heterostructure grown by molecular beam epitaxy with $x=0.29$. It is designated as GaAs(7), has a zero magnetic field mobility of 100,000 $cm^2/(V\cdot s)$ at 4.2 K, exhibits excellent integral quantum Hall effect properties, and is the device most frequently used as the United States resistance standard. The inset of Fig. 1 shows the geometry of this sample. It is 4.6 mm long and 0.4 mm wide. The two outer Hall potential probe pairs are displaced from the central pair by ± 1 mm. The magnetic field is perpendicular to the sample; its direction is such that probes 2, 4, and 6 are near the source potential S, which is grounded. Probes 1, 3, and 5 are near the potential of the drain D. The dissipative voltages V_x for this paper were measured between potential probe pair 2 and 4, hereafter denoted as $V_x(2,4) \equiv V_x(2) - V_x(4)$.

2.2 Data

Figure 1 shows sweeps of $V_x(2,4)$ versus the magnetic field B for the $i=2$ (12,906.4 Ω) quantized Hall resistance plateau at a temperature of 1.3 K and a current, I, of +210 μA, where positive current corresponds to electrons entering the source and exiting the drain. This current is approaching the 230 μA critical current value for this plateau at which V_x never reaches zero for these particular potential probes. One of two distinct paths always occurred for positive current when magnetic field sweeps were made in the direction of increasing B. Those distinct paths are labeled 1 and 2 in the figure. This path "bifurcation" is unusual. It occurred only for the $V_x(2,4)$ probe pair at positive current, and only for the $i=2$ plateau. A pronounced hysteresis was observed when magnetic field sweeps were made in the opposite direction; this path is indicated by the dashed line, labeled 3. The dashed-line curve was repeatable for all sweeps with decreasing B, varying only slightly for the value of B at which V_x again rose to path 1. The fact that V_x is zero over such a large magnetic field region for path 3 indicates the existence of a dissipationless state between 11.2–12.2 T.

Figure 2 shows eight consecutive sweeps of $V_x(2,4)$ versus an increasing B over a magnified region on the low magnetic field side of V_x minimum at +210 μA. Four of the sweeps happened to be

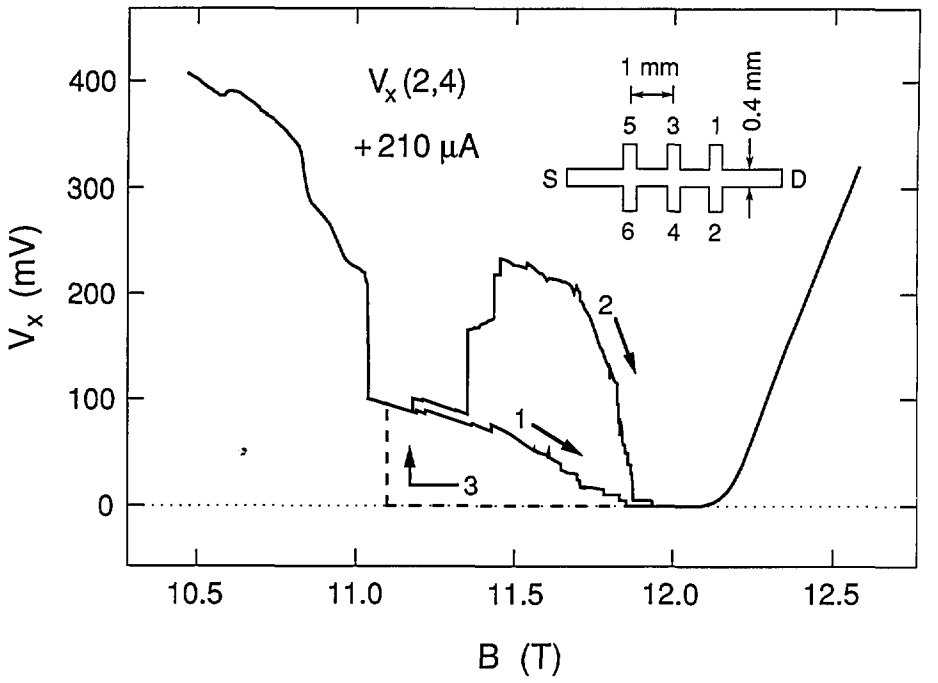

Fig. 1. Sweeps of $V_x(2,4)$ versus B for the $i=2$ plateau at +210 μA and 1.3 K. Two of the sweeps (paths 1 and 2) are in the increasing B direction. The dashed line (path 3) shows hysteresis for a sweep in the decreasing B direction. The inset displays the sample geometry.

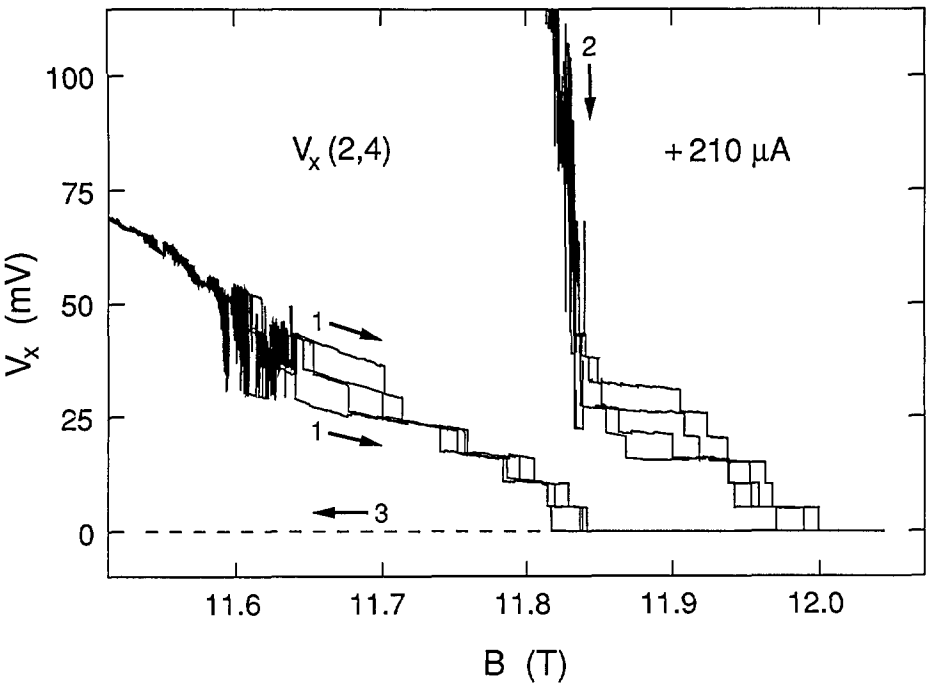

Fig. 2. Eight sweeps of $V_x(2,4)$ versus B at +210 μA for paths 1 and 2, plus a path 3 sweep.

along path 1, forming one family of curves. Another family was generated by the four sweeps over path 2. A ninth sweep is shown for decreasing B along path 3. The data clearly show discrete, well-defined voltage states, with switching between states. The voltage states often have slopes which depend on the magnitude of B. Individual sweeps are not identified in the figure because the magnetic field values at which the states switch have no correlation with sweep number.

Figure 3 shows eight consecutive sweeps of $V_x(2,4)$ for increasing B at −210 μA. No bifurcation was observed for such sweeps. The family of curves is labeled path 4 in the figure. The curves lie between those of paths 1 and 2 at +210 μA. Curves for decreasing B always followed the dashed line of path 3.

The data of Figs. 2 and 3 are combined in Fig. 4 to show the 16 consecutive sweeps for increasing B at ±210 μA and the two identical sweeps for decreasing B. Nothing is unique about these sweeps. Additional sweeps could have been displayed, but at the expense of reducing the overall clarity.

We next demonstrate that the discrete voltage states of Fig. 4 are quantized, and that this quantization is a function of magnetic field. This is done by drawing a family of 20 shaded curves through the data in Fig. 4. The curves have equal (quantized) voltage separations at each value of magnetic field. The quantized voltage separations are, however, allowed to vary with B in order to obtain the best fit to the data. The family of curves was generated by first drawing a set of 20 equally-spaced vertical points at a particular value of B. The lowest point of the vertical set was constrained to be at 0.0 mV because V_x is always zero in the dashed-line sweep of path 3, which indicates that a dissipationless state exists over the magnetic field region of this figure. The spacing between the 19 other vertical points was then varied to obtain the best fit with uniform (equal) voltage intervals. This procedure was repeated for approximately 30 other values of B. Finally, a family of 20 smooth shaded curves was drawn through the corresponding points of every vertical set. The 20 shaded curves, which correspond to a $V_x = 0.0$ mV ground state and 19 excited states, are labeled in brackets as [0] through [19]. The voltage separation (quantization) varies between 5.22 and 7.85 mV over the magnetic field range of this figure.

The breakdown activity shown in Fig. 4 is confined to the region between, but not including, the Hall probe pairs 1,2 and 3,4 of Fig. 1. This was demonstrated by measuring the quantum Hall voltages of both Hall probe pairs at this current. The resulting curves of both probe pairs had struc-

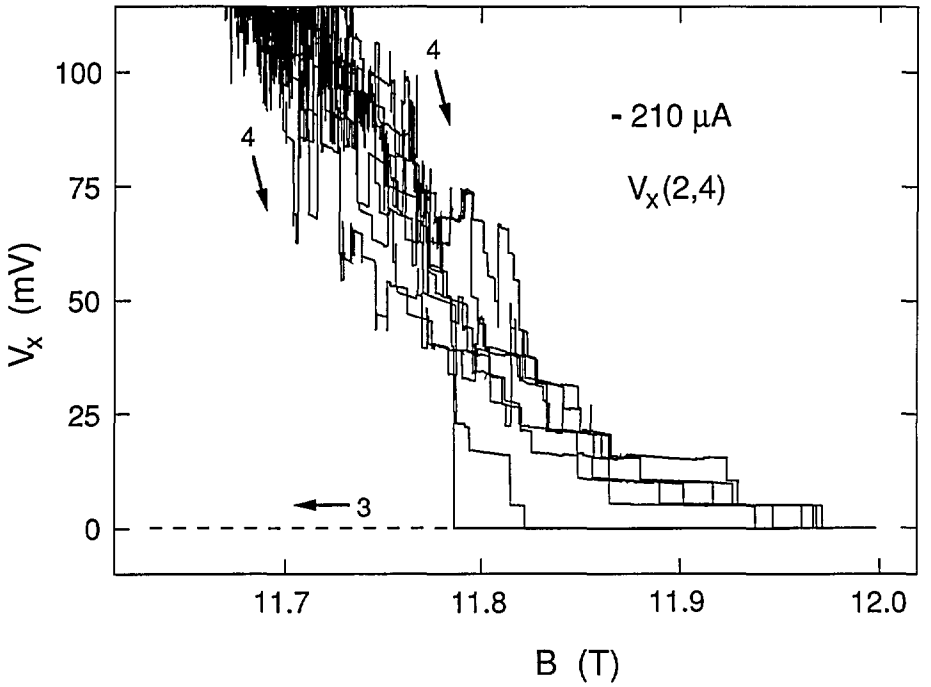

Fig. 3. Eight sweeps of $V_x(2,4)$ versus B at -210 μA for path 4, and a path 3 sweep.

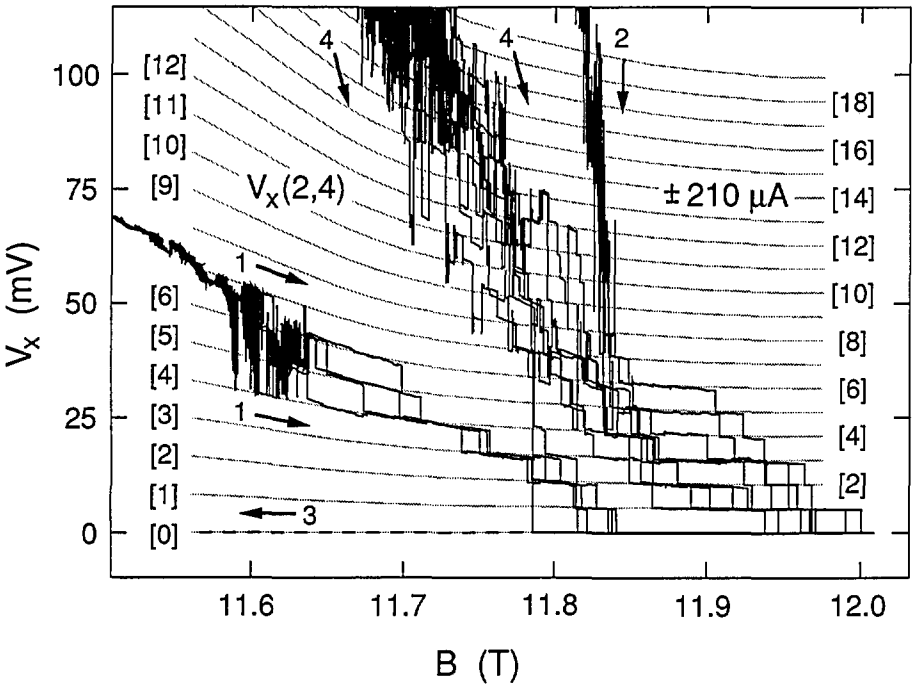

Fig. 4. Combination of the data in Figs. 2 and 3 at ±210 μA. A family of 20 shaded curves is fitted to these data. Refer to Sec. 2.2 for an explanation of how the shaded curves were generated. The voltage quantization numbers are shown in brackets.

tures with deviations of only about ±0.1 mV from the expected ±2,710.3 mV quantum Hall voltage over the plateau region, and therefore were horizontal, straight lines when plotted to the same resolution as in Fig. 4. In addition, the V_x signals were the same on both sides of the sample for probe pairs 1,3 and 2,4.

The higher-lying excited states are difficult to see in the multiple sweeps of Fig. 4 because of switching between states. Figure 5, therefore, shows one of those sweeps along path 4 at −210 μA. It is remarkable that the higher-lying states are just as well-quantized (i.e., well-fitted by the shaded curves) as the lower-lying states. The quantization is by no means perfect. Deviations from the shaded curves do occur, but the overall trend is clear.

2.3 Histograms

Cage et al. [8] and Hein et al. [6] have seen that the V_x signal can sometimes be time-averages of two or more discrete dc voltage levels in which only one level is occupied at a time, but where switching occurs between the levels. Therefore, histograms were made to ensure that the signals in Fig. 4 were not time-averages of several levels. Each histogram consisted of 16,000 measurements of the V_x signal in a 2.4 s sampling period. Figure 6(a) shows the time-dependence of one such sampling period for a path 4 sweep at 11.77 T; Fig. 6(b) shows the associated histogram. It is referred to as a histogram, rather than a spectrum, because the areas under the peaks do not correspond to the excitation probabilities. One would have to accumulate many histograms to ascertain the excitation probabilities. For example, peaks corresponding to quantum states 7 through 10 appear in Fig. 6, while other histograms at 11.77 T had missing peaks or additional peaks. These histograms never yielded any voltage states other than the ones which appear in Fig. 4. Figure 7(b) shows another histogram for a path 2 sweep at 11.83 T. The time-dependence of that histogram, shown in Fig. 7(a), suggests several discrete voltage states interspersed with noise, but the histogram is actually composed of voltage quantum states 9 through 14. Histograms of all other high-speed measurements also indicated that there are no subdivisions of the displayed states in Fig. 4.

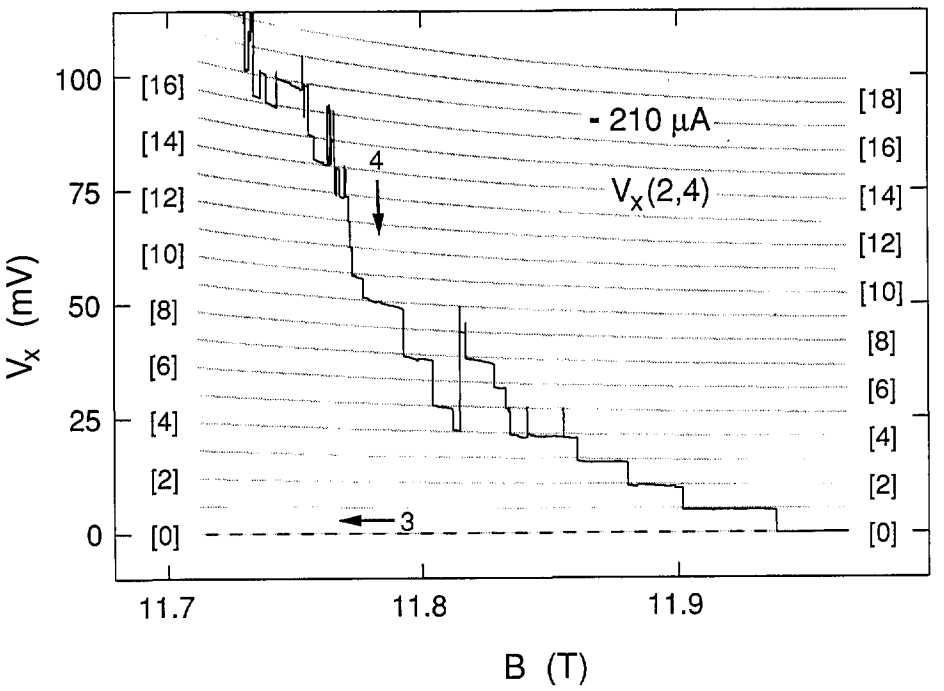

Fig. 5. One of the $V_x(2,4)$ versus B path 4 sweeps shown in Fig. 4.

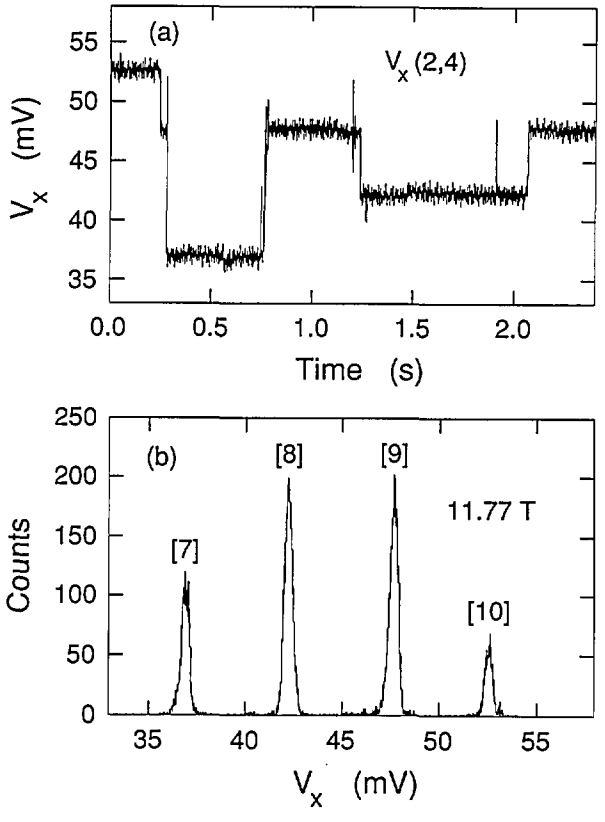

Fig. 6. Histogram for a path 4 sweep at 11.77 T. Section 2.3 explains how the histogram was obtained.

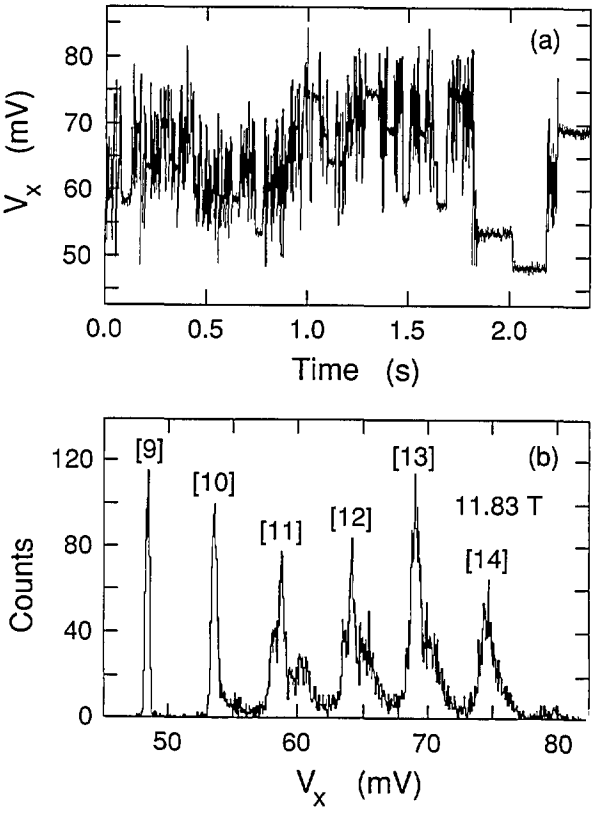

Fig. 7. Histogram for a path 2 sweep at +210 μA and 11.83 T.

2.4 Other Currents

We next investigate the effect of changing the sample current. The smallest current for which breakdown structures could be observed was at −203 μA; no structures were observed, however, at +203 μA. Figure 8 shows data for three successive path 4 sweeps at −203 μA, plus a path 3 sweep. The individual data points displayed near 11.84 T were generated by slowly increasing the magnetic field and selecting data points when the voltage switched to new states. Switching to new states was sometimes induced by momentarily increasing the sample current and then reducing it back to −203 μA. This procedure allowed additional data to be included without sacrificing clarity. Figure 8 also shows 17 shaded curves from the same family used to fit the data displayed in Figs. 4 and 5 at ±210 μA. The excellent fit would suggest that the voltage quantization was a function of magnetic field, but not a function of current. However, it will be seen in Sec. 3.3 that, in general, the voltage quantization is a function of current.

We chose 225 μA as the highest current because the ground state was still occupied. This current approached the 230 μA critical current value at which V_x was still quantized, but never zero. Figure 9 shows five successive sweeps along path 1 and four successive sweeps for path 2 at +225 μA. Note that there is a gradual deviation from zero voltage on the high magnetic field side of the sweeps. Also, interesting features occur on the high field side of the curves at this current. Figure 10 shows four successive path 4 sweeps for increasing magnetic field at −225 μA, as well as a sweep for decreasing magnetic field. That sweep is also labeled path 4 since it follows much of that path; however, it has hysteresis like that of path 3 sweeps where V_x is zero. Many individual path 4 data points, obtained with increasing magnetic field, are also included in Fig. 10 using the procedure described above. Figure 11 combines the data for the two current directions and displays a family of 17 shaded curves which provide the best fit to the data. The ground state begins deviating from zero at 11.97 T, so the lowest point of each vertical set

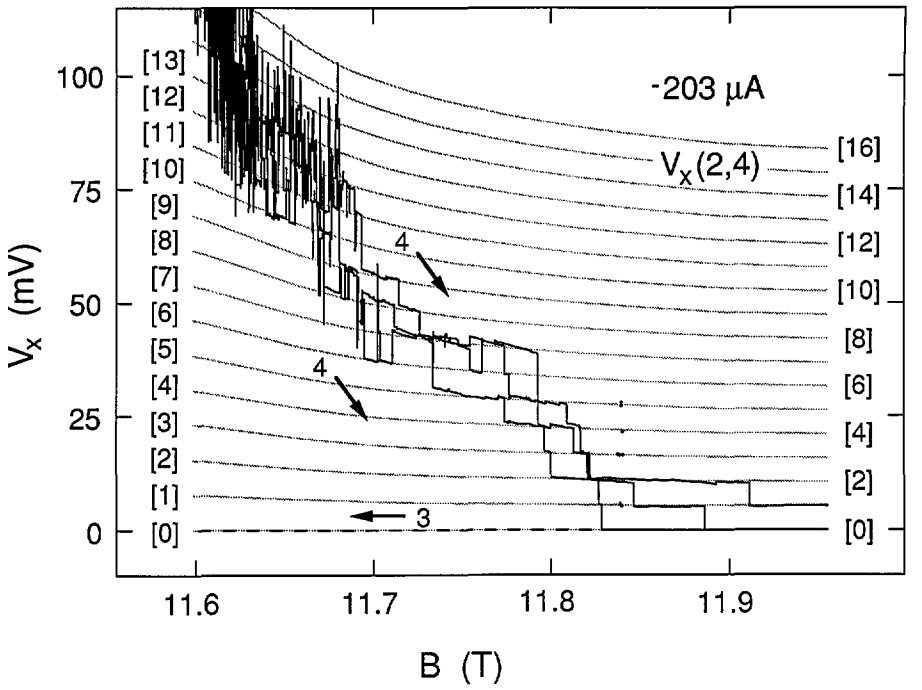

Fig. 8. Three sweeps of $V_x(2,4)$ versus B at -203 μA for path 4, and a path 3 sweep. Sec. 2.4 describes the individual data points at 11.84 T. The shaded curves are the same family used in Fig. 4.

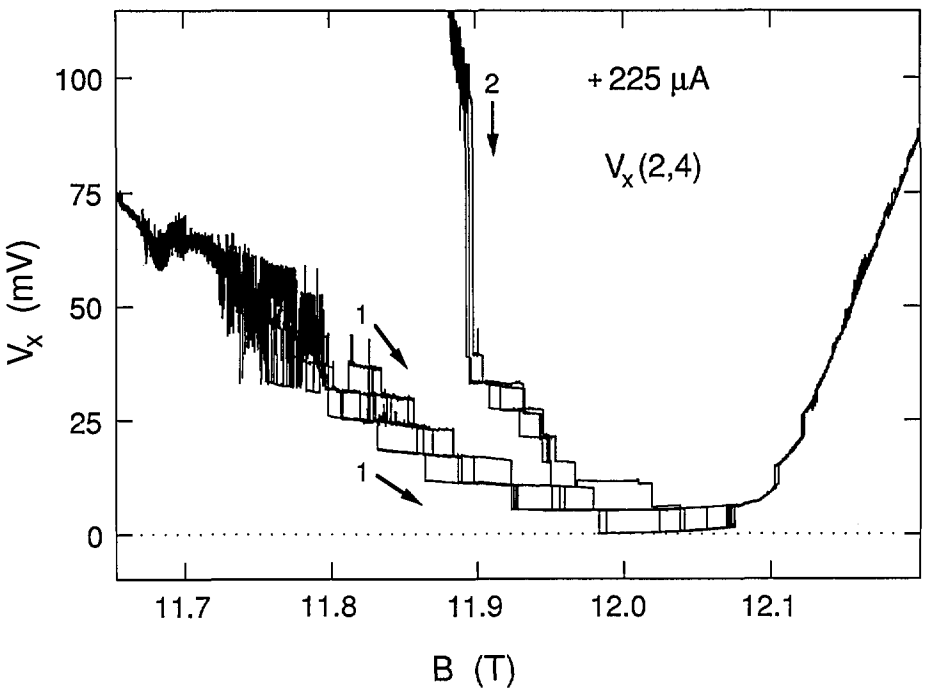

Fig. 9. Five sweeps of $V_x(2,4)$ versus B at $+225$ μA for path 1, and four sweeps for path 2.

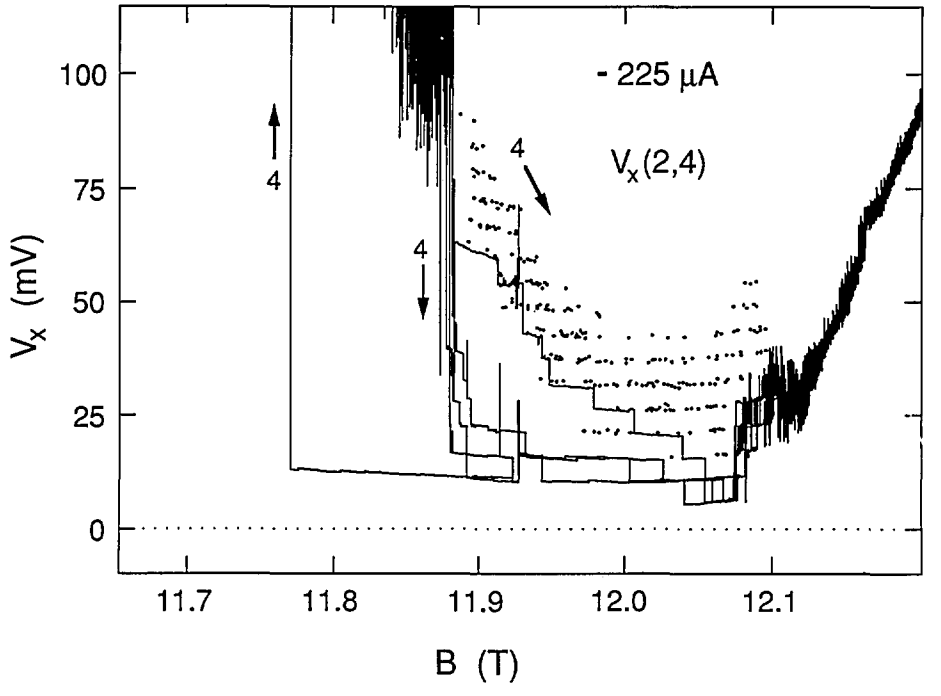

Fig. 10. Four sweeps of $V_x(2,4)$ versus B at -225 μA for path 4 (along with individual data points), and a sweep along path 4 in the opposite direction.

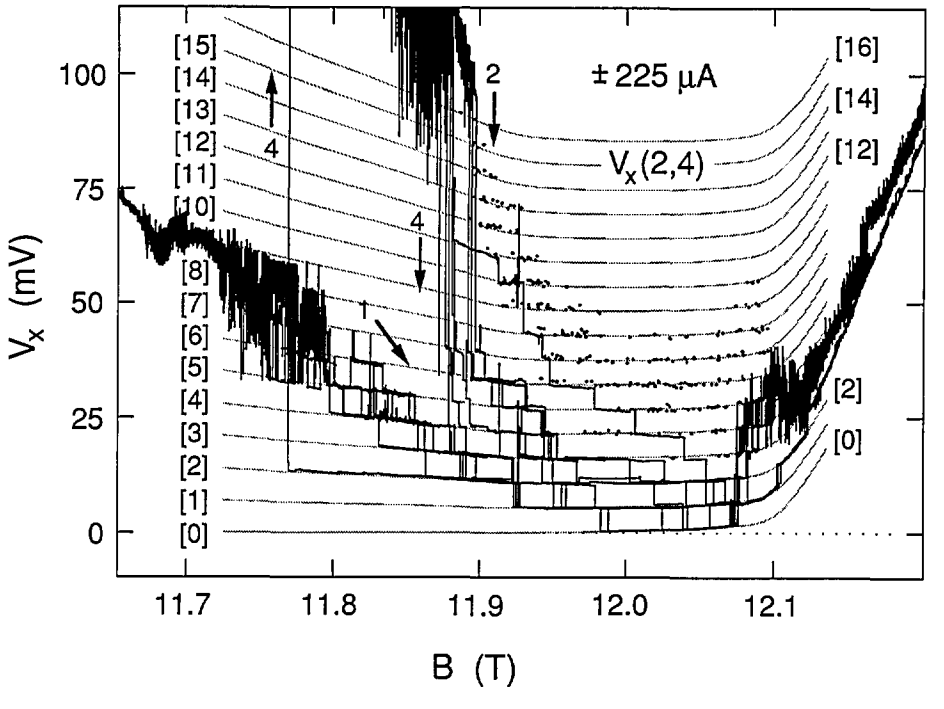

Fig. 11. Combination of the data in Figs. 9 and 10 at ±225 μA. A family of 17 shaded curves is fitted to these data.

of 17 points used to generate the 17 shaded curves was no longer constrained to be zero on the right hand side of the figure. This deviation from zero presumably arises from some other dissipative mechanism. It will be shown in Sec. 3.3 that this family of shaded curves for 225 μA is different than that for 203 and 210 μA.

3. Interpretation

3.1 Microscopic Models

The dissipative voltage states displayed in Figs. 4, 5, 8, and 11 are clearly quantized. We next try to interpret this quantization. Many explanations of breakdown have been proposed. Some mechanisms, such as electron heating instabilities [9] and inhomogeneous resistive channels [10], are inapplicable here since they are classical effects which do not provide quantization. Quantization exists in the quantum Hall effect because the quantized Hall resistance occurs when the conducting electrons in the 2DEG occupy all the allowed states of the lowest Landau levels. It is therefore natural to assume that the quantized dissipation arises from transitions *between* Landau levels.

There are several mechanisms to excite electrons into higher Landau levels that can be considered: (a) the emission of acoustic phonons to conserve energy and momentum, as employed by Heinonen, Taylor, and Girvin [11] and later used in the quasi-elastic inter-Landau level scattering (QUILLS) model of Eaves and Sheard [12], with refinements and extensions by Cage et al. [8]; (b) Zener tunneling [13]; (c) impurity-assisted resonant tunneling [14]; and (d) transitions between edge states [15,16]. To complicate matters, both bulk and edge states exist at high currents [17]. For bulk transitions, a large electric field (of order 10^6 V/m) is required somewhere across the width of the sample [8]; sample impurities and inhomogeneities might provide this high local field. The confining potential provides a high electric field for edge states, but if breakdown is due to edge states then it is difficult to understand why breakdown does not always occur at very low currents since there is probably an insignificant change in the slope of the confining potential with current. In addition to the above considerations, one must also take into account the return of the electrons to the ground state via emission of either photons or optical phonons. Furthermore, the dissipative V_x signals are quite large. Most of this dissipation must occur *outside* the breakdown region, otherwise heating effects would depopulate the electron states within the Landau levels and thereby wash-out the quantization.

3.2 Simple Model

To avoid controversy about which of those microscopic models [8,11–16] satisfy the above considerations and are appropriate, we use a simple model based on energy conservation arguments, and treat the breakdown region between the Hall probe pairs 1,2 and 3,4 as a black box. We assume that the dissipation arises from transitions in which electrons from the originally full Landau levels are excited to states in higher Landau levels and then return to the lower Landau levels. V_x is then the difference in potential between the initial and final states of the lower Landau level. The electrical energy loss per carrier for M Landau level transitions is $M\hbar\omega_c$, where $\omega_c = eB/m^*$ is the cyclotron angular frequency, and m^* is the reduced mass of the electron (0.068 times the free electron mass in GaAs). The power loss is IV_x. If: (a) the ground state involves several filled Landau levels; (b) only electrons in the highest-filled Landau level undergo transitions; and (c) electrons of both spin sublevels of a Landau level undergo the transitions, then $IV_x = r(2/i)M\hbar\omega_c$, where r is the total transition rate and i is the Hall plateau number. Thus

$$fM = \left(\frac{re}{I}\right)M = \left(\frac{i}{2}\right)\left(\frac{m^*}{\hbar}\right)\left(\frac{V_x}{B}\right), \qquad (1)$$

where f is the ratio of the transition rate r within the breakdown region to the rate I/e that electrons transit the device; f can also be interpreted as the fraction of conducting electrons that undergo transitions. Equation (1) is appropriate for even values of i. For odd vales of i, the factor $i/2$ should be replaced by the factor i.

We associate the quantized values of M with the numbers in brackets for the shaded curves in Figs. 4, 5, 8, and 11. I, V_x, and B are measured quantities, and i, m^*, and $\hbar$ are constants. Therefore, f and r can be determined from the V_x versus B plots and Eq. (1) if M is known.

3.3 Analysis

If f and r were constant, then $V_x \propto B$ in Eq. (1), but it is clear from Fig. 4 that this is not the case for these data because the slope of V_x versus B has the opposite sign. Therefore, both f and r must vary with magnetic field. The fractions f (expressed as a percentage) of electrons that make the transitions

in the shaded curves of Fig. 4 were calculated using Eq. (1), and are shown in Fig. 12 at 0.05 T intervals; f varies between 25.7% and 38.8%, corresponding to transition rates between 3.4×10^{14}/s and 5.1×10^{14}/s. Histograms obtained in a previous experiment [5] yielded 26.5% for the value of f in the vicinity of 11.75 T, whereas Fig. 12 indicates that f is 29.3% at 11.75 T. The apparent discrepancy arises because the position of the V_x minimum varies slightly with B on each cool-down. The minimum position was about 0.06 T higher for the present cool-down, giving 27.8% for f at 11.81 T, which is in reasonable agreement with the previous result.

Shifted peaks were observed in the previous histograms [5], and were attributed to changes in the V_x zero. There is no evidence for ground state shifts in the present experiment. Instead, the shifted states result from the data deviating from the shaded curves of Fig. 4. This is consistent with having to use peaks from many histograms to obtain the ±0.6% quantization accuracy of the previous experiment [5].

The family of shaded curves in Fig. 8 is the same as that in Fig. 4. Therefore the values of f obtained at 203 μA are the same as those shown in Fig. 12 at 210 μA. An independent family of curves was also fitted to the data of Fig. 8. The resulting values of f for the independent family are displayed in Fig. 13. They differ from those in Fig. 12 by as much as 0.9%, indicating that f can be determined to a precision of about 0.1% and an accuracy of about 1% for these particular data. Figure 14 shows values of f for the data of Fig. 11 at 225 μA. The results of f versus B from Figs. 12–14 are combined in Fig. 15 for the three currents investigated. The difference between the f versus B curves for −203 μA and ±210 μA in Fig. 15 illustrates the 1% accuracy at which the values of f can be determined for these data since they both yielded good fits to the V_x versus B curves at −203 μA. The minimum value of f at 225 μA is essentially the same as at 203 and 210 μA; however, at lower magnetic field values, f is larger at this higher current.

3.4 Discussion

The fraction f of conducting electrons that make the transitions can be quite large. This suggests that either, all the current enters the breakdown region (in which case f is the probability for single transitions), or that some of the current bypasses

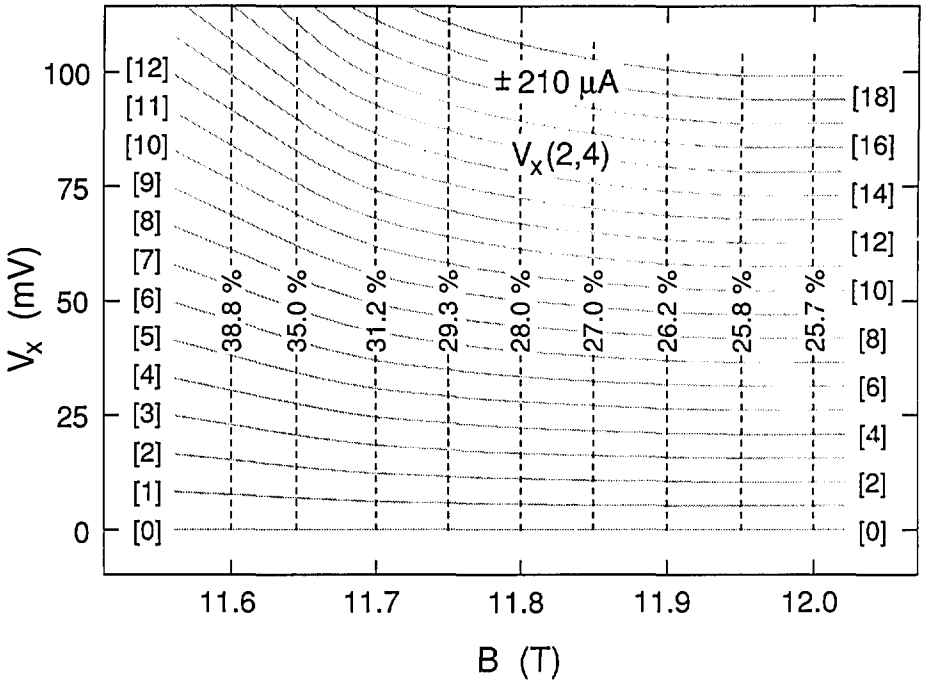

Fig. 12. The fractions f (expressed as a percentage) of electrons making the Landau level transitions for the 20 shaded curves shown in Fig. 4 at ±210 μA. See Eq. (1) for the definition of f. The shaded curves were generated with an accuracy of ~1% and a resolution of ~0.1%.

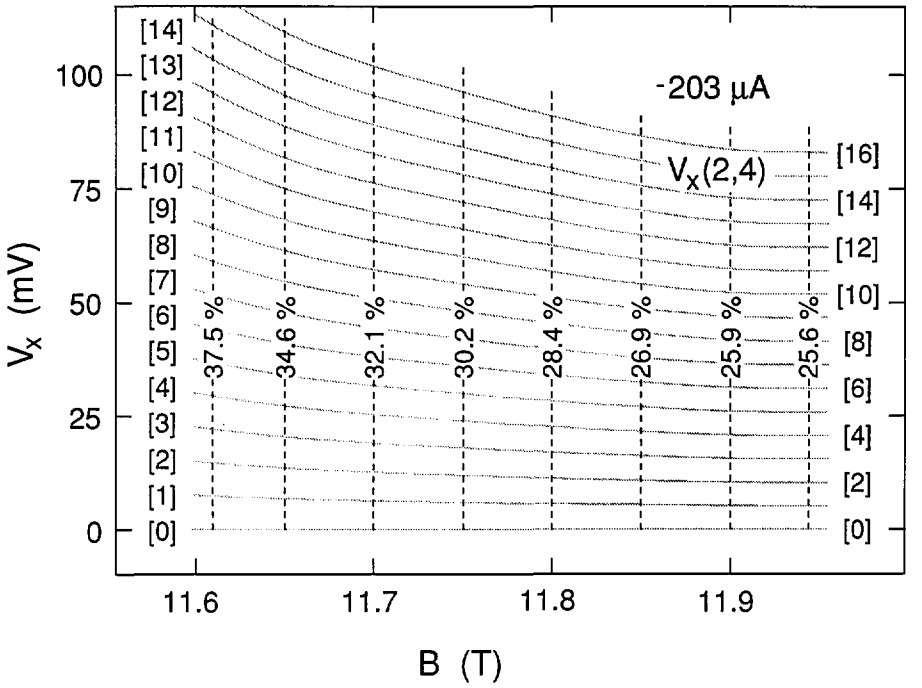

Fig. 13. The fractions f for a family of curves used to fit the data obtained at -203 μA. This family is slightly different from the one displayed in Fig. 8.

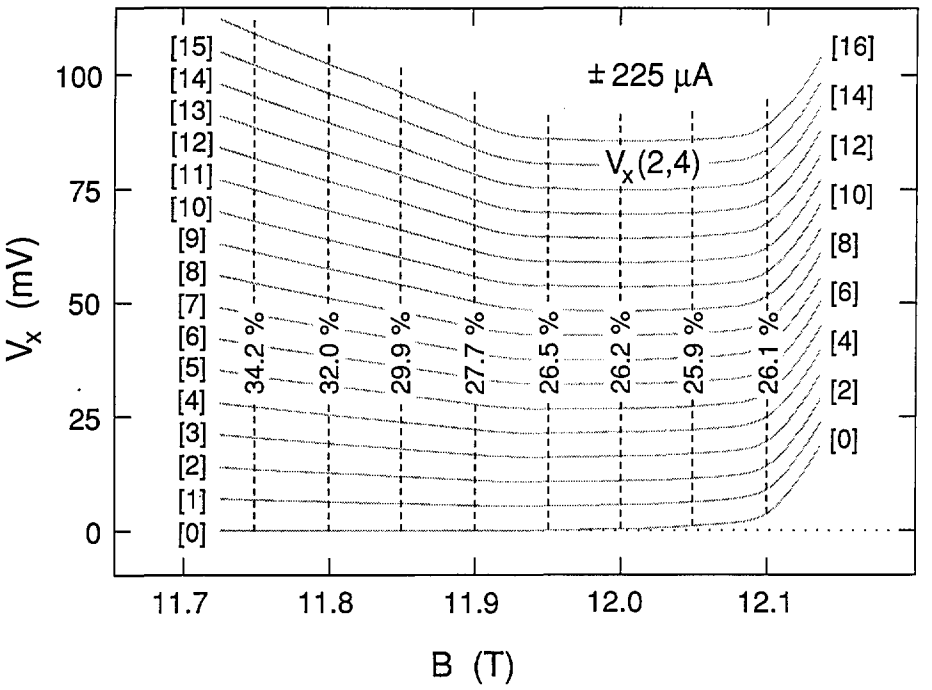

Fig. 14. The fractions f for the 17 shaded curves shown in Fig. 11 at ±225 μA.

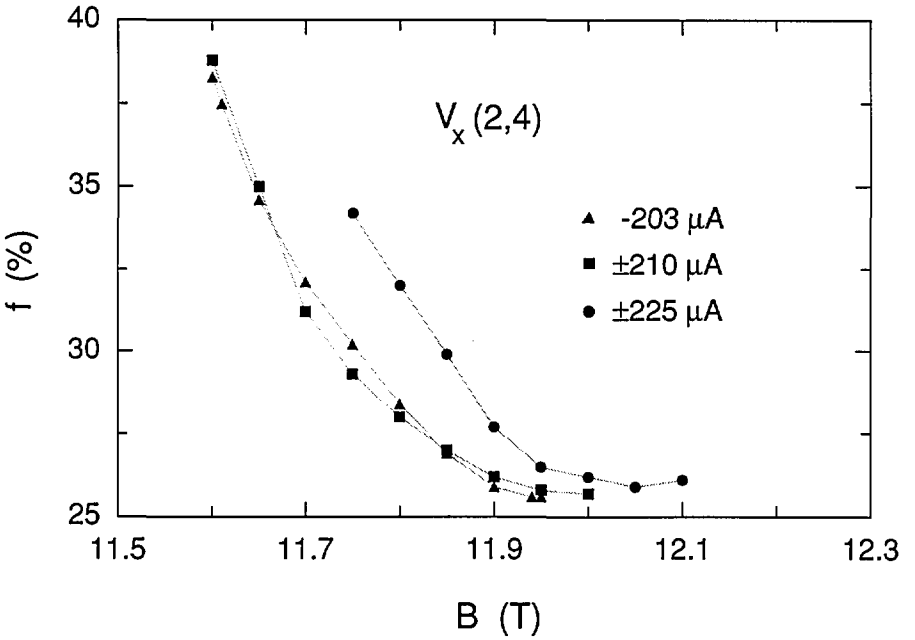

Fig. 15. The combined results of f versus B from Figs. 12–14 for the three currents investigated. The values of f have an accuracy of ~1% and a resolution of ~0.1%.

the breakdown region (in which case f would correspond to the fraction of current passing through the breakdown region if the transition probability was always 100%).

The fraction f is not necessarily 100%, and, in general, is a function of B and I. These facts can greatly complicate the identification of voltage quantization for most breakdown data because the voltage separations will not be constant if f and r are not constant across the magnetic field range, so the voltages will appear to not be quantized even when they actually are.

One can always obtain the *product fM* from the data by using Eq. (1), but the value of f can only be determined if M can be unambiguously deduced. The data presented here are particularly striking and clear, with sharp vertical transitions, switching between states, and sufficient variations between sweeps to generate the families of shaded curves. Although time-consuming, it was thus relatively easy to determine the quantization. We can therefore be reasonably assured that the values of M, and thereby the values of f, have been properly determined. Most breakdown data, however, require very careful measurements to deduce the quantization, and in many cases there may be insufficient structure, switching, and variation to definitively determine M.

4. Conclusions

Quantized dissipative voltage states exist in the breakdown regime of the quantum Hall effect. This quantization has been interpreted using a simple model in which electrons make transitions consisting of excitations from a lower Landau level to a higher level and then a return to the lower level. Voltage quantization suggests that individual electrons either make a single transition or make a fixed number of multiple transitions because varying numbers of transitions would result in a continuum of V_x values rather than voltage quantization.

We have demonstrated that the dissipative voltage states are quantized, and that, in general, the quantization is a function of magnetic field and current. The actual transition mechanisms are no doubt very complicated, so the breakdown region has been treated as a black box, and we used a simple model to interpret the data.

One normally expects quantization phenomena to be predictable, whereas the values of V_x and f are not predictable in the present experiment unless the transition probability is actually always 100% and f is thus the fraction of current passing through the breakdown region. The quantization is not perfect, but it is surprising just how well quantized the dissipative voltage states are, up to at least the nineteenth excited state.

Acknowledgments

The author thanks A. C. Gossard (now at the University of California at Santa Barbara) who made the MBE-grown GaAs/AlGaAs heterostructure at AT&T Bell Laboratories, D. C. Tsui of Princeton University who did the photolithography and made ohmic contacts to the heterostructure sample, M. D. Stiles who assisted in the interpretation of the data, C. T. Van Degrift who designed and built the quantum Hall effect laboratory, and O. Heinonen, G. Marullo Reedtz, R. E. Elmquist, K. C. Lee, A. F. Clark, and E. R. Williams for their discussions and comments. This work was supported in part by the Calibration Coordination Group of the Department of Defense.

5. References

[1] K. v. Klitzing, G. Dorda, and M. Pepper, Phys. Rev. Lett. **45**, 494 (1980); The Quantum Hall Effect, edited by R. E. Prange and S. M. Girvin, Springer-Verlag, New York (1987).
[2] G. Ebert, K. v. Klitzing, K. Ploog, and G. Weimann, J. Phys. C **16**, 5441 (1983).
[3] M. E. Cage, R. F. Dziuba, B. F. Field, E. R. Williams, S. M. Girvin, A. C. Gossard, D. C. Tsui, and R. J. Wagner, Phys. Rev. Lett. **51**, 1374 (1983).
[4] L. Bliek, G. Hein, V. Kose, J. Niemeyer, G. Weimann, and W. Schlapp, in Proc. Int. Conf. on the Application of High Magnetic Fields in Semiconductor Phys. **71**, G. Landwehr, ed., Springer-Verlag, Berlin (1987) p. 113.
[5] M. E. Cage, G. Marullo Reedtz, D. Y. Yu, and C. T. Van Degrift, Semicond. Sci. Technol. **5**, 351 (1990).
[6] G. Hein, P. Schneider, L. Schweitzer, F. J. Ahlers, L. Bliek, H. Nickel, R. Losch, and W. Schlapp, Surf. Sci. **263**, 293 (1992).
[7] M. E. Cage, Semicond. Sci. Technol. **7**, 1119 (1992).
[8] M. E. Cage, D. Y. Yu, and G. Marullo Reedtz, J. Res. Natl. Inst. Stand. Technol. **95**, 93 (1990).
[9] S. Komiyama, T. Takamasu, S. Hiyamizu, and S. Sasa, Solid State Commun. **54**, 479 (1985); Surf. Sci. **170**, 193 (1986).
[10] A. S. Sachrajda, D. Landheer, R. Boulet, and T. Moore, Phys. Rev. B **39**, 10460 (1989).
[11] O. Heinonen, P. L. Taylor, and S. M. Girvin, Phys. Rev. **30**, 3016 (1984).
[12] L. Eaves and F. W. Sheard, Semicond. Sci. Technol. **1**, 346 (1986).
[13] D. C. Tsui, G. J. Dolan, and A. C. Gossard, Bull. Am. Phys. Soc. **28**, 365 (1983).
[14] V. L. Pokrovsky, L. P. Pryadko, and A. L. Talapov, Sov. Phys. JETP **68**, 376 (1989); J. Phys. (Condensed Matter) **2**, 1583 (1990).
[15] J. R. Kirtley, Z. Schlesinger, T. N. Theis, F. P. Milliken, S. L. Wright, and L. F. Palamateer, Phys. Rev. B **34**, 5414 (1986).
[16] A. J. Kent, D. J. McKitterick, L. J. Challis, P. Hawker, C. J. Mellor, and M. Henini, Phys. Rev. Lett. **69**, 1684 (1992).
[17] B. E. Kane, D. C. Tsui, and G. Weimann, Phys. Rev. Lett. **59**, 1353 (1987).

About the author: *Marvin E. Cage is a physicist in the Electricity Division of the NIST Electronics and Electrical Engineering Laboratory. The National Institute of Standards and Technology is an agency of the Technology Administration, U.S. Department of Commerce.*

Volume 98, Number 3, May–June 1993
Journal of Research of the National Institute of Standards and Technology

Conference Report

WORKSHOP ON CHARACTERIZING DIAMOND FILMS II Gaithersburg, MD February 24–25, 1993

Report prepared by

Albert Feldman

National Institute of Standards and Technology,
Gaithersburg, MD 20899-0001

Charles Beetz

Advanced Technology Materials,
7 Commerce Dr.,
Danbury, CT 06810

Paul Klocek

Texas Instruments,
P.O. Box 655012,
Dallas, TX 75265

and

Grant Lu

Norton Diamond Film,
Goddard Rd.,
Northboro, MA 01532

1. Introduction

The second in a series of workshops was held at NIST on February 24–25, 1993 to discuss in depth specific topics deemed important to the characterization of diamond films made by chemical vapor deposition (CVD) and to address the need for standards in diamond technology. The topics chosen for this workshop were based on feedback from the attenders of the first workshop [1]. The audience targeted for this workshop was the producers and potential users of CVD diamond technology. University scientists and scientists from government laboratories were invited as experts in properties measurements. There were 44 attenders at the workshop.

We focused on three technical topics for discussion: characterization of optical absorption and scattering for optical applications; electronic characterization—metallization and electronic contacts for electronic applications; and standardization of thermal conductivity measurement. In addition, a short session presented some new developments in Raman measurements and in thermal conductivity measurements.

An important session of the workshop was devoted to the formation of a working group for standardizing thermal conductivity measurements. Grant Lu of Norton Diamond Film was informally chosen to chair the working group. At this session, a round-robin comparison of thermal conductivity and thermal diffusivity measurements was agreed upon. A set of specimens prepared voluntarily by producers of CVD diamond will be circulated among experts in the measurement methodologies. NIST will coordinate the circulation of the specimens among the measurement laboratories and will collate the results of the measurements for presentation at the next working group meeting.

All registrants have been asked to evaluate the workshop. The purpose for this evaluation was to determine the usefulness of the workshop, the desire for further workshops, topics for future workshops, and the need for additional standards related activities. The feedback received will be

included in a NIST Internal Report to be distributed to workshop participants.

The sections that follow contain summaries of the main sessions of the workshop. The principal conclusions of the workshop include:

- There is no apparent need for special techniques to optically characterize CVD diamond. Techniques used on other materials appear to be adequate.
- Sessions on optical characterization and electrical characterization should be part of future workshops in order to maintain a free exchange of information among workers in the field.
- A working group to investigate standardization of thermal conductivity measurements on CVD diamond has been formed.
- Planning was begun for an interlaboratory round-robin comparison of thermal conductivity and thermal diffusivity measurements. NIST will coordinate this activity.

2. Characterization of Optical Absorption and Scattering

Seven presentations that discussed procedures for measuring the optical absorption and scattering in CVD diamond were given.

The first presentation was by P. Klocek of Texas Instruments who discussed and compared the physical properties of diamond with other optical materials. While the broadband transparency, low thermooptic constant, and low dispersion of diamond are very attractive, it is the combination of these properties with exemplary mechanical and thermal properties that make diamond compelling for passive optics, i.e., infrared windows, coatings, geometric optics, diffractive optics. Specific application requirements such as transmission, emission and optical phase were discussed in terms of measurable optical properties, i.e., refractive index n, and extinction coefficient k, absorption coefficient, scattering coefficient, and modulation transfer function. Microscopic theory (quantum theory of phonons) and macroscopic theory (Maxwell's equations) were used to introduce the various optical measurement techniques for the optical properties. Tolerances or variances were suggested for these properties for the various passive optical applications along with a simple statistical method for determining the required measurement technique accuracy.

J. M. Trombetta of Texas Instruments presented a discussion of the common methods for determining the infrared absorption coefficient spectrum of an optical material specimen. CVD diamond now under development is thin, typically less than 1 mm thick. This translates into a small material response and therefore low precision in transmission and emission measurements. While background noise is low in Fourier-transform infrared (FTIR) spectrometers, signal drift and reflection artifacts in the instrument cause errors in the absolute transmittance. Photoacoustic spectroscopy can assist in distinguishing absorption loss features from scattering loss but the technique is generally nonquantitative. Therefore, for highly accurate properties determinations, a combination of techniques would be most valuable. Dr. Trombetta indicated that a proper identification of the various contributions to transmission loss requires a complete optical analysis, including measurement of both scattering and absorption spectra.

C. A. Klein of Raytheon, discussed laser damage in diamond. He stated that the laser damage threshold of diamond is high but not uniquely so. While diamond's exceptionally large figure-of-merit for thermal shock resistance suggests an outstanding laser damage threshold for high average-power optical radiation, its large nonlinear refractive index n_2, suggests a low critical power for self-focusing and, hence, a low peak-power damage threshold. The low self-focusing threshold combined with the occurrence of surface damage due to graphitization will thus limit diamond's usefulness as a window for transmission of high peak-power laser radiation. Measured data from various sources was reviewed. Type IIa natural diamond crystals exposed to picosecond pulses of 355 nm radiation exhibited surface ablation at threshold intensities of roughly 60 GW/cm^2. Surface damage (melting) was observed at peak intensities of 6 TW/cm^2 when diamond was irradiated with femtosecond pulses at 620 nm. Single picosecond pulses of 1.06 μm radiation from a Nd:YAG laser resulted in internal damage due to dielectric breakdown. The large value of $n_2(2.3\times10^{-13})$ resulted in a self-focusing critical power of 1.7 MW and a breakdown intensity of 1 to 3 TW/cm^2. Another study showed that type IIa diamond, exposed to nanosecond pulses of CO_2 laser radiation at 10.6 μm, exhibited sub-surface damage at intensities in the low GW/cm^2 range. The results suggested that the breakdown intensity depended on laser wavelength and pulse characteristics. To date, the only laser damage studies reported on CVD diamond were performed on poor quality samples. Laser damage studies are needed on high-quality CVD diamond.

K. A. Snail of the Naval Research Laboratory discussed the need to determine the amount of bulk and surface light scattering in CVD diamond, particularly for infrared window/dome applications. Scattering measurements performed at 0.633 and 10.6 μm on polished specimens of poor quality CVD diamond revealed significant bulk scattering which was much greater than scatter exhibited by typical optical materials. A first order scattering theory was described which allows for distinguishing between bulk scatter and surface scatter. Studies with a microscope equipped FTIR spectrometer suggested that the grain boundaries of the CVD diamond are the major source of bulk scatter. Commercial light scattering equipment capable of measuring the bidirectional distribution function is available; however, its use is limited to only a few laser sources.

R. P. Miller of Raytheon discussed the use of laser calorimetry to measure optical absorption coefficients. The basic techniques for measuring optical absorption were discussed. Transmittance or photometric techniques possess spectral information but lack sensitivity; absorption coefficients not much less than $10^{-2}\,cm^{-1}$ can be measured with these techniques. Emittance techniques are sensitive to much smaller absorption coefficients ($10^{-5}\,cm^{-1}$) but are subject to background noise. Laser calorimetry is sensitive to small absorption coefficients ($10^{-5}\,cm^{-1}$) and relatively straightforward to perform. However, spectral information is limited to the wavelengths of the laser sources used; thus, the technique has limited usefulness if one requires spectral information about materials that exhibit complex absorption spectra. Because CVD diamond is thin, one has difficulty in separating the surface from bulk contributions to absorption. Bulk scattering in the diamond also complicates the calculation of absorption coefficient; if the scattering is not properly taken into account, one can overestimate the absorption coefficient. Data from several sources were discussed. A CO_2 laser was the optical source. Typical absorption coefficients for natural type IIa diamond were found to be $0.06\,cm^{-1}$ at 9.2 μm and $0.04\,cm^{-1}$ at 10.6 μm, although values as high as $0.4\,cm^{-1}$ at 10.6 μm were found. This may result from sample to sample variability or from slight differences in the wavelength of measurement on a specimen with an absorption coefficient that has a strong wavelength dependence. (CO_2 lasers can operate at several closely spaced wavelengths such as 10.591 and 10.67 μm.) Data at local spots in high quality CVD diamond showed absorption coefficients of $0.094\,cm^{-1}$ at 9.27 μm and $0.067\,cm^{-1}$ at 10.591 μm, without correction for surface absorption which was believed to be small.

L. H. Robbins of NIST discussed the use of specular transmittance and reflectance to measure the optical constants of CVD diamond. Expressions for transmittance and reflectance in the presence of surface scatter and bulk absorption were presented. By fitting the measured transmittance and reflectance to these expressions, values are obtained for the sample thickness, root-mean-squared surface roughness, refractive index and extinction or absorption coefficient. The model was developed for the study of thin unpolished optical films, less than several micrometers thick, where the surface scatter only partially attenuates the specular beams. This corresponds to a surface roughness to wavelength ratio close to unity. Transmittance and reflectance measurement on CVD diamond samples 0.42 μm thick with surface roughness 10 nm, and 1.90 μm thick with surface roughness 30 nm were fit to the model. The calculated absorption coefficients were significantly higher than the absorption coefficients of type IIa diamond. Because most CVD diamond material produced is much thicker than the specimens measured, the typical roughnesses will be much greater. For these types of specimens, unless they are polished, the model has limited usefulness in the ultraviolet-visible range, but the model may prove useful in the infrared.

In the final presentation, M. E. Thomas of Johns Hopkins University discussed how emissivity measurements can be used to obtain optical properties of diamond. In the two-phonon region, 4 to 7 μm, diamond has a fairly high absorptivity and therefore a high emissivity. The emissivity of diamond in this region was found to be 0.8 and not very sensitive to temperature; thus, the emission signal is large. In the three- and four-phonon regions, 2 to 4 μm, diamond is weakly emissive. However, if the specimen is sufficiently thick, the emitted radiation in this spectral band can have a useful signal:noise ratio. Thomas pointed out that in the 7 to 12 μm region, which is of great interest, emissivity measurements are difficult to make because the background emission in this spectral band is large relative to the diamond emission. Because the optical phonon spectrum in diamond begins at wavelengths below this spectral range, emission is exceedingly weak and the signal:noise ratio is small. Work is now in progress to overcome this difficulty. Other difficulties with emission measurements on diamond include oxidation

above 800 K when high temperature measurements are performed and light scattering within the sample. At this time, emission measurements on CVD diamond appear to be most useful in the 2 to 7 μm region and perhaps in the visible region in low scatter specimens. However, measurement of absorption by emissivity measurements in the 7 to 12 μm region is difficult.

In summary, the session on optical characterization of CVD diamond benefitted both speakers and other participants because of the free exchange of information.

3. Electronic Characterization—Metallization and Electronic Contacts

Seven speakers presented different aspects of the electrical properties of semiconducting diamond and the formation of ohmic and Schottky contacts.

The first paper was given by J. Vandersande from the Jet Propulsion Laboratory. He presented the results of recent electrical resistivity measurements on diamond between room temperature and 1200 °C. He described a special apparatus designed for making resistivity measurements up to 1200 °C and showed that resistivity values of $\sim 10^{16}\ \Omega$ cm typically reported in the literature for type IIa natural diamond represent a lower limit to the true values because of limitations in the measurement instrumentation. The resistivity of type IIa diamonds was found to drop from $\sim 10^{15}\ \Omega$ cm at 200 °C to $10^{4}\ \Omega$ cm at 1200 °C, with an activation energy of ~1.5 to 1.6 eV. Results were also presented for CVD diamond films that showed electrical resistivities comparable to or greater than those for natural type IIa diamonds; the CVD films also had similar activation energies. Dr. Vandersande cautioned that during high temperature measurements, surface graphitization can occur, leading to a decrease in specimen resistance on cooling. The surface graphitization layer can be removed by cleaning in acid solutions, thus restoring the original specimen resistance.

C. Hewett from the Naval Command, Control and Ocean Surveillance Center discussed the importance of low resistance ohmic contacts to high power device applications of semiconducting diamond. Ohmic contact formation is based on a solid state reaction in which a transition metal reacts with the diamond to form a carbide layer during high temperature annealing. This carbide interface layer is in intimate contact with both the metal contact and the underlying diamond, thus promoting good adhesion between the metal contact to the diamond. Dr. Hewett described a technique for measuring the specific contact resistance using a circular transmission line model. This technique eliminates the need for mesa etching, a procedure that is usually needed for minimizing artifacts due to three dimensional current flow.

M. Geis of Lincoln Laboratories reviewed the device properties of diamond and discussed the advantages and disadvantages of diamond in high power, high frequency devices. He discussed the use of various surface treatments for passivating the diamond surface in order to eliminate surface leakage currents. Exposing diamonds to CF_4O_2 or N_2 plasmas gave the best results. Dr. Geis also presented interesting results which illustrated that artifacts in capacitance-voltage measurements can be caused by back surface contact resistance. He also discussed interesting approaches to achieving large area single crystal diamond substrates; a novel method was developed for placing of highly oriented diamond seed crystals on patterned Si substrates. He also discussed applications of diamond as a cold electron emitter.

J. von Windheim from Kobe Steel USA, Inc., discussed electronic transport measurements on natural single crystal diamonds, homoepitaxial CVD diamond, and polycrystalline CVD diamond films. He reviewed the results of various measurements such as high temperature resistivity, ac conductivity, dc current-voltage measurements, and space charge limited currents. In addition, he described the role of these measurements in identifying various trapping centers. Results of Hall effect and resistivity measurements indicate a complex conduction process in which 2 to 20 percent of the boron atoms used to dope the diamond specimens are compensated. The nature of the compensating center has not been elucidated but it is believed to be nitrogen, possibly in the A-aggregate form. Comparisons were made between the transport properties of polycrystalline diamond films and diamond single crystals. The transport properties of the polycrystalline films were much poorer than those of the single crystals.

J. Glesener of the Naval Research Laboratory presented additional results describing the electrical characterization of impurities in diamond. He employed admittance spectroscopy to characterize deep levels associated with boron impurities. The technique consisted of measuring the ac conductivity of a Schottky-barrier diode fabricated on the diamond. The conductance of the sample was

measured as a function of temperature and as a function of the ac frequency. The ac voltage applied to the Schottky diode modulates the intersection of the Fermi level with the impurity level, providing a time dependent source of carriers. Dr. Glesener showed that the conductance peaked when the carrier emission rate from the trap became comparable to the ac frequency. The trap emission rate could be changed by lowering the temperature of the diamond. From these measurements, the energy level of the deep trap was found to be 0.33 eV and the hole capture cross-section was estimated to be $\sim 2 \times 10^{-12}$ cm^2. The deep trap was believed to be due to boron that had been present in the gas used to grow the diamond.

K. Das from Kobe Steel USA, Inc. discussed contacts on diamond. He reviewed the results for a wide range of metals, semiconductors, silicides and metal carbides as rectifying contacts on semiconducting diamond. He showed that direct metallization on CVD grown films does not always produce good rectifying contacts; it is sometimes necessary to introduce an insulating diamond or dielectric film between the doped diamond and the metal in order to get a good rectifying characteristic. He also showed that the rectification properties of metal contacts can be improved by near surface implantation of boron into the diamond prior to the metallization step. Dr. Das also discussed the formation of low resistance ohmic contacts using carbide forming transition metals deposited on heavily doped diamond films. He also presented data on the chemical composition of the formed contact structures.

The last presentation was given by C. P. Beetz of Advanced Technology Materials, Inc. He discussed the measurement of Schottky-barrier heights of metals on diamond using the method of internal photoemission. He listed the Schottky barrier heights of various metals on diamond and discussed the observation of a region showing two thresholds in the photo-yield of metals on type IIa natural diamond. Dr. Beetz pointed out that the upper threshold values presented in some of the literature must be corrected to take into account contributions from the lower threshold. He also discussed controlling the Schottky-barrier height of metals on diamond by using shallow near surface silicon implants. These implants would favor reactions with silicide forming metals. He showed results for platinum, molybdenum, and titanium contacts in which the barrier height decreased with increasing silicon implant dose.

4. Work in Progress and New Developments

A special session was organized for presentation of new results and to cover miscellaneous topics not covered by the principal sessions.

E. Etz of NIST presented recent results of Raman spectroscopy measurements on several specimens provided by two producers of CVD diamond. This work was presented in the context of a proposed Raman standard reference material discussed at the previous workshop. The Raman spectrum is being used as a measure of diamond quality. The quality of diamond is considered to decrease with increasing line width of the diamond Raman line at 1332 cm^{-3}, increasing background luminescence intensity, and increasing intensity of the sp^2 carbon peak near 1550 cm^{-1}. In high quality films, the sp^2 peak may not be observable. Freestanding diamond wafers of high quality with thicknesses ranging from 300 μm to 1.7 mm were examined. A cross-sectional examination by Raman spectroscopy indicated that the diamond in the bottom layer (the material closest to the substrate during deposition) was of poorer quality than the diamond in the top layer. The width of the diamond Raman line in one of the specimens was equal to the width of the diamond Raman line in a type IIa single crystal natural diamond. This result suggests that the specimen was essentially strain free. The Raman spectrum of a specimen deliberately doped with nitrogen indicated a deterioration in the quality of the diamond. A trace analysis of a cross-section indicated the presence of Na, K, Ca, and Mg, possibly due to contamination of the specimen during preparation.

At the previous workshop, D. Morelli of the General Motors Research Laboratory discussed the thermal conductivity of CVD diamond as a function of temperature. The curve representing the temperature dependence at low temperature showed a kink that could not be explained satisfactorily. At this workshop, Dr. Morelli presented the results of an experiment that appears to explain the effect. In this experiment, thermal conductivity measurements were made on single crystal diamond specimens before and after exposure to neutron radiation. Prior to irradiation, the specimens did not exhibit the kink in the thermal conductivity whereas after irradiation and heat treatment, a kink appeared. The temperature at which the kink occurred was correlated with the expected sizes of the defects produced. At low

temperatures, the mean wavelength of thermal phonons is greater than the size of the defect so that scattering is reduced. As the temperature increases, the mean phonon wavelength decreases and scattering increases resulting in a decrease in the expected thermal conductivity behavior. The result is a kink in the dependence of thermal conductivity on temperature. The larger the size of the defect, the lower the temperature at which the kink will occur. The work also demonstrated that grain boundaries are transparent to phonon propagation, at least at the low temperatures.

L. Wei of Wayne State University described the method of photothermal deflection for measuring the thermal diffusivities of diamond. Measurements had been performed on a large number of diamond specimens over the last several years at Wayne State. Dr. Wei discussed the measurement of thermal diffusivity as a function of temperature of diamond crystals containing higher ratios of C^{12}:C^{13} than the natural abundance ratio. She found that the thermal conductivity increased with decreasing C^{13} content. The temperature dependence of the thermal conductivity could be explained by a theory that took into account both Umklapp phonon scattering processes and normal phonon scattering processes.

5. Thermal Conductivity of Diamond: Standardization Issues

Six presentations were given that discussed general standardization issues and specific measurement techniques related to measuring thermal conductivity. R. Tye from Ulvac Sinku-Riko reviewed the ideal requirements for a standard measurement method, standard methods now in use for determining thermal conductivity, and related international standards. Some of the ideal requirements for a standard method are: a generally accepted and proven technique; the availability of a related current standard; relative simplicity in the concept, design and operation of the equipment; rapid and minimal specimen preparation; a capability of providing absolute values to a known precision or a required precision. The advantages and disadvantages of techniques such as axial rod heat flow, 3 omega, flash, converging wave, and ac calorimetry were discussed. The flash method is used in three international standards (ASTM, UK/BS and Japan/JIS) for thermal diffusivity measurements. However, these standards would need modification to be applicable to CVD diamond.

R. Taylor from the Thermophysical Properties Research Laboratory at Purdue University stressed the difficulty of accurately measuring thermal transport properties. He showed that published thermal conductivity values of 99.9+% pure tungsten and TiC show very large variations; values differing by factors of two to three were observed. Professor Taylor then described a new measurement technique developed at Purdue University. In this technique, a thin strip of diamond 50 mm long ×4 mm wide is partially masked. The unmasked portion is uniformly exposed to a step input of heat from an infrared lamp by means of a shutter. Three thermocouples, attached along the length of the masked portion of the sample, monitor the rise in temperature as heat flows from the unmasked portion of the specimen to the heat sink at the other end. The time dependence of the temperature is used to compute the thermal diffusivity.

D. Slutz from General Electric Superabrasives discussed the development of two methods suitable for quality control monitoring of thermal conductivity rather than for obtaining absolute accuracy. The first is based on Ångström's method [2]. A modulated laser beam focused to a line at one edge of the specimen provides the heat source. An infrared detector monitors the phase lag of the traveling thermal wave as a function of the distance from the heating source. The thermal diffusivity is calculated from the data. In the second method, the specimen is heated in the same manner as above but data is collected at a single point on the specimen. A Fast Fourier Transform analyzer is used to analyze the collected data, from which the thermal diffusivity is calculated. The measurement time for each specimen is 20 min.

J. Graebner of AT&T Bell Laboratories described measurement techniques to measure the thermal conductivity in the plane of a specimen and the thermal diffusivity perpendicular to the plane of the specimen. The in-plane measurement is performed with a two-heater steady state technique; one of the heaters allows for a correction due to radiative heat loss and conductive heat loss through the electrical leads. The perpendicular thermal diffusivity is measured by the laser flash technique. A thermal conductivity of 26 W/(cm K) has been calculated from laser flash measurements on high quality CVD diamond.

S. Preston described laser flash measurements of thermal diffusivity at AEA Technology in Great Britain. A high power Q-switched ruby laser was used as the heating source. A relatively thick metallic coating (10 μm thick) was deposited on

the diamond to absorb the laser beam without being ablated away. In order to account for the transient delay due the coating, a measurement was performed on a piece of high purity copper foil coated along with the diamond films. Because the thermal diffusivity of the copper foil was known, he was able to calculate the thermal diffusivity of the coating; this value was used in calculating the thermal diffusivity of the diamond.

G. Lu of Norton Diamond Film described the results of thermal modelling to determine the relative importance of in-plane thermal conductivity vs perpendicular thermal conductivity for lowering the temperatures of junctions of diamond with other materials. In most cases, a higher perpendicular thermal conductivity led to a lower junction temperature. The one exception was the case of a small circular heat source having a diameter much less than the diamond thickness; in this case, in-plane heat spreading plays the major role in removing heat from the junction region. Results were also presented which showed that incremental decreases in junction temperature were minimal when the diamond thermal conductivity increased beyond three to four times the thermal conductivity of the heat sink on which it is placed.

6. Organization of Working Group

Thermal management applications are leading the way in large-scale commercialization of CVD diamond. Recent press announcements [3] show the incorporation of CVD diamond into the production of high power electronic packages. However, not only is there no accepted method of measuring the thermal conductivity of CVD diamond, but different methods can frequently yield significantly different results. Therefore, a working group has been formed to examine the issues and formulate a recommendation on standardizing thermal conductivity measurements of CVD diamond. The members of the working group are:

Grant Lu, Norton Diamond Film—Chairman
Albert Feldman, NIST
John Graebner, AT&T
Ronald Tye, ULVAC Sinku-Riko
David Slutz, General Electric
Pao-Kuang Kuo, Wayne State University
Steven Preston, AEA Technology—Associate Member

As one of the first steps in the process, an interlaboratory round-robin test will be conducted to assess differences in the results of measurements made at different laboratories using different methods. A set of samples will be fabricated by several manufacturers and sent to different laboratories for measurement of thermal conductivity. At the workshop, Norton Diamond Film, General Electric, and Raytheon agreed to supply specimens. AT&T, Wayne State University, Purdue University, AEA Technology, Sinku Riko, General Electric, and Norton Diamond Film offered to perform the measurements. Other manufacturers and measurement laboratories will be asked to participate. The results will be compiled by NIST and presented at the next workshop.

7. References

[1] A. Feldman, C. P. Beetz, M. Drory, and S. Holly, Workshop on Characterizing Diamond Films, NISTIR 4849 (1992).
[2] M. A. Ångström, A New Method of determining the Thermal Conductibility of Bodies, Phil. Mag. **25**, 130-142 (1863); Ann. Phys. **114**, 513-521 (1861).
[3] Photonics Spectra, Laurin Publishing Company, Inc., November 1992.

Volume 98, Number 3, May–June 1993
Journal of Research of the National Institute of Standards and Technology

Conference Report

NIST-INDUSTRY WORKSHOP ON THERMAL SPRAY COATINGS RESEARCH Gaithersburg, MD July 20, 1992

Report prepared by

S. J. Dapkunas

National Institute of Standards and Technology, Gaithersburg, MD 20899-0001

1. Introduction

In 1992, a comprehensive survey of current Federal materials research programs and plans for new initiatives, known as the Advanced Materials and Processing Program (AMPP), was developed under the auspices of the Office of Science and Technology Policy. The goal of the AMPP is to improve the manufacture and performance of materials to enhance the nation's quality of life, security, industrial productivity, and economic growth [1]. One element of the program addresses what have become known as "Functionally Gradient Materials" (FGM). This class of materials is distinguished by properties which vary with material thickness. These gradients in properties such as hardness, thermal conductivity and chemical stability contribute to the improved performance of components. For example, the wear resistance of a soft but tough material can be greatly improved by the application of a harder but compliant surface deposit overlayed with a very hard but brittle material. The concept of gradations of material properties to optimize performance is not new but increased awareness of the opportunities for improved control of properties and the ability to tailor microstructures continuously through a thickness has fostered a view of these materials as a distinctive class whose potential has not been fulfilled. Typically these materials' compositions vary from metallic to ceramic over a thickness of up to several millimeters. The unique approach now taken to graded materials in FGM research is to target specific properties at the extremes of the material's thickness, thermal conductivity, and thermal expansion, for example, and to tailor microstructure, porosity or other features to meet those properties. Extensive research to achieve this capability through understanding of processing-microstructure-property relationships has been initiated through material synthesis techniques as varied as thermal spray, chemical vapor deposition, and self propagating high temperature synthesis [2].

Thermal spraying of coatings, due to high material deposition rates and relatively low capital cost, has become a primary industrial method of synthesizing materials with varying composition and microstructure. The North American thermal spray market was over $600 million in 1990 and is projected to reach $2 billion per year by the year 2000, a growth rate of 7-8% per year. The largest portions of this market are in powder consumables and coating services. The growth projected is largely based on the increased use of ceramic coatings for thermal barriers and clearance control on aircraft gas turbines, some of which have close to 5500 parts which are thermal spray coated [3]. Similarly, the market for ceramic powders used in

thermal spraying is a significant portion of the advanced ceramic powders market and is expected to experience a growth rate of 4% per year through 1995 [4] with annual consumption of oxides and carbides reaching over 2 million kilograms by the turn of the century [5].

The thermal spray industry is diverse. In addition to the aircraft engine applications noted above, thermal spray deposited coatings are applied to fossil fueled boilers and chemical processing vessels to control corrosion, to automotive bodies and mechanical components for cosmetic and wear reduction purposes, to electrical components for insulation, and research is under way to increase efficiency of reciprocating engines through application of thermal barrier coatings to piston crowns. Thermal spray processes are also used to refurbish worn mechanical components, thereby reducing scrap and replacement costs [6]. The companies which supply materials and services for these applications are likewise diverse in size and capabilities. The 1992 Thermal Spray Buyers Guide lists 38 powder suppliers, 25 equipment suppliers, and 40 contract applicators [7] in addition to the major automotive and aerospace companies which are the large single site users of the technology.

Recognition of the size of this industry, the varied interests and skills of the scientists and engineers involved, and the changes in the field have fostered the growth of technical and trade organizations to serve the field's technical communication needs. The primary domestic technical society addressing the community is the Thermal Spray Division of ASM International, which was formed in 1987 and now sponsors the publication of the Journal of Thermal Spray Research. Trade and marketing issues are served by the International Thermal Spray Association. Although research results are available in a wide venue of scientific and engineering journals, the most comprehensive summaries of current research and technical developments are found in the proceedings of the 13 International Thermal Spray Conferences (1956-1992) and the 4 National Thermal Spray Conferences (1981-1991). These conferences now attract over 1000 attendees each.

2. Thermay Spray Processing

Thermal spray coatings are applied by injecting the material to be deposited into a high velocity hot gas directed to the substrate of interest. The coating feedstock is generally a powder but wires and rods are also widely used and the controlled feeding of this material allows the development of a coating whose composition and microstructure varies with thickness. The high temperature gas is obtained either by the development of a plasma generated by passing an inert gas through a set of high voltage electrodes or by combustion of reactive gases in the torch itself. Plasma spraying and flame or high velocity oxygen fuel (HVOF) are the general descriptions of these processes respectively. Process conditions can vary widely and have significant influence on the microstructure and properties of the deposited material. Table 1, taken from Ref. [8], identifies some of the pertinent features of the various thermal spray processes. The plasma spray process has been adapted for operation in vacuum to increase the density of the deposit and in inert gas filled chambers to prevent oxidation of the material sprayed.

The high temperatures and velocities of the thermal spray processes make measurement and control of process parameters difficult. Therefore, although widely used, production of quality coatings largely depends on the experience and intuition of skilled equipment operators.

Table 1. Characteristics of thermal spray deposition of tungsten carbide-cobalt coatings

Typical bond strength, MPA	HVOF	Standard plasma	High velocity plasma
Flame temperature, °C	2760	11,100	11,100
Gas velocity	Mach 4	Subsonic	Mach 1
Hardness, DPH 300	1,050	750	950
Porosity, %	0	<2	<1
Typical bond strength, MPa	69	55	69
Thickness limit, mm	1.52	0.76	0.38

Microstructures of deposited coatings are complex, particularly for graded structures. The extreme thermal conditions to which feedstocks are subjected, high cooling or solidification rates, reaction during transit to the workpiece (substrate), and morphological features resulting from high but variable impact velocities combine to make prediction and control of microstructures difficult. Hence, much of the material produced commercially is the result of empirical studies relating gross process parameters to microstructures and to performance in actual application. Typical thermal sprayed coatings exhibit overlapping lamella resulting from successive impacting particles of molten or very plastic material, oxide films surrounding the lamella, irregularly distributed porosity, rough interfaces between layers of different composition, and cracks resulting from shrinkage during cooling. These features make quantitative analysis and specification difficult.

Properties of thermal sprayed coatings are difficult to measure, especially in service. Tensile strength, elastic modulus, thermal conductivity, and fracture toughness are important coating properties but the most sought after property is adhesion to the substrate. Typically this is determined by the tensile adhesion test, ASTM-C633-79. Large variations in adhesion strength measured by C633-79 have been shown to be typical [9]. Other properties related to performance, such as erosion or corrosion resistance, are routinely measured and related to operating conditions in specific applications.

3. Workshop Objective and Structure

The objectives of the workshop were to identify (1) the research required to improve processing reproducibility and performance prediction, (2) opportunities for collaboration between NIST and industrial researchers, and (3) mechanisms of effective dissemination of research results to the thermal spray community. This approach is more focused than some earlier studies, Refs. [10] and [11] for example, which include thermal spray in general assessments of coating research needs and do not specifically address industrial processing concerns.

Invited attendees represented a broad spectrum of the thermal spray industry including powder suppliers, equipment manufacturers, and applicators and users of thermal spray coatings. In addition, researchers from academia and federal laboratories with active programs in thermal spray, as well as representatives of the principal organizations through which the thermal spray community communicates were invited.

The workshop was structured to present visitors with an overview of unique NIST analytical and materials characterization techniques which are viewed as providing improved capabilities to understand the role of processing on performance and properties. Members of the Materials Science and Engineering Laboratory and the Chemical Science and Technology Laboratory staffs reviewed chemical and compositional mapping of microstructures, thermal properties measurements, and powder characterization techniques developed and utilized at NIST.

A crucial aspect of the workshop was to solicit the view of industry on their requirements for measurement related research. To accomplish this, industrial and academic representatives described the general requirements for measurement of process parameters, mechanical properties, microstructural analysis, and modeling of the thermal spray process. The specific issues of the automotive industry were addressed by representatives from Ford and General Motors, who emphasized performance prediction.

To facilitate implementation of research results, NIST personnel described the various mechanisms, such as Cooperative Research and Development Agreements and the Advanced Technology Program, through which collaborative research can be conducted. Similarly, the past chairman of the ASM International Thermal Spray Division described that organization's structure and means of coordinating dissemination of information.

Following these general presentations, working groups convened to determine specific research topics which are of importance to the thermal spray industry. These groups addressed process measurement and control with an emphasis on powder characterization, coating evaluation, performance evaluation, and process modeling.

4. Research Issues

The following research issues and needs were determined by consensus through the working group discussions.

4.1 Processing Measurement and Control

Powders are the predominant form of thermal spray feedstock and are increasingly recognized as having a strong influence on the microstructure

and performance of coatings. Therefore, consideration of powder characteristics as a process variable is warranted. Powders for thermal spray deposition are synthesized by several techniques and are generally specified by bulk composition and particle size. Metallic powders are usually formed by atomization from an alloy melt while oxide, carbide and other ceramic compositions are formed by crushing and grinding larger material to the desired size or by spray drying fine powder with an organic binder to obtain the size required. The type of ceramic processing used influences properties such as powder shape, phase content, friability, and flowability.

The powder characterization working group aimed to identify those powders which were of greatest interest to industry, to determine which powder properties were most critical to spray process control, and types of standardized testing which are required or need improved technique.

Powders can be divided into those that are intended for coating use at elevated temperatures and those that are exposed to ambient temperatures. Among the former are the zirconia containing thermal barrier and M-CrAlY (Nickel, Cobalt, and Iron as the primary constituent(s) with Chromium, Aluminum and Yttrium alloying additions) coatings applied to gas turbine components and among the latter are tungsten carbide and aluminum oxide utilized for wear protection. For high temperature applications, 7-8% yttria stabilized zirconia was found to be of greatest interest. For this powder, in particular, synthesis technique has a pronounced effect on powder shape, porosity and other features which affect both spraying and deposit formation. These synthesis related features were felt to be the cause of variations in measurements required for powder specification. Specific working group recommendations for research to resolve these issues are as follows:

- Calibration and cross correlation of powder size measurements by powder producers and users should be conducted using well characterized reference lots of material as has been done in the fine ceramics industry. This would be most effectively conducted through the distribution of captive cells of material. This research would have immediate benefits to the thermal spray industry.
- A standard should be written for the size analysis of powders in the 10 μm size range including sample preparation technique. Major interest focused on the analysis of gas atomized and spray dried powder which should be the primary materials studied. Size analysis of non-spherical powders is not currently conducted in spite of the fact that significant amounts of this material are used. Optical size measurement methods are desired, particularly by users.
- Techniques for measurement of specific surface area, phase composition, and chemical composition require development for thermal spray powders. In particular, analysis techniques for impurities such as silica, alumina, sodium, hafnium, uranium, and thorium in zirconia are needed. Apparent density measurement techniques for spray dried powders require development to allow improved process control.
- The ultimate test of a powder is its behavior in the thermal spray process and the working group opined that development of a standardized spray test which would determine deposition efficiency is warranted. It was the group consensus that an impartial institution such as NIST would be extended cooperation from the thermal spray community to develop such testing procedures.
- Sensors to measure thermal spray process conditions were clearly identified as requiring development. Conditions which require measurement include particle temperature, particle velocity, in-process coating density, and deposit thickness. It was felt that an emphasis should be placed on high velocity spraying techniques.

Significantly, powder producers expressed willingness to contribute to the development of the research recommended through contribution of materials, analysis procedures, and the conduct of analyses as part of a collaborative research effort.

4.2 Coating Evaluation

Measurement of coating properties and analysis of coating microstructure and microchemistry are critical to both the evaluation of thermal spray processes as well as the prediction of performance. Working group members identified this broad range of immediately useful research which would enhance productivity and effective application:

- The inhomogeneous microstructure typically produced is difficult to analyze due to the presence of constituents as diverse as gross porosity, interlamellar phases, metallic glasses, and oxides. The situation is made more complex

by the presence of metastable phases resulting from rapid solidification of powders upon impact with the substrate. Development of reproducible methods to provide quantitative analysis of both gross and subtle features by optical and electron microscopy are needed. It was suggested that a microstructural atlas of coatings would be of use to industry.

- Development of techniques of x-ray diffraction which can routinely be utilized to determine phase content and composition presents challenges which if overcome could provide improved understanding of the role of processing conditions. Similarly, techniques to quantitatively assess phase fraction, residual stress, grain size, and solute levels requires development. The identification of metastable phases which have weak x-ray diffraction patterns is confounded by accompanying fine grain sizes, internal stresses, solute gradients, and texturing effects. This analysis is not performed although the presence of these features can have a significant effect on performance. Characterization of microcracking, which can have significant effects on strength, fracture toughness, thermal conductivity, and corrosion protection, is not easily or well conducted. Development of methods to analyze microcracking can also provide insight into the mechanisms of coating failure.

- Measurement techniques to determine the mechanical properties of thermal sprayed coatings are not well defined although research addressing this topic has been conducted [12-13]. Adhesion to the substrate, cohesion within a coating, and properties of the coating material, particularly when graded, are important to coating design and understanding of the role of processing parameters. Typically adhesion is measured by use of the tensile adhesion test (TAT, ASTM-C633-79) originally developed for evaluation of zinc coatings on steel. This test, which consists of pulling the coating from the substrate by means of a tab epoxied to the coating, is limited to the strength of the epoxy. It is not conducted above 200 °C and provides only rough quality control guidance in contrast to more elegant techniques applied to homogeneous thin films [14]. A test methodology which can be readily conducted by applicators and provides an understanding of mode of failure, failure initiation site, strain to failure, and other pertinent data for the coating-substrate system is desired. Data on the properties of coating materials is either gathered from handbook values of bulk material of similar composition or measured on coatings removed from a substrate. These data are either not representative of the coating or neglect the role of interfacial constraint at the substrate.

- Thermal properties are particularly important for graded, insulating coatings. It was noted that developing both an ability to measure thermal conductivity and to model this property based on microstructural parameters would enhance industry's ability to design coatings for particular applications.

- Group participants suggested that round robin programs to establish a basis for comparison of test methodologies would be productive as has been shown in a recent exercise to evaluate techniques of metallographic preparation of tungsten carbide coatings. This latter effort which entailed the distribution and analysis of 1800 samples has provided evidence of the value of standard reference materials and standard evaluation techniques. In the long-term, databases on thermal, mechanical, and other properties may be feasibly developed by industry if accepted measurement and analysis techniques are available.

4.3 Performance Evaluation

Performance evaluation and prediction techniques are vital to the competitiveness of material producers and coating vendors and hence are usually closely held. The performance evaluation group identified several general service related issues which should guide the development of a research agenda.

- Although research on current applications is of value, attention should be directed to emerging applications with major growth potential. These applications include thermal barrier coatings for non-aircraft engine applications in the automotive industry, corrosion resistant coatings of value to the chemical industry, and electrical insulators applied to elecromechanical equipment used in various commercial products.

- Tungsten carbide/cobalt wear resistant coatings are a large thermal spray market. Less costly alternatives to this material are of interest and research to assess their performance limits would be of benefit.

- Corrosion resistant coatings for aqueous and other environments are of interest to several industries. An improved understanding of mechanisms of deterioration which would allow better material selection and performance prediction is desired. In terms of characterization techniques, the ability to measure permeability of coatings on a substrate was specifically cited.
- Measures of performance are application specific and the occurrence of unforeseen unmeasured operating conditions limit predictive capabilities. In this context, it was emphasized that understanding mechanisms of coating failure would be of value, particularly in relating laboratory assessments to field measurements.
- The ability to determine the condition and predict the remaining life of coatings is valuable. This capability and the desire to inspect coatings, without reliance on test coupons included in production lines, led to the recommendation of development of *in situ* nondestructive evaluation techniques.

In the extreme, industrial representatives stated the desire to be able to specify performance based solely on processing conditions. This is recognized as a long-term goal which requires significant understanding of the particular mechanisms of deterioration likely for an application and the role of coating properties and microstructure in that mechanism.

4.4 Process Modeling

Process modeling was recognized as the activity which binds several aspects of thermal spray coating together. Modeling of the process from the torch to the coating deposition was cited as necessary for process design, control, and automation. Group recommendations for research included the following specific items:

- Most modeling research has been directed to plasma spraying. The increased interest in high velocity oxygen fueled spraying argues for the development of models of this process wherein higher velocities and deposition rates present challenges.
- For all processes, models of the development or evolution of the complex microstructure are needed. Microstructural development models would provide a link between processing and properties with the potential for better property control and consistency.
- Microstructural development models should include understanding of the nature of impaction and coalescence of droplets, the formation of defects, and the fine features of bonding to the substrate.
- Modeling of thermal spray torch parameters is important for process improvement. Specifically, models of the thermal and flow behavior of the hot gases emanating from the torch and the behavior of particles in flight to the workpiece were cited as necessary.

Significantly, it was stated that the process modeling efforts should be integrated with both diagnostic developments and process design and that the specific classes of material addressed should be recommended by industry.

5. Conclusions

The workshop was successful in identifying many of the key problem areas in thermal spray coating technology. A broad spectrum of issues in this complex process was addressed in the discussion groups which reflected the concerns of different industries. The active participation of the attendees reflects the interest industry has in the development of a research agenda which addresses improved process reproducibility and performance prediction. It is significant to note that most attendees expressed a willingness both to identify important issues which limit the technology and to participate in collaborative research projects to which they would contribute materials, services, and expertise. A key to this willingness was the realization that industrial and academic capabilities in material processing could be effectively utilized in conjunction with NIST's measurement, modeling, and characterization capabilities. Opportunities for transfer of research results to industry through established thermal spray technical organizations were clarified. As a result of the workshop, NIST will synthesize consensus project plans for the consideration of the attendees and initiate collaborative research where sufficient interest warrants.

6. References

[1] Advanced Materials and Processing: Fiscal 1993 Program, The Federal Program in Materials Science and Technology, A report by the Committee on Industry and Technology. Federal Coordinating Council for Science, Engineering and Technology, Office of Science and Technology Policy (1992).

[2] Recent developments in functionally gradient materials, Materials and Processing Report, Elsevier Science Publishing Co., Inc., March/April 1992.
[3] Thermal spray market projected at $2B by 2000, Ceramic Bull. **70** (1), 16 (1991).
[4] Advanced ceramic powders technology challenges conventional processes, Ceramic Bull. **69** (5), 768 (1990).
[5] North American market forecast for thermal spray coatings, powders, and equipment: part II, Materials and Processing Report, Elsevier Science Publishing Co. Inc., May 1991.
[6] P. O. Buzby and J. Nikitich, HVOF thermal spraying of nitrided parts, Adv. Mater. Processes **141** (12), 35-36 (1991).
[7] Thermal Spray Buyers Guide, Adv. Mater. Processes **141** (5), 1 (1992).
[8] D. W. Parker, and G. L. Kutner, HVOF-spray technology poised for growth, Adv. Mater. Processes **141** (4), 68-70 (1991).
[9] P. Ostojic and C. C. Berndt, The variability in strength of thermally sprayed coatings, Surface Coating Technol. **34** (1), 43-50 (1988).
[10] W. J. Lackey, D. P. Stinton, G. A. Cerny, L. L. Fehrenbacher, and A. C. Schaffhauser, Ceramic Coatings for Heat Engine Materials-Status and Future Needs, ORNL/TM-8959, Oak Ridge National Laboratory, December 1984.
[11] M. H. Van De Voorde, M. G. Hocking, and V. Vasantasree, A Comprehensive review on the development of ceramic coatings for thermomechanical applications, High Temp. Mater. Processes **7** (2,3), 107-121 (1986).
[12] S. D. Brown, B. A. Chapman, and G. P. Wirtz, Fracture kinetics and the mechanical measurement of adherence, The National Thermal Spray Conference, Cincinnati, Ohio (1988) pp. 147-157.
[13] A. K. Battacharya and J. J. Petrovic, Indentation method for determining the macroscopic fracture energy of brittle bimaterial interfaces, J. Am. Ceram. Soc. **75** (2), 413-417 (1992).
[14] J. E. Pawel, Analysis of Adhesion Test Methods and the Evaluation of Their Use for Ion-beam-mixed Metal/Ceramic Systems, ORNL/TM-10468, Oak Ridge National Laboratory, July 1988.

Volume 98, Number 3, May–June 1993
Journal of Research of the National Institute of Standards and Technology

News Briefs

General Developments

Inquiries about News Briefs, where no contact person is identified, should be referred to the Managing Editor, Journal of Research, National Institute of Standards and Technology, Administration Building, A635, Gaithersburg, MD 20899; telephone: 301/975-3572.

FEDERAL LABS JOIN FORCES TO HELP U.S. INDUSTRY

NIST and Sandia National Laboratories in Albuquerque, NM, have signed an agreement that will combine their technological resources to help boost the competitiveness of U.S. companies in world markets. Covering microelectronics, advanced manufacturing, materials and standards, the agreement will be driven by industrial needs and build on the success of existing programs at the two laboratories. Initially, NIST and Sandia will concentrate on microelectronics research and target efforts at improving the quality of U.S. semiconductor products. The first joint projects under this agreement will be in semiconductor packaging and manufacturing process control. In packaging, NIST and Sandia have special facilities for resolving obstacles, such as the production of test chips, which allow producers to gauge chip and packaging performance.

BRIDGE BUILDER GETS HELPING "HAND" FROM ROBOCRANE

Under terms of a new cooperative research and development agreement, a private company plans to use NIST's novel robot crane technology to install temporary bridges over beaches or wetlands. The CRADA partners initially will develop a prototype system for integrating NIST's RoboCrane and the company's Modular Bridging System (MBS). RoboCrane, a device that can lift more than five times its own weight and precisely maneuver loads over a large working volume, will be able to install the MBS more rapidly than conventional manual techniques. The MBS also may permit traffic to flow over construction sites while road work proceeds underneath it. Long-range CRADA objectives call for expanding the integrated system for general bridge and road construction/repair jobs, military transport over obstacles, hazardous material handling, and lunar and other space construction. For more information, contact James S. Albus, Robot Systems Division, B124 Metrology Building, Gaithersburg, MD 20899-0001, (301) 975-3418.

NIST/U.S.&FCS JOINT EFFORT TACKLES EXPORT CONCERNS

In recognition of mutual objectives in promoting export of goods and services from the United States, NIST and the U.S. and Foreign Commercial Service (FCS), a unit of the Commerce Department's International Trade Administration, have agreed to work together to achieve common goals concerning standards and exports. A recent memorandum covers formal and working relationships between the agencies for assignment of NIST employees as standards experts to selected U.S. embassies and missions. Under its Standards Assistance Program, NIST works to facilitate exports by encouraging harmonization of foreign and U.S. standards and conformity assessment practices at key locations. NIST currently is furnishing support for U.S. standards advisors to the Saudi Arabian Standards Organization and the U.S. Mission to the European Community. Through its Office of Standards Services, NIST assists industry and the federal agencies in efforts to improve the acceptance of U.S. technology and manufacturing practices, and to promote more effective U.S. contributions to international standardization, conformity assessment, quality assurance, and testing.

INITIAL GRANTEES SAY ATP MAKES A DIFFERENCE

An early study of the short-term effects generated by NIST's Advanced Technology Program suggests that, as intended, the ATP fosters promising lines of research that otherwise would have fallen to budgetary decisions, and improves industrial cooperation. According to the consulting firm that surveyed the 11 companies awarded grants in the ATP's first competition in 1991, the ATP also enhanced the credibility of the grantees in the marketplace. Difficulty in forming and operating a research consortium under the federal government's strict financial rules was among the few problems noted by survey respondents. The ATP makes awards to private companies and industry-led cooperative ventures to support research on promising but high-risk technologies. To obtain a single copy of the 30-page study, The Advanced Technology Program, An Assessment of Short-Term Impacts: First Competition Participants, contact ATP office.

NEW GUIDE CAN HELP STATES BUILD A QUALITY AWARD

Getting the commitment of state leaders, including the governor, should be one of the first steps in creating a successful state quality award program, recommends a new guide developed for NIST by the National Governors' Association. Several states and cities already have established quality awards, with many using the Malcolm Baldrige National Quality Award as a model. These awards are used not only as an economic development tool but also to encourage private industry, schools, and state and local governments to use quality management to improve the way they do business. Recognizing this fact, NIST commissioned the new guide to outline questions and issues raised in establishing an award program. Included are areas such as developing a core group of experts to help guide the effort, setting up criteria and the application and evaluation processes, establishing fees and securing funding. Designing and Implementing a State Quality Award Program (NIST GCR 92-620) is available from the National Technical Information Service, Springfield, VA 22161, (703) 487-4650, for $19.50. Order by PB 93-154458.

NEW DIRECTORY ACCESSES OVER 900 TESTING LABS

Laboratory accreditation is growing in importance as industry and government establish or enhance their efforts to improve the quality of testing and calibration services. The National Voluntary Laboratory Accreditation Program 1993 Directory lists more than 900 domestic and foreign laboratories accredited by the NIST NVLAP program for specific test methods as of January 1993. The current fields of testing are acoustical, asbestos fiber analysis, carpet, commercial products (paint, paper, plastics, plumbing, and seals and sealants), computer applications, construction materials, electromagnetic compatibility and telecommunications, ionizing radiation dosimetry, solid fuel room heaters and thermal insulation. The labs are listed alphabetically, by field of testing and by state. For a copy of NIST SP 810, send a self-addressed mailing label to NVLAP, Rm. A162, Building 411, NIST, Gaithersburg, MD 20899-0001, (301) 975-4016, fax: (301) 926-2884.

TWO AGENCIES JOIN FORCES, COORDINATE RESEARCH

Both NIST and the National Science Foundation have long histories of supporting and conducting a variety of research programs. NIST's work is primarily directed toward industrial outreach, and NSF's activities are geared to academia. A new agreement between the two agencies links NSF and NIST in order to transfer basic technology discoveries from academic laboratories to the marketplace. The agreement will coordinate research common to the two agencies in four areas: advanced materials and processing; manufacturing technology; chemical science and engineering, including biotechnology; and high-performance computing and communications. The joint agreement is geared to help key industrial sectors of the U.S. economy. For example, chemists and chemical engineers account for 51 percent of the U.S. workforce in research and development. NIST and NSF programs in chemical sciences such as biotechnology, materials processing, health care, energy and petroleum refining can help enhance the competitive position of these industries in world markets.

U.S., SAUDI ARABIA TO CONTINUE STANDARDS WORK

A formal memorandum of understanding was signed March 19, 1993, between NIST and the Saudi Arabian Standards Organization to continue technical cooperation and standards development activities. The agreement, which recognizes the importance of the SASO in business relations between the United States and Saudi Arabia, also reflects the significance to the SASO of obtaining

continued U.S. technical assistance. The MOU formalizes cooperative linkages with U.S. private-sector and government technical experts. Saudi Arabia is the leading member of the Gulf Co-operation Council Standardization and Metrology Organization. Other members are Bahrain, Kuwait, Oman, Qatar and the United Arab Emirates. SASO technical standards are generally adopted by the other members of the GCC. These countries represent a market potential for U.S. manufacturers estimated to be more than $7 billion annually. The MOU officially acknowledges NIST's successful pilot program, initiated in 1990, for providing technical assistance to countries that desire standards on domestic products compatible with those in the United States.

PARTNERS WORK TO PROVIDE CORROSION INFORMATION

Since 1982, researchers from the National Association of Corrosion Engineers and NIST have been working to minimize corrosion's negative impact on U.S. industry, as well as on the safety of structures and facilities. Together, the two organizations are developing a series of personal computer software modules that provide rapid access to reliable information on the performance of engineering materials in corrosive environments. These expert systems contain "critically evaluated" scientific data for the design of industrial plants, pipelines, petrochemical facilities, structures, equipment and other products susceptible to the effects of corrosion. With user-friendly software, the PC modules cover the spectrum from classic databases to true "expert systems" that mimic a consultant. For information on the corrosion program, contact Richard Ricker, B254 Materials Building, NIST, Gaithersburg, MD 20899-0001, (301) 975-6023. For a listing of NACE/NIST products, contact NACE, P.O. Box 218340, Houston, TX 77218, (713) 492-0535, fax: (713) 492-8254.

KEEP COMPUTERS "ON-TIME" WITH NEW SERVICE

NIST and the University of Colorado at Boulder, CO, have jointly announced a new service for computer users that allows them to obtain precise time from an international computer network. Any computer connected to the Internet network can utilize the Network Time Service without additional charges or fees. Time information is traceable directly to the NIST primary clock system. Users can access the host computer in Boulder using several protocols, including the Network Time Protocol or the simpler "daytime" protocol (that provides complete timing information, including advance notice of leap seconds and Daylight Savings Time/Standard Time transitions). For information about the Network Time Service or instructions for its use, leave an electronic mail message at TIME@TIME_A.TIMEFREQ.BLDRDOC.GOV or write to NTS, Div. 847, NIST, Boulder, CO 80303-3328.

1993 BALDRIGE AWARD APPLICATIONS TOTAL 76

Seventy-six U.S. companies are in the running for a 1993 Malcolm Baldrige National Quality Award. They include 32 manufacturing firms, 13 service companies and 31 small businesses. Last year, 90 companies applied and five won. The award program was established in 1987 to recognize the quality achievements of U.S. companies and also to promote national awareness about the importance of improving quality management. The award program has helped stimulate a grassroots effort throughout the United States, and the world, to improve quality in many organizations. Many state, local, trade association and international quality award programs are modeled after the Baldrige Award. Firms applying for the 1993 award must provide details on their quality management system citing achievements and improvements in seven areas. Applications are evaluated by an independent NIST-appointed board. Announcement of the 1993 winners and an award ceremony will take place later in the fall. The award program is managed by NIST with the active involvement of the private sector.

PREFERRED METRIC UNITS LISTED IN NEW STANDARD

Government and industry officials concerned with metric usage in grants, contracts and other business-related activities of federal agencies will be interested in Federal Standard 376B, Preferred Metric Units for General Use by the Federal Government. The standard was approved by the 40 federal agencies that make up the Metrication Operating Committee. It was developed by the Standards and Metric Practices Subcommittee. Both groups operate under the Interagency Council on Metric Policy. The 376B standard is a revised and improved version of a 1983 standard, 376A. The new standard lists metric units recommended for use throughout the federal government and is

specified in the Federal Standardization Handbook issued by the General Services Administration. GSA has authorized the use of the standard by all federal agencies. Copies of 376B are available from GSA, Specifications Section (3FBP-W), Suite 8100, 470 L'Enfant Plaza SW, Washington, DC 20407, (202) 755-0325.

MORE QUESTIONS, MORE ANSWERS: ISO 9000

Exporters, manufacturers, testing labs and others concerned about quality, quality systems and registration will find answers to previously unaddressed questions on the ISO 9000 standards and related issues in a new NIST report. More Questions and Answers on the ISO 9000 Standard Series and Related Issues (NISTIR 5122) is a sequel to a widely distributed report on quality standards (NISTIR 4721). Special attention is given to ISO-9000-related events within the European Community that might affect U.S. trade. Information is provided on the EC conformity assessment scheme, quality system registration/approval, and the distinction between quality system certification and quality system registration. Also described is the federal government's use of ISO 9000, how to select a quality system registrar, and the accreditation programs of the Registrar Accreditation Board (an American Society for Quality Control affiliate) and other foreign accreditation bodies. Copies of NISTIR 5122 are not available from NIST. It may be obtained for $19.50 prepaid from the National Technical Information Service, Springfield, VA 22161, (703) 487-4650. Order by PB 93-140689.

NEW CLOCK IS "ONE IN A MILLION" FOR ACCURACY

NIST-7, an atomic clock that will neither gain nor lose a second in 1 million years, recently debuted at NIST's Boulder, CO, laboratory. When fully evaluated in a year, it is expected to show an accuracy of one second in 3 million years—making NIST-7 the world's most accurate clock. Who needs such accuracy? Examples of atomic clock time users are NASA (for guiding deep space probes), the Department of Defense (for operating a satellite-based navigation network), the investment banking firm Salomon Brothers (for time stamping international financial transactions) and California's Los Angeles County (for timing traffic signals). NIST-7 is the seventh generation of atomic clocks built by NIST (and its predecessor, the National Bureau of Standards) since 1949, and replaces NBS-6, which was accurate to one second in 300000 years. While both clocks measure time by counting the vibrations of a beam of cesium-133 atoms (one second elapses after 9192631770 vibrations), NIST-7 uses lasers rather than magnetic fields to better manipulate the beam and increase the clock's accuracy.

TRAPPING ATOMS MAY "CAPTURE" TIME IN LESS SPACE

A new cooperative research and development agreement between NIST and a private company seeks to develop advanced atomic clocks that use super-cold cesium atoms to measure time. The collaborators hope that the new timekeepers will provide private industry with a field standard comparable to current national laboratory standards. Traditional atomic clocks measure time by counting vibrations of cesium atoms streaming through a tube at speeds of around 200 m/s. For the advanced clocks, NIST physicists are slowing these atoms to about 1 cm/s by laser cooling them to very near absolute zero. NIST and the private company plan to design clocks that will be much smaller than those currently keeping the international time standard, yet potentially just as accurate.

"CLIPPER CHIP" OFFERS ADDED COMMUNICATIONS PRIVACY

The White House has announced a voluntary program for use of a new technology that improves the security and privacy of telephone communications while meeting law enforcement needs. Developed by the National Security Agency with NIST assistance, the state-of-the-art "Clipper Chip" can be used in new, relatively inexpensive encryption devices that can be attached to telephones. The microcircuit scrambles communications using a powerful encryption algorithm. Each device containing the chip will have two unique "keys" that must both be used to decode messages. "Key escrow" agents will retain the keys and provide access only to government officials with legal authorization to conduct a wiretap. Companies and individuals will gain protection for proprietary and private information, while law enforcement agencies still will be able to intercept lawfully the phone conversations of criminals. NIST is working on a standard to facilitate federal government procurement and use of the "Clipper Chip."

Volume 98, Number 3, May–June 1993
Journal of Research of the National Institute of Standards and Technology

GO WITH THE FLOW: IMPROVING GAS MEASUREMENTS

Gas measurement facilities that calibrate devices for regulating gas flow during the manufacture of semiconductors and other products now can have their accuracy assessed by a new NIST service. Tests of facilities can be conducted using a new gas flow measurement artifact designed by NIST and SEMATECH. A tandem arrangement of two flow meters in a portable case, the artifact serves as a transfer standard to link the gas flow measurement capabilities of laboratories to national standards. NIST personnel will conduct on-site evaluations of gas measurement facilities on a cost-recovery basis. Data produced can be analyzed graphically to document both the imprecision uncertainties of the tested laboratory and an estimate of its systematic error for the tested conditions. For more information or to schedule a test session, contact George E. Mattingly, Fluid Mechanics Building, Room 105, NIST, Gaithersburg, MD 20899-0001, (301) 975-5939, E-mail: gem@micf.nist.gov, fax: (301) 258-9201.

CATALOG HELPS USERS BUILD ISDN SOLUTIONS

The ISDN, or Integrated Services Digital Network, is a telecommunications technology that makes it possible to send and receive voice, data and pictures simultaneously over telephone lines. However, many potential ISDN users are confused about how the technology can be applied and what type of equipment is needed. A new catalog describing over 30 ISDN applications should help clear up much of the confusion. Each application lists the type of equipment and services the user needs to build the application. More than 120 products from 60 suppliers are described. The catalog was developed by the North American ISDN Users' Forum. In 1988, NIST organized NIUF with industry to help users and manufacturers agree on ISDN applications, relevant standards, and options and conformance tests. The catalog focuses on applications identified as high priority by NIUF members. A Catalog of National ISDN Solutions for Selected NIUF Applications is available for $44.50 prepaid from the National Technical Information Service, Springfield, VA 22161, (703) 487-4650. Order by PB 93-162881.

U.S./RUSSIAN STANDARDS GROUP REPORT AVAILABLE

The Proceedings of the Second Meeting of the Intergovernmental U.S./Russian Business Development Committee's Standards Working Group, March 23–24, 1993 (NISTIR 5166) reports on the exchange of information regarding standards and conformity assessment practices of each country, and an understanding of new standards-related legislative initiatives within Russia. Of particular significance at the meeting was the signing of an MOU for cooperation on standards, certification, testing and metrology between the United States (NIST) and Russia (GOSSTANDART). The Department of Commerce used this opportunity to make the first public announcement of a new initiative to provide financial support to Russians desiring to learn more about U.S. standardization practices within industrial and commercial enterprises. Copies of NISTIR 5166 are available for $36.50 prepaid from the National Technical Information Service, Springfield, VA 22161, (703) 487-4650. Order by PB 93-179968.

CRADA MILESTONE MARKED; FY92 COUNT EQUALED

Last month, NIST entered into its 300th cooperative research and development agreement since the CRADA mechanism was established by Congress in 1988. The agreement, with the South Carolina Research Authority of North Charleston, SC, calls for the partners to establish and operate a testbed facility for the manufacture of electrical products designed in conformance to STEP (STandard for Exchange of Product model data). STEP is the U.S.-led drive to create a universal system for exchanging information on a product's design, manufacture, and support. A new monthly record for CRADA signings was set in April when NIST entered into 20 agreements. This brought the total number of CRADAs (through April 30, 1993) to 316, and for the first 7 months of fiscal year 1993 to 82. The latter figure equals the entire CRADA count for the previous fiscal year. For information on establishing a CRADA partnership with NIST, contact Bruce E. Mattson, B256 Physics Building, NIST, Gaithersburg, MD 20899-0001, (301) 975-3084.

NEW REFERENCE "MEASURES UP" FOR ELECTRONICS

Measurement capability for the electronics industry is critical to research and development, manufacturing, marketplace entry, and after-sales support functions. It affects the performance, quality, reliability, and cost of products. A new NIST publication, Measurements for Competitiveness in Electronics (NISTIR 4583), identifies those currently unmet measurement needs most critical for the U.S. electronics industry to compete successfully worldwide. Nine fields of electronics are covered: semiconductors, magnetics, superconductors, microwaves, lasers, optical-fiber communications, optical-fiber sensors, video, and electromagnetic compatibility. Each field's section contains a technology review, an overview of economic importance to the world market, a look at U.S. industry goals for competing internationally, and a discussion of measurements needed to meet those goals. Examinations of the importance of measurements in competitiveness, NIST's role in measurements and the U.S. electronics industry as a whole also are included. NISTIR 4583 is available for $52 (print) and $19.50 (microfiche) prepaid from the National Technical Information Service, Springfield, VA 22161, (703) 487-4650. Order by PB 93-160588.

BIBLIOGRAPHIES LIST WHAT'S NEW IN NIST EM STUDIES

Persons interested in NIST electromagnetics research can now obtain two bibliographies that list publications by the institute's EM scientists in Boulder, CO, from 1970 to the present. A Bibliography of the NIST Electromagnetic Fields Division Publications (NISTIR 3993) covers antennas, dielectric measurements, electromagnetic interference, microwave metrology, noise, remote sensing, time domain and waveform metrology. The second reference, Metrology for Electromagnetic Technology: A Bibliography of NIST Publications (NISTIR 3994) covers optical electronic metrology, cryoelectronic metrology, and superconductor and magnetic measurement. Copies of these bibliographies may be ordered from the National Technical Information Service, Springfield, VA 22161, (703) 487-4650. NISTIR 3993 is available for $27 (print) and $12.50 (microfiche) prepaid; order by PB 92-116367. NISTIR 3994 is available for $19.50 (print) and $9 (microfiche); order by PB 92-116375.

NATIONAL CONFERENCE ON WEIGHTS AND MEASURES HOLDS "INTERIM MEETING"

The National Conference on Weights and Measures held its "Interim Meeting" at the Bethesda Hyatt Jan. 10–14. Technical committees met concurrently throughout the week to develop legal metrology standards and manage other study programs, many of which will be recommended to the conference in July 1993, at its 78th Annual Meeting in Kansas City, MO. The Specifications and Tolerances Committee will recommend that the conference should permit custody transfer (controlling $1.6 trillion revenue metric ton-km) of individual railroad cars by means of coupled-in-motion weighing technology, and that electronic audit trails, already permitted, should meet minimum standards of protection and provide increasing amounts of information, depending upon how much metrological control is accessible remotely.

The Laws and Regulations Committee met with representatives of the Food and Drug Administration, Federal Trade Commission, the U.S. Department of Agriculture, and more than 200 trade associations and packagers to implement new requirements and coordinate manufacturing and other interests for labeling all consumer and nonconsumer packages in metric units of measure by 1994.

Both the Specifications and Tolerances and Laws and Regulations Committees resolved measurement and method of sale issues for the retail sale of compressed natural gas as a motor fuel. The Education, Administration, and Consumer Affairs Committee concluded review of a training module on general legal metrology administration. The Liaison Committee concluded management and development of a new consumer pamphlet that will be available in February from the Consumer Information Center in Pueblo, CO. Several representatives of the executive committee met with staff of Congressmen to discuss the importance of state and local weights and measures agencies as the infrastructure of the marketplace, to provide measurement traceability to local and international business concerns through their weights and measures laboratories, and to maintain a fair marketplace for honest business.

COLLABORATION WITH INDUSTRIAL PARTNER EXTENDED FOR ANOTHER YEAR

The cooperative research and development agreement between a major U.S. roller bearing manufacturer, and NIST recently was extended for another

year. The original agreement was signed last year to carry out research in spindle characterization for implementation of hard-turning applications. Hard turning is referred to single point turning of materials harder than 55 R_c such as tool steels and bearing steels. Precision turning of hard materials is a critical and potentially cost-effective technology, especially for small-batch production, because it eliminates costly grinding setups or multiple heat treatment processes to obtain proper hardness after cutting. Under last year's agreement, the manufacturer has loaned a state-of-the-art roller bearing spindle to be characterized. Under this year's agreement, the company will upgrade this spindle and send a researcher for a period of 6 mo to work with NIST researchers to evaluate the new spindle for hard-turning applications.

NIST HELPS KICK OFF THE NGIS PROGRAM

On Nov. 5, NIST hosted the kickoff meeting marking the beginning of the Next Generation Inspection System (NGIS) program. NGIS is a development effort by a consortium of U.S. companies and NIST whose goal is to improve current manufacturing inspection methods and demonstrate practical results. NGIS is administered by the National Center for Manufacturing Sciences.

The next generation of inspection systems will contribute to higher quality products and reduced manufacturing costs through faster inspection, inspection of complex surfaces, better integration of computer-based inspection systems into the factory through use of part models for inspection programming and results analysis, data formats for inspection results, and provision of feedback of inspection results to manufacturing processes.

NIST's contribution to the program centers around a testbed that supports experiments in developing advanced systems and techniques for manufacturing inspection. A goal is to improve on current part inspection that uses touch-trigger probes. Testbed facilities include a coordinate measuring machine, sensor systems developed by industry, sensor systems developed at NIST, control systems, and computer hardware and software.

Projects that will use this testbed include: development of advanced sensor systems, such as vision and laser probes; integration of multiple sensor systems; development of advanced data analysis systems; and development of a NIST hierarchical control system for inspection tasks.

CIM STANDARDS FOR APPAREL INDUSTRY

The Apparel Product Data Exchange Standard (APDES) Project Team at NIST published two reports entitled, "Report on Scoping the Apparel Manufacturing Enterprise" and "A Prototype Application Protocol for Ready-to-Wear Pattern Making." The first report identifies a set of manufacturing data interfaces that could be standardized for the effective computer integration of the information required to operate an apparel manufacturing enterprise. The second report describes an information model for ready-to-wear pattern making, one of the manufacturing data interfaces defined in the first report, along with its testing procedures.

The Defense Logistics Agency (DLA) is sponsoring the NIST project to extend the emerging international Standard for the Exchange of Product Model Data (STEP) to include apparel product data. This work is part of a larger DLA program to improve apparel manufacturing technology. These extensions will lay the groundwork for computer integration of the apparel product life cycle, and it will enable clothing manufacturers to reap the benefits of standardized product data representation. NIST is working with the American Apparel Manufacturers Association, the Fashion Institute of Technology, and several other organizations and companies to develop official STEP standards for apparel. These reports will serve as input for developing such standards.

LIQUID-HYDROGEN COLD NEUTRON SOURCE MODELED BY NIST RESEARCHERS

A novel design has been developed for a new, second-generation cold neutron source to be installed in the NIST Research Reactor as part of the Cold Neutron Research Facility (CNRF). The new source is an essential element in the successful completion of the CNRF, which is a major national resource. The design, developed at NIST uses a spherical cavity with an annular blanket of liquid hydrogen to moderate the neutrons and deliver the cold neutron beam through an aperture. It is preferable to have no moving parts in the hydrogen system and to remove any heat generated using natural circulation. Of prime importance is the stability of the fluid cooling system and the ability to maintain a minimum overall hydrogen density.

To verify the design, a full-scale engineering simulation was constructed and tested at NIST. The

engineering simulation was realized by building a glass model of the moderator cavity whose mass could be determined by direct weighing, with liquid hydrogen circulating under design heat-loads. In addition, a NIST scientist developed a numerical model of the complete fluid circulation system to permit exploration of operating parameter space. These tests and the numerical model confirmed the basic soundness of the design, identified areas that could be improved, established the heat load that could be handled, and led to further insights regarding the fluid circulation and the relationship between vapor-void fraction and heat load. As a result, full-scale construction of the actual source is now under way, with full confidence that the system will meet all requirements.

LASER-ENHANCED-IONIZATION SPECTROSCOPY USING DIODE LASERS

NIST scientists have used diode lasers to detect trace impurities by laser-enhanced ionization in flames. In one experiment they demonstrated a detection sensitivity of 300 ppt (parts/trillion) of rubidium in water. Their first experiments were performed on rubidium and cesium since the spectral lines for these could be reached easily with readily available diode lasers.

The results demonstrate a promise for diode lasers in analytical chemistry. There are many other optical methods that would be applied in chemical analysis if the lasers required were not as cumbersome and expensive as conventional lasers (e.g., dye lasers). The simplicity, low cost, and small size of the diode lasers make them attractive for such analytical applications. However, in some cases it will be important to reduce the natural linewidth, and it is important to extend the frequency coverage, particularly to the blue/green region where many important chemical lines are found.

The very simple experimental system consists of an atmospheric-pressure, air-hydrogen (or acetylene) flame and water samples that contain the atoms of interest at low concentrations. The water samples are aspirated into the flame where the diode laser excites the atoms, which are then ionized by the flame. The ionization is detected by the increased flame conductivity using probe electrodes.

TRANSFER OF ARC WELDING TECHNOLOGY

A private company has signed a second cooperative research and development agreement (CRADA) with NIST. In the previous CRADA, NIST's weld sensing technology was evaluated for its ability to monitor the weld quality of the company's production lines. It was found that the NIST weld sensors could improve the detection of welding problems when evaluated with the electrodeshielding gas combination used in production. As a result of the success of the first CRADA, the company plans to use the NIST technology in both production and research applications.

In the second CRADA, NIST will help the company implement this technology and the company will evaluate the NIST technology under high-volume production conditions. The private company has decided to replicate the entire NIST weld sensing capability (the sensing systems as well as special calibration equipment) in its welding research laboratory, with equipment selection advice from NIST. This in-house capability will permit new applications to be developed and improve the technology transfer between NIST and the company. NIST also will assist with the interpretation of the production data, using the sensing strategies and algorithms evaluated under the first CRADA.

MOISTURE PROFILES NEAR A DIELECTRIC/SILICON INTERFACE

Scientists at NIST made the first definitive measurements of the moisture profile in a dielectric film deposited on a silicon substrate. The sample, a polyimide resin (PI) used in electronic packaging, was supplied by a private company as part of a cooperative program begun under a recent CRADA. The observed high concentration of moisture in the polymer adjacent to a solid interface had long been postulated to explain various moisture-related problems encountered in composites, protective coatings, and electronic packagings. However, despite the importance of this effect, there was no direct evidence prior to these measurements.

The measurements were made using a neutron reflectivity (NR) technique developed at NIST. A significant difference in the NR results was

observed between a dry sample and one exposed to deuterated water vapor. This difference can be accounted for by the presence of a moisture rich layer about 25 Å thick near the PI/ silicon interface in the wet sample. The water content within this thin layer reached 16 percent by volume as compared to the bulk saturation level in PI of 2.4 percent. The work here not only provides the first direct evidence but also permits quantification of the effect.

EXPANDED RESEARCH WORK ON SUBSTITUTED DERIVATIVES OF THE 123 SUPERCONDUCTOR

Much recent materials research worldwide on high-temperature superconductivity is focused on the effect of different parts of the structure of 123-type superconductors on the electric properties of these materials. Substitution compounds in which the Y, Ba, chain Cu, and plane Cu atoms are replaced selectively by impurity metal atoms of different species are being intensely studied. A critical component of these efforts is the determination of atomic arrangements with high precision in order to establish correlations between selected bond distances and values of the critical temperature T_c, and the superconducting properties. An expanded program of research in this field is under way at NIST in collaboration with private industry and the National Center for Scientific Research (Grenoble, France). A visiting scientist from France is supported jointly by private industry and NIST to accelerate this materials research effort. Compounds of general formula $RL_2Cu_{3-x}M_xO_y$ (R=rare earth; L=Ba, Sr; M=Co, Fe, ...) are being investigated with neutron powder diffraction methods. The new high-resolution powder diffractometer now being tested at the NIST reactor will be a key to more rapid progress in this critical area.

VISIBILITY THROUGH SMOKE CLOUDS

NIST scientists and a university professor have obtained results critical to (a) assessing the visibility through plumes from burning oil spills and (b) the climatic effect of large fires such as in Kuwait. Jointly funded by the Mineral Management Service (Department of the Interior) and NIST, the team found that light transmission through a cloud of smoke is unchanged as the average agglomerate size grows by a factor of 24. The smoke, produced by the burning of crude oil in a 60 cm diameter pan, was drawn into a 1 m^3 cubical chamber. The team measured the transmittance of light through the chamber at three wavelengths spanning the visible range over a 2 h period. They then demonstrated that this constancy of the transmittance is inconsistent with predictions of the commonly used Mie theory, but fully consistent with predictions based on fractal optics.

NEW MECHANISM FOR SOOT FORMATION IN FLAMES

NIST scientists have developed critical new insights into the formation of soot in turbulent flames. Soot formation is desirable in such applications as furnaces and the production of carbon black, but is not beneficial in fires, since its incandescence is the primary cause of heat transfer and flame spread. At present there is no model for predicting the soot yields from various fuels. The NIST team obtained time- and spatially resolved planar images of hydroxyl (OH·) radicals using laser-induced fluorescence, as well as simultaneous soot density profiles from elastic scattering of the particles themselves. [OH· is the species responsible for burnout of the soot formed in flames.]

The experiments were performed in time-varying, laminar CH4/air diffusion flames burning in a co-flowing, axisymmetric configuration at atmospheric pressure. Acoustic forcing was used to phase lock the periodic flame flicker to the pulsed laser system operating at 10 Hz. For conditions where the tip of the flame is clipped, the soot signals increased by more than a factor of seven compared to a steady-state, laminar flame with the same mean fuel flow velocity. Quantitative absorption measurements with a He-Ne laser also showed an order-of-magnitude increase in soot volume fraction for the flickering flames. The time-varying flames exhibited a larger range of combustion conditions than observed in corresponding steady-state flames, including different residence times, temperature histories, local stoichiometries, and strain and scalar dissipation rates. Future work will focus on elucidating the particular combination of these parameters responsible for the greatly increased soot production observed in the time-varying flames. A manuscript detailing these revolutionary findings has been submitted to Combustion and Flame.

NIST SUPPORTS COMPUTER-AIDED ACQUISITION AND LOGISTIC SUPPORT (CALS) PROGRAM IN RASTER GRAPHICS

In its continuing support of the CALS initiative of the Department of Defense, NIST contributed to the development of raster graphics file formats for

large documents. NISTIR 5108, Raster Graphics: A Tutorial and Implementation Guide, examines the technical issues facing an implementor of the raster data interchange format defined in the Open Document Architecture (ODA) Raster Document Application Profile. Intended for system architects and programmers, the tutorial provides an overview of relevant standards, discusses the benefits of ODA, and gives an overview of ODA.

NIST SPONSORS SYMPOSIUM ON DIGITAL SIGNATURE APPLICATIONS

Recently NIST's Federal Digital Signature Applications Symposium attracted about 200 participants from government and industry. The symposium provided a forum for discussion of common problems and issues in the application of digital signature technology to federal government systems.

The Digital Signature Standard (DSS) has been proposed to provide a digital signature that can be used to identify and authenticate the originator of electronic information and to verify that information has not been altered after it is signed, providing message integrity. Incorporating the proposed DSS into government applications would allow federal agencies to completely replace many paper-based systems with automated electronic systems, resulting in increased efficiency and reduced costs.

NORTH AMERICAN INTEGRATED SERVICES DIGITAL NETWORK (ISDN) USERS' FORUM (NIUF) MEETS

The NIUF drew over 200 users and implementors of ISDN technology to its recent meeting held at NIST. The NIUF now has 32 signatories to the cooperative research and development agreement with industry, which governs the management of the forum. Highlights included meetings hosted by a private company to discuss National ISDN-2 Customer Equipment Guidelines, the submission of three new ISDN user applications, and the approval of six working group charters. The plenary approved two documents for publication: A Catalog of National ISDN Solutions for Selected NIUF Applications and Unified Message Notification (Application Profile).

NIST LEADS DEMONSTRATION OF ELECTRONIC COMMERCE REPLY CARD

NIST has been selected by industry to lead the Electronic Business Reply Card demonstration targeted for the 1993 CALS Expo in Atlanta in December, one of two high-visibility "scenario" demonstrations in the new Electronic Commerce of Component Information (ECCI) program. ECCI was formed in the context of the industry-government National Initiative for Product Data Exchange in response to urgent needs of the electronics sector. The demonstration is intended to highlight the electronic transfer of information associated with the release and distribution of new components and products and also establishes the networking and interface framework for the ECCI project.

Currently, the exchange of component information for electronic products is paper intensive and "data books" are out of date from the moment they are received by customers. The dissemination of new product announcements and response to requests for detailed component information are other drains on industry resources. One company, for example, spends approximately $9 to respond to each request for information on a new product, not including the cost of the product announcement or the preparation of the information package to be distributed. Electronic notification of new products, requests for information, and receipt of requested information would represent a substantial cost savings to information providers and would increase the timeliness and quality of the data received by end users.

The second scenario project demonstrates the exchange of digital information associated with the selection and acquisition of components during the product design process, allowing the end user to incorporate the information received directly into computer-aided engineering/design systems. Taken together, the two scenarios will demonstrate the concept of a virtual enterprise of trading partners and information brokers using electronic commerce in the production, distribution, and application of electronic component information and products.

LASER FOCUS WORLD ARTICLE REPORTS NIST CONCLUSIONS ON NEED FOR LASER BEAM ANALYSIS

In the article "Laser Beam Analysis Pinpoints Critical Parameters," NIST scientists report and substantiate their conclusions that accurate analysis of laser beam parameters—beam width, divergence, shape, and a factor relating to propagation constant—is needed to match a laser with a given application. Total power alone is not a sufficient consideration to ensure that a laser is used efficiently and effectively.

This article was featured as a special "technology guide" on beam diagnostics in the January 1993 issue of Laser Focus World. Referring to specific applications, the authors state "Beam attributes affect quality for applications such as laser printers and laser machining . . . these attributes also affect barcode-scanning reliability, fiberoptic-coupling efficiency, optical-recording density, and surgical efficiency." Another major conclusion based on the authors' NIST experience is that diffraction effects on near-field beam profiles result in sufficiently rapid changes of profile with distance that beam analysis should be carried out in the far field.

NIST has received numerous requests over the past 10 years to provide more support to laser users in the area of beam-profile analysis. In this regard, NIST has been participating for the past 2 years in Subcommittee 9 on lasers of the International Organization for Standardization; a working group of the subcommittee is in the process of developing a standard procedure for beam analysis.

NIST HAS NEW MASS COMPARISON CAPABILITY

NIST has installed a new mass comparator. The comparator is an electronic balance capable of comparing nominally equal weights of any value from 100 g to 1 kg. The built-in weight handler of the balance is essentially a computer-controlled pick-and-place robot so that measurements are typically made without the environmentally altering presence of an operator. Readability of the device is 1 μg. The device is to be used for state-of-the-art transfer of the national unit of mass to NIST clients and other NIST groups. When environmental factors such as barometric pressure, temperature, humidity, and CO_2 content of air are accounted for or controlled, the comparator will yield measurements with a precision approaching a part in 10^9.

INITIAL RELEASE OF STEP READY FOR COMMERCIAL USE

By unanimous vote of 10 countries, the International Organization for Standardization Subcommittee TC184/SC4 registered all documents of the STEP Initial Release as Draft International Standards. The Standard for Exchange of Product Model Data (STEP) specifies how to represent all elements of product data in digital form and how to share them among business partners in the form of physical files. This is the same type of data typically generated and used by CAD, CAE, and CAM applications.

The decision is indicative of a broad consensus across Europe, the United States, and Japan that the initial release of STEP is now technically complete and that widespread commercialization of this important technology can now proceed. This vote gives a "green light" to multiple implementation efforts worldwide at both vendor companies and at the five STEP centers in France, Germany, Japan, the United Kingdom, and the United States. The release caps a major technical collaboration of over 300 experts across 16 countries who worked together to produce the 2,300 pages of standards documentation.

The initial release addresses two priority application areas, drafting and product configuration management, and many more are under way. Work is progressing nicely on 17 additional application protocols that will be added to STEP in the near future.

MAMMOGRAPHY, X RAYS, AND QUALITY CONTROL

General improvement of image quality for mammography requires more accurate control and measurement of x-ray source voltage than is available through current non-invasive methods such as penetrameters and filter packs. Although the needed refinement is accessible through traditional (invasive) measurements using high-potential dividers, there are complications due to the wide range of frequencies and voltage waveforms which must be accommodated. In response to this situation, scientists at NIST have devised an alternative approach using moderate resolution, wavelength dispersive, diffraction spectroscopy. Using a prototype system, they have demonstrated that the needed precision and accuracy can be achieved. The approach, is readily generalized for measurements throughout the range of radiological and radiographical x-ray imaging.

The device uses Laue diffraction to obtain two images of the spectrum of the source symmetrically disposed with respect to the centerline or zero wavelength position. A wavelength contained in the source spectrum appears at two points in the "focal plane" separated by a readily calculated distance. At the high-frequency limit of the continuous spectrum, photons are emitted with the full energy, $E = eV$, of the electrons being accelerated by the x-ray source voltage, V. The spectrograph is thus an absolute instrument requiring only a measurement of a length ratio to establish the x-ray tube voltage without reference to any external standardization. In practice it is more convenient to note the locations of the characteristic emission lines of the target and use these to indirectly establish the camera scale.

NIST/INDUSTRY CONSORTIUM ON POLYMER BLENDS

Representatives from seven companies met recently with staff from NIST to form an industrial consortium on polymer blends and alloys. The purpose of the consortium is to develop the science base to control the microstructure of polymer blends through interfacial modification and shear mixing. The focus of the consortium derived from input provided by industrial representatives at a workshop held at NIST in April 1992.

Polymer blends are mixtures of two or more polymers that produce a material with superior properties over those of the constituents. The enhancement of properties derives from the microstructure formed in the course of processing. The ability to control and manipulate the microstructure in predictable ways is key to the more efficient processing and enhancement of properties.

NIST and industrial scientists will collaborate on small-angle neutron and light-scattering studies of a particular polymer blend under shear fields and temperature variations. The active participation by industrial scientists is considered critical to transferring the knowledge to industry. Researchers from member companies of the consortium will then have access to sophisticated measurement facilities at NIST for conducting independent investigations on systems of particular interest to their companies.

NIST EVALUATES ALTERNATIVE REFRIGERANTS FOR INDUSTRY

NIST researchers completed an evaluation of Refrigerant 22 (R-22) and Refrigerant 502 (R-502) alternatives and presented the results at a special January meeting of the Air-Conditioning and Refrigeration Institute, the trade association of 170 U.S. refrigeration and air-conditioning companies. Finding replacements for these refrigerants is critical to U.S. competitiveness because more than 5000 U.S. companies rely on HCFCs and CFCs to produce goods and services valued at over $28 billion a year. Over 700000 jobs and $200 billion worth of installed refrigeration equipment face certain servicing problems, reduced energy efficiency, and possible obsolescence.

Using a semi-theoretical model, CYCLE II, NIST staff screened a broad range of fluids and their mixtures at different compositions. Two pure fluids, one azeotrope, and nine zeotropes were evaluated, both as potential "drop-ins" for existing equipment and assuming a system modified to take advantage of the fluid's properties. Although the final selection of replacement refrigerants will be based on laboratory tests, the simulation study limited the list of fluids that warrant expensive laboratory evaluations.

NIST CONDUCTS SUCCESSFUL MULTIVENDOR OPEN SYSTEMS INTERCONNECTION (OSI)/FRAME RELAY INTEROPERABILITY TRIAL

In a cooperative project with industry, NIST recently carried out a multivendor trial and interoperability demonstration of the use of frame relay technology in OSI networks. Several private companies participated in the demonstration. The trial's primary objective was to illustrate the viability of frame relay technology to support OSI applications and the integration of frame relay into existing OSI networking environments. OSI applications demonstrated included X.400 electronic mail, file transfer access and management, and virtual terminal. The trial confirmed the technical feasibility of OSI end and intermediate systems operating OSI higher-layer protocols directly over user interfaces to frame relay networks. Also shown was the interworking of frame relay with other networks commonly used in OSI environments, such as IEEE 802.3-based local-area networks (LANs) and X.25 wide-area networks (WANs). In these scenarios, the frame relay networks acted as transit networks to concatenate geographically separated LANs and WANs. It is expected that the trial success will open the door for frame relay to be included in the emerging Industry/Government Open Systems Specification (IGOSS).

NEW PUBLICATION FOCUSES ON DATABASE MANAGEMENT IN ENGINEERING

NIST researchers collaborated on a study of the applicability of database technology to engineering systems. NISTIR 4987, Database Management Systems in Engineering, describes the new generation of database systems that support the evolutionary nature of the engineering environment by focusing on the temporal dimensions of data management. In addition, the trend in manufacturing toward concurrent engineering raises new considerations for the cooperative use of data in a distributed engineering environment.

OPTICAL CHARACTER RECOGNITION (OCR) RESEARCH ADVANCES

NIST researchers are evaluating techniques to measure the performance of OCR systems that capture data from forms. Many large data entry systems are being designed to collect data from specified areas of forms, some of which may be multipart and completed with machine-printed or handprinted characters. As this technology advances, the number of OCR products available in the marketplace increases. Many of these products accomplish the data capture with a high degree of accuracy, but each product is based on a different, often proprietary, set of algorithms. NISTIR 5129, Methods for Evaluating the Performance of Systems Intended to Recognize Characters from Image Data Scanned from Forms, assists system developers and users of OCR technology in selecting the OCR system best suited to their requirements.

ANALYSIS OF COMMENTS ON PROPOSAL FOR CONFORMITY ASSESSMENT SYSTEM EVALUATION (CASE) PROGRAM

In response to a March 1992 Federal Register notice proposing the establishment of a voluntary Conformity Assessment System Evaluation (CASE) program, NIST received comments from 173 respondents. CASE would enable the Department of Commerce, acting through NIST, to provide required assurances to foreign governments that designated U.S.-based conformity assessment activities related to product sample testing, product certification, and quality systems registration satisfy international guidelines for their acceptance. The comments indicate a preference for NIST to provide recognition of privately operated accreditation programs, although considerable support was also received for NIST to provide both accreditation as well as recognition. The results of the analysis are reported in NISTIR 5138, A Program for Conformity Assessment System Evaluation: Analysis of Comments on the NIST Proposal.

NIST DEMONSTRATES WORLD-RECORD FREQUENCY RESPONSE OF 8 TERAHERTZ IN HIGH-TEMPERATURE JOSEPHSON JUNCTION

NIST recently demonstrated the highest frequency response ever achieved—8 THz—in a lithographed Josephson junction, thus showing the speed potential for a reproducible element of an integrated circuit (as opposed to a special one-of-a-kind point-contact device). At the same time, researchers demonstrated the highest switching voltage of any microfabricated Josephson junction, showing that the fabrication process is robust with achievable allowances for manufacturing variation.

The demonstration of frequency response required developing a very high-frequency far-infrared laser to serve as the source and fabrication of the first antenna-coupled high-temperature superconductor-normal metal-superconductor junction, a development depending on the capability of the division to make both litho-graphed micro-antennas and step-edge junctions. These junctions are formed over a nearly vertical, 100 nm high step in a substrate. A yttrium-barium-copper oxide (YBCO) thin film is then deposited at an angle onto the substrate so that it is not continuous across the step. Next, a layer of normal metal is deposited on top of the YBCO to connect the two superconducting regions. The normal metal becomes weakly superconducting as electrons move back and forth between the superconducting and normal films. This phenomenon is called the "proximity effect" and causes the device to behave like a Josephson junction.

Application areas for the NIST (patent applied for) technology include electrical standards, specialized digital circuitry, sensitive radiation detectors, and biomagnetic instrumentation. U.S. manufacturers already have incorporated results from the NIST work in their advanced development programs.

GUILDLINE OFFERS AC VOLTAGE REFERENCE BASED ON NIST-DEVELOPED DIGITALLY SYNTHESIZED SOURCE

A calculable rms ac voltage source developed by NIST has become the basis for a new product developed by a private company. The company's instrument depends on NIST's digital waveform synthesis technology to generate 16 precision waveforms stored in non-volatile memory. The NIST design is patented and a licensing agreement between the company and NIST has been negotiated.

NIST scientists have been developing variants of the basic source design; the company's instrument is patterned on a version producing stepped sine-wave voltages at a nominal level of 7.07 V rms from 0.01 to 50 kHz, with an uncertainty of less than 10 parts per million (ppm) to 1 kHz and less than 50 ppm to 50 kHz. The design principle of applying digital methods to creating waveforms from data

stored in memory provides great flexibility, including the capability of generating sine waves with known amounts of distortion, as well as a variety of other useful test waveforms. The team currently is developing an enhanced version of the source incorporating features such as active attenuators for scaling the output to as low as 1 mV, frequency capability to 100 kHz with 128 steps per period, and an IEEE 488 bus interface.

ISO PROJECT STARTED ON STEP APPLICATION PROTOCOL FOR DIMENSIONAL INSPECTION PLANS

At its meeting, in early 1993 in Turin, Italy, ISO TC184/SC4 approved an application protocol (AP) project for ISO 10303, Product Data Representation and Exchange. (ISO 10303 is also known as STEP.) The AP will allow industries to use STEP integrated resources to represent and exchange data with dimensional inspection planning applications. The project is sponsored by NIST.

The Inspection Planning AP will specify information requirements for exchange, access, and use of STEP for inspecting manufactured parts using coordinate measuring machines and vision systems. The project is a collaboration between the NIST National PDES Testbed and the ESPRIT VIMP (vision-based, on-line inspection of manufactured part) project. This AP will enable specification of data structures consistent with the ANSI/CAM-I DMIS standard (Dimensional Measurement Interface Specification). With this AP, companies will be able to create standard inspection plans based on product definitions in digital form.

NIST TEAM DEVELOPS TAILORED STATIONARY PHASES FOR CAROTENOID ISOMER SEPARATIONS

As part of an ongoing research effort to understand and utilize molecular interactions that provide for separations in liquid chromatography, researchers at NIST have developed new stationary phases optimized for the separation of carotenoid isomers. Carotenoids are a class of organic compounds that occur naturally in fruits and vegetables and are beginning to be of significant interest in a variety of industrial and health fields. Carotenoids, used widely as natural pigments and as nutrients in food, are being investigated for their effect in the reduction of various diseases, including cancer. Because of the economic and medicinal significance of these compounds, the ability to separate individual carotenoid compounds is of considerable importance. Subtle differences in the geometry of carotenoid molecules give rise to numerous isomers and related compounds, making the separation and measurement of individual carotenoid species very difficult.

The ability to separate and measure carotenoids has been enhanced recently by the development of a new stationary phase for liquid chromatography tailored specifically to "recognize" the subtle structural variations among carotenoid compounds. To a large extent, the ability of a column to provide separation is controlled by the structure of the bonded phase at the molecular level. The selection of suitable substrate properties (particle size, pore size, and surface area) and surface modification procedures (ligand and phase type) permits wide variations to be created in the retention properties of the resulting bonded stationary phase. By optimizing each of these parameters for carotenoids, a column was developed that provides significantly improved separations of complex isomer mixtures. The development of a carotenoid column represents a practical application of years of basic research into the nature of fundamental chromatographic retention processes.

MAGNETIC ENGINEERING OF THIN FILMS

The recent discovery of the "giant magnetoresistance (GMR) effect" in magnetic multilayers has stimulated much interest in the antiferromagnetic coupling between magnetic layers, which is associated with the GMR effect. This effect could serve as the basis for producing new, improved nonvolatile memory chips, critical to the personal computer industry.

Scientists at NIST recently studied selected samples from a private company because some thin films they produced, containing layers of cobalt and copper, exhibit the largest GMR effect found to date. These films were found to be nearly polycrystalline (made up of many crystallites). This surprising result raised the question of which crystallite was most important in determining the observed physical properties. Accordingly, several different single-crystal cobalt-copper multilayers were produced and studied. These studies indicated that the (100) crystallites are responsible for the antiferromagnetic coupling. These results suggest that controlling the (100) crystallite concentration in these multilayers will be a way to control the antiferromagnetic coupling and, thus, to engineer the desired values of the antiferromagnetic coupling strength for thin-film device applications.

Volume 98, Number 3, May–June 1993
Journal of Research of the National Institute of Standards and Technology

NEW CARBON-DIOXIDE LASER LINES OBSERVED

The laser spectroscopy group at NIST recently observed 40 new continuous-wave laser lines of carbon dioxide. These lines, the 9 μm hot-band lines, some developing over 8 W of output power, will provide a new source of laser radiation for spectroscopy. Frequencies of 36 of the 40 lines have been directly measured relative to other well-known CO_2 lines using a heterodyne technique.

The carbon-dioxide laser has been so thoroughly studied over many years that it is surprising to find new laser lines in the system. The new observations were made possible by the use of a special high-resolution grating (a grating-coupled laser cavity was used), a ribbed laser tube, and a higher than normal discharge current. The lines had been predicted by theory but never observed until this work.

PATENT DISCLOSURE ON LASER REFRIGERATOR

The current best means for cooling solids to low temperatures are cryogenic liquids and Sterling cycle refrigerators. Cryogenic fluids are messy, expensive, and difficult to regulate and automate. Sterling cycle pumps are unreliable and vibrate. A NIST scientist has invented an all solid-state refrigerator, which consists of a laser beam directed onto a semitransparent crystalline solid and exploits internal quantum mechanisms to cool the solid. The laser beam frequency is set to be a little lower than the direct band gap of the solid, so that the solid absorbs the photon from the laser beam and then re-emits it at slightly higher energy. The result is a net loss of energy and a cooling of the solid. The invention would substitute for a Sterling refrigerator over temperatures ranging from 40 to 200 K. It is estimated that more than 95 percent of Sterling refrigerators are used in this temperature range. Currently, Sterling refrigerators are most often used in infrared viewing systems, but if high-temperature superconductors become practical, cryogenic cooling devices may be important for a wider range of applications.

IMPROVING AMORPHOUS SILICON FILMS FOR ELECTRONIC APPLICATIONS

Because hydrogenated amorphous silicon (a-Si:H) films are inexpensive to produce in very large areas, they are leading contenders for solar electricity generation. They also are used for thin-film transistors in display and reading devices. However, for reasons not well understood, the properties of these devices depend critically on the plasma deposition conditions, and their electrical properties do not attain what is believed possible. A major cause of this uncertainty is an inadequate understanding of the atomic structure of this amorphous material, knowledge that a novel application of a scanning tunneling microscope (STM) is beginning to provide. Using an STM a NIST scientist has directly measured the atomic-scale structure of the surface of these films as a function of time during growth. The films are found initially to grow very homogeneously and compactly, but with increasing thickness this degenerates into rough and relatively porous materials (on an atomic scale). These observations have forced a rethinking of deposition processes and plasma chemistry, as well as of the properties and defects of this semiconductor material. These results, as well as NMR and x-ray scattering observations from other laboratories, implicate small voids in the material as primary determinants of electrical imperfections. This is stimulating researchers and engineers to develop more optimal deposition methods.

INVESTIGATION OF POLYMER/METAL INTERFACES USING ULTRA SOFT X-RAY ABSORPTION SPECTROSCOPY

Researchers from private industry are collaborating with a NIST scientist of a University of Michigan researcher to study polymer surfaces and metal polymer interfaces using ultra soft x-ray absorption spectroscopy at the National Synchrotron Light Source, Brookhaven National Laboratory. They have been able to study the buried interface between DVS bis-BCB (divinyl siloxane bis-benzocyclobutene) coated with 10 to 50 nm of aluminum. The functional groups at the surface of the polymer undergo a dramatic orientation change upon metal over coating during the formation of the polymer metal interface. DVS bis-BCB is used for dielectric layers in new generation multilayer interconnect devices. Their experiments provide new detailed chemical information critical for predicting and optimizing the adhesion at metal/polymer interfaces.

CRACK PROPAGATION IN AGING AIRCRAFT

In one design approach for airplane fuselages, circumferential rings or frames are intended to steer dangerous longitudinal cracks—if they should

appear—in the less-threatening circumferential direction around the fuselage. However, since the highly publicized Aloha Airlines accident in 1988, in which the roof of a Boeing 737 ripped off and exposed passengers to the open sky, it has been hypothesized that in the case of aging aircraft, cracks that start running longitudinally may continue to do so because cracked rivet holes may provide a path of lesser resistance.

To gain an understanding of this crack propagation mechanism, the Federal Aviation Administration, through the National Aging Aircraft Research Program, contracted with NIST to investigate the process of fracture in aircraft structural aluminum-alloy sheet in the presence of multiple cracks. Under this contract, NIST scientists will use its specialized facilities and capabilities to carry out a series of 12 instrumented tension tests on 4 m (13 ft) precracked aluminum-alloy panels to characterize the manner in which cracks propagate and link up to produce failure.

AISI PROJECT ON MICROSTRUCTURAL ENGINEERING

The American Iron and Steel Institute (AISI) is sponsoring an industry/NIST/university R&D project entitled "Microstructural Engineering in Hot-Strip Mills." The collaborators are U.S. Steel, University of British Columbia, and NIST. The objective of the project is to develop a predictive tool (model) that quantitatively links the properties of hot-rolled products to the processing parameters of a hot-strip mill. The project will focus on the microalloyed steel grades. Successful completion of the project will be invaluable in determining the optimal processing conditions to achieve the desired product properties and in shortening the alloy development cycle.

NIST/MIT NEUTRON DIFFRACTOMETER OPERATIONAL

NIST scientists in cooperation with researchers at the Massachusetts Institute of Technology (MIT), have completed development of a new, state-of-the-art powder neutron diffractometer for materials research at the NIST Reactor. The instrument is a 32-detector ultra high resolution powder diffractometer installed at the BT-1 thermal neutron port. The new instrument features a unique array of focusing monochromators in which any one of three can be remotely selected according to the characteristics of the sample under study. This feature, along with the detector system, increases the rate of data collection by about a factor of 10 (and with better resolution) when compared to the highly productive five-detector instrument which the new one replaces.

As is now well known, Rietveld analysis of neutron powder diffraction data provides details of atomic arrangements in technologically important materials, which is not possible with other diffraction methods. With this capability, this experimental station is expected to play a major role in research programs of mutual interest to NIST, MIT, and many other industrial and university collaborators. High-temperature superconductors, advanced magnetic materials, intercalation compounds, fast-ion conductors, advanced ceramics, and catalysts are examples of materials to be characterized with the new instrument.

NIST CONDUCTS ROUND-ROBIN OF HEAT-FLOW-METER-APPARATUS FOR THERMAL INSULATION TESTING

Under the auspices of ASTM Committee C-16 on thermal insulation, NIST has begun the first phase of a round-robin to investigate the precision of small heat-flow-meter apparatus. The heat-flow-meter apparatus is used widely by the insulation industry to determine the thermal conductivity of insulation and building products as both a research tool and for quality control. Presently, the precision of the small class of heat-flow-meter apparatus has not been determined. Using NIST's 1 m guarded hot plate, a NIST scientist has characterized the thermal conductivity of three specimens of fibrous-glass board for circulation to 14 participating laboratories in the United States and Canada. Results of the round-robin will be used to modify the precision and bias statement of the ASTM test method for heat-flow-meter apparatus (ASTM C518).

THERMAL ENVELOPE DESIGN GUIDELINES

NIST has published a thermal envelope design guide for federal office buildings for the General Services Administration, which addresses design issues related to the thermal integrity and airtightness of office building envelopes. This document was developed to present current guidance on thermal envelope design and performance from the building research, design, and construction communities in a form that will assist building design professionals in designing office buildings with improved performance. The resultant performance improvements include reduced energy consump-

tion, the ability to maintain thermal comfort within the building, and improved indoor air quality.

While office building envelopes are generally successful in meeting a range of structural, aesthetic, and thermal requirements, poor thermal envelope performance often occurs due to the existence of defects in the thermal insulation, air barrier, and vapor retarder systems. These defects result from designs that do not adequately account for heat, air, and moisture transmission, with many being associated with inappropriate or inadequate detailing of the connections of envelope components. Other defects result from designs that appear adequate but cannot be constructed in the field or will not maintain adequate performance over time. Despite the existence of these thermal-envelope performance problems, information is available to design and construct envelopes that do perform well. To bridge the gap between available knowledge and current practice, NIST developed these guidelines based on research performed, published research results, guidance from the design and construction industry, and input from selected technical experts in the field.

NIST PUBLISHES MANUAL FOR DATA ADMINISTRATION

NIST Special Publication 500-208, Manual for Data Administration, provides guidance to data administrators in developing and carry out a data administration (DA) function. It assists data administrators in establishing an organization's DA function, or with adding, reviewing, developing, or implementing related activities and responsibilities. The manual resulted from 2 years of research and development by the Data Administration Standards and Procedures Working Group, sponsored by the National Capital Region chapter of the Data Administration Management Association.

NIST HOSTS SIGCAT '93

NIST recently hosted the second National Conference and Educational Symposium on Compact Disc-Read Only Memory (CD-ROM) Applications and Technology (SIGCAT '93), which was sponsored by the U.S. Geological Survey in conjunction with the Federation of Government Information Processing Councils. Addressing the theme of "Mainstreaming CD-ROM," the conference featured government and industry speakers on key CD-ROM issues involving software, standards, production, and media reliability. Topics included data compression, handicapped environments, education, licensing, encryption, and software. The applications track showcased over 20 separate CD-ROM success stories from the federal sector.

INTEGRATED SERVICES DIGITAL NETWORK (ISDN) AGREEMENTS PUBLISHED

NIST Special Publication 823-3, North American Integrated Services Digital Network Users' Forum (NIUF) Agreements on ISDN, compiles the existing NIUF agreements for an ISDN developed and approved in the forum as of October 1991. ISDN is an advanced telecommunications technology which allows the exchange of voice, data, and image information concurrently over telephone lines. The document also references the conformance tests that had been completed by the NIUF.

Standard Reference Materials

STANDARD REFERENCE MATERIAL 2520—OPTICAL FIBER DIAMETER STANDARD

The use of fiber optics in communication has revolutionized the way in which information is transferred between locations. Maintaining the integrity of the information during transfer requires stringent quality control of fiber geometry on a micrometer scale.

The Standard Reference Materials Program announces the availability of Standard Reference Material (SRM) 2520 for calibrating video microscopes or gray-scale systems used for fiber geometry measurements. Certified values, in micrometers, are given for the diameter of a bare, cleaved end of a single-mode fiber measured with a contact micrometer approximately 1 mm from the fiber end. Individual diameters at four angular orientations, 0, 45, 90, and 135 are given in addition to the mean diameter.

SRM 2520 consists of a short length of bare optical fiber in an aluminum housing constructed with a barrel mechanism which allows the certified end of the fiber to be pushed out and rotated into position for use and then retracted back into its protective housing for storage. The entire housing and an attached 102 m length of fiber pigtail are mounted in an aluminum block equipped with a screwdown cover. Each SRM unit measures $14 \times 8.2 \times 2$ cm and is individually serialized.

Volume 98, Number 3, May–June 1993
Journal of Research of the National Institute of Standards and Technology

STANDARD REFERENCE MATERIAL 2063a—TRANSMISSION ELECTRON MICROSCOPE THIN FILM

Microanalysis using a range of analytical techniques based on x-ray spectrometry is playing an increasing role in many fields of science. Accurate calibration of chemical composition in microanalysis cannot be performed using Standard Reference Materials developed for bulk chemistry, primarily because of homogeneity considerations.

The Standard Reference Materials Program announces the availability of Standard Reference Material 2063a, replacing SRM 2063 which has been out of stock for a number of years. SRM 2063a consists of a mineral glass film that has been deposited onto a 20 nm carbon support film on a 3 mm diameter copper transmission electron microscope grid. The film is certified for the concentrations of Mg, Si, Ca, Fe, and O, which are nominally 8, 25, 12, 11, and 43 weight percent, respectively. An information value is given for weight percent Ar, and information values are also given for film density and thickness.

STANDARD REFERENCE MATERIAL 3144—RHODIUM SPECTROMETRIC SOLUTION

The automotive industry and the precious metals industry have long recognized the need for highly accurate calibration solutions for valuation of the precious metals which are the active agents in automotive catalytic converters. Rhodium catalyzes the conversion of nitrogen oxide emissions to harmless nitrogen gas. While it is the least abundant of the precious metals in a catalytic converter, its value equals that of the Pt and Pd, by virtue of its greater scarcity in precious metal ores.

The Standard Reference Materials Program announces the availability of Standard Reference Material (SRM) 3144, rhodium spectrometric solution, to meet this need. The platinum and palladium spectrometric solutions (SRMs 3140 and 3138) also required for this purpose have been available since 1986. NIST collaborated with industry in verifying the stoichiometry of rhodium salts and in establishing totality of the dissolution of rhodium metal to provide two alternate routes to the preparation of the solution, agreeing within the required few parts per thousand. SRM 3144 is available in 50 mL units of solution containing 1000 ug/mL of Rh in 10 percent (V/V) HCl.

CERTIFICATION OF HIGH-PURITY SILVER AS STANDARD REFERENCE MATERIAL 1746—A FREEZING-POINT STANDARD

Scientists at NIST, with support from the Standard Reference Materials Program, recently completed the certification of Standard Reference Material (SRM) 1746 as a freezing-point standard. This new SRM of high-purity silver (99.999 97 percent) can be used for realizing one of the defining thermometric fixed points (961.78 °C) of the International Temperature Scale of 1990 (ITS-90) for the calibration of standard platinum resistance thermometers and optical radiation thermometers. The fixed point is realized as the plateau temperature (or liquidus point) of the freezing curve of the high-purity silver at 101325 Pa.

The thermal tests used to confirm the purity of the silver, and to ascertain that the silver is suitable as a freezing-point standard, involved the evaluation of three silver freezing-point cells, each containing 1400 g of the silver. The freezing and melting curves obtained for these cells were compared directly with the NIST laboratory standard. Based on the random samples of silver tested, the range of the melting temperatures for this material should not exceed 0.003 °C. The plateau temperatures for freezing curves of this silver should not differ by more than 0.001 °C from each other, nor by more than 0.002 °C from the assigned temperature.

The metal is in the form of millimeter-size "shot" and is packaged in 300 g units in the presence of argon in plastic envelopes. The "shot" form of the silver minimizes the need to handle the metal during freezing-point cell construction. This material provides a valuable measurement tool for those industries, ranging from aerospace to chemicals, which require accurate temperature standards to monitor a wide variety of industrial processes.

STANDARD REFERENCE MATERIALS 1710–1715—ALUMINUM ALLOYS 3004 AND 5182

When using recycled aluminum in the food canning industry, it is essential that the aluminum be free of toxic heavy metals such as Pb and Cd. Quality control procedures designed to limit the concentration of Pb and Cd in food cans require the availability of aluminum standards whose concentrations of Cd and Pb are accurately known at very low concentration levels.

The Standard Reference Materials Program announces the availability of six aluminum alloys, SRMs 1710–1715, specially prepared to include certified low levels of Cd and Pb to meet this need. Three (SRMs 1710–1712) are prepared of aluminum alloy 3004, spiked to cover the Pb content range of approximately 18 to 156 μg/g, and the Cd content range of approximately 8 to 51 μg/g. SRMs 1713–1715 cover the same Pb and Cd ranges in alloy 5182. Isotope dilution thermal ionization mass spectrometry analyses were performed as the primary certification analyses. This method is the most precise and accurate of the methods available at NIST. Additional analyses were performed by a number of atomic spectrometric methods that might be utilized in SRM user laboratories.

The SRMs are available in the form of discs approximately 63 mm (2.5 in) in diameter and 19 mm (0.75 in) thick. The industry will use these SRMs primarily as calibration standards for optical emission and x-ray fluorescence analyses monitoring recycling plant operations.

REFERENCE MATERIALS 8412–8418 AND 8432–8438 AGRICULTURAL/FOOD REFERENCE MATERIALS

To meet the requirements of nutritional labeling and food safety programs, it is necessary to have reference materials for which "best estimate" concentrations of essential nutrients and toxic contaminants are well-established.

The NIST Standard Reference Materials Program announces the availability of 10 new Agricultural/Food Reference Materials (RMs) to complement previously available RM 8412 Corn Stalk and RM 8413 Corn Kernel. These RMs are: 8414–Bovine Muscle Powder, RM 8415–Whole Egg Powder, RM 8416–Microcrystalline Cellulose, RM 8418–Wheat Gluten, RM 8432–Corn Starch, RM 8433–Corn Bran, RM 8435–Whole Milk Powder, RM 8436–Duram Wheat Flour, RM 8437–Hard Red Spring Wheat Flour, and RM 8438–Soft Winter Wheat Flour.

Each RM is accompanied by a report of investigation that gives the "best estimate" concentrations in addition to methods and procedures employed to arrive at the recommended value. These reports list "best estimate" or information only concentrations for more than 30 elements in each material.

RMs 8412–8418 and 8432–8438 are available in units of approximately 35 g, depending on the individual RM.

STANDARD REFERENCE MATERIAL 931e–LIQUID ABSORBANCE STANDARD FOR ULTRAVIOLET AND VISIBLE SPECTROPHOTOMETRY

Since more than 90 percent of the determinations in the clinical laboratory involve photometric measurements, an important task of the laboratory worker is to ensure that the instrument is performing properly and reliably in both the UV and visible regions of the photometric scale. The implementation of the new Clinical Laboratory Improvement Amendments of 1988 in clinical labs makes this task vital. The types of calibrations needed for quality assurance documentation require reference standards having certified absorbances at differing concentration levels.

The Standard Reference Materials Program announces the availability of the renewal issue of Standard Reference Material (SRM) 931e, for the routine critical evaluation of daily working standards used in spectrophotometry. The SRM also is used to calibrate and verify the accuracy of the photometric scale of narrow effective spectral bandpass spectrometers.

SRM 931e is certified as solutions of known net absorbencies, for a 10.00 mm measurement pathlength, at four specific spectral wavelengths: 302, 395, 512, and 678 nm. Four known absorbencies, for a 10.00 mm pathlength nominally 0.0 (blank), 0.3, 0.6, and 0.9 are provided.

SRM 931e is provided as three sets of the above four liquid filters; each set is packaged in its own tray. Each set consists of four ampoules containing approximately 10 mL each of the individual liquid filter solutions. Each ampoule is prescored for ease in opening and transferring to the measurement cell.

Standard Reference Data

NEW BIOTECHNOLOGY DATABASE ON LIPIDS OFFERED

Detailed properties on more than 900 lipids are just a few keystrokes away thanks to a new database available from NIST. The system, known as LIPIDAT, holds a library of information on lipid molecules in a single, easy-to-access database. The personal computer database lets a user select lipids from among the 50 more common lipid structures, or search for lipids by traits such as chain, headgroup and backbone types. LIPIDAT was developed at Ohio State University with a grant from

the National Science Foundation through NIST. The database is designed for IBM-compatible computers with MS-DOS or PC-DOS version 2.1 or later, and with at least 512 kB memory. It also can be run on Macintosh computers having a PC emulator program or card. LIPIDAT is available from the NIST Standard Reference Data Program for $265. For more information contact the SRDP, A320 Physics Building, NIST, Gaithersburg, MD 20899-0001, (301) 975-2208, fax: (301) 926-0416.

1993 SRD PRODUCTS CATALOG PUBLISHED

The NIST Standard Reference Data Program has been providing critically evaluated, high-quality data for a wide range of applications to industry, government and academic institutions for more than 30 years. The NIST Standard Reference Data Products Catalog 1993 (SP 782, 1993 Edition), lists 80 data publications and computerized databases available from SRDP and other sources. Data compilations are available in the following areas: analytical chemistry, atomic physics, biotechnology, chemical kinetics, materials properties, molecular structure and spectroscopy, thermodynamics and thermochemistry, and thermophysical properties of fluids. Also provided are special databases of binary images, structured forms and optical character recognition. For a copy of SP 782, 1993 Edition, send a self-addressed mailing label to the SRD Program, A320 Physics Building, NIST, Gaithersburg, MD 20899-0001, (301) 975-2208, fax: (301) 926-0416.

NIST CHEMICAL KINETICS DATABASE UPDATED

The best-selling Standard Reference Database, Number 17, has been updated. Version 5.0 of the Chemical Kinetics Database contains 23500 rate constants, 7800 reactions, 3800 compounds, and 6000 literature references. This database is a valuable tool for producers and users of gas-phase kinetic data and allows searching by reactants, author, reactions in a particular paper, and reactions producing a given product. The literature is current through 1992.

NIST SURFACE STRUCTURE DATABASE RELEASED

Standard Reference Database 42 is a new and powerful tool for scientists to assess and compare detailed atomic-scale structures of surfaces and interfaces obtained from experiments. Nearly 600 structure analyses are included, covering a wide variety of materials of scientific and technological importance, including catalysts. Extensive search facilities enable the user to locate desired structures rapidly. The database may be searched by chemical element(s) in substrate or adsorbate, crystallographic face of substrate, substrate lattice, surface superlattice, substrate or overlayer space-group symmetry, experimental technique, author, journal, or year of publication.